Design of Carbon Nanotube-based Sensors for the Detection of Catalytic Activity

par Béatrice Vanhorenbeke

Thèse effectuée en cotutelle
à l'Institut de la Matière Condensée et des Nanosciences
Université catholique de Louvain (Belgique)
et
au Département de Chimie
Faculté des Arts et des Sciences
Université de Montréal (Canada)

Thèse présentée à l'Université catholique de Louvain en vue de l'obtention du grade de Docteur en Sciences et à la Faculté des Etudes Supérieures et Postdoctorales de l'Université de Montréal en vue de l'obtention du grade de *Philosophiæ Doctor* (Ph.D.) en Chimie

Août 2016

COMMITTEE COMPOSITION

Thesis supervisors

Prof. Sophie HERMANS (Université catholique de Louvain, Belgium)

Prof. Richard MARTEL (Université de Montréal, Canada)

Committee members

Prof. Jacques DEVAUX, *President* (Université catholique de Louvain, Belgium)

Prof. Christian REBER, *co-President* and *Secretary* (Université de Montréal, Canada)

Dr. Pascale CHENEVIER (CEA/Grenoble, INAC, France)

Prof. Alexandru VLAD (Université catholique de Louvain, Belgium)

Prof. Antonella BADIA (Université de Montréal, Canada)

Prof. Andrea BIANCHI, *Dean representative* (Université de Montréal, Canada)

RÉSUMÉ

Les nanotubes de carbone possèdent des propriétés uniques qui en font des matériaux prometteurs dans de nombreux domaines. En particulier, leur structure quasi-unidimensionnelle et leur rapport surface/volume élevé font de ces matériaux des candidats de choix pour leur utilisation comme senseurs. A ce jour, les études concernant l'utilisation des nanotubes de carbone pour la conception de senseurs se concentrent principalement sur la détection de gaz, de molécules biologiques ou chimiques. Dans le cadre de cette thèse, nous nous intéressons à l'utilisation des nanotubes de carbone comme senseurs pour détecter en temps réel une transformation chimique, au travers d'une réaction catalytique.

Pour ce faire, des catalyseurs supportés sur nanotubes de carbone sont préparés grâce à des méthodes de fonctionnalisation appropriées de ces matériaux. En pratique, nous développons dans ce travail deux approches distinctes pour la préparation de catalyseurs supportés sur nanotubes de carbone. D'une part, nous mettons au point une méthode de fonctionnalisation monovalente des nanotubes de carbone, permettant de déposer des nanoparticules métalliques à la surface des nanotubes en vue de la préparation de catalyseurs hétérogènes supportés. A cette fin, les nanotubes sont dans un premier temps fonctionnalisés par des sels de diazonium. Cette première étape permet d'établir un point d'accroche sur les nanotubes permettant une *post*-fonctionnalisation ultérieure, en vue de l'ancrage de clusters métalliques. Une étape d'activation thermique permet ensuite de former des nanoparticules métalliques, au départ de ces

Résumé

---

précurseurs moléculaires. D'autre part, un catalyseur homogène supporté est préparé via l'ancrage de complexes à base de Pd(0) sur des nanotubes de carbone fonctionnalisés de manière à présenter des liaisons triples. Pour ce faire, les nanotubes de carbone sont fonctionnalisés de façon divalente, par la réaction de Bingel-Hirsch. Cette approche divalente assure l'ancrage covalent des sites actifs, tout en préservant la conductivité électrique des nanotubes de carbone.

Quelle que soit l'approche envisagée, la préparation de ces catalyseurs est attentivement suivie par des méthodes classiques de caractérisation telles que la spectroscopie Raman, la spectroscopie des photoélectrons X et l'analyse thermogravimétrique. En outre, une caractérisation électrique est également effectuée à chaque étape de la préparation des catalyseurs, afin d'étudier l'influence des différentes étapes de fonctionnalisation sur les propriétés électriques du nanotube.

Ces matériaux sont ensuite testés en catalyse, pour la transformation hydrolytique du diméthylphénylsilane en diméthylphénylsilanol ou pour la réaction de couplage croisée de Suzuki-Miyaura, respectivement pour les catalyseurs hétérogènes et homogènes supportés. L'activité de ces catalyseurs, ainsi que leur recyclabilité, est étudiée grâce à un suivi réactionnel par chromatographie gazeuse.

Enfin, nous démontrons dans cette thèse la possibilité d'utiliser les nanotubes de carbone comme senseurs pour détecter *in situ* l'activité catalytique. A cette fin, des mesures électriques en temps réel sont enregistrées au cours de la réaction de catalyse. L'activité catalytique se traduit par des changements de la conductivité des nanotubes au cours du temps.

ii

Mots-clés : Nanotubes de carbone − senseurs − catalyse − fonctionnalisation − transport électrique

ABSTRACT

Due to their outstanding properties, carbon nanotubes are being considered as promising materials in various fields. Namely, their quasi-one-dimensionality and their high surface/volume ratio make them ideal candidates for sensing applications. To date, studies dealing with the use of carbon nanotubes in sensing mainly focus on gas, biological and chemical molecules detection. In this thesis, we aim to use carbon nanotubes as sensors for the real-time detection of a chemical transformation through a catalytic reaction.

In order to do this, carbon nanotube supported catalysts are prepared thanks to appropriate functionalization methods. In practice, we develop in this work two distinct approaches for the preparation of carbon nanotube supported catalysts. On one hand, we develop a monovalent functionalization pathway for the deposition of metallic nanoparticles on carbon nanotube surface. For this purpose, carbon nanotubes are first functionalized by diazonium salts. This first step allows to bind a tethering point for a subsequent *post*-functionalization. Metallic clusters are then coordinated on these functionalized moieties. A thermal activation step ensures the formation of metallic nanoparticles from these nanoparticle molecular precursors. On the second hand, a homogeneous supported catalyst is prepared by anchoring Pd(0) complexes on carbon nanotube surface. In order to do this, carbon nanotubes are divalently functionalized by Bingel-Hirsch reaction to present dangling triple bonds at their surfaces. This divalent approach ensures a covalent anchoring of the active sites on the nanotube surface, while preserving their electrical conductivity.

Abstract

___

Whichever the considered approach, the catalyst preparation is carefully analyzed by common characterization techniques, such as Raman spectroscopy, X-ray photoelectron spectroscopy and thermogravimetric analysis. Moreover, the materials are also electrically characterized at each step of the catalyst preparation process. This electrical characterization allows to study the influence of the different steps of the functionalization strategy on the nanotube electrical properties.

These materials are then tested in catalysis, for the hydrolytic transformation of dimethylphenylsilane in dimethylphenylsilanol or for the Suzuki-Miyaura cross-coupling reaction, respectively for heterogeneous and homogeneous supported catalysts. The activity and recyclability of these catalysts is monitored by gas chromatography.

Finally, we demonstrate in this thesis the possibility of using carbon nanotubes as sensors for the *in situ* detection of catalytic activity. For this purpose, real-time electrical measurements are recorded during the catalytic reaction. The catalytic activity is revealed by fluctuations of the nanotube conductivity over time.

Keywords: Carbon nanotubes − sensors − catalysis − functionalization − electrical transport

TABLE OF CONTENTS

LIST OF TABLES

List of Tables

LIST OF FIGURES

List of Figures

films on Si/SiO$_2$ substrates.

hydrosilanes on the surface of metal nanoparticles.

LIST OF ABBREVIATIONS
AND SYMBOLS

AcOEt	Ethyl acetate
a_1, a_2	Primitive vectors of the graphene lattice
AAS	Atomic Absorption Spectroscopy
AFM	Atomic force microscopy
APTES	(3-aminopropyl)triethoxysilane
CBr_4	Carbon tetrabromide
C_h	Helicity vector
CNT	Carbon nanotube
COD	Cyclooctadiene
CVD	Chemical vapor deposition
dba	Dibenzylideneacetone
DBU	1,8-diazabicyclo[5.4.0]-7-undecene
DCM	Dichloromethane
DOS	Density of states
DWCNT	Double-walled carbon nanotube
EA	Elemental analysis
EDX	Energy-dispersive X-ray spectroscopy
E_F	Fermi level
EtOH	Ethanol
f-CNTs	Functionalized carbon nanotubes
FET	Field-effect transistor
GC	Gas chromatography
HPLC	High performance liquid chromatography

ICP-AES	Inductively coupled plasma atomic emission spectroscopy
ICP-OES	Inductively coupled plasma optical emission spectroscopy
I_{DS}	Drain-source current
IR	Infrared spectroscopy
(m)	medium band
(s)	strong band
(vs)	very strong band
(w)	weak band
LA	Laser ablation
MeCN	Acetonitrile
MeOH	Methanol
MS	Mass spectrometry
MWCNT	Multi-walled carbon nanotube
NMR	Nuclear magnetic resonance
NP	Nanoparticle
o-DCB	1,2-dichlorobenzene
p-CNTs	Pristine carbon nanotubes
PDMS	Polydimethylsiloxane
PEG	Poly(ethylene glycol)
PEI	Poly(ethylene imine)
PMMA	Polymethylmethacrylate
PPh_3	Triphenylphosphine
PPNCl	Bis(triphenylphosphoranylidene)ammonium chloride
PTFE	Polytetrafluoroethylene
PVDF	Polyvinylidene fluoride
RBM	Radial breathing mode
RIE	Reactive ion etching
RIE	Reactive ion etching

RT	Room temperature
SEM	Scanning electron microscopy
SMU	Source measure unit
STEM-EDX	Scanning transmission electron microscopy coupled with energy dispersive X-ray
SWCNT	Single-walled carbon nanotube
TEM	Transmission electron microscopy
TFA	Trifluoroacetic acid
TGA	Thermogravimetric analysis
V_{DS}	Drain-source voltage
V_G	Gate voltage
XAS	X-ray absorption spectroscopy
XPS	X-ray photoelectron spectroscopy
XRD	X-ray diffraction

"Information is not knowledge.
The only source of knowledge is experience."
Albert Einstein

ACKNOWLEDGEMENTS

Si la thèse est avant tout un cheminement scientifique, l'aboutissement de plusieurs années de recherche sur un sujet passionnant et prometteur, elle ne se limite pas qu'à cela. C'est aussi, et surtout, une véritable expérience humaine, parsemée de joies comme de déceptions, de bonnes nouvelles mais aussi d'embûches. Une thèse, c'est un apprentissage accéléré de la vie. Vous l'aurez compris, une thèse est déjà une aventure en soi, alors que dire d'une thèse en cotutelle... Malgré les difficultés quelquefois rencontrées au cours de ce périple, cette thèse a été enrichissante tant d'un point de vue scientifique qu'humain. Ce doctorat m'a permis d'apprendre à mieux me connaître et à découvrir mes forces et mes faiblesses. Mais un doctorat est loin d'être un travail solitaire. En effet, ce travail n'aurait pas pu être réalisé sans le soutien de nombreuses personnes.

J'aimerais tout d'abord remercier mes deux promoteurs, les professeurs Sophie Hermans et Richard Martel. Sophie, merci d'avoir accepté de mettre au point cette collaboration et d'avoir cru en moi. Richard, merci de m'avoir accueillie dans ton laboratoire au Canada, merci pour ta confiance, ta compréhension et tes conseils avisés, merci de nous transmettre à tous ton amour de la recherche. A deux, vous avez su m'apporter l'expertise et les moyens nécessaires à l'élaboration de cette thèse.

Je remercie également les membres de mon jury, qui ont accepté de lire cette thèse et de l'améliorer grâce à leurs précieux conseils et commentaires.

Merci aussi à tous les membres de mon labo belge. Merci à Charly, les deux Nath, Nico, Antoine, Anaëlle, Nadya, Dodji, Samuel et Sébastien. Je remercie tout particulièrement Francis... co! pour son soutien et sa gentillesse, Anto pour sa bonne humeur, Tommy pour les nombreux moments passés ensemble, dans et en-dehors du labo, qui ont vu naître une réelle amitié, et Flo, avec qui j'ai partagé tout mon parcours universitaire, et que j'espère revoir par la suite, malgré la distance ;-).

Je tiens également à remercier tous les membres du groupe Martel. Merci à Nathalie pour son accueil au sein du labo, à François et Delphine pour leur gentillesse, leur aide et leurs nombreuses discussions scientifiques. Merci aussi à Minh, Philippe, May, Pierre, Maxime et Benoit. Merci tout particulièrement à Saman, Dhan et Natasha pour la bonne ambiance au sein du bureau.

Merci également à Patrick et Annie-Claude, ma "famille du Québec", pour leur accueil, leur gentillesse, et les nombreux bons moments partagés avec eux. Les soirées hockey, la musique de Patrick et les cocktails d'Annie-Claude, le montage de meubles Ikea jusqu'au bout de la nuit, la gentillesse de vos familles respectives, sans oublier ce nouvel an mémorable en Beauce, ne sont qu'une petite partie des nombreux souvenirs que je garde de mes passages à Montréal à vos côtés. J'espère de tout cœur que ce n'est que le début d'une vraie amitié, et que malgré la distance, nous aurons l'occasion de nous revoir !

Enfin, je tiens à remercier Jean-Pierre, pour l'amour et le soutien qu'il a su m'apporter au quotidien. JP, merci pour tes encouragements et ton soutien. Tu as toujours su être présent pour moi, même lorsqu'un océan nous séparait, et je ne t'en remercierai jamais assez. Sans toi, je ne serais pas devenue la personne que je suis aujourd'hui. Merci pour tout !

CHAPTER I - INTRODUCTION

Abstract

This thesis aims at exploring ways to detect dynamically chemical reactions at the level of single events. For this purpose, carbon nanotubes constitute ideal candidates, since their electrical properties are very sensitive to slight modification of their environment. As a result, carbon nanotube based sensors are appropriate tools to probe chemical reactions in real-time. In this thesis, we selected catalysis for its ability to induce charge transfer reactions at the surface of the active sites.

This chapter intends to introduce the context of this thesis. Hence, the first part of this introduction will be devoted to sensors, a technology which is omnipresent in our modern world. We will particularly focus on current advances in the field of carbon nanotube-based sensors. A second section will provide an overview of the techniques commonly used for in situ detection of catalysis. Our attention will be focused on operando catalysis, a field in constant development. Finally, this chapter will be concluded with a description of the thesis objectives and an outline of the present manuscript.

The key concepts required for the understanding of this thesis will be developed further in the next chapter.

I.1 Sensors

Sensors are inherent parts of the world. They can be either natural or man-made. Humans are endowed with five senses: hearing, sight, smell, taste and touch. These five senses can be regarded as natural sensors, enabling us to detect various stimuli.[1] The perception of sound is based on the transformation of vibration waves to electrical nerve impulses. This transformation is ensured by the ear, while the interpretation of the electrical nerve signal is done by the brain. In a similar way, the sight results from the capacity of the eyes to generate electrical nerve impulses from the visible light rays reflected from objects. The brain is then able to recreate an image from these electrical impulses. Smell and taste perceptions are ensured by sensory organs: olfactory receptors and taste buds, respectively. Finally, touch results from the stimulation of neural receptors located on the skin. Certain animals and plants also possess other natural sensors, which act as detection methods for their protection. The chameleon changes its color as camouflage,[2] while carnivorous plants are able to trap their prey, thanks to the presence of trigger hairs.[3]

Sensors have also been fabricated by humans. In 1714, Fahrenheit invented the mercury thermometer,[4] which can be viewed as a temperature sensor: upon temperature variation, the mercury contained in this thermometer indeed dilates or compresses. As a consequence, the mercury level changes, enabling us to detect the temperature change.

Today, more than ever, our daily lives are surrounded by sensors. Our houses are equipped with smoke detectors, room thermostat, motion and light detectors, alarm systems equipped with windows and doors sensors, etc.[5] Modern cars are equipped of up to hundreds of sensors, such

as tire pressure detector, oil and fuel level gauges, automatic doors and windows, cruise control, rain detectors, parking assistance, etc.[5] Often without realizing it, we use other sensors everyday: when using household appliances, when passing through automatic doors when entering a commercial center, when pushing on touch-sensitive elevator buttons, when using our smartphones, etc. Sensors are also present in very common medical devices, such as glucose and insulin test systems, ethyl tests, blood pressure tests and pregnancy tests.[5]

This non-exhaustive list of practical applications of sensors emphasizes the importance of these devices for innovation progress. As a consequence, many efforts are placed on the development of improved sensors.

I.1.1   *Definition and characteristics*

A sensor can be defined as a device that responds to a chemical, physical or biological event or stimulus by generating a processable signal, most of the time electrical or optical (Figure I.1).[1,5,6] Generally, a sensor is composed of a sensitive element and a transducer. As it name suggests, the sensitive element is able to detect a physical, chemical or biological event, while the transducer converts this event in a signal that is readable by an observer or an instrument.[5,7]

Practically, different transduction processes can be involved in sensors. The processes are based on various physical phenomena, such as optical, electrical, mechanical and magnetic effects. Depending on the nature of the detected input, the sensor is called either a chemical sensor, a physical sensor, or a biosensor.
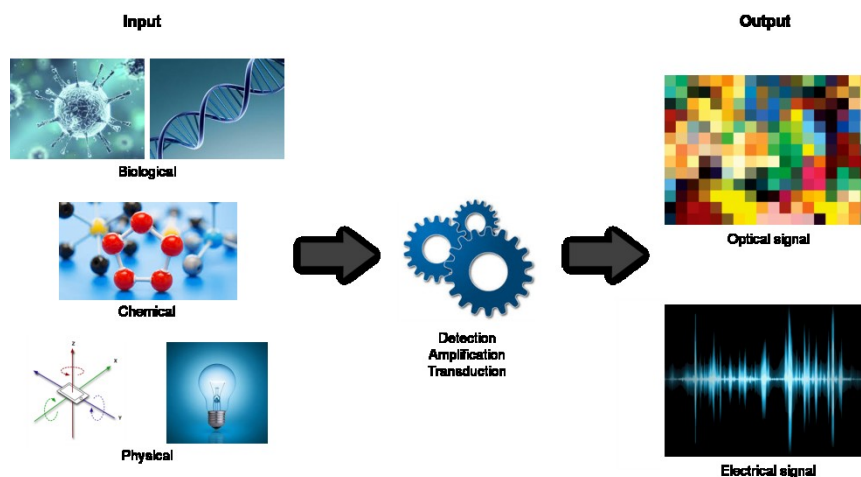
Figure I.1. Schematic representation of the sensing process: the sensor detects a biological, physical or chemical stimulus; this measurement is then converted in a readable electrical or optical signal. Figure inspired from McGrath *et al.*[7]

To be efficient, a sensor must meet several requirements such as **sensitivity** (i.e. the variation of the output response induced by a unit change of the input[5,7,8]) and **selectivity** (i.e. the ability to detect a specific analyte, without interferences of other analytes present during the measurement[5,8]). In addition, a sensor should be able to respond quickly to the external stimuli.

I.1.2   *Nanotechnology-enabled sensors*

Innovation in the field of sensors points toward the conception of sensing arrays composed of multiple sensing devices, able to selectively detect multiple analytes. Additionally, these sensing arrays are expected to be miniaturized. In this respect, nanotechnology appears to be a powerful tool.[6,8] Nanotechnology can be defined as the understanding and control of the matter at dimensions on the order of nanometer (i.e. comprised between 1 and 100 nm).[9] The interest of nanotechnology lies in the ability

to create materials exhibiting novel properties compared to their micro- or macroscopic analogues.[9,10] At the nanoscale, materials possess high surface-to-volume ratios, favoring surface reactions, such as the detection processes implied in chemical sensors. Moreover, when dealing with materials at the nanoscale, unique optical, electrical, mechanical and magnetic properties are obtained.[6,10] Since these properties are generally involved in the transduction process of sensors, nanotechnology offers the possibility to design novel sensor systems, exhibiting enhanced sensitivity and selectivity.[6,11]

Among the possible applications of nanotechnology for sensor design, semiconducting nanomaterials can be used to probe the presence of specific analytes through conductance modification. One-dimensional nanomaterials, such as carbon nanotubes (CNTs) or metal-oxide nanowires, can be advantageously used for this application. Thanks to their unidimensionality, these materials exhibit enhanced sensitivity, compared to 2D materials, as depicted in Figure I.2. Moreover, these nanomaterials can be implemented into high-density sensing arrays, thanks to an appropriate lithographic pattern.
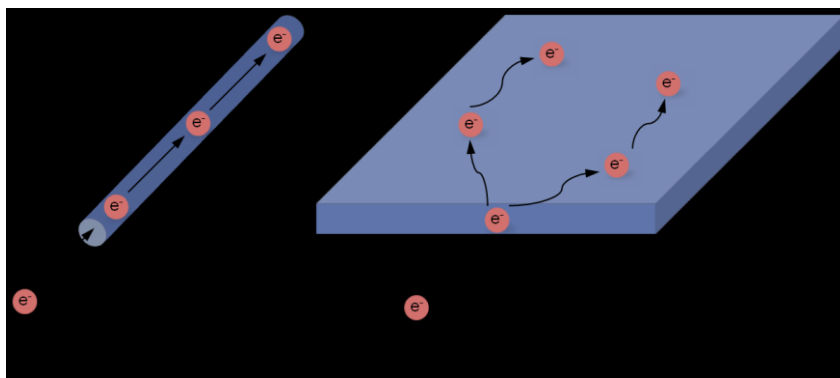
Figure I.2. Schematic representation of the localization of the electrical effects induced in 1D-nanomaterials, compared to 2D-nanomaterials. Figure inspired from [6,12].

I.1.3 *Carbon nanotube-based sensors*

I.1.3.1 Interest of carbon nanotubes for sensors

To date, thousands of studies have investigated the usability of carbon nanotubes for the design of chemical sensors. Carbon nanotubes indeed constitute ideal candidates for this application, since they exhibit remarkable electronic properties, which are extremely sensitive toward chemical changes.[11] In addition, CNTs also possess an extremely high aspect ratio, i.e. the ratio between their length and diameter. This feature facilitates their assembly in electronic devices, for an efficient detection of the chemical sensing.

Carbon nanotubes also possess extremely high surface area (ca. 1600 m^2g^{-1} for single-walled carbon nanotubes[i]).[13] This property, coupled with the fact that each atom is exposed at the surface (at least for SWCNTs), makes them particularly sensitive to variation of their chemical environment.[11] Their nanometer scale makes them particularly suitable for the detection of biological and molecular events. In addition, their all-carbon composition ensures an appropriate match for organic and biological molecules.[14]

Lastly, many efforts have been placed during the last decades on the functionalization of these materials. Such functionalization enables the

---

[i] Carbon nanotubes can be distinguished according to their number of concentric carbon cylinders: CNTs composed of only one carbon cylinder are called single-walled carbon nanotubes (SWCNTs), while CNTs composed of multiple concentric cylinders are known as multi-walled carbon nanotubes (MWCNTs).

design of very selective sensors, by anchoring specific receptor sites on carbon nanotubes.

I.1.3.2   Incorporation of carbon nanotubes in sensors

A convenient approach for the preparation of carbon nanotube-based sensors consists in integrating them into field-effect transistors (FETs). As will be deeply discussed in the next chapter, the electronic properties of CNTs allow them to be used as semiconducting channels in such electronic devices. These CNT-FETs are particularly adapted to probe environment modification, since such changes induce modifications of the nanotube electrical conductivity. Two different effects can be induced by analyte-CNT interactions: (i) charge transfer from analyte to the CNT can induce a modification of the charge carrier concentration in carbon nanotubes, which directly impacts their conductivity[11,13,14] and (ii) adsorption of analyte species can also introduce scattering sites across the nanotube, hence reducing the charge carrier mobility.[11,14,15] These two effects directly impact the nanotube conductivity. As a consequence, measuring the nanotube conductance enables to probe chemical changes in their environment.

The following section gives a brief and non-exhaustive overview of the applications of carbon nanotubes in sensing devices which have been reported so far.

It is worth noting that, besides these above-described major advantages of carbon nanotubes for sensing applications, the commercialization of carbon nanotube-based sensors is limited by the cost, reproducibility and stability of the fabricated sensors. There is indeed a need for controlled synthesis of CNTs, which would lead to reproducible

batches of CNTs. Notwithstanding the achievements developed with CNT-based technologies, substantive research efforts still need to be placed on the fabrication of reproducible and high-performance electronic devices.[16]

Despite these limitations, carbon nanotubes are particularly suited for sensing applications due to their open-structure, high sensitivity, time resolution, versatility, etc. Therefore, carbon nanotube-based sensors are mostly interesting as a tool to carry fundamental research, without foreseeable industrial perspectives in the near term.

I.1.3.3   State of the art

I.1.3.3.1   *Gas and vapor sensors*

Gas sensors are of critical importance for many applications, going from environmental considerations, toxicity control, medical applications to explosives detection for military and defense applications. Such applications require extremely sensitive and selective sensors able to operate at room temperature, three critical parameters that can be met by the use of carbon nanotubes. For this reason, numerous studies have investigated the application of carbon nanotubes in gas sensing.[11,12,17–24]

The ability of using carbon nanotubes for gas sensing was demonstrated for the first time in 2000, when J. Kong *et al.* observed that the conductance of CNTs could be significantly altered (i.e. decreased or increased) by exposure to ammonia (NH_3) or nitrogen dioxide (NO_2).[25] Figure I.3a shows the sharp decrease of CNT conductance after exposure to NH_3. On the other hand, exposure to NO_2 resulted in a large increase of the nanotube conductance (Figure I.3b). These conductance changes were attributed to charge transfer between the nanotube and the exposed gas.

8

NH_3 indeed possesses a lone pair of electrons that can be donated to the nanotube, resulting in n-doping, decreasing the intrinsic p-conductance of the nanotube. On the contrary, NO_2 is an electron-withdrawing molecule, and its exposure to CNT sensor results in a p-doping, increasing the nanotube conductance.[25]

(a)　　　　　　　(b)
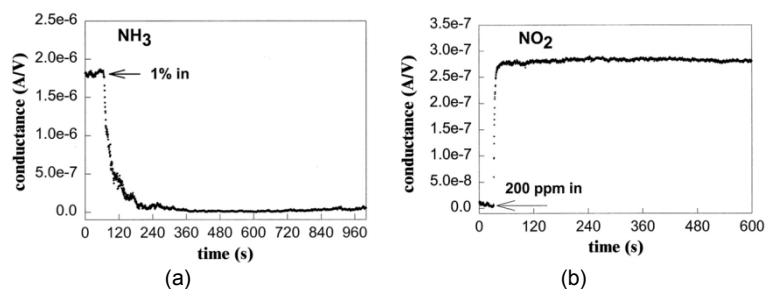
Figure I.3. Electrical response of a CNT-FET sensor to exposure of (a) NH_3 and (b) NO_2 gas. Reprinted from [25] with permission from AAAS, http://science.sciencemag.org/content/287/5453/622.

A few weeks later, P.G. Collins *et al.* reported the extreme sensitivity of carbon nanotube electronic properties toward oxygen exposure.[26] As depicted in Figure I.4, the CNT resistance decreased by 10-15 % upon exposure to air instead of vacuum. Independent experiments performed with the different constituting gas of air demonstrated that this effect is due to the presence of oxygen. This effect was later attributed to charge transfer between adsorbed oxygen/water redox couple and carbon nanotubes.[26,27]
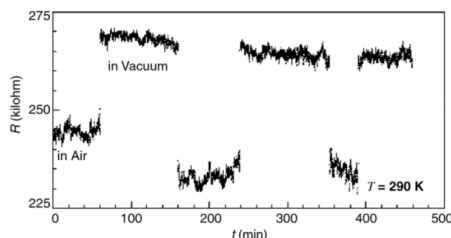
Figure I.4. Variation of the electrical resistance of a CNT film under exposure to vacuum or air. Reprinted from [26] with permission from AAAS, http://science.sciencemag.org/content/287/5459/1801.

In 2003, K. Someya *et al.* observed changes in electrical response of individual CNT-FETs upon exposure to various alcohol vapors.[28] Depending on the nature and partial pressure of the alcohol, various electrical responses were observed (Figure I.5), which was promising for the preparation of specific sensors.
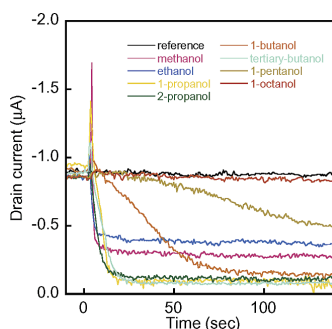
Figure I.5. Electrical response of an individual CNT-FET upon exposure to various alcohol vapors. Reprinted with permission from [28]. Copyright © 2003 American Chemical Society.

Despite these tremendous advances for the detection of gases using carbon nanotubes, these materials sometimes lack of sensitivity towards common gases such as hydrogen, methane, carbon monoxide and hydrogen sulfide. Decoration of CNTs with specific functions or metal nanoparticles was shown to enhance the sensor sensitivity and selectivity. Figure I.6 depicts the influence of various metal on the sensitivity of CNT-based sensors toward NH_3 and NO_2 exposure.[29] As can be seen, the electrical response of Pt/CNTs toward NH_3 was significantly improved compared to bare CNT-based sensors. In a similar way, addition of Au or Pt nanoparticles on CNT sensors significantly improved its electrical response on NO_2 exposure. This sensitivity increase was explained by an intimate interaction between the detected gas and the metal: the gas likely

dissociated at the metal surface, which induced the decrease of the metal work function, and a charge transfer between the metal and the nanotube.[29]
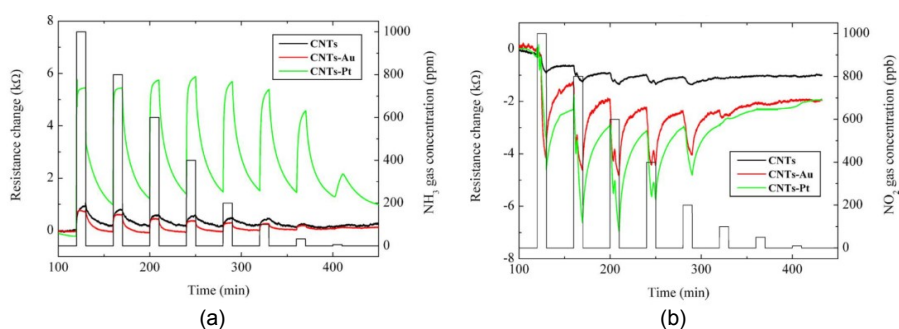
Figure I.6. Electrical response of bare-MWCNTs film and metal decorated MWCNTs films on 10 minute exposures to (a) NH_3 and (b) NO_2. Reprinted from [29] with the permission of AIP Publishing.

The detection of H_2 by metal nanoparticle decorated carbon nanotubes has also extensively been investigated.[30–36] While bare CNTs do not show sensitivity to H_2, Pd decorated CNTs are able to detect hydrogen in proportion as low as 10 ppm.[33] Pt particles also enhance CNT sensitivity toward H_2.[31,34,37] In a similar way, Pd and Sn decorated CNTs were used to detect the presence of methane,[37,38] Pd nanoparticles supported on CNTs were shown to be efficient for the detection of H_2S[37] and Rh was used to modify CNTs for the detection of CO.[37] Table I.1 summarizes the main metal-decorated carbon nanotube gas sensors reported to date.

11

Table I.1. Summary of the main metal-decorated carbon nanotube-based gas sensors.

Gas	Nature of the metal	CNT material
H₂	Pd	Individual SWCNT-FET[32]
		Thin films of MWCNTs[31]
		Network SWCNTs-FET[30]
		Thin films of SWCNTs[33,35]
	Pt	Theoretical study[34]
		Thin films of MWCNTs[31]
		Individual SWCNT-FET[37]
CH₄	Sn	Individual SWCNT-FET[37]
CO	Rh	Individual SWCNT-FET[37]
	Au	Network of SWNCTs[39]
H₂S	Pd	Individual SWCNT-FET[37]
	Au	Network MWCNTs-FET[40]
NH₃	Pt	Thin films of MWCNTs[29]
	Au	Network of SWNCTs[39]
NO₂	Pt	Thin films of MWCNTs[29]
	Au	Thin films of MWCNTs[29]
		Network of SWNCTs[39]

I.1.3.3.2   Biosensors

The detection of biological species is of critical importance for biomedical diagnostics. Since most of the biological and chemical processes involve electrostatic interactions, electronic detection emerges as a powerful alternative to optical detection methods.[15] Given the low dimensions of biological species − about 10 nanometers for proteins, while DNA possesses a diameter of about 2 nm only − the use of nanometer scale sensitive materials, such as carbon nanotubes, is desirable.[13,15,41–47]

The next sections briefly describe selected examples showing the scope of carbon nanotube-based biosensors for various biomedical applications.

a) *Protein detection*

The interaction between streptavidin and carbon nanotubes has been investigated with carbon nanotube-based bioelectronic sensors.[48] In this experiment, CNT-FETs were incubated in a buffer solution containing streptavidin and the current passing through the nanotube was measured during the incubation. As depicted in Figure I.7, the current increased gradually immediately after the addition of the protein in the solution. This current shift was interpreted as resulting from interactions between amine functions of streptavidin and carbon nanotube surface, while the gradual variation was explained by the progressive formation of a monolayer of proteins.[48]
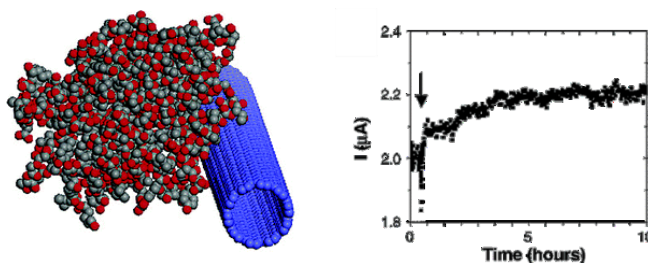
Figure I.7. Detection of streptavidin with carbon nanotube-based sensor: (left) representation of the interaction between the streptavidin and the CNT; (right) current versus time response of a CNT-FET device incubated in a solution containing streptavidin. The arrow indicates the addition of the streptavidin in the solution. Adapted with permission from [48]. Copyright © 2004 American Chemical Society.

In order to increase the sensor sensitivity and selectivity, Star *et al.* integrated biotin-functionalized carbon nanotubes in field-effect transistor, for the selective detection of streptavidin.[49] The nanotubes were preliminarly coated with two polymers. The first one, poly(ethylene imine)

(PEI), provided amino groups for the anchoring of biotin functions, while the second one, poly(ethylene glycol) (PEG), prevented the non-specific adsorption of species on the CNT surface during the sensing experiment. As depicted in Figure I.8, the nanotube conductivity was significantly decreased by the presence of the specific protein. This conductivity loss was attributed to geometric deformation induced by the formation of the biotin-streptavidin complex, leading to scattering sites on the nanotube, hence decreasing its conductivity.[49]
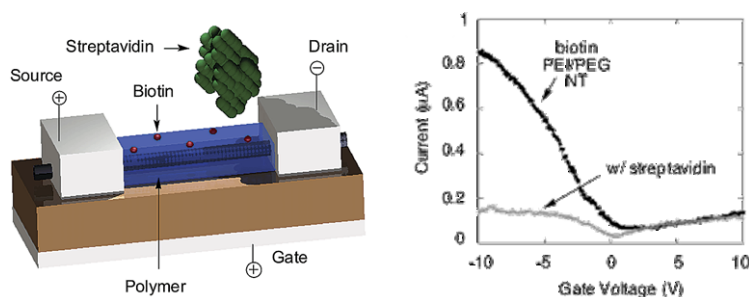
Figure I.8. (Left) Schematic representation of a biotin-functionalized CNT sensor for the selective detection of streptavidin. (Right) Electrical response of the device in absence and presence of streptavidin. Adapted with permission from [49]. Copyright © 2003 American Chemical Society.

b) *Detection of specific ligand-receptor interactions*

In a similar way, carbon nanotubes have been functionalized to anchor specific receptor sites, able to selectively detect other biomolecules.[50–52]

For example, the specific antigen-antibody interaction has been used to design CNT-based biosensors.[53,54] Li *et al.* investigated the specific recognition of a prostate specific antigen (PSA), a marker for the presence of prostate cancer, with modified carbon nanotube-based sensors.[53] First, carbon nanotubes were non-covalently functionalized to present amine

functions. This linker was then used for the coordination of PSA antibody. Finally, these PSA antibody-modified CNTs were integrated into electronic devices, and incubated in a buffer solution. As shown in Figure I.9, the introduction of the specific PSA antigen resulted in a decrease of the nanotube conductivity, in response to the antigen-antibody interaction. On the contrary, when the sensor was incubated in a solution containing bovine serum albumin (BSA), the sensor did not show any response to this protein. This result indicated the selectivity of this sensor for the desired PSA antigen, thanks to the prior functionalization of the nanotubes. Moreover, this system allowed to detect PSA in amount as low as 50 ng/ml, which is the level expected for clinical diagnosis of prostate cancer.[53]
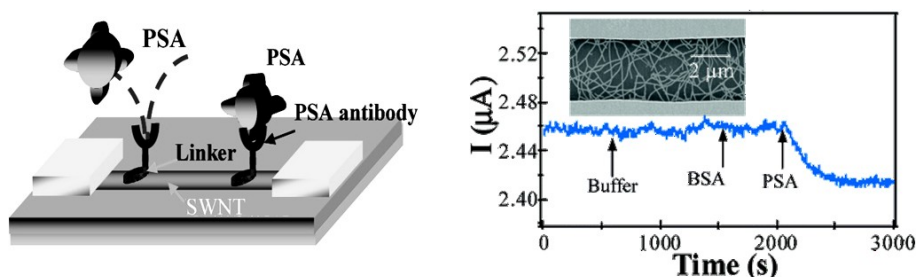
Figure I.9. (Left) Schematic representation of a CNT-based sensor designed for the specific recognition of a prostate specific antigen (PSA). Dotted line shows the anchoring and desorption of PSA on its specific antibody. (Right) Electrical response of the device in presence of the specific PSA antigen, and in presence of the non specific BSA protein. Adapted with permission from [53]. Copyright © 2005 American Chemical Society.

Based on the same principle, carbon nanotube-based biosensors have proved to be efficient for the detection of viruses, with direct applications for medical diagnosis.[55–57] Singh *et al.* demonstrated the possibility of detecting influenza virus H1N1 with carbon nanotubes.[57] Viral antibodies were immobilized on the nanotube thanks to a functionalization process,

and these biomaterials were then used to probe in real time the presence of H1N1 virus. As depicted in Figure I.10, the nanotube resistance increased in presence of the influenza virus, as a consequence of the specific antibody-antigen interaction.
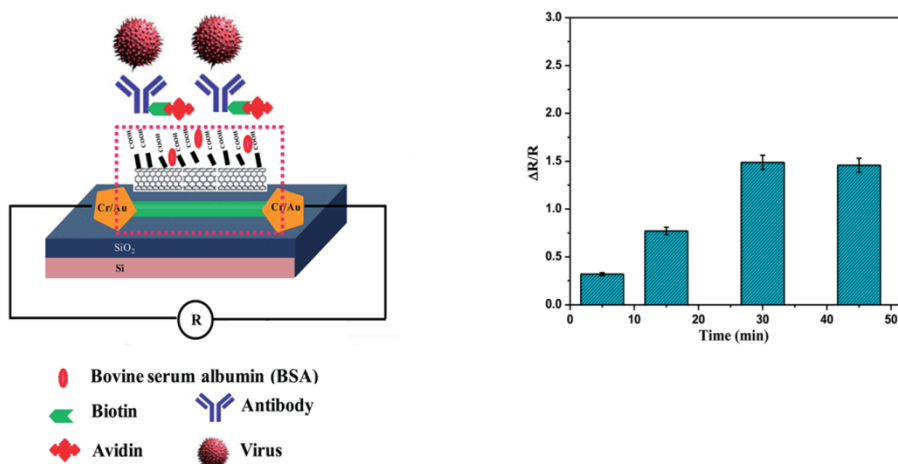
Figure I.10. (Left) Schematic representation of a CNT-based sensor designed for the specific recognition of influenza virus H1N1. (Right) Increase of the nanotube resistance for various incubation time in a solution containing the H1N1 virus. Adapted from [57] with permission of The Royal Society of Chemistry, http://dx.doi.org/10.1039/C4AN01335B.

c) *Glucose detection*

The possibility of detecting glucose with carbon nanotube-based sensors has also been widely investigated. This research area is motivated by the importance of glucose level monitoring for diabetes management.[58–61] Recently, Lerner *et al.* fabricated carbon nanotube-based glucose sensors, with high sensitivity and selectivity.[61] CNT-FET devices were non-covalently functionalized by pyrene-1-boronic acid (Figure I.11a). Upon exposure to glucose, a complex was formed between boronic acid and glucose, leading to the formation of a boronate anion. This anion had electrostatic effects on the nanotube conductivity. Figure I.11b shows the

16

electrical response of the sensor after exposure to gradually increased concentrations of glucose. As can be seen, the nanotube electrical conductivity decreased as the glucose concentration increased. The experiment was repeated on several devices with various concentration sequences, highlighting that the electrical response was only dependent on the glucose concentration, regardless the concentration sequence. Control experiments were performed to demonstrate the selectivity of this sensor for glucose (Figure I.11c).
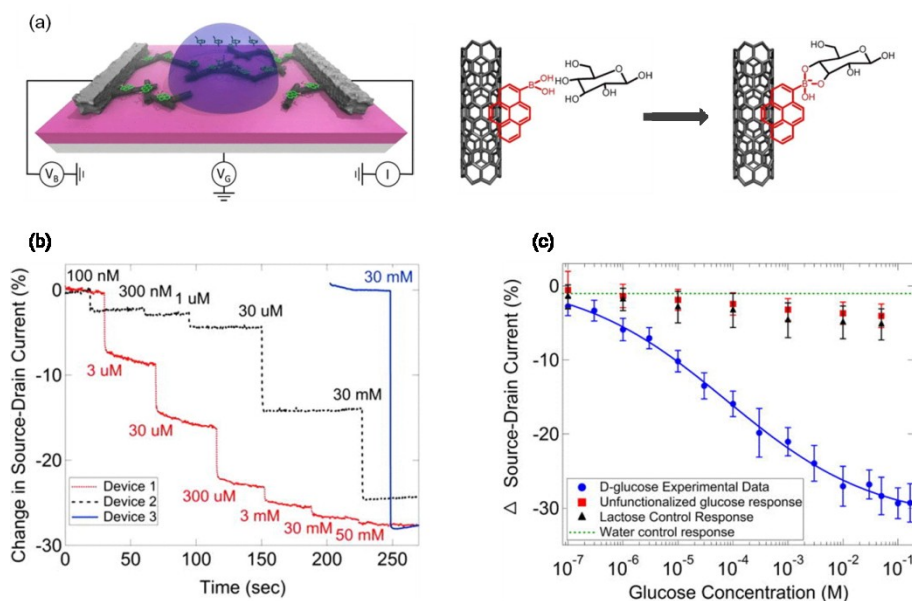
Figure I.11. (a) Schematic representation of the CNT-based glucose sensor and illustration of the glucose binding on the functionalized nanotube; (b) electrical response of three sensors upon exposure to increasing concentration of glucose, added in various sequences and (c) electrical response of the sensor as a function of glucose concentration (blue), in comparison with three control experiments: response of unfunctionalized CNT-FET to glucose (red), response of the glucose sensor on exposure to lactose (black) and response of the glucose sensor on exposure to water (green). Reprinted from [61] with the permission of AIP Publishing.

d) DNA detection

Detection of DNA sequence is of critical importance for the diagnosis of genetic diseases. Since DNA hybridization involves electrostatic interactions and charge transfer, CNT-FETs were successfully used to probe such biological processes.

C. Nuckolls and coworkers prepared carbon nanotube-based sensors for the detection of DNA hybridization at the single-molecule level.[62] They prepared individual CNT-FET by using standard lithography techniques. Following an electrochemical method previously reported,[63] they created a single point oxidation defect on the nanotube sidewall. A probe single-stranded DNA terminated by an amine function was then covalently attached to the carboxyl defect induced in the nanotube. The authors investigated the electrical response of these devices upon exposure to the complementary DNA strand. As shown in Figure I.12, the device fluctuated between two states when immersed in a solution containing the target DNA, while they did not show particular features in absence of the target DNA. Moreover, the measurements were performed at different temperatures, revealing a strong temperature dependence for the two-state conductance. At low temperature (21 °C), the device was mostly in the low-state conductance. When the temperature was increased, the high-state conductance became progressively preferential. This effect of the presence of target DNA on the conductance, as well as its temperature dependence, was attributed to scattering and charge transfer induced by the probe-target DNA hybridization. The two conductance states were attributed to an equilibrium between the double-stranded DNA (low-state conductance) and the single-stranded DNA (high-state conductance).
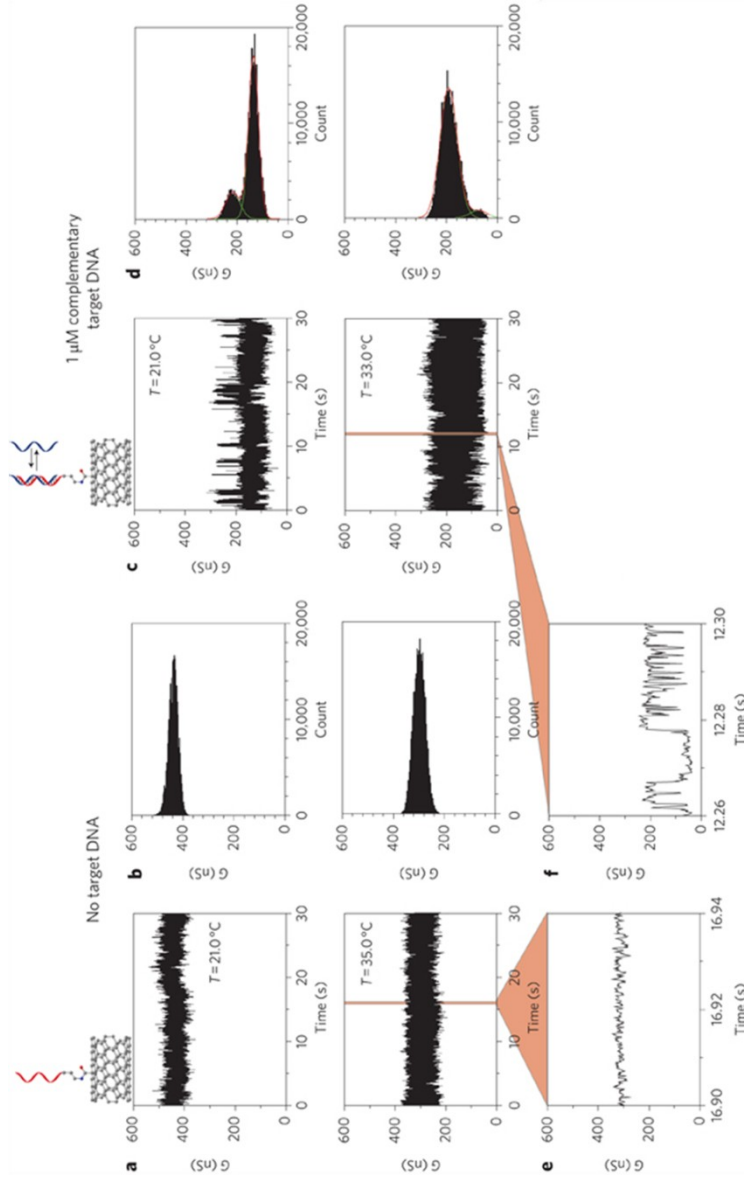
Figure I.12. Real-time electrical response of DNA hybridization: (a,c) Conductance over 30 s in absence (a) or presence (c) of the target DNA; (b,d) Conductance-based histograms of time intervals shown in (a,c); (e,f) short-time 40 ms interval for real-time conductance in absence (e) or presence (f) of the target DNA. Adapted by permission from Macmillan Publishers Ltd: Nature Nanotechnology.[62] Copyright © 2011.

e) *Detection of enzymatic reactions*

P. G. Collins, G. A. Weiss and coworkers focused their research on single-molecule enzymatic activity detection by using carbon nanotube-based sensors.[64–71] In this respect, they extensively studied lysozyme activity.[64,65,70] Lysozyme is an enzyme that catalyzes the destruction of bacterial cell wall by hydrolyzing their glycosidic bonds. This enzyme is known to possess two domains (represented in orange and yellow in Figure I.13a), which are connected by a "hinge" section. During its operation, the enzyme moves around this hinge, switching between open and closed configurations, as observed by fluorescence.[71] By linking a lysozyme on an individual CNT-FET, Collins *et al.* recorded the enzymatic activity over long duration when immersed in presence of its specific substrate (Figure I.13b). These electrical measurements allowed to analyze the response generated when the target substrate is linked to the enzyme and during the enzymatic reaction. Three different types of electronic signals were recorded, as depicted in Figure I.13c. In absence of its specific substrate, *ΔG(t)* was quite stable, without significant fluctuations. In presence of the substrate, this background was also observed approximately 5 % of the time (black curve). This electrical response was attributed to the lysozyme open configuration. The remaining 95 % of the recordings were shared between two different fluctuation states: fast fluctuations (200 to 300 s^{-1}, blue curve) and slow fluctuations (10 to 70 s^{-1}, green curve). These two-level fluctuation states were attributed to the lysozyme closed configuration, oscillating between catalytic activity (slow fluctuations) and non-productive activity (fast fluctuations).
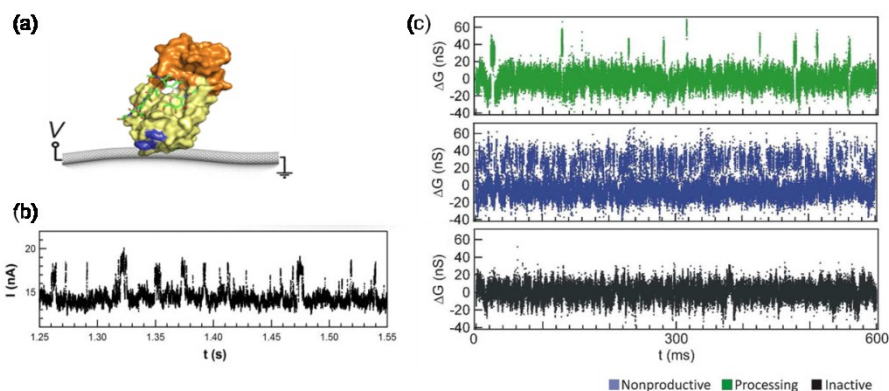
Figure I.13. (a) Schematic representation of a single-lysozyme CNT-FET sensor; (b) electrical response of the sensor on exposure to the lysozyme specific substrate and (c) three different *ΔG(t)* signal responses. Figures a and b adapted with permission from [67]. Copyright © 2013, American Chemical Society. Figure c adapted with permission from [65]. Copyright © 2012, American Chemical Society.

I.1.3.4 Summary and challenges related to carbon nanotube-based sensors

As shown in the typical examples of carbon nanotube-based sensors described above, the remarkable electrical properties of CNTs can be used to probe various reagents or reactions. Most of the time, the electrical signal changed as a result of adsorption of specific molecules. In certain cases, this electrical response was due to conformational changes induced by the receptor-substrate interaction. For the first time, Collins *et al.* reported the possibility of electrical response due to a chemical transformation, which was clearly distinguishable from the signal due to conformational changes or adsorption of specific molecules.[64,65,67] This possibility of detecting in real-time chemical transformation by electrical measurements opens the door to many applications in the field of carbon nanotube-based sensors.

21

Similarly, carbon nanotubes can be modified to support catalysts on their sidewalls. By using such supported catalysts, we should be able to detect in real-time the catalytic transformation of one compound into another, as will be explored throughout this thesis.

I.2 Catalysis

I.2.1 *Homogeneous vs heterogeneous catalysts*

According to Ostwald, a catalyst can be defined as *"a substance that change the velocity of a chemical reaction, without itself appearing in the end products"*.[72] Catalysis naturally occurs in human life, since our organisms are controlled by enzymatic processes. Moreover, catalysis is also ubiquitous in chemical and pharmaceutical industry. In a context of increasing demand for sustainable processes, reducing waste generation and atom economy, catalysts turned out to be of paramount importance. It is estimated that approximately 90 % of the chemical processes in the industry rely on catalysis.[73] Among them, about 80 % of these catalytic processes involve heterogeneous catalysts, while the other 20 % involves homogeneous catalysts.[74] A homogeneous catalyst is a catalyst that operates in the same phase than the reaction mixture (typically a metal complex dissolved in an organic solvent), while a heterogeneous catalyst is in another phase (typically a solid used in liquid or gas phase). Moreover, heterogeneous catalysts are distinguished according to their form, namely **bulk** or **supported** catalysts. Table I.2 summarizes the main advantages and disadvantages of both homogeneous and heterogeneous catalysis. The main drawback of homogeneous catalysis lies in the difficulty of catalyst recovery at the end of the reaction, leading to cost increase, and more critically, to possible poisoning of the synthesized product. On the

contrary, heterogeneous catalysts can easily be recovered by filtration after the reaction. Moreover, these catalysts are generally more robust and therefore more adapted for industrial applications.

For these reasons, recent attempts appeared for the heterogenization of homogeneous catalysts.[75] This strategy, also known as homogeneous supported catalysis, consists in anchoring a homogeneous catalyst on a solid support, in order to combine advantages of both homogeneous and heterogeneous catalysis.

Table I.2. Comparison of the main advantages and disadvantages of homogeneous *vs* heterogeneous catalysis. Table inspired from Farnetti *et al.*[76]

	Homogeneous catalysis	Heterogeneous catalysis
Selectivity	Good	Poor
Activity	Good	Poor
Recyclability	Difficult, risk of poisoning	Easy
Active site	Clearly defined	Large variety of active sites, difficult to characterize
Robustness	Poor	Strong

Various supports can be used for the preparation of both homogeneous and heterogeneous supported catalysts, namely metal oxides such as silica or alumina,[77] zeolites[78] or carbonaceous supports.[79] These supporting materials should meet the following criteria: thermal and mechanical stabilities, high specific surface area, appropriate porosity, and chemical inertia for the catalytic reaction. Carbon meets these conditions, while allowing to easily recover the active metallic sites by burning the support. Various forms of carbon can be used as catalyst support,[79,80] including both amorphous allotropes or nanoscopic forms such as carbon nanofibers,[81,82] carbon nanotubes[82–84] or graphene.[85] The main advantages

of using nanocarbons as catalyst support are the following: (i) mesoporous structure, decreasing diffusional limitations;[86] (ii) good mechanical resistance to attrition; (iii) good surface homogeneity, allowing to control surface chemistry for the preparation of catalysts and (iv) possible spectroscopic characterization.

I.2.2 *Characterization of the catalyst active sites and evaluation of the catalytic performance*

Activity and selectivity are two key parameters to estimate the efficiency of a catalyst for a given reaction. Although the reaction feasibility can easily be tracked by several techniques (e.g. nuclear magnetic resonance (NMR), mass spectrometry (MS), thin layer chromatography (TLC), infrared spectroscopy (IR), etc.), quantitative characterization techniques are required to determine catalyst activity and selectivity. These parameters are generally determined by analysis of the reaction mixture at the end of the reaction, thanks to quantitative separation techniques such as gas chromatography (GC) or high performance liquid chromatography (HPLC).

However, in order to get comprehensive understanding of the catalytic reaction, it is important to characterize the active sites composition and structure, which can greatly affect the efficiency. Nevertheless, as evidenced in Table I.2, one difficulty encountered when dealing with heterogeneous catalysis precisely lies in the characterization of the active sites. More specifically, the characterization of heterogeneous supported catalysts is even more challenging.[87,88] Indeed, the active sites in supported catalysts constitute only a small part of the catalyst as a whole, rendering their characterization even more difficult. Moreover, since

catalysis is a surface reaction, only the external layer of the active site, such as a metal nanoparticle, is actively implied in the catalytic reaction.

Knowing this, heterogeneous supported catalysts are usually characterized by surface analysis techniques, such as X-ray photoelectron spectroscopy (XPS). XPS provides information about the composition and oxidation state of the elements present on the catalyst surface. X-ray absorption spectroscopy (XAS) is also commonly used for the characterization of catalysts since this technique gives valuable information about the metals:[89] nature and number of the neighboring atoms in the vicinity of metal atoms, distance between metal atoms and redox properties. The catalyst structure is also analyzed by microscopy techniques such as transmission and scanning electron microscopy (TEM and SEM), as well as by X-ray diffraction (XRD). Finally, specific surface area of a catalyst is a crucial parameter that is usually determined by chemisorption of gas like carbon monoxide or hydrogen.[90] After several catalytic cycles, catalyst sometimes suffers from deactivation, leading to a decrease of their activity. By comparing the catalyst structure and composition before and after catalysis, one can conclude the reasons for deactivation.

I.2.3   *Operando catalysis*

Despite giving precious information on the catalyst composition and structure, the above-mentioned *ex situ* characterization is of limited relevance since the catalyst is expected to undergo some transformations during the catalytic reaction, and the active site might be produced only during the reaction. For this reason, real-time *in situ* characterization methods of the catalyst are required, under the reaction conditions.[91]

Moreover, in order to get information about the catalytic reaction mechanism, it is of critical importance to establish the relationship between the catalyst structure and its activity/selectivity.[92] The term **operando spectroscopy** was hence introduced to describe *in situ* characterization of the catalyst under the catalysis conditions simultaneously coupled with activity and/or selectivity measurements.[88,92,93] Operando spectroscopy requires adapted *in situ* spectroscopic-reaction cells, enabling to characterize the catalyst in real-time during the catalytic reaction.[94]

Common spectroscopic methods such as IR, UV-Vis and Raman spectroscopy, as well as X-ray absorption spectroscopy (XAS) have been reported for real-time *in situ* characterization of solid catalysts.[92,94–98] These *in situ* characterization methods provide information about the structure of the catalytic active sites, as well as their redox properties, i.e. oxidation state. These two parameters are particularly important for the purpose of mechanistic study of the catalytic cycle. Catalytic reactions indeed often imply restructuration of the catalytic active site *via* redox reactions. In addition, the catalytic activity and selectivity are determined by real-time measurement of the reaction mixture composition, by mass spectrometry (MS), gas chromatography (GC) or high performance liquid chromatography (HPLC).[94]

I.2.3.1 State of the art

a) *Operando Raman spectroscopy*

B. Weckhuysen *et al.* investigated the deactivation of Pt/Al_2O_3 catalyst during propane dehydrogenation by operando Raman spectroscopy.[99] In order to do this, the authors recorded *in situ* Raman spectra of the catalyst during 10 successive cycles of dehydrogenation followed by regeneration in air. Simultaneously, GC was used for the quantitative determination of the reaction products. The experiment revealed that the reaction was less efficient after several catalytic runs, as well as within a dehydrogenation cycle, highlighting catalyst deactivation. Interestingly, this deactivation phenomenon was significantly reduced in presence of hydrogen. Time-resolved Raman spectra allowed to investigate modifications of the active site during the catalyst operation. As shown in Figure I.14a, two bands appeared directly after exposure of the catalyst to propane: D-band, at 1320 cm^{-1} and G-band, at 1584 cm^{-1}. These two bands typically arise from carbonaceous species, and since previous studies on this specific reaction revealed a deactivation induced by the formation of coke residuals,[100] the authors concluded in a similar poisoning effect. Figure I.14b depicts the Raman spectra at the end of the reaction, for various propane/H_2 ratios. As can be seen, the D/G band ratio increased when the proportion of H_2 increased. This observation was attributed to a decrease of the coke accumulation on the catalyst surface in presence of hydrogen, since smaller coke areas result in an increase of the ratio between edge carbon (D-band) and bulk carbon (G-band).[99]
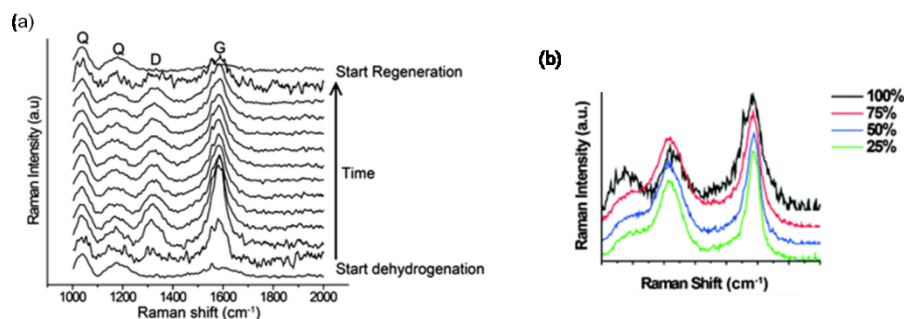
Figure I.14. (a) Operando Raman spectra obtained during the first propane dehydrogenation cycle over a 0.5 wt. % Pt/Al_2O_3 catalyst; (b) Operando Raman spectra of Pt/Al_2O_3 at the end of the first dehydrogenation cycle for various propane/H_2 ratios. Adapted from [99] with permission of The Royal Society of Chemistry, http://dx.doi.org/10.1039/c3cp50646k.

b) Time-resolved XPS

Wilson *et al.* used operando XPS to study the catalytic dehydrochlorination of 1,1,1-trichloroethane over platinum at low temperature.[101] Fast XPS spectra of C 1s and Cl 2p were acquired every 30 seconds while increasing the temperature from 95 K to above 500 K. C 1s spectra (Figure I.15a) revealed the presence of two carbon peaks at 95 K, at 284.6 and 288.1 eV, respectively corresponding to $-CH_3$ and $-CCl_3$ functions. When the temperature increased above 130 K, these peaks disappeared. The appearance of a transient peak (286.7 eV) corresponding to $-CHCl_2$ suggested that the dechlorination occured via a stepwise process. At around 300 K, a peak at 284 eV revealed the presence of a stable $Pt_3\equiv C-CH_3$ ethylidyne complex. Above 350 K, catalytic dehydrogenation of ethylidyne occurred. Simultaneously, Cl 2p XPS spectra (Figure I.15b) revealed that CCl_3 bond disrupted at ~ 130 K, leading to the appearance of atomic chlorine. This peak intensity progressively decreased to finally completely disappear above 450 K, due

28

to the recombination of Cl and H atoms to form gaseous HCl. These time-resolved XPS measurements allowed the authors to conclude with the following mechanism of dehydrochlorination of 1,1,1-trichloroethane:

$$CH_3CCl_3 \qquad\qquad 95 \text{ K} \qquad\qquad (I.1)$$

$$CH_3CCl_3 \longrightarrow CH_3C{\equiv}Pt_3 + 3\ Cl \qquad 130 - 300 \text{ K} \qquad (I.2)$$

$$CH_3C{\equiv}Pt_3 \longrightarrow C_xH_y + H \qquad > 350 \text{ K} \qquad (I.3)$$

$$Cl + H \longrightarrow HCl \qquad\qquad 350 - 450 \text{ K} \qquad (I.4)$$
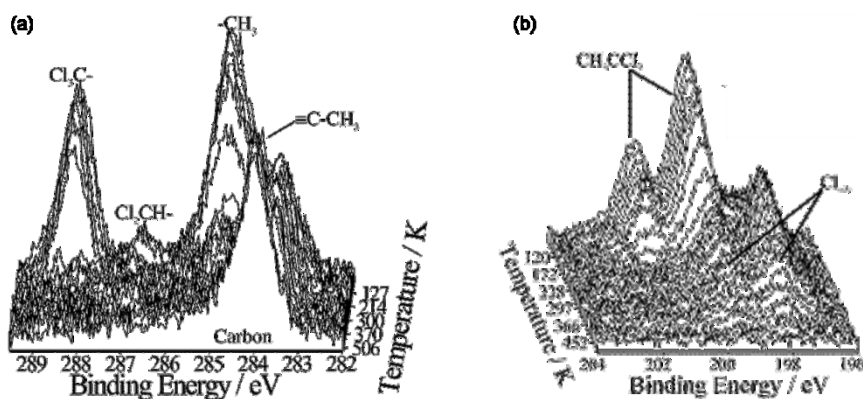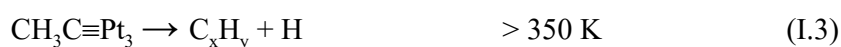
Figure I.15. Time resolved XPS spectra of 1,1,1-trichloroethane reaction in function of temperature: (a) C 1s and (b) Cl 2p spectra. Adapted with permission from [101]. Copyright © 2004 American Chemical Society.

c) *Operando XAS*

Although being extensively used in organic chemistry, the mechanism of Suzuki-Miyaura cross-coupling reaction catalyzed by heterogeneous supported catalysts is not yet fully understood. In particular, some authors suggested that the catalytic reaction could occur in solution, after leaching of Pd from the heterogeneously supported active sites.

Operando X-ray absorption spectroscopy was used to characterize the Pd active sites during the catalytic reaction, in order to get some information about the evolution of the active site structure during the reaction.[97,102] More precisely, the authors studied the cross-coupling reaction of iodoanisole with phenylboronic acid catalyzed by Pd nanoparticles stabilized by polyvinylpyrrolidone (PVP). Red dots on Figure I.16 shows the evolution of the Pd–Pd coordination number ($CN_{Pd–Pd}$), as determined by real-time XAS measurements (shown in inset). As can be seen, the nanoparticles are really stable over time. The authors concluded that no sintering or leaching occurred during the reaction, since these phenomenon would have resulted in a $CN_{Pd–Pd}$ increase or decrease, respectively.[97] This operando study allowed to conclude that this reaction was catalyzed in a heterogeneous way, without dissolution of Pd species in the reaction mixture. However, other experiments have proved that leached Pd was active in the Suzuki-Miyaura cross-coupling reaction.[103] As a consequence, the mechanism of this reaction, i.e. heterogeneous *vs* homogeneous catalysis, is still debated. Further experiments are required to get a comprehensive understanding of this reaction.
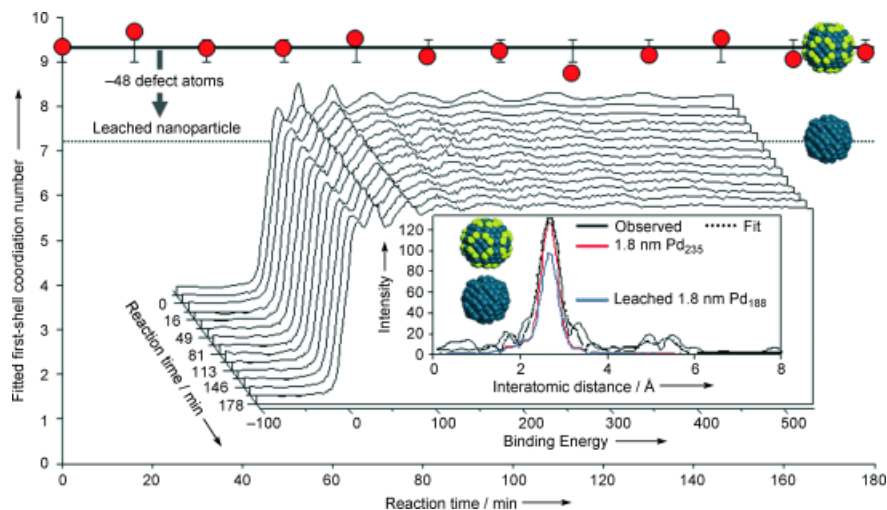
Figure I.16. Pd−Pd coordination number as determined by operando XAS (inset). Red dots corresponds to CN_{Pd-Pd} as determined by XAS; full line corresponds to the CN_{Pd-Pd} value simulated for as-prepared Pd-PVP nanoparticles; dotted line corresponds to the CN_{Pd} value simulated for Pd nanoparticles unstabilized by PVP. Reproduced with permission from [97]. Copyright © 2010 Wiley-VCH Verlag GmbH & Co. KGaA, Weinheim.

I.2.3.2   Challenges related to operando catalysis

As can be seen in the examples described above, each characterization technique gives its own information and possesses its own limitations. As a consequence, one single technique cannot provide all the information about the catalyst. For this reason, several research groups have investigated the possible use of a combination of techniques, which could provide complementary information, for a better comprehension of the catalyst operation.[96,104–110]

However, there is a major drawback when using operando catalysis: the optimal conditions for catalysis are often really different from the characterization ones. As a consequence, a compromise is chosen between

these two optimal conditions, and the catalysis is often performed in suboptimal conditions. Moreover, the sources used for the *in situ* characterization can sometimes induce catalyst damage, affecting its performance.[94]

For this reason, development of less compelling *in situ* characterization methods is highly desirable. For this purpose, electrical characterization is promising, as it can be performed under ambient atmosphere and pressure, unlike most spectroscopic techniques, which often require vacuum conditions, and at a large range of temperatures. By using carbon nanotube-supported catalysts, the CNT support could be used as a sensor to probe in real-time the catalytic activity, giving precious information concerning the mechanism involved in the catalytic reaction.

I.3   Scope of the thesis and objectives

In this thesis, we aim to use carbon nanotubes as sensors to detect *in situ* catalytic activity. In order to do this, carbon nanotubes are modified to support catalytic active sites. These functional nanotubes are then integrated into field-effect transistors. Such electronic devices are used to detect small variations in the nanotube conductance induced by the catalysis.

In this context, it should be emphasized that it is not the object of the present thesis to develop a marketable CNT-based sensor, but rather to use carbon nanotubes as a tool to probe chemical reactions in real-time. For this purpose, we selected catalysis in our investigations for its ability to induce charge transfer reactions at the surface of the active sites.

In practice, this thesis deals with three different parts: preparation of catalysts supported on carbon nanotubes, catalysis and *in situ* detection of catalytic activity by real-time electrical measurements.

Two different catalysts are prepared, a **heterogeneous supported catalysis** and a **homogeneous supported catalysis**. For this purpose, two distinct approaches are developed:

(i) *Heterogeneous supported catalysis*:

In this first approach, a functionalization pathway is developed in order to deposit nanoparticle precursors on carbon nanotube surface. This functionalization process is followed by a thermal activation step, in order to form metallic nanoparticles while removing organic functionalities. Thanks to this thermal annealing step, the defects introduced in the nanotube during the functionalization are removed. Electrical properties of the nanotube is thus preserved, enabling sensor experiments to be performed.

(ii) *Homogeneous supported catalysis*:

In this second approach, homogeneous catalysts are anchored on carbon nanotubes. Particular attention is paid to the preservation of nanotube conductance during the functionalization process. In order to do this, we opt for the divalent functionalization which is known to preserve the sp^2 structure of the nanotube, hence preserving its electronic properties.

The catalytic performance of these two catalysts is then studied, through two different reactions. The heterogeneous supported catalyst is used for the hydrolytic transformation of dimethylphenylsilane into dimethylphenylsilanol, while the catalytic activity of the homogeneous

supported catalyst is demonstrated for the well-known Suzuki-Miyaura cross-coupling reaction. These reactions are selected for their reported possibility to operate in ambient conditions.[111] This feature facilitates the experimental setup for the subsequent *in situ* detection of catalysis by real-time electrical measurements. This experiment indeed constitutes the very first attempt at using carbon nanotube-based sensors for the detection of catalytic activity. As a consequence, this assay is very challenging, hence justifying that we wanted to simplify as much as possible the experimental setup, i.e. avoiding high temperature and pressure. However, it is worth noting that it would also be possible to consider more stringent reaction conditions for future experiments in this field.

For these real-time experiments, we select the first approach, i.e. heterogeneous supported catalysts. This choice was motivated by the demonstrations shown in this thesis of the presence of a strong electrostatic coupling between the nanotube and the supported nanoparticles. These catalysts are thus integrated into electronic devices and their activity for the hydrolytic transformation of dimethylphenylsilane is probed through real-time electrical measurements.

In summary, the objectives of this thesis are the following:

❖ Development of a functionalization process for the deposition of metallic nanoparticles (NPs) on carbon nanotubes, denoted NPs/CNTs, for the purpose of heterogeneous catalytic applications;

❖ Development of a divalent functionalization pathway for the anchoring of homogeneous catalysts, in order to obtain homogeneous supported catalysts, denoted M-CNTs;

34

❖ Electrical characterization of these two types of samples;

❖ Testing of these NPs/CNTs and M-CNTs in catalysis in bulk form;

❖ Integration of NPs/CNTs in electronic devices for the real-time detection of catalytic activity, by means of current measurements.

I.4 Contribution of the different laboratories

A particular feature of this thesis consists in its integration between three distinct laboratories. These active collaborations allowed to beneficiate from the complementary expertise present in each laboratory and needed for this multidisciplinary project.

On one hand, Pr. S. Hermans (Université catholique de Louvain, Belgium) conducts research in the field of heterogeneous catalysis, with a particular focus on carbonaceous supports and molecular cluster precursors. Her laboratory is particularly adapted for chemical synthesis and catalytic tests, while a large panel of characterization techniques is available at UCL facilities.

On the other hand, Pr. R. Martel (Université de Montréal, Canada) is recognized for his work on carbon nanotube based electronics. His laboratory is appropriately equipped for the electrical characterization of electronic devices, while UdeM facilities provide the required equipment for microfabrication in clean-room environment.

Finally, short-term stays were also conducted in Pr. C. Nuckolls laboratory (Columbia University in the City of New York, US). Pr. Nuckolls focuses his research on the integration of reaction chemistry into

electrical devices. Thanks to this collaboration, we beneficiated from Columbia facilities, providing namely an autoprobe station and a setup for real-time electrical measurements.

This multidisciplinary project would not have been possible without these close partnerships and the precious support of Dr. D. Bouilly, allowing to include a proper combination of chemical and physical aspects of materials in this project.

I.5   Thesis outline

After this overview of the context surrounding the present work, *Chapter II* will be devoted to the description of the basic concepts necessary for a comprehensive understanding of this thesis. *Chapter III* will cover the fabrication of carbon nanotube field-effect transistors, electronic devices that will be used throughout this thesis.

Chapter IV will cover the development of the monovalent functionalization of carbon nanotubes for the deposition of metallic nanoparticles, with a complete chemical and electrical characterization. These materials will be used in *Chapter V* as heterogeneous supported catalysts for the hydrolytic transformation of dimethylphenylsilane into dimethylphenylsilanol.

Chapter VI will focus on the divalent functionalization of single-walled carbon nanotubes, through Bingel-Hirsch reaction. These functionalized SWCNTs will be used to anchor homogeneous catalysts. A chemical characterization will be performed to prove the success of the functionalization process, while electrical characterization will be used to demonstrate the preservation of the electrical properties of the nanotube.

These materials will then be used as homogeneous supported catalysts for the Suzuki-Miyaura cross-coupling reaction.

Chapter VII will be devoted to the use of carbon nanotubes as sensors for the *in situ* detection of catalytic activity, by means of electrical measurements.

Finally, a general conclusion on the scientific contribution of this thesis will be summarized in *Chapter VIII*. This work paves the way to various prospects which will be discussed in this last chapter.

Experimental details concerning Chapters IV to VII will be given at the end of the respective chapters. When necessary, appendixes will be annexed at the end of the manuscript.

CHAPTER II - MAIN CONCEPTS

Abstract

This chapter intends to give a brief description of the fundamental concepts that will be necessary throughout this thesis. A first section of this chapter is devoted to carbon nanotubes. The unique properties of these materials are discussed, in connection with their potential applications. A second section is devoted to the carbon nanotube field-effect transistor (CNT-FET), that is used throughout this thesis as a tool for studying the impact of chemical functionalization on carbon nanotube electronic properties, but also as sensors to detect a catalytic activity.

II.1 Carbon nanotubes

II.1.1 From elemental carbon to carbon nanotubes

Carbon is earth abundant and constitutes the chemical basis of life. For a long time, graphite and diamond were considered as the only allotropes of carbon, both of them showing unique physical properties.[112] Graphite is indeed known as a very good electrical conductor, while diamond is an electrical insulator. Diamond is the hardest natural material on Earth, while graphite is so soft that it can be used as a lubricant. Conceptually, there are many other ways to form carbon allotropes. In 1985, Kroto *et al.* observed fullerenes for the first time (1996 Nobel Prize in Chemistry).[113] The most famous fullerene, C_{60}, is composed of 60 sp^2 carbon atoms arranged in the form of a truncated icosahedron made of 20 hexagons and 12 pentagons. This "football" like shape gives it a quasi-zero-dimensional feature. This discovery marked the starting point of the research in nanoscopic forms of carbon. A few years later, Iijima reported in 1991 the first observation of concentric *"helical microtubules of graphitic carbon"*,[114] today known as multi-walled carbon nanotubes (MWCNTs). Two years later, the first single-walled carbon nanotubes (SWCNTs) were observed simultaneously by Bethune *et al.*[115] and Iijima *et al.*[116] during experiments aiming to synthesize MWCNTs. Carbon nanotubes (CNTs) are composed of sp^2 carbon atoms arranged in benzene ring, spatially organized to form cylinders. These materials exhibit diameters of a few nanometers, for a length that may reach up to a few centimeters. This high aspect ratio makes them quasi-one-dimensional materials. The latest member of nanoscopic carbon is the two-dimensional graphene, defined as *"a single layer of carbon atoms densely packed into a benzene-ring structure"*.[117] This carbon allotrope was isolated by

mechanical exfoliation of graphite in 2004 by Geim and Novoselov.[117] They were awarded the 2010 Nobel Prize in physics for this discovery. Due to its simple structure, graphene can be visualized as a building block for other sp^2 carbon materials, as shown in Figure II.1.
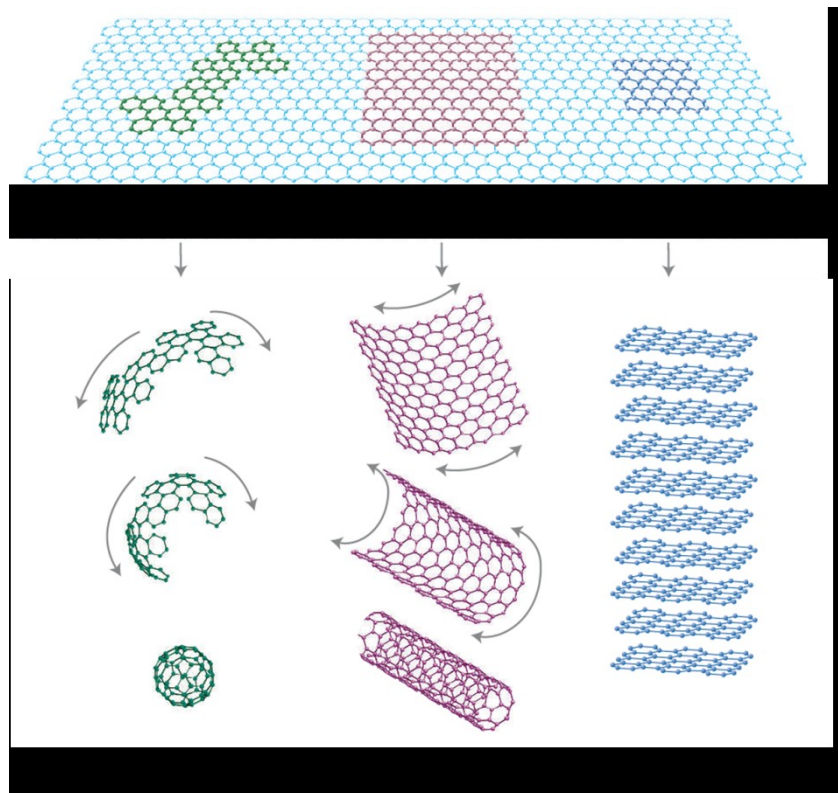
Figure II.1. Schematic representation of graphene as a building block for sp^2 carbon materials of other dimensionalities. Graphene can be wrapped up into 0D fullerenes, rolled up into 1D carbon nanotubes, or stacked into 3D graphite. Adapted by permission from Macmillan Publishers Ltd: Nature Materials.[118] Copyright © 2007.

In this thesis, we will focus our attention on carbon nanotubes. These materials indeed exhibit unique properties, making them promising for applications in many fields, such as electronics,[119–121] material

engineering,[122] sensor design[42] and catalysis.[82,86] The next section will give a brief overview of the synthesis processes used for the preparation of these quasi-1D materials. Then, we will briefly describe their outstanding properties. Chemical functionalization of carbon nanotubes is often required to use them in practical applications and will be discussed in a subsequent section.

II.1.2   Synthesis of carbon nanotubes

Since the discovery of carbon nanotubes by Iijima in 1991,[114] various methods have been developed for the synthesis of carbon nanotubes. Whatever the method used, synthesis of carbon nanotubes requires two mandatory elements: a carbon source and an energy source. A catalyst is also often used, especially for the selective synthesis of single-walled carbon nanotubes.[123] Three methods are commonly used for the production of carbon nanotubes: electric arc plasma, laser ablation and chemical vapor deposition (CVD).

- **Electric arc plasma**

    The first observed carbon nanotubes were synthesized by electric arc plasma.[114] In this method, two high purity graphite electrodes are separated from ~ 1 mm, under a helium or argon atmosphere. A current is applied between the two electrodes until an arc electric is created. The anode is consumed, forming a plasma. This plasma deposits on the cathode to form multi-walled carbon nanotubes. SWCNTs can be obtained by doping electrodes with a low amount of metal catalysts.[124]

- **Laser ablation**

  For this second synthesis method, graphite is heated in a furnace at ~ 1200 °C under inert atmosphere of He or Ar. A laser beam is focused on the graphite target, causing vaporization of carbon atoms, which rearrange to form MWCNTs. SWCNTs can be obtained when using transition metal doped graphite as carbon source.[124]

- **Chemical vapor deposition**

  Finally, CVD allows to obtain carbon nanotubes by flowing a gaseous carbon source (e.g. hydrocarbon, CO, alcohol) over a transition metal catalyst, at temperature ranging between 500 to 1200 °C. The formation of carbon nanotubes involves several steps. First, carbon feedstock dissociates at the catalyst surface. Carbon atoms are then solubilized in the metal catalyst particles. Since at the operated temperature, carbon has a limited solubility in transition metals, precipitation of carbon occurs, leading to the formation of sp^2 tubular structure.[125] Both MWCNTs or SWCNTs can be obtained by using this synthesis process, depending on the composition and properties of the catalyst, the nature of carbon feedstock and the synthesis conditions (i.e. temperature, pressure and gas debit).

CVD is currently the most common approach for the synthesis of commercially available carbon nanotubes. The two former synthetic processes indeed require high temperature (~ 1200 °C and beyond) while CVD growth of carbon nanotubes requires lower temperature (< 1000 °C), leading to more precise control of the sample purity.[124,126] Moreover, CVD is a continuous process, allowing the preparation of large quantities of

carbon nanotubes. CVD is also particularly useful for the synthesis of aligned arrays or individualized carbon nanotubes on substrates (Figure II.2).[127,128] This is of particular interest for the integration of carbon nanotubes in electronic devices.
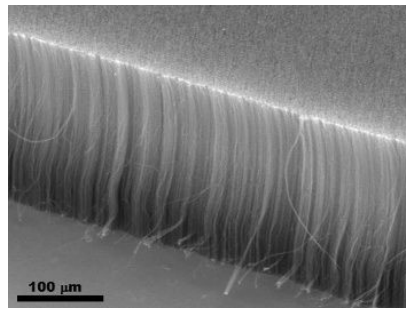
Figure II.2. SEM images of vertically aligned CVD grown carbon nanotube arrays. Reproduced from ref [127], Copyright © 2013 Van Hooijdonk *et al.*, licensee Beilstein-Institut, under the terms of the Creative Commons Attribution License.

II.1.3   *Properties of carbon nanotubes*

As mentioned above, carbon nanotubes exhibit remarkable properties. The present section will give a brief overview of the particular properties of these materials, with an emphasis on electrical properties, which will be used throughout this thesis.

II.1.3.1   Electronic dispersion

Due to their unique structure, carbon nanotubes present an electrical conductivity up to eight times higher than copper,[129] and a charge carrier mobility about a hundred times higher than silicon.[130] However, their electrical properties may significantly vary from one nanotube to another. As illustrated in Figure II.1, carbon nanotubes can be represented as a graphene sheet which has been rolled up to form a 1D cylinder. Depending

on the way the graphene sheet is rolled up, also known as its "helicity", carbon nanotubes exhibit very distinct electrical properties, varying from semiconducting to metallic behavior. In order to unambiguously describe carbon nanotube structures, Hamada proposed a notation using helicity indexes.[131] To each CNT is attributed an helicity vector $\boldsymbol{C_h}$ which corresponds to the circumference of the nanotube. This helicity vector may be decomposed into two vectors, each of them being a multiple of $\boldsymbol{a_1}$ and $\boldsymbol{a_2}$, the two primitive vectors of the graphene lattice (Figure II.3). The expression of the helicity vector $\boldsymbol{C_h}$ is defined in equation (II.1).

$$\boldsymbol{C_h} = n\boldsymbol{a_1} + m\boldsymbol{a_2} \qquad \text{where } n,m \text{ are integers and } n \geq m \geq 0 \qquad \text{(II.1)}$$

Each carbon nanotube is hence described by its helicity index (n,m).
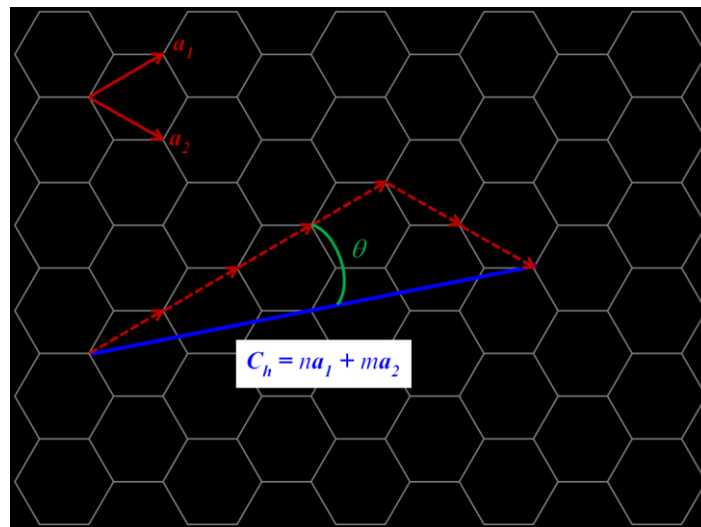
Figure II.3. Schematic representation of the unrolled hexagonal lattice of a carbon nanotube. $\boldsymbol{C_h}$ is the helicity vector, $\boldsymbol{a_1}$ and $\boldsymbol{a_2}$ are the primitive vectors of the graphene lattice, θ is the helicity angle and (n,m) is the helicity index. The nanotube represented here is (4,2).

Carbon nanotubes can also be described by a unique helicity angle θ, which corresponds to the angle formed between $\mathbf{C_h}$ and $\mathbf{a_1}$ (see Figure II.3) Depending on the value of this angle, three different kinds of nanotubes are defined: **zigzag** ($\theta = 0°$), **armchair** ($\theta = 30°$), or **chiral** ($0° < \theta < 30°$) (Figure II.4).

| (13,0) | (13,1) | (10,4) | (8,6) | (8,8) |

zigzag	**chiral**	**armchair**
$\theta = 0°$	$0° < \theta < 30°$	$\theta = 30°$
$(n,0)$	(n, m) with $n \neq m \neq 0$	(n, n)
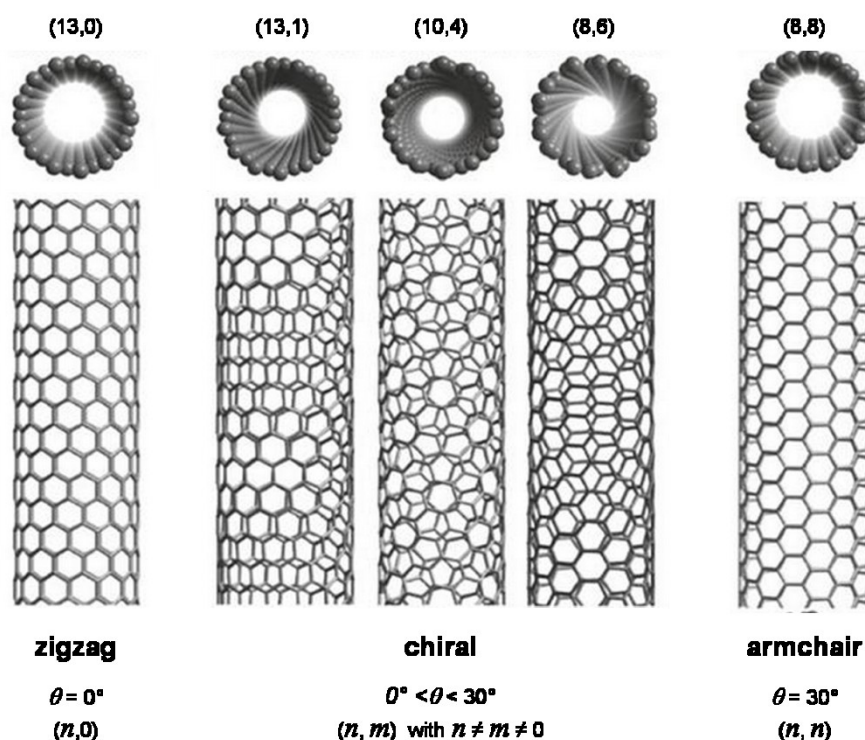
Figure II.4. Examples of zigzag, chiral and armchair SWCNTs and summary of the classification parameters. Reproduced with permission from [123]. Copyright © 2012 John Wiley & Sons Ltd.

Due to their cylindrical shape, electrons in carbon nanotubes are confined in one direction, along the nanotube axis. For this reason, electronic properties of CNTs strongly depend on their helicity. Typical density of states (DOS) of semiconducting (sc-) and metallic (m-) SWCNT are shown in Figure II.5. DOS defines the number of available electronic

states at a given energy. As can be seen from Figure II.5, DOS of carbon nanotubes have a specific pattern, composed of a band structure, typical of solid materials, in which sharp spikes are distinguished. These spikes are related to quasi-discrete electronic levels, known as **van Hove singularities**, and come from the one-dimensionality confinement of the electrons.[132] As can be seen from Figure II.5, the density of states at the Fermi level (E_F) is non-zero for m-nanotubes, while sc-CNTs possess a bandgap between valence and conduction bands. In practice, all (***n,m***) SWCNTs with the difference (***n*** - ***m***) being an integer multiple of 3 are metallic, all others are semiconducting. All armchair SWCNTs are therefore metallic, while statistically one third of the non-armchair nanotubes are metallic and two thirds are semiconducting.
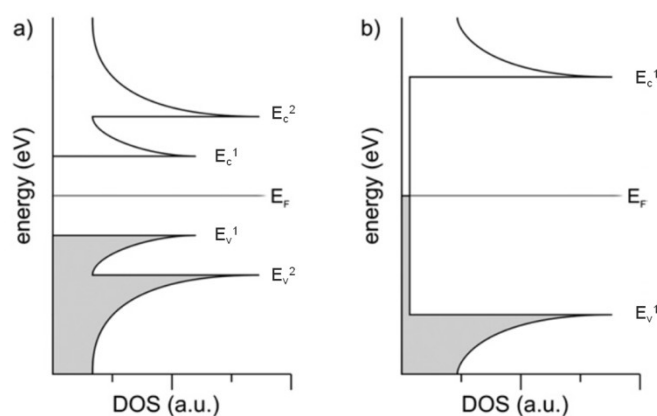
Figure II.5. Typical density of states (DOS) of (a) semiconducting SWCNT and (b) metallic SWCNT. Adapted from [133] with permission of The Royal Society of Chemistry, http://dx.doi.org/10.1039/b716732f.

II.1.3.2   Optical properties

Due to their high aspect ratio, giving them a quasi-one-dimensionality, carbon nanotubes possess unique optical behavior, between band structure and discrete energy levels, the so-called van Hove singularities. These singularities are denoted E_v^1, E_v^2... in the valence band and E_c^1, E_c^2,... in the conduction band (Figure II.5). Optical transitions are allowed between electronic levels of the same index singularities, i.e. E_{11}, corresponding to transitions between E_v^1 and E_c^1, E_{22} for transition between E_v^2 and E_c^2, etc.[134]

Given that each (***n,m***) carbon nanotube possesses its own density of states, the singularities energy depends on the nanotube helicity. For this reason, each carbon nanotube exhibits a unique optical behavior. Two parameters mainly affect the van Hove singularities level: (i) the nanotube diameter and (ii) the metallic or semiconducting character. The overall trend can be summarized as follow:

- The lower is the nanotube diameter, the higher are the van Hove singularities energy levels;[135]
- For a given diameter, van Hove singularities of metallic CNTs are more energetic than those of semiconducting ones.

The allowed optical transitions for each SWCNTs have been calculated and are displayed in the Kataura plot (Figure II.6), as a function of the SWCNT diameter.[136]
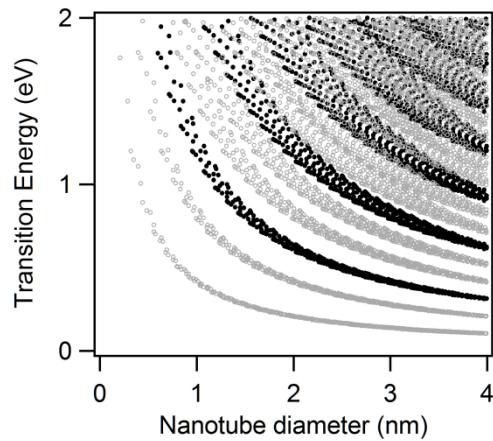
Figure II.6. Kataura plot, showing allowed optical transitions in function of the SWCNT diameter. Black and grey points are for m- and sc-SWCNTs, respectively. Data collected from [137].

II.1.3.3   Raman spectroscopy of carbon nanotubes

Among the various techniques commonly used for the characterization of CNTs, Raman spectroscopy is a powerful tool. Raman spectroscopy studies the inelastic scattering of photons by a material. Usually, Raman scattering signal of carbon nanotubes is weak. However, its intensity can be greatly enhanced by matching the laser energy with an allowed electronic transition energy. This phenomena is called resonance Raman scattering.[138] Raman spectra of carbon nanotubes are unique and easily recognizable. Each carbon nanotube of a given helicity possesses its own Raman signature.[139] Figure II.7a shows a typical Raman spectrum of SWCNTs. As can be seen, three bunches of peaks are easily distinguished in the Raman spectrum:

- **Radial breathing mode (RBM)**

These bands appear between ~ 150 and 350 cm^{-1}. They are due to radial vibration of the carbon atoms, as if the tube was breathing (Figure II.7b).[139–141]

The position of these bands is specific of the nanotube diameter, through the equation (II.2).

$$\omega_{RBM} = \frac{A}{d_{CNT}} + B \quad \text{where} \quad \begin{aligned} &\omega_{RBM} = \text{frequency} \\ &A, B = \text{exp. parameters} \\ &d_{CNT} = \text{CNT diameter} \end{aligned} \quad \text{(II.2)}$$

For a CNT supported on SiO$_2$ substrate, A and B parameters are such that:[142]

$$\omega_{RBM} = \frac{248}{d_{CNT}} \quad \text{(II.3)}$$

This relation between RBM wavenumber and nanotube diameter can be added to the Kataura-Plot (see Annex IX.3.1).[137]

- **G-band**

This so-called "graphitic band" appears at around 1500 - 1600 cm^{-1} and is due to elongation of carbon-carbon bonds (Figure II.7c). This mode is also called tangential mode, as it is attributed to atomic vibrations in the graphene sheet plan.[139–141]

- **D-band**

This "diamond-band", commonly called "defect-band", appears between 1300 and 1400 cm^{-1}. This band is caused by elastic diffusion of an electron by a structural defect, such as an impurity, vacancy, or sp^3 carbon atom. For this reason, D-band

50

on G-band ratio is often used to probe the covalent functionalization of nanotube samples, since covalent functionalization is expected to transform sp^2 carbon atoms into sp^3 carbon atoms, hence increasing this ratio.[139] However, the I_D/I_G ratio should be used with caution due to complications associated to resonances, which depend on the electronic properties of the nanotube sample. Since the functionalization is known to modify the electronic properties of the nanotube, the Raman spectra of pristine and functionalized CNTs can be compared qualitatively and require a careful calibration for quantitative analysis.[139]
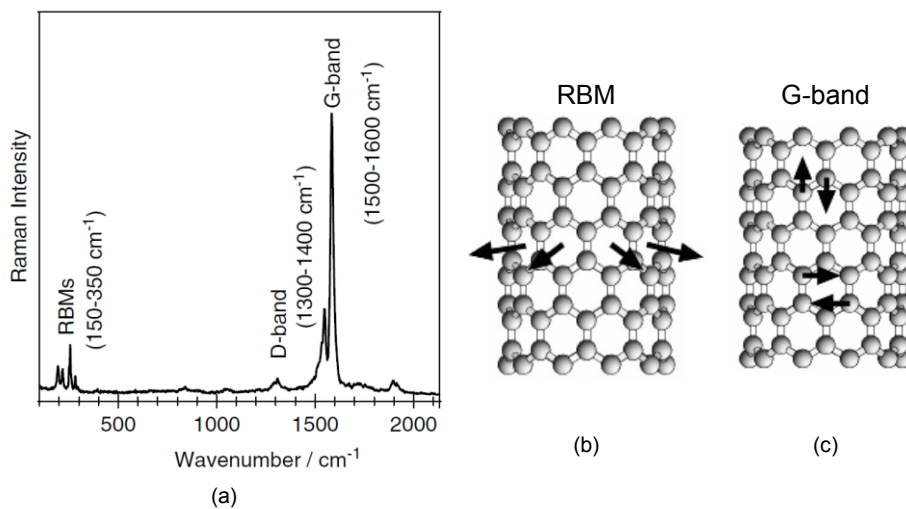
Figure II.7. (a) Typical Raman spectrum of SWCNTs; Schematic representation of the atomic vibrations for (b) radial breathing mode and (c) G-band. Figure a adapted from [141]. Copyright © 2007 John Wiley & Sons, Ltd. Figure b and c reproduced from [140]. 2003 IOP Publishing Ltd and Deutsche Physikalische Gesellschaft, under the terms of the Creative Commons Attribution-NonCommercial-ShareAlike 3.0 Unported.

G- and D- bands can also be used to probe the possible degradation of the sample induced by the energetic laser during the analysis. The positions of G- and D-bands of carbon nanotubes are indeed reported to be downshifted when increasing the temperature (see Annex IX.3.2) or, to a lesser extent, the laser power (see Annex IX.3.3).[143] In this thesis, Raman spectra were recorded using a 514 nm or 1064 nm laser, while keeping a low laser power to avoid experimental issues such as heating.

II.1.4   *Functionalization of carbon nanotubes*

Because of their structure, carbon nanotubes attract each other by means of van der Waals interactions. This attraction was estimated to be 0.5 and 1.8 eV per nanometer of CNT-CNT contact, depending on the nanotube diameter.[144,145] For this reason, carbon nanotubes usually exist as bundles (Figure II.8) and are insoluble in both organic and aqueous solvents.[146] Moreover, the combination of high aspect ratio and high flexibility makes them entangled, thus fostering their aggregation. It is thus necessary to improve their solubility for the purpose of further applications. Chemical functionalization of carbon nanotubes has been successfully used to improve their processibility and solubility.[147] Functionalization also allows to anchor specific functions for certain applications of carbon nanotubes, such as sensors, catalysis, or composite materials.

In the last 20 years, numerous approaches have been developed for the functionalization of carbon nanotubes.[138,146,147,149–152] These approaches can be grouped in three main categories: non-covalent functionalization,[148,153–155] covalent functionalization of the defects[156,157] and covalent functionalization of the sidewalls.[158–160]
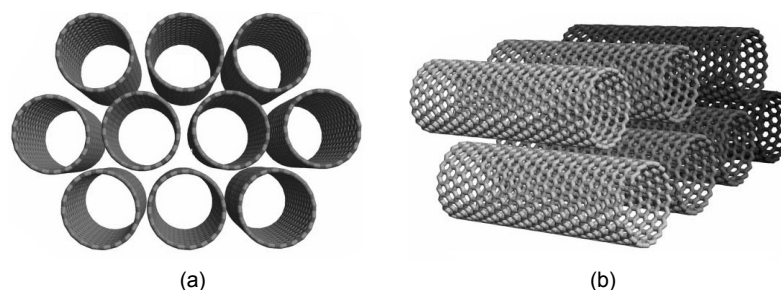
II.1.4.1   Non-covalent functionalization

Non-covalent functionalization of carbon nanotubes consists in adsorbing specific compounds on a nanotube surface. As the name suggests, this adsorption is based on non-covalent interactions, such as π-π stacking, van der Waals interactions or hydrophobic interactions.[148,155] Using this non-covalent approach, CNT properties can be preserved while improving their solubility and processibility.[155] However, the functionalized moieties are weakly bonded to the nanotube surface, and desorption could occur, depending on the solution/adsorbent/nanotube equilibrium.

Polyaromatic compounds, such as pyrenes, can be adsorbed on the nanotube surface (Figure II.9a).[161,162] Carbon nanotubes indeed possess delocalized π electrons in p_z orbitals, which can be used for the adsorption of aromatic compounds by means of π-π stacking.[148] Pyrene derivatives have been successfully used for the non-covalent immobilization of proteins and biological species, with potential applications for the preparation of biological sensors,[161,162] as well as for the immobilization of metallic active sites for catalytic applications.[163]

Furthermore, surfactants can also be used to increase carbon nanotube solubility. Sodium dodecyl sulfate (SDS) is commonly used as ionic surfactant for the preparation of aqueous solution of carbon nanotubes.[153] Adsorption of this kind of surfactant is done by Coulomb attraction between charges located on carbon nanotubes and on the surfactant ions. Non-ionic surfactants are also used for the dispersion of carbon nanotubes in organic solvents. By this way, the adsorption of the surfactant is ensured by hydrophobic interactions.[153] These CNT-adsorbed surfactants were already used for further covalent functionalization.[164] The individualization of carbon nanotubes thanks to surfactants prior to their functionalization allows to considerably improve the functionalization rate.

Similarly, polymers can be used for the non-covalent functionalization of carbon nanotubes. In order to minimize unfavorable conformation strain, polymers commonly wrap around the nanotube sidewall, forming a helicoidal structure (Figure II.9b).[148,165]

Finally, due to their hollow structure, small compounds can be encapsulated inside carbon nanotubes. Hydrogen was first inserted inside SWCNTs,[166] paving the way to applications of CNTs as containers of molecules. Later, C_{60} et C_{70} fullerenes were inserted inside SWCNTs (Figure II.9c).[167] Inorganic compounds were also successfully inserted inside carbon nanotubes, increasing their solubility.[168] Crystallization of the encapsulated compounds sometimes occurs inside the nanotube, leading to new types of materials, exhibiting specific properties.[169]
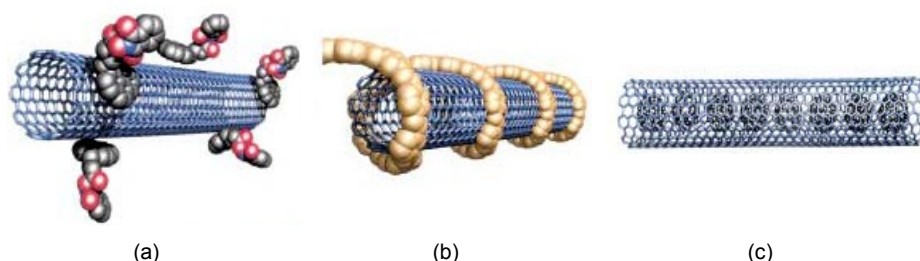
Figure II.9. Schematic representation of non-covalent functionalization of carbon nanotubes: (a) exohedral adsorption of polyaromatic compounds; (b) exohedral wrapping of CNTs by polymers and (c) endohedral encapsulation of compounds (here, fullerenes) inside CNTs. Adapted with permission from [147]. Copyright © Wiley-VCH Verlag GmbH, 2002.

II.1.4.2   Covalent functionalization of the defects

Unlike the ideal vision of perfectly straight-lined carbon nanotubes, scanning electron microscopy (SEM) and transmission electron microscopy (TEM) revealed that carbon nanotubes are actually curved. This observation implies the presence of structural defects, in which 6 membered-rings are replaced by 5 or 7 membered rings.[156] Moreover, the ends of the nanotube are often closed by remaining catalyst particles, left from the synthesis. These catalyst particles are usually removed by oxidative purification process, leading to the formation of oxygenated functions at the nanotube ends. Other defects are also present on the nanotube, such as sp^3 hybridized carbon atoms or holes.[147] These various kinds of defects, resulting from the synthesis and purification processes, are part of the nanotube (Figure II.10).
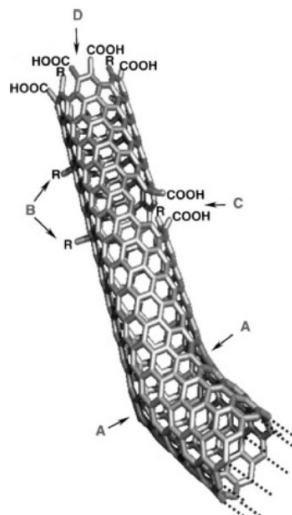
Figure II.10. Schematic representation of the typical defects present in carbon nanotubes: A) 5- or 7-membered rings, leading to a curvature of the CNT; B) sp^3-hybridized carbon atoms; C) defects resulting from oxidative treatment; D) open end of the nanotube, decorated with carboxy groups. Reproduced with permission from [147]. Copyright © Wiley-VCH Verlag GmbH, 2002.

These defects constitute the most reactive sites of the nanotube sidewalls. For this reason, they are preferentially functionalized. Typically, oxygenated functions, arising from the purification process, are derivatized to form esters or amides functions, for the purpose of further applications.[156,170] This defect functionalization approach allows to obtain strongly grafted functions on carbon nanotubes. However, limited number of functions can be anchored by using this approach. Moreover, the grafted moieties are heterogeneously dispersed on the nanotube surface, with a high concentration on extremities and curvature areas of the nanotube. Other more homogeneous covalent functionalization processes were thus developed, as will be described in the next section.

II.1.4.3   Covalent functionalization of the sidewalls

Due to their structure, carbon nanotubes are recognized as being chemically stable materials. CNTs are indeed composed of sp^2 hybridized carbon atoms, in which π electrons are delocalized. This electron delocalization, together with strong C=C bonds (~ 6.29 eV) makes them particularly stable. However, carbon nanotubes are known to be more reactive than "2D"-graphene. This increase in reactivity arises from the curvature of the graphene sheet in carbon nanotubes.[171] This curved structure causes two phenomena, that are responsible for the reactivity of CNTs towards chemical reagents.

First, the curvature of the graphene sheet results in a strain, forcing sp^2 carbon atoms to adopt a non-ideal structure. In a perfect sp^2 geometry, three sp^2 orbitals are aligned in the same plane, while one orthogonal p orbital allows the formation of the π bond. Graphene nearly adopts this geometry, while carbon nanotubes adopt a modified geometry, intermediary between sp^2 and sp^3 hybridization (Figure II.11). This phenomenon, known as "pyramidalization", enables the anchoring of functions on the external face of CNTs, through addition reactions.[172]

Second, the curvature of the graphene sheet induces a misalignment of the p orbitals (Figure II.12). This misalignment results in a distortion of the π electrons delocalization, significantly increasing chemical reactivity of the nanotube.
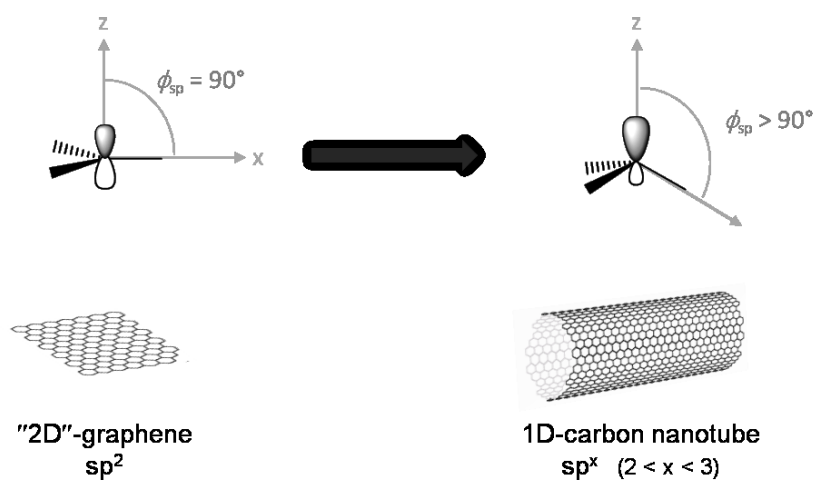
Figure II.11. Schematic representation of the pyramidalization effect induced by the wrapping of the graphene sheet to form carbon nanotubes: due to the curvature of the graphene sheet to form carbon nanotubes, the sp^2 orbitals are not coplanar anymore, while p orbital is asymmetrically distributed, with a pronounced delocalization on the external face of the CNT. Figure inspired from Haddon *et al.*[171]
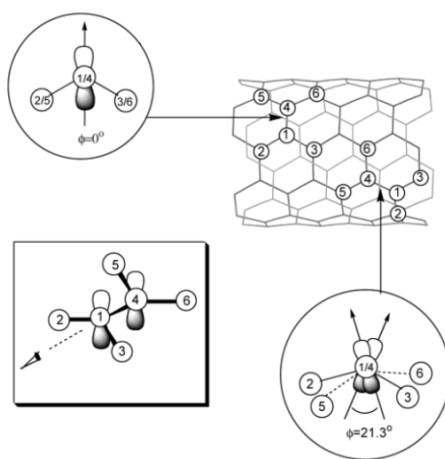
Figure II.12. Schematic representation of the misalignment of p-orbitals in carbon nanotubes. Reprinted with permission from [171]. Copyright © 2002 American Chemical Society.

Both pyramidalization and orbital misalignment depends on the nanotube helicity. For this reason, substantial difference in reactivity occurs from one tube to another. Typically, smaller diameter SWCNTs are more reactive than larger SWCNTs.[159] MWCNTs generally exhibit higher diameter than SWCNTs. For this reason, they are less reactive. The reactivity of carbon nanotube towards addition reactions also depends on the electrical type. Typically, metallic nanotubes are recognized to be more reactive than semiconducting ones. This reactivity difference arises from the non zero DOS at the Fermi level for metallic nanotubes, as shown in Figure II.5. The bandgap between occupied valence bands and unoccupied conduction bands in sc-CNTs makes the addition/subtraction of electrons difficult for covalent addition chemistry. The presence of electrons at the Fermi level for m-CNTs facilitates the formation of covalent bonds with external compounds.[173] This difference in reactivity, depending on the electronic properties of the nanotube, allows the separation of m- and sc-CNTs by controlled functionalization processes.[174,175]

Despite these phenomena, carbon nanotubes are very stable materials, and highly reactive reagents are needed for their covalent functionalization. Various methods have been developed lately for the covalent functionalization of carbon nanotube sidewalls. Due to the covalent nature of the bond formed between the grafted function and the nanotube, rehybridization of sp^2 carbon atoms into sp^3 occurs, altering π conjugated system. This results in modification of the electronic properties of the nanotube. Addition reactions of CNTs can be sorted depending on their impact on their electronic properties. We will hence make a distinction between **monovalent** and **divalent** functionalization processes. When using monovalent functionalization, grafted functions are anchored

to one carbon atom of the nanotube, while divalent functionalization consists in grafting the function by means of two covalent bonds on two adjacent carbon atoms of the CNT (Figure II.13, left and right). Both theoretical[176–178] and experimental[179,180] studies have demonstrated the advantage of using divalent functionalization for the preservation of electrical conductivity. This notion will be further detailed in Chapter VI.

Figure II.13 shows several addition reactions commonly used for the covalent functionalization of carbon nanotubes. On the left, various approaches developed for the monovalent functionalization of CNTs are presented: (a) halogenation;[181] (b) radical addition of diazonium salts;[164,182–184] (c) radical addition of peroxides[185] and (d) radical addition of xanthates.[186] On the right, typical divalent reactions are shown: (e) addition of carbene;[187] (f) addition of nitrene;[188] (g) Diels-Alder reaction[189] and (h) Bingel reaction.[190]

In this thesis, we will use two different functionalization pathways: the radical monovalent addition of diazonium salts and the divalent addition of malonate compounds by Bingel reaction. Detailed reaction mechanisms of these functionalization routes will be described in the relevant chapters.
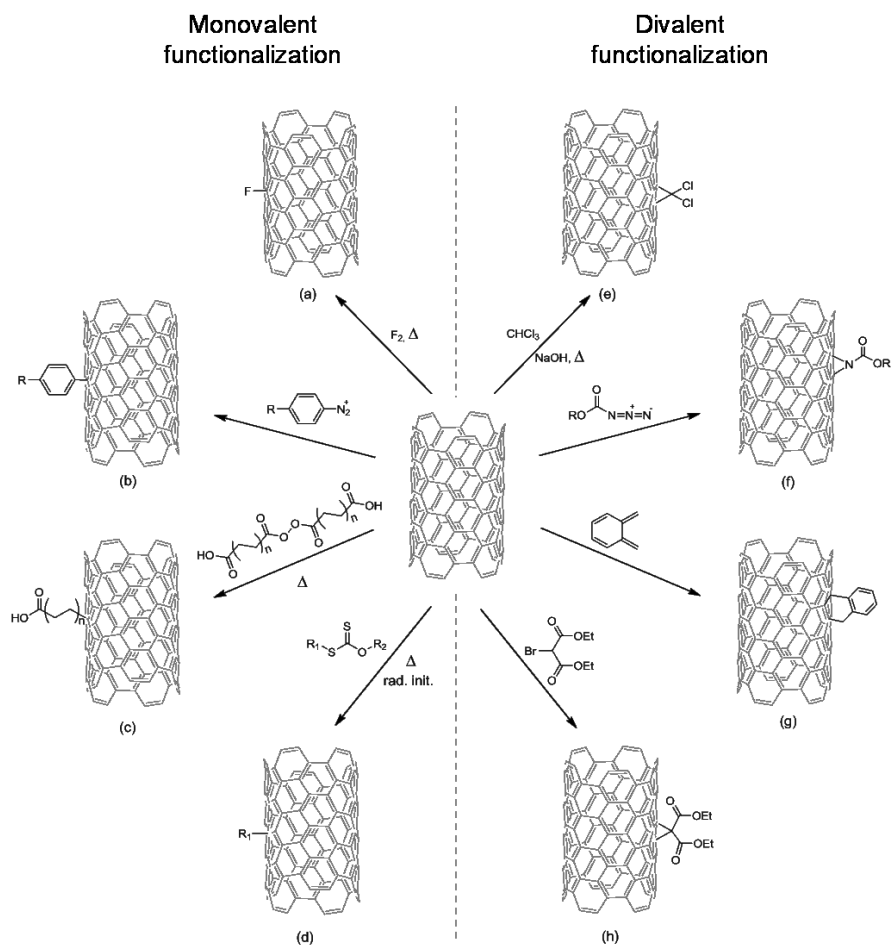
Figure II.13. Schematic representation of commonly used addition reactions for covalent functionalization of CNTs: (a) fluorination; (b) addition of diazonium salt; (c) addition of peroxide; (d) addition of xanthate; (e) addition of carbene; (f) addition of nitrene; (g) Diels-Alder reaction and (h) Bingel reaction.

II.1.5 *Difficulties related to the use of carbon nanotubes*

Due to their structure and properties, processing of carbon nanotubes is tricky. Indeed, as mentioned in the previous section, carbon nanotubes are insoluble in both organic and aqueous solvents.[146] Although the functionalization improves their solubility, the manipulation of carbon nanotubes remains challenging. Their characterization is therefore limited to techniques adapted to solid analysis, such as XPS, TGA, elemental analysis and electron microscopy. Moreover, carbon nanotubes are highly diffusive compounds, which makes their characterization by spectroscopic methods more difficult. UV-vis, IR and Raman spectroscopy can give precious information about CNT properties or functionalization, but are limited for SWCNTs due to the absence of permanent dipole moment.

In addition, the reactivity of carbon nanotubes strongly depends on their diameter and electric type (i.e. semiconducting or metallic).[191–194] Since carbon nanotubes are grown with a mixture of chirality, an inhomogeneity of reactivity is observed inside a batch. This diversity of species results in lack of reproducibility of the functionalization yield from batch to batch and, to a lesser extent, inside the same batch.

II.2 Electronic devices

As described above, carbon nanotubes exhibit unique electrical properties, giving rise to many potential applications, such as logic circuit components or sensor designs. In order to measure these electrical properties, carbon nanotubes can be integrated into electronic transistors.

The first transistors were discovered in 1947 by William Shockley, John Bardeen and Walter Brattain, who were awarded the 1956 Nobel Prize in Physics for their invention.[195] A transistor is a semiconductor device, composed of at least three electrodes, allowing to control an electrical current or voltage. Such electronic devices can be used to amplify and/or switch electronic signals, composing logic circuits. Transistors are present in everyday life electronics, such as computer, television, smartphones, but also in vehicles, household appliances, automatic dispenser, etc.

As described above, carbon nanotubes possess unique electrical properties. In particular, these materials exhibit extremely high electron mobility ($\sim 10^5$ cm^2.V^{-1}.s^{-1}, compared to $\sim 10^3$ for silicon).[130] This unique property arises from the low charge carrier scattering, due to their confinement in the 1D-structure of the nanotube. For this reason, defect-free carbon nanotubes are regarded at low bias as truly ballistic conductors.

Carbon nanotubes are therefore particularly suited for being embedded into electronic devices, as evidenced in 1998, when Tans *et al.*[196] and Martel *et al.*[197] simultaneously reported the first individual carbon nanotube field-effect transistor, CNT-FET.

II.2.1 Carbon nanotube field-effect transistors

In typical field-effect transistors, a semiconducting channel is connected by two electrodes, called "drain" and "source". The channel is separated from the silicon "gate" electrode by a thin insulating layer. This gate electrode allows control of the channel conductivity by accumulation or depletion of charge carriers in the semiconducting channel.

Figure II.14 illustrates the typical geometry of a CNT-FET. Carbon nanotubes are deposited on a silicon substrate, covered by a thin SiO_2 insulating layer. The CNT constitutes the channel through which the charge carriers (i.e. electrons or hole) flow. The CNT ends are connected by drain and source metallic electrodes. These electrodes enable to apply a voltage (V_{DS}) to drive the electrical current in the nanotube.[119] The conducting Si substrate acts as a back gate electrode modulating the CNT conductance and is activated by applying a voltage between this gate and the source electrodes (V_G). For semiconducting CNTs, the electrical conductance of the nanotube is modulated by several orders of magnitude, which can be recorded using the source source and drain electrodes current (I_{DS}) and bias (V_{DS}). This nanotube electrical conductance modulation or field-effect transistor effect is a key feature enabling the CNT sensors to operate.
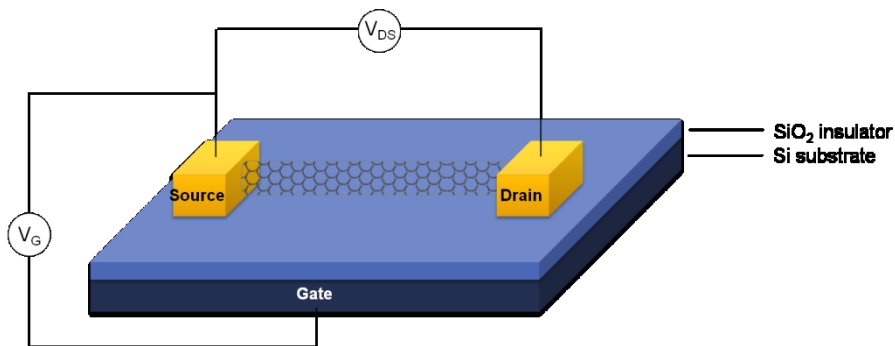
Figure II.14. Schematic representation of individual carbon nanotube field-effect transistor, CNT-FET.

II.2.2   Transfer curves

In this thesis, electrical characterization of carbon nanotubes consists in **transfer curves**, or $\mathbf{I_{DS}}$-$\mathbf{V_G}$ **curves**. For these measurements, a constant voltage is applied between source and drain electrodes (V_{DS} = 1 V). The drain-source current (I_{DS}) is measured while sweeping the gate voltage (V_G) back and forth between -20 V to +20 V (V_{step} = 0.2 V). Typical transfer curves of CNT-FETs are depicted in Figure II.15. As can be seen, electrical behavior of metallic and semiconducting nanotubes is really different. Indeed, transfer curves of metallic nanotubes remain roughly constant notwithstanding the gate voltage. This can be explained by the absence of bandgap in the density of states of metallic nanotubes (see Figure II.5b). For semiconducting nanotubes, a bandgap is present, decreasing the density of states to zero between valence and conduction bands (Figure II.5a). When applying a voltage to the gate, charge carriers accumulate in the nanotube, changing its doping state. This results in a large modification of the current I_{DS} with the applied V_G (Figure II.15b). As a consequence, electrical properties of semiconducting carbon nanotubes are strongly affected by their environment, while metallic nanotubes remain almost unaffected even after modification of their chemical environment. For this reason, semiconducting carbon nanotubes were advantageously selected for this thesis, since they can be used to probe chemical modifications by means of electrical measurement. The determination of the metallic or semiconducting character of the various CNT-FETs was made by observation of the transfer curves.
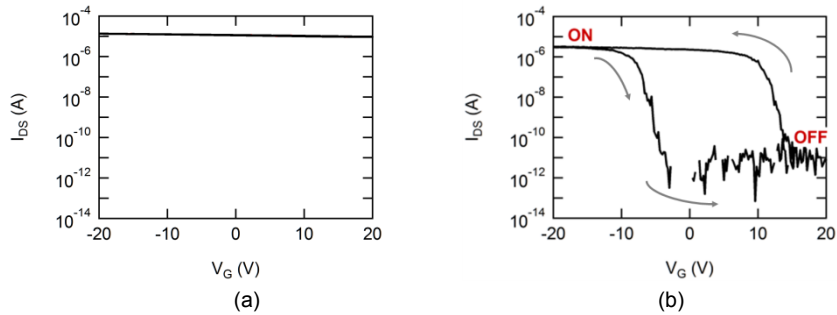
Figure II.15. Typical transfer curves for (a) metallic and (b) semiconducting carbon nanotubes.

As can be seen in Figure II.15b, conductance of semiconducting carbon nanotubes can be varied by several orders of magnitude. This conductance modulation is due to a modification of the nanotube doping state induced by the gate voltage. Figure II.16 illustrates the effect of the gate voltage on the nanotube doping. As can be seen, application of a negative gate voltage results in hole accumulation in the nanotube, hence allowing the hole conduction. On the contrary, application of a positive voltage to the gate induces electron accumulation and promotes the electron conduction. In other words, the Fermi level moves through the density of states when the gate voltage is swept.

As illustrated in Figure II.16, carbon nanotubes are often ambipolar and carry both hole (Figure II.16a) or electron currents (Figure II.16c). Figure II.17 illustrates a transfer curve of such ambipolar device. At large negative or positive V_G, the electrical conductivity of CNTs is ensured by holes (p-branch) or by electrons (n-branch), respectively (Figure II.17).
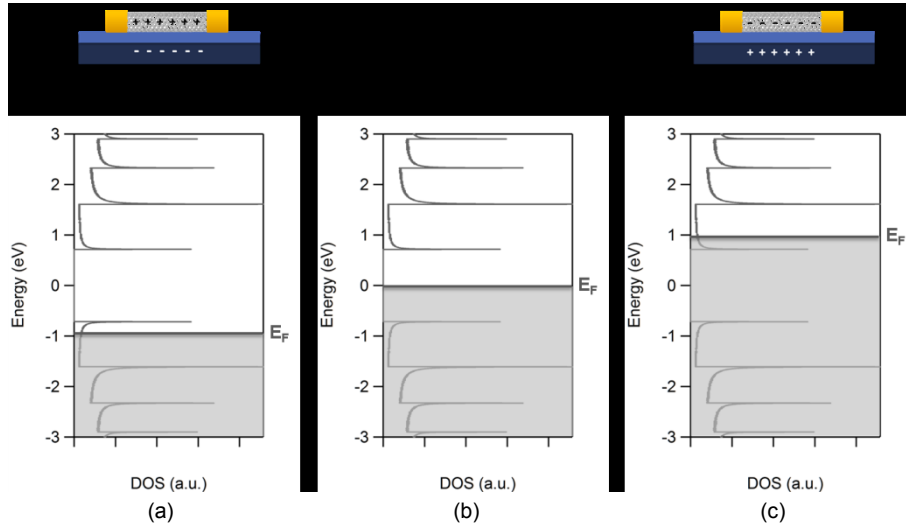
Figure II.16. Representation of the effect of the gate voltage on the doping of sc-nanotube: (a) hole conduction; (b) absence of conduction and (c) electron conduction.
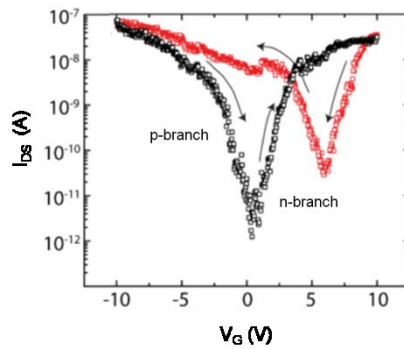
Figure II.17. Transfer curve of an ambipolar CNT-FET, in absence of oxygen/water layer, exhibiting p-branch and n-branch. Adapted with permission from [27]. © 2009 WILEY-VCH Verlag GmbH & Co.

In practice, the transfer curves are recorded in air, which are conditions that suppress the n-branch (Figure II.15b). This absence of ambipolarity is attributed to the presence of an oxygen/water layer at the surface of the silicon oxide.[27] More precisely, the chemical potential of H_2O/O_2 redox couple in mildly acidic conditions (pH = 6) is aligned with the position of the valence band of small diameter CNTs and induces an electron transfer from the nanotube to the oxygen/water layer, resulting in the trapping of negative species at the nanotube-silicon dioxide interface. This charge transfer can be suppressed by annealing at high temperature the devices in vacuum to desorb H_2O/O_2. This annealing indeed converts CNT-FETs from unipolar to ambipolar conduction.

As a consequence of this effect, the n-branch is generally not observed in air, which is the conditions used in this thesis. As depicted in Figure II.15b, a hole current flows through the nanotube at large negative voltage (-20 V). This hole conductivity state is designated as the ON state. At large positive voltage (+20 V), the current zero, a state designated as OFF state.[135]

Figure II.15b also revealed the presence of a large hysteresis in the I-V_G curve. This hysteresis is attributed to charge transfer between the CNT and shallow traps for charges at the interface between CNT and the gate dielectric.[198] During V_G sweep, these charge traps shift from neutral to charged states, which continuously shifts the threshold voltage in the CNT transfer curve. This phenomenon depends on the rate of gate voltage sweep because these traps have different potential depths and dynamic responses. For this reason, it is of critical importance to always sweep the gate voltage in the same direction and at the same rate, to obtain comparable I-V_G curves for each measurement. A constant sweeping rate indeed allows

obtaining a similar charge history for each measurement. It is also worth noting that this hysteresis is induced by the modulation of the gate voltage. As a result, if the gate voltage is kept constant, as is the case for sensing experiments in Chapter VII, this hysteresis does not raise any concern.

II.2.3 *Electrical characterization of CNT-FETs*

Electrical features of the devices were characterized using a probe station. In this instrument, the sample is placed on a moving stage, which controls the gate voltage. Two metallic probes are used to connect drain and source electrodes. These probes can be moved in x, y and z directions thanks to accurate manipulators. This tool is also equipped with an optical microscope, enabling to place the probes on the desired electrode pads. Data acquisition is performed thanks to a semiconductor parameter analyzer (Agilent SPA). This instrument is able to measure both at once a current (or voltage) while applying a voltage (or current). Source and drain electrodes are connected using source measure units (SMU). These SMU are able to detect very low current and voltage with high accuracy.[199]

This instrument can also be automated. In this case, the stage movement is controlled by a computer, according to the device configuration. In addition to being more time-efficient, this automated system ensures a uniform contact between probes and electrodes, for each analyzed device. Columbia University possesses this kind of "autoprobe" station. A short term stay in Colin Nuckolls' group allowed to beneficiate from this facility.

II.2.4 *Functionalization of CNT-FETs*

Two approaches can be used to study the impact of functionalization of carbon nanotubes on their electrical properties. First, distinct transistors can be used for the characterization of pristine and functionalized nanotubes. This strategy involves the preparation of field-effect transistors for each material that needs to be characterized. Using this approach, a large number of functioning transistors is required to obtain a sufficient statistic, because each nanotube possesses its own features. Since transistor fabrication process involves several steps, this approach is obviously not the ideal solution.

The second approach consists in functionalizing the carbon nanotube after being integrated in an electronic device. This approach allows to characterize the same device at each step of the functionalization process. It helps to overcome the problems related to variability of nanotube features in one sample. For this reason, we opted for this strategy throughout this thesis project. However, this approach also raises some difficulties. First, the reaction mixture should not leave residues on CNT-FET surface that could alter the electrical measurements. This point implies to avoid insoluble compounds and solid metallic catalysts. The functionalization process must therefore be adapted accordingly. Second, the chemical process should not corrode the metallic electrodes. This would result in a modification of the injection of charge carriers in the nanotube, decreasing the nanotube conductance. In order to prevent this phenomenon, titanium electrodes could be used. A passivation layer would indeed quickly be formed on the Ti surface, reducing its interaction with external compounds. In practice, Ti electrodes were used for the

fabrication of devices using geometry 1 and 3, while Au electrodes were used for the fabrication of devices in geometry 2.

II.2.5 Impact of the functionalization on CNT electrical conductance

Chemical functionalization of carbon nanotubes has a significant impact on their electronic properties. Covalent functionalization indeed introduces disorder in the nanotube sp^2 structure, dramatically altering its electrical conductivity.[200] Adsorption of selective gas[26] or organic molecules[201] on the SWCNT surface is also known to modify transport properties of this material. Knowing this, electrical measurements can be used to probe the functionalization of carbon nanotubes.

II.2.5.1   Monovalent functionalization

Single-walled carbon nanotube properties are strongly modified by monovalent functionalization. In pristine nanotubes, each carbon atom have sp^2 hybridization. Three valence electrons are engaged in the formation of covalent σ bonds with their neighbors, while the third one is delocalized by its π bonding character. This delocalized π electron system is responsible for optical and electronic properties of the nanotube. For a monovalent functionalization of CNTs, two π electrons become localized in the new chemical bonds, resulting in a breaking of one double C-C bond and hence the two functionalized carbon atoms undergo a rehybridization from sp^2 to sp^3. Those sp^3 carbon atoms, also known as structural defects, act like scattering points by disrupting the delocalization of π electrons through the nanotube.[202] This phenomenon is accompanied by a significant decrease of the nanotube conductivity.[202] Despite the localization of the

71

functionalization-induced defect, the consequences of this defect on the CNT properties are extended over a large distance.[200] For this reason, even the introduction of a single point functionalization defect has a significant impact on the nanotube conductance.[63,203,204] Furthermore, as demonstrated by both theoretical[202,203] and experimental studies[205–207], the higher the grafting yield, the lower is the conductivity.

However, a thermal annealing (under vacuum or inert atmosphere) of the functionalized CNTs is able to remove the covalent grafted functions. The initial properties of the nanotube are then almost recovered, as predicted by theory[208] and demonstrated by experiments.[209–211]

II.2.5.2   Divalent functionalization

Divalent functionalization appears to be an interesting alternative to monovalent functionalization (Figure II.18a) because it preserves the nanotube conductance.[179,180,203,212–214] In this case, the functionalization process implies the formation of two bonds between the grafted functionality and two adjacent carbon atoms on the nanotube surface. Two configurations can be adopted as illustrated in Figures II.18b and c.[176,213] On the one hand, the "*closed*" configuration (Fig. II.18b) implies rehybridization of the two adjacent carbon atoms from sp^2 to sp^3, leading to an alteration of the CNT electrical properties. On the other hand, in the "*open*" configuration (Fig. II.19c), the bond between the two adjacent carbon atoms in the divalent functionalization is broken. In this latter configuration, the sp^2 hybridization is preserved, as well as the electrical properties of the nanotube.
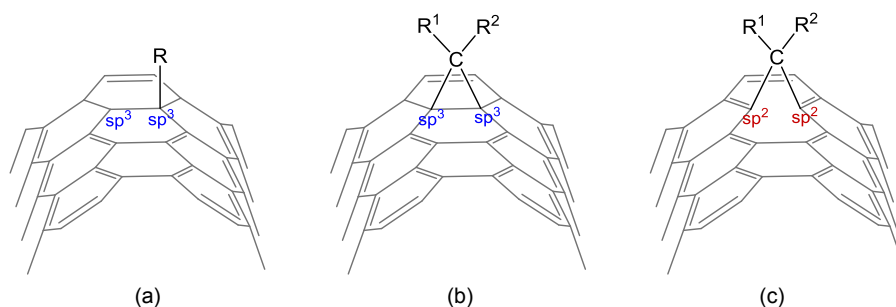
Figure II.18. Schematic representation of the bonds formed between the carbon nanotube and the grafted functionality after (a) a monovalent functionalization; (b) a divalent functionalization in "*closed*" configuration and (c) a divalent functionalization in "*open*" configuration.

The *open* configuration is generally considered as the most stable, according to theoretical calculations.[176–178] Indeed, three-membered rings resulting from the addition of divalent adducts on carbon nanotubes in the *closed* configuration exhibit high strain, in a similar way than cyclopropanes, which are known to be less stable in classical organic chemistry than propene.[176,177] As a consequence, the structure naturally relaxes to the *open* configuration. Moreover, the *open* configuration is also preferred for its higher aromaticity.[176] The structure of a divalent adduct attached on carbon nanotube surface can indeed be compared to a bridged 1,6-X-[10]annulene (Figure II.19). As one can see, two resonant forms exist. The first one possesses a strained three-membered ring. The second one, resulting from the 1,6 C−C bond breaking, leads to a system composed of 10 delocalized π electrons. According to Hückel's rules[ii], this structure is aromatic and is therefore more stable.[215] Theoretical studies also demonstrate that the addition of divalent adducts on the carbon

---

[ii] As defined by Hückel's rules, a planar cyclic molecule is aromatic if it has (4n+2) conjugated, delocalized π electrons, with n being an integer.

nanotube surface is preferably done on the C−C bonds perpendicular to the tube axis, in the case of armchair (metallic) nanotubes, or C−C bonds slanted to the tube axis, in the case of zigzag nanotubes. These C−C bonds are the most incurved ones in the structure. This curvature promotes the opening of the bridged C−C bond.[176,177] For these reasons, attachment of divalent adducts on carbon nanotube surface preferably leads to an *open* configuration (Figure II.18c). This configuration preserves the sp^2 hybridization of carbon atoms, resulting in a very slight perturbation of the electrical properties of the nanotubes.
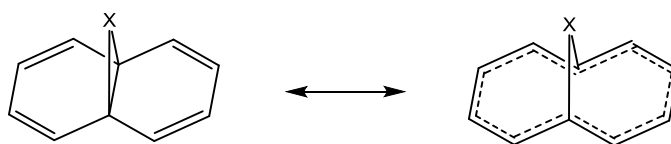
Figure II.19. Schematic representation of the resonant forms of 1,6-X-[10]annulene.

These theoretical predictions have been experimentally confirmed a few years ago. A first experiment demonstrated that divalent addition of dichlorocarbene ($>CCl_2$) functions preserves the conductance of metallic nanotubes, while the conductance of semiconducting ones is greatly affected by this functionalization.[179] However, this study was only performed on two individual nanotubes, one semiconducting and the other metallic, and is therefore not statistically significant. A more systematic study, revealed that the divalent addition of methylene ($>CH_2$) and dichlorocarbene ($>CCl_2$) functions preserves the conductance of single-walled carbon nanotubes.[180] This latter investigation was performed on a large number of individual SWCNT-FETs and led to the same conclusion, regardless the semiconducting or metallic nature of the nanotube.

II.2.5.3   Functionalization-induced midgap states

Covalent functionalization is also known to induce the formation of states in the nanotube bandgap. These functionalization-induced midgap states allow the charge carriers to flow by alternative pathways. This effect is experimentally observed by an increase of the OFF-state conductance after functionalization, as illustrated in Figure II.20. This current leakage can reach several orders of magnitude over the highly insulating OFF state.
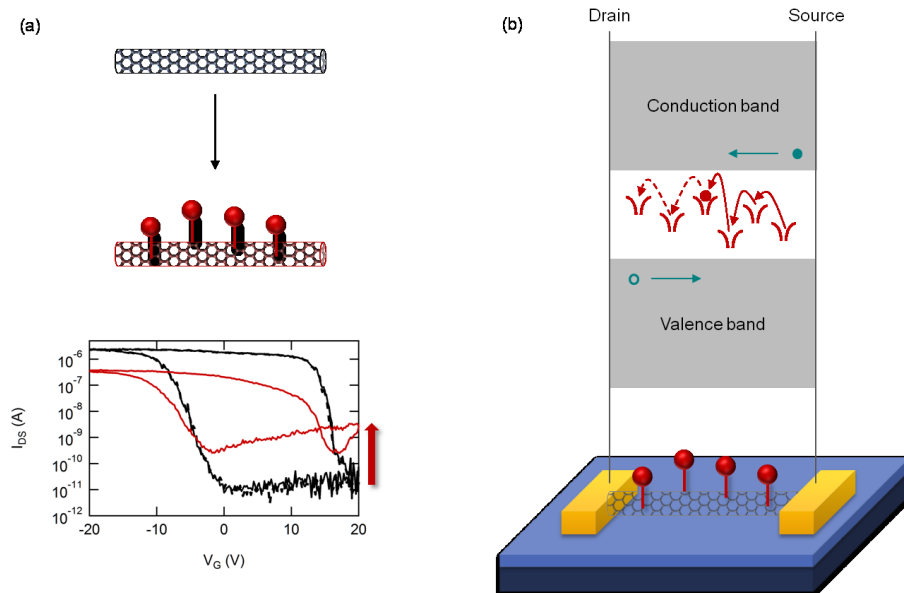
Figure II.20. (a) Transfer curves of pristine and covalent functionalized SWCNTs, highlighting the increase of the OFF-state and (b) representation of the hopping transport between functionalization induced gap states.

CHAPTER III - PREPARATION OF INDIVIDUAL CARBON NANOTUBE FIELD-EFFECT TRANSISTORS

Abstract

Individual carbon nanotube field-effect transistors (CNT-FETs) are used throughout this thesis as a tool for studying the impact of chemical functionalization on carbon nanotube electronic properties. These devices were also used as sensors to detect a catalytic activity. This chapter intends to give a brief description of the fabrication process of these individual CNT-FETs. We also discuss in this chapter the main advantages and disadvantages of the various geometries of devices considered in this thesis.

III.1 Carbon nanotube sources

In this thesis, different sources of SWCNTs were integrated into field-effect transistors: (a) laser-ablation (LA) SWCNTs, received from the National Research Council of Canada;[216] (b) CVD-grown SWCNTs, purchased from Sigma-Aldrich[217] and (c) flow aligned CVD-grown SWCNTs on silicon oxide substrate,[218] synthesized by D. Bouilly at Columbia University. The two former sources were in powder form, while the latter one is composed of carbon nanotubes directly synthesized on a Si/SiO$_2$ substrate.

- **Source (a)** of SWCNTs has already largely been used in Martel's laboratory for the preparation of electronic devices. These CNTs possess good transport properties and have been chosen for their large bandgap. However, these SWCNTs contain impurities (namely amorphous carbon and catalyst particles) that need to be removed before using them for further applications. This purification process is time consuming and involves a significant loss of materials. For this reason, this source was not adapted to "bulk" functionalization and catalytic applications.

- SWCNTs of **source (b)** were commercially available in purified form. This point makes them the ideal source for "bulk" functionalization and catalysis, as they can be used as received, without further purification steps. These SWCNTs were also integrated in electronic devices, in order to test the reproducibility of the conclusions drawn from electrical characterization, whichever the carbon nanotube source used.

- Finally, SWCNTs grow-aligned on Si/SiO$_2$ (**source (c)**) were selected. Their "substrate-supported" form is particularly suited for their integration in electronic devices. C. Nuckolls and coworkers recently developed a method for the fabrication of hundreds of devices on one single carbon nanotube.[219] This process allows to conduct statistical studies on one nanotube. Short-term stays in Nuckolls laboratory were accomplished during this thesis to benefit from this kind of devices, which were synthesized by Dr D. Bouilly. More information about this configuration of devices will be given in section III.2.2.

III.2 CNT-FETs fabrication

Fabrication of CNT-FETs implies a multi-step process. First, carbon nanotubes are deposited on a silicon substrate, which acts as gate electrode. This step is performed during the synthesis when using CNTs directly grown on Si/SiO$_2$ substrate, as is the case for source (c). Second, metallic electrodes are deposited. This second step requires lithography process to design the electrode pattern, followed by e-beam evaporation of the desired metal. Finally, a thermal annealing of the devices is performed to improve the electrical contact between electrodes and carbon nanotubes.[220]

Two main approaches are generally used for the connection of source and drain electrodes on an individual CNT. On the one hand, electrodes can be patterned on the ends of the nanotubes. This method requires a prior location of carbon nanotubes on the chip. On the other hand, electrodes can be deposited according to a predefined pattern. This second approach yields to a pattern of electrodes, randomly positioned

with respect to nanotube location. Even if some devices are not connected, this procedure affords a large number of devices, while being more time-efficient than the first approach. These two approaches were used throughout this thesis (Table III.1), depending on the nanotube source concerned. The next paragraphs of this section describe the fabrication process of the different configurations of devices used during this thesis. More experimental details can be found in Annex IX.4.1.

Table III.1. Summary of the different device configurations used throughout this thesis, in relation with the SWCNT source and the electrical characterization type.

Device configuration	Fabrication approach	SWCNT source	Measurement type
Geometry 1	Random pattern of electrodes	(a) LA, powder (b) CVD, powder	I-V_G
Geometry 2	Electrodes fabricated at CNT ends	(c) CVD, Si/SiO$_2$ supported	I-V_G
Geometry 3			I(t)

III.2.1   Geometry 1

This section describes the fabrication process of the first geometry of electronic devices used during this thesis. Figure III.1 gives a schematic representation of the electrode pattern. As can be seen, the electrodes are gathered by groups of four, forming three potential devices. Electrode 2 can be connected to electrodes 1, 3 or 4. This design is reproduced three times, with varying spacing between the electrodes in each row (1, 2 and 3 μm). This pattern is reproduced 77 times over the chip, for a total of 693 possible devices.
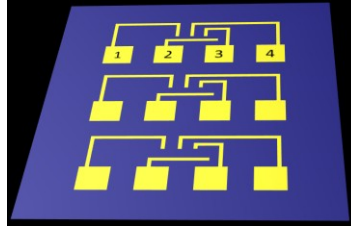
Figure III.1. Schematic representation of the electrode pattern in CNT-FET in geometry 1.

The first step in the fabrication process of this first geometry of electronic devices consisted in depositing SWCNTs on a Si/SiO_2 substrate. In order to do this, prior functionalization of nanotubes and of the Si/SiO_2 substrates were performed. This ensures a good adhesion of the nanotubes on the substrate. The oxidized silicon substrate was modified by 3-(aminopropyl)triethoxysilane (APTES) in order to anchor amine functions (Figure III.2).[221,222] Those amine functions were able to react with carboxylic functions present on carbon nanotubes, previously refluxed in nitric acid.

Figure III.2. Schematic representation of the functionalization of oxidized silicon substrate by APTES. Figure inspired from Howarter *et al*.[222]

This deposition of carbon nanotubes on Si/SiO_2 substrates includes two critical parameters: (i) nanotube concentration and (ii) nanotube alignment. Indeed, a sufficient concentration of nanotube is necessary in order to get a high probability of connection of CNTs between drain and source electrodes. However, excessive concentration of nanotubes may dramatically increase junctions and multiple connections between nanotubes, which makes interpretation of current-voltage curves difficult. Testing performed over the years in Martel's laboratory indicated that the ideal concentration of nanotubes was comprised between 0.3 and 0.5 $CNTs/\mu m^2$. It is also important that carbon nanotubes are aligned with each other on the silicon substrate. This also enables to avoid undesirable CNT-CNT junctions while optimizing the chance of connection of nanotubes between electrodes.

SWCNTs were deposited on APTES-functionalized Si/SiO_2 substrates, by spin-coating of desired amount of a diluted suspension of purified SWCNTs. Adjustment of the rate of spin-coating, amount of spin-coated suspension and concentration of the suspension enables to control the concentration of nanotubes deposited on the substrates. Alignment of nanotubes in a radial direction was obtained thanks to centrifugal forces implied by the spin-coating process. Atomic force microscopy was used to control both concentration and alignment of the deposited nanotubes (Figure III.3).
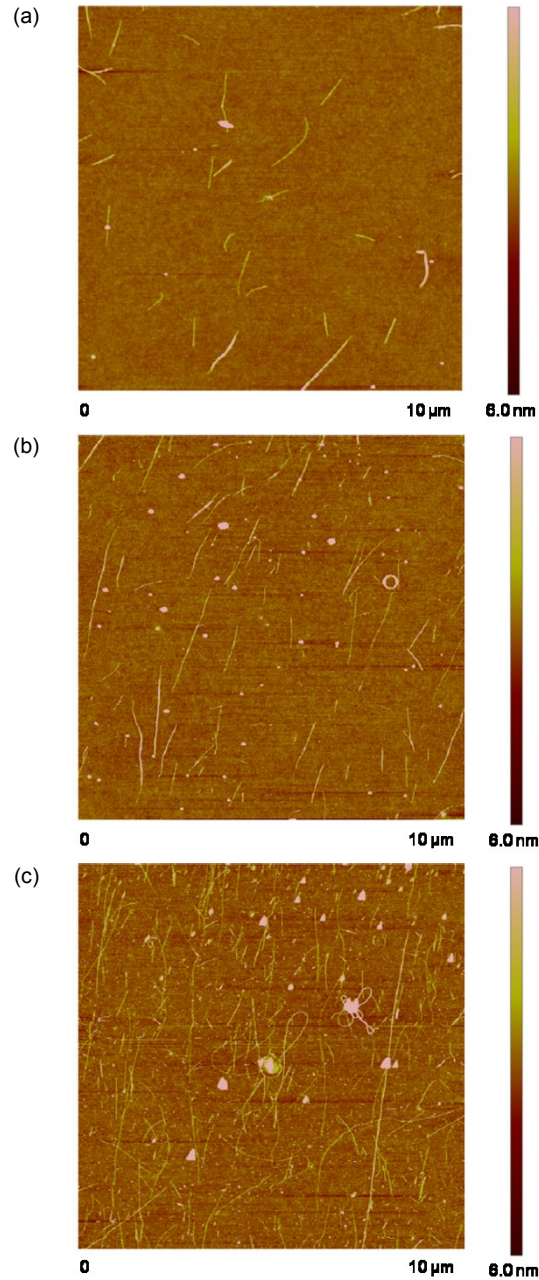
Figure III.3. Height AFM images of various concentrations of aligned SWCNTs deposited on a Si/SiO$_2$ substrate: (a) low concentration of SWCNTs, which would result in low yield of connected devices; (b) ideal concentration of well-aligned SWCNTs and (c) too high concentration of SWCNTs for multi-connected devices.

Once the SWCNTs are deposited on Si/SiO$_2$ substrates, source and drain electrodes can be patterned. This step was performed by conventional photolithography process (Figure III.4). First, a photoresist is spin-coated on the SWCNTs supported on Si/SiO$_2$ chip (Fig. III.4b). Then, photolithography through a predefined mask is performed. This step irradiates the future electrode positions. A development step removes the irradiated section of the resist (Fig. III.4c). Metallic electrodes are then deposited on the sample by electron beam evaporation (Fig. III.4d). Lift-off in PG-Remover removes residual resist, leaving metallic electrodes on the predefined areas (Fig. III.4e). A thermal annealing (500 °C) under vacuum is finally performed to improve nanotube-electrode contacts.
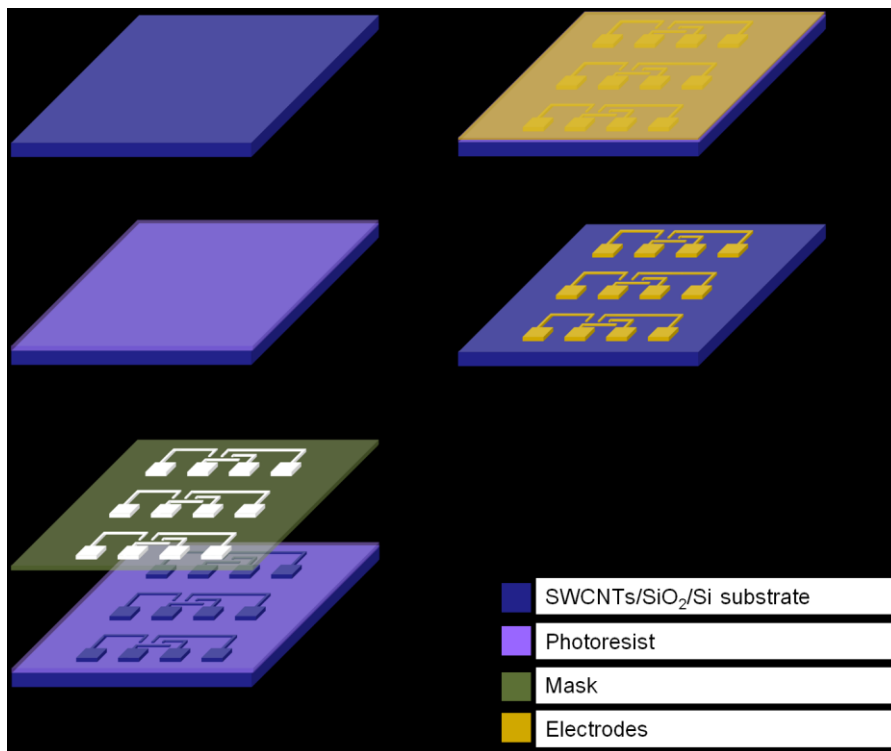
Figure III.4. Schematic representation of the fabrication process of SWCNT-FETs (Geometry 1).

Given the fabrication process of these devices, electrodes are randomly deposited with respect to carbon nanotube position. For this reason, not all the devices were actually connected to carbon nanotubes. In order to identify the functioning devices, current-voltage curves were recorded for each potential device. Measurements of current revealed the presence of connection between electrode pair by one or more conducting carbon nanotube(s). Functioning devices were then imaged by AFM or SEM to verify the number of connected nanotubes and the potential presence of junctions or multiple connections (Figure III.5).
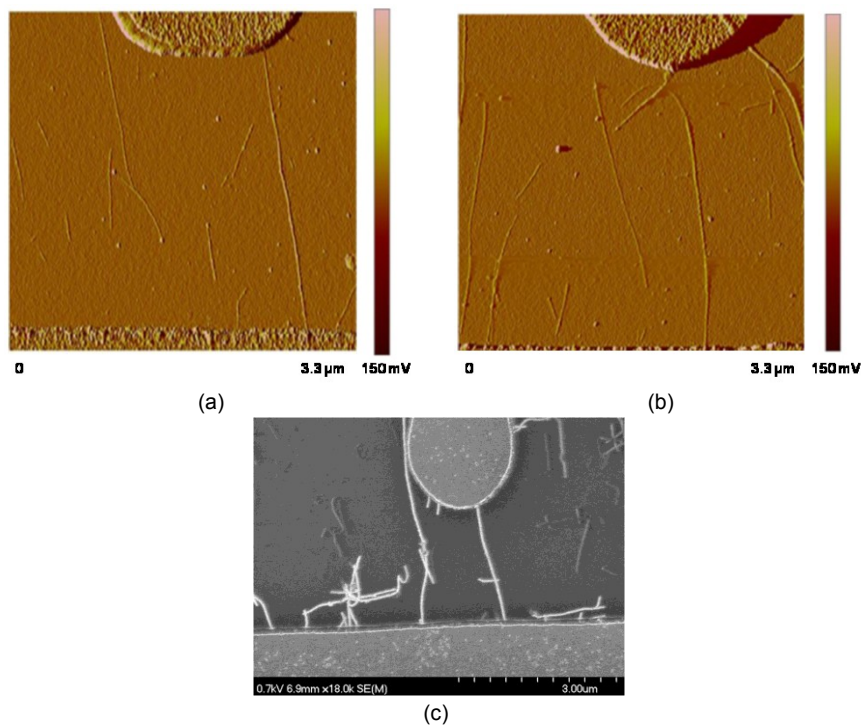
Figure III.5. AFM (a, b) and SEM (c) images of connected devices: (a) connection of one individualized SWCNT between source and drain electrodes; (b) connection of drain and source electrodes by junctions between two nanotubes and (c) multiple connections of source and drain electrodes by two nanotubes.

AFM was also used to measure the nanotube diameter. This information was particularly useful to distinguish individual nanotubes from nanotube bundles, as illustrated in Figure III.6.
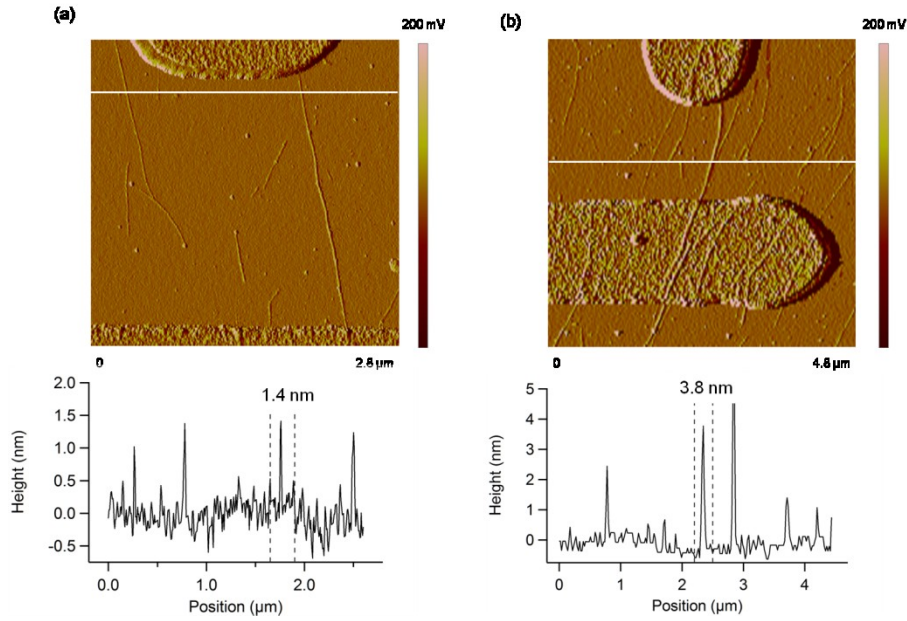
Figure III.6. (Top) AFM amplitude images and (bottom) height cross-section of (a) an individual SWCNT and (b) a CNT bundle connected between two electrodes.

During this thesis, we prepared numerous samples of devices using this geometry. We obtained between 30 and 145 connected devices out of the 693 possible devices, i.e. ~ 4 to 21 % of connection. Among these connected devices, only about one third does not contain multiple connections or junctions. As a consequence, this fabrication process allowed to prepare a limited number of individual SWCNT-FETs.

III.2.2 Geometry 2

A second geometry was used for the electrical characterization of the catalyst. Unlike the fabrication process used for geometry 1, SWCNTs were directly synthesized on Si/SiO$_2$ wafer, by flow-aligned CVD growth. The long and tedious step of deposition of nanotubes on silicon substrate is thus avoided. Figure III.7a gives a schematic representation of the electrode pattern. Series of adjacent electrodes (source and drain) are patterned in the center of the chip, along the nanotube. Each source and drain electrodes are connected to ~ 100 µm^2 pads for the probing of each electrode pair during electrical characterization. Each CNT channel is 4 µm in length.
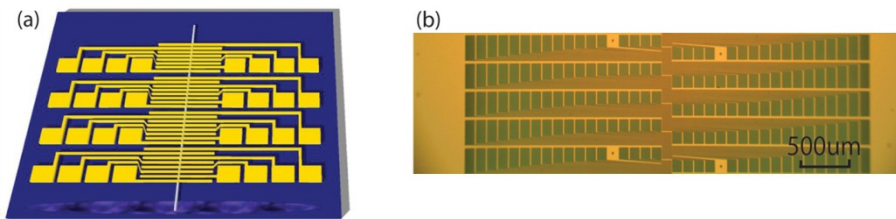
Figure III.7. (a) Schematic representation of the electrode pattern in CNT-FET geometry 2; (b) Optical microscopy image of the photolithography mask used for the design of electrodes pattern. Reprinted with permission from [219]. Copyright © 2013 American Vacuum Society.

The fabrication process of these devices contains two successive lithography steps, as shown in Figure III.8. First, 285 nm oxidized silicon wafers were diced into ~ 1 cm^2 substrates (Fig. III.8a). SWCNTs were grown by flow-aligned CVD growth (Fig. III.8b). One single long CNT was identified and localized by SEM. Electrical contacts were patterned by e-beam lithography, through a predefined pattern (Fig. III.7b), centered on the selected nanotube (Fig. III.8c). Metal electrodes (3 nm of Ti followed

by 50 nm of Au) were deposited by electron beam evaporation. A second lithography was performed to remove carbon nanotubes outside the interest area. This step is crucial to avoid short circuits from additional nanotube connections. First, the substrate was coated with polymethylmethacrylate (PMMA) (Fig. III.8d). E-beam lithography was performed to define the area of interest (Fig. III.8e). The samples were then exposed to an oxygen plasma in order to etch away the unprotected carbon nanotubes (Fig. III.8f).
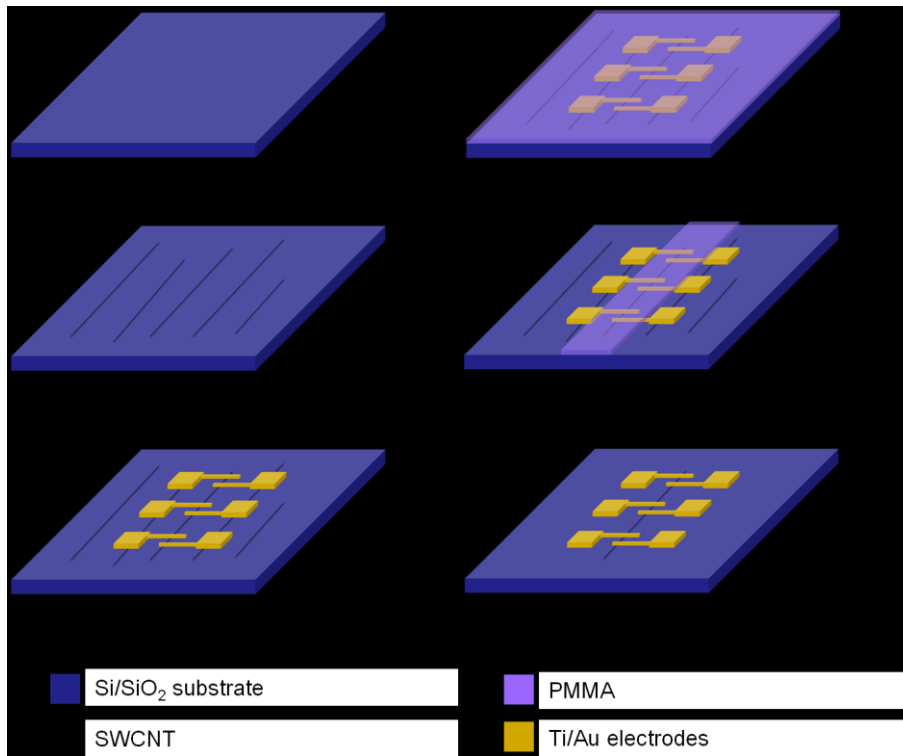
Figure III.8. Fabrication process of multiple CNT-FETs on one single SWCNT (Geometry 2). Figure inspired from Zhang *et al.*[219]

The advantage of using this second CNT-FET geometry is that a large number of devices (175) are fabricated on the same nanotube (Figure III.9). High reproducibility is thus expected from such devices.
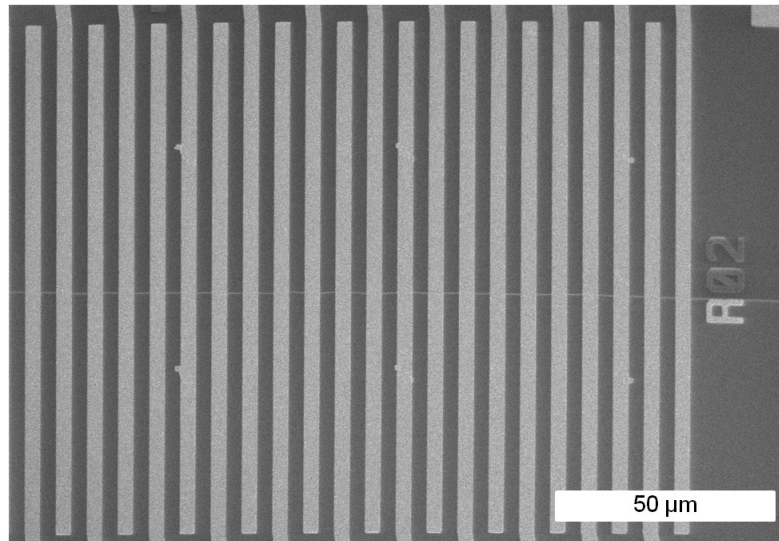
Figure III.9. SEM image of a section of chip in geometry 2. Each chip is composed of five similar sections, each of them containing 35 devices. This image shows the presence of one single SWCNT. Each device is thus connected to the same SWCNT.

III.2.3 Geometry 3

Finally, a third geometry was used for the sensing experiments of catalytic activity (Chapter VII). These devices were provided by Jason Hon and Delphine Bouilly, at Columbia University. Figure III.10 shows the electrode pattern. Each CNT channel is ~ 4 μm long. Drain and source electrodes are connected to large square pads for wire-bonding. Those pads are separated by a large distance (about 8 mm), in order to give room for a flow-cell for sensing experiments. The fabrication process of this third kind of device is similar to the second one. This geometry of devices yields to a maximum of 32 functioning devices. These devices were measured

simultaneously thanks to an adapted real-time measurement setup (See Chapter VII for more details).
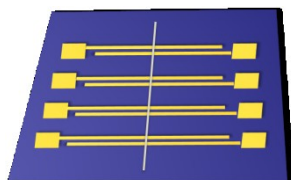
Figure III.10. Schematic representation of the electrode pattern in CNT-FET geometry 3, used for sensing experiments.

III.2.4 *Comparison of the three geometries of devices*

As described above, three types of devices were used in this thesis. Devices of geometries 1 and 2 were used for the electrical characterization of functionalized carbon nanotubes in air, while devices of geometry 3 were used for the real-time electrical measurements performed for the *in situ* detection of catalytic activity.

The particularity of geometries 2 and 3 lies in the fact that each device is prepared on the same carbon nanotube. This approach allows obtaining a large number of devices exhibiting uniform properties. The fabrication process of this kind of devices, developed by C. Nuckolls *et al.*, was indeed reported to deliver hundreds of CNT-FETs exhibiting similar ON-state conductance and same threshold voltage.[219] Nevertheless, in practice, a low variation of electrical features is observed in the same nanotube. This electrical dispersion is due to the presence of defects created during the synthesis. These defects change the nanotube helicity, hence modifying its electrical properties. Moreover, the ON-state conductance varies slightly from device to device, due to small variations of the CNT-electrode contact quality.

90

To stay focus on the objective of the real-time sensing experiments, we did not reproduce a statistical study of the electrical behavior of this kind of devices. The reader is referred to Annex IX.4.2 and reference [219] for additional information. However, these devices fabricated around the same carbon nanotube allow assessing the reproducibility of the functionalization. Since each device is made of the same CNT, the reactivity is expected to be the same in each one. This is particularly interesting since the electric type of the nanotube highly impacts its reactivity.

Nevertheless, since carbon nanotube sources are composed of a mixture of m- and sc-CNTs, it is possible to estimate the reproducibility of the functionalization from one nanotube to another. To achieve this, geometry 1 of CNT-FETs is better adapted, since all the devices are made of different nanotubes, hence exhibiting a statistical dispersion of m- and sc-CNTs.

The major drawback of geometry 1 lies in the random position of the CNTs towards the electrode pattern. As a result, the number of connected CNT-FET is limited (See Annex IX.4.3). Figure III.11 (geometry 1) highlights the standard deviation (± 7 %) of the proportion of connected devices, relatively to the mean value. This reveals a lack of reproducibility from one chip to another. This observation can be attributed to the fact that the CNT network density significantly differs from one chip to another, giving a proportion of connected devices between 1 and 24 %. Furthermore, about two thirds of the connected devices contain CNT-CNT junctions, multiple connections, or are connected by CNT bundle rather than by individualized CNTs.
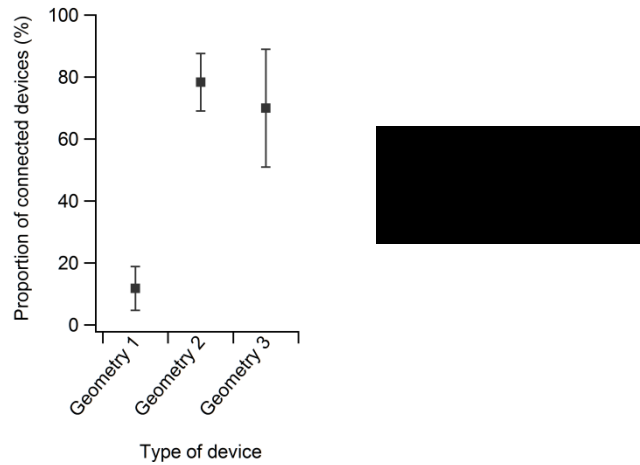
Figure III.11. Proportion of connected devices for the three geometries of devices. (Data are given in Annex IX.4.3)

Concerning the second geometry of devices, the proportion of connection is substantially higher. This is easily explained by the fact that the electrodes are patterned around the nanotube, and not randomly as for geometry 1.

Finally, the proportion of connected devices for geometry 3 reported in Figure III.11 is lower than the result obtained for geometry 2. The CNT-FET fabrication process is the same, but geometry 3 requires an adapted design for the integration of these devices in a real-time measurement setup. Hence, the number of measured devices is significantly lower (160 tested devices in geometry 3 *vs.* 909 in geometry 2).

Table III.2 summarizes the main features leading to advantages and disadvantages of each different type of devices.

Table III.2. Comparison of the main advantages and disadvantages of the three geometries of devices considered in this thesis.

	Geometry 1	Geometry 2	Geometry 3
Advantages	√ Each device is made of distinct CNTs → **CNT-CNT reproducibility** √ **Representative of a standard CNT sample**	√ Numerous (> 100) devices on the same CNT → **Adapted to statistical studies** √ High yield of connected devices	√ Several (i.e. 15 to 32) devices on the same CNT → **Reproducibility** √ Design adapted for the placement of a flow cell √ Large pads for wire bonding → **Design adapted for real-time electrical measurements**
Disadvantages	✗ Poor proportion of connected devices ✗ Undesired connections (junctions, CNT bundles, multiple connections) ✗ Tedious process for the determination of connected devices	✗ Not representative of a standard CNT sample	✗ Not representative of a standard CNT sample

While geometry 1 of devices is particularly adapted for studying the reproducibility of the functionalization, its fabrication process involves several drawbacks: e.g. yield of only 12 % on average, chip-to-chip variation of reproducibility due to density and alignment of the deposited CNTs. In addition, approximately two thirds of the connected devices involve poorly defined channels, such as multiple connections, tube-tube junctions, bundles, etc. Finally, the determination of the number of connected devices is a long process and involves electrical measurements and SEM and/or AFM for each structure to determine which devices have individual CNT.

Geometry 2 allows the fabrication of a large number of devices on the same carbon nanotube. This feature allows studying the reproducibility of the functionalization on the same nanotube and is therefore well adapted to statistical studies. Moreover, the fabrication process provides a high yield of connected devices (78 % on average).

III.3 Conclusion

In summary, geometry 2 is well adapted to assess the reproducibility of the functionalization whereas geometry 1 requires larger effort for a limited number of devices. For these reasons, geometry 2 was favored in this thesis. Nevertheless, geometry 1 remains representative as a standard for different CNTs because it provides a higher sampling of CNTs having various electronic types.

CHAPTER IV - MONOVALENT FUNCTIONALIZATION

Abstract

This chapter deals with the monovalent functionalization of single-walled carbon nanotubes for the preparation of heterogeneous catalysts. The first section is devoted to the development of a chemical route for anchoring bimetallic nanoparticle precursors on functionalized carbon nanotubes. A thermal activation allows depositing nanoparticles homogeneously dispersed on carbon nanotube surface, with a diameter comprised between 0.5 and 1.7 nm. The second part of this chapter provides an overview of electrical characterization of the materials at each step of the catalyst preparation process. Current-voltage measurements highlight a decrease of nanotube conductance after monovalent functionalization, which is related to the rehybridization of sp^2 carbon atoms into sp^3. Thermal activation of the nanoparticles results in a partial recovery of initial conductivity, together with a large p-doping of the carbon nanotube, revealing a charge transfer between carbon nanotube and supported nanoparticles.

IV.1 Introduction

IV.1.1 Addition of aryl diazonium salts on CNTs

Among the large panel of covalent processes developed for the functionalization of carbon nanotubes,[138,146,147,149,151,152,160] addition of aryl diazonium salts on carbon nanotubes surface remains one of the most commonly used methods.[182] In classical organic chemistry, aryl diazonium salts are able to react with olefins and aromatic compounds through the Meerwein reaction (Figure IV.1).[223,224]
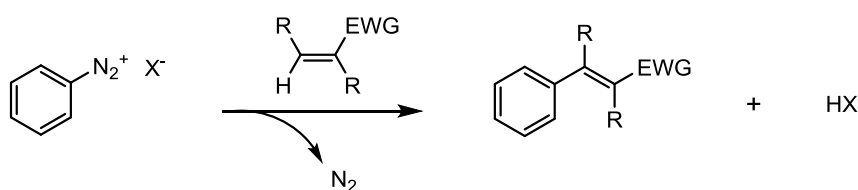
EWG = Electron Withdrawing Group

Figure IV.1. Schematic representation of the Meerwein reaction between an aryl diazonium salt and an alkene.

In a similar way, such diazonium salts can be grafted on a carbon nanotube surface, as demonstrated by J. M. Tour.[182] Aryl radicals were initially generated by electrochemical reduction of phenyl diazonium salts using bucky-paper electrode.[182] These radicals react with the nanotubes, leading to aryl-functionalized CNTs. This method leads to highly functionalized CNTs, with up to 1 out of 20 carbon atoms bearing a functionalized moiety. Rapidly, Tour demonstrated the possibility of functionalizing CNTs by aryl diazonium salts without electrochemical induction. In this case, preformed diazonium salts can be used,[164] as well as aryl diazonium salts generated *in situ* from aniline derivatives.[183,184] This variety of approaches, together with high functionalization rate,[225] easy

96

processing and large panel of grafted functions, made this reaction the most widely used for the covalent functionalization of carbon nanotubes so far.

Although being extensively used for the functionalization of CNTs, the precise mechanism of addition of diazonium salts on a nanotube surface is not yet fully understood. Schmidt *et al.* investigated the mechanism of this reaction by a kinetic study.[226] This study leads to formulating a proposition of free-radical chain mechanism, which is described in Figure IV.2. During the initiation step, aryl radicals are generated from the phenyldiazonium salt. These radicals can either be produced by the formation of a diazonium anhydride intermediate (step A), or by a single electron transfer from the nanotube to the diazonium salt (step B). This aryl radical can then be attached to the nanotube surface (step C). The produced *f*-CNT radicals regenerate aryl radicals (step D), allowing the reaction to propagate. Termination step occurs when radicals recombinate with each other (steps E, F or G).
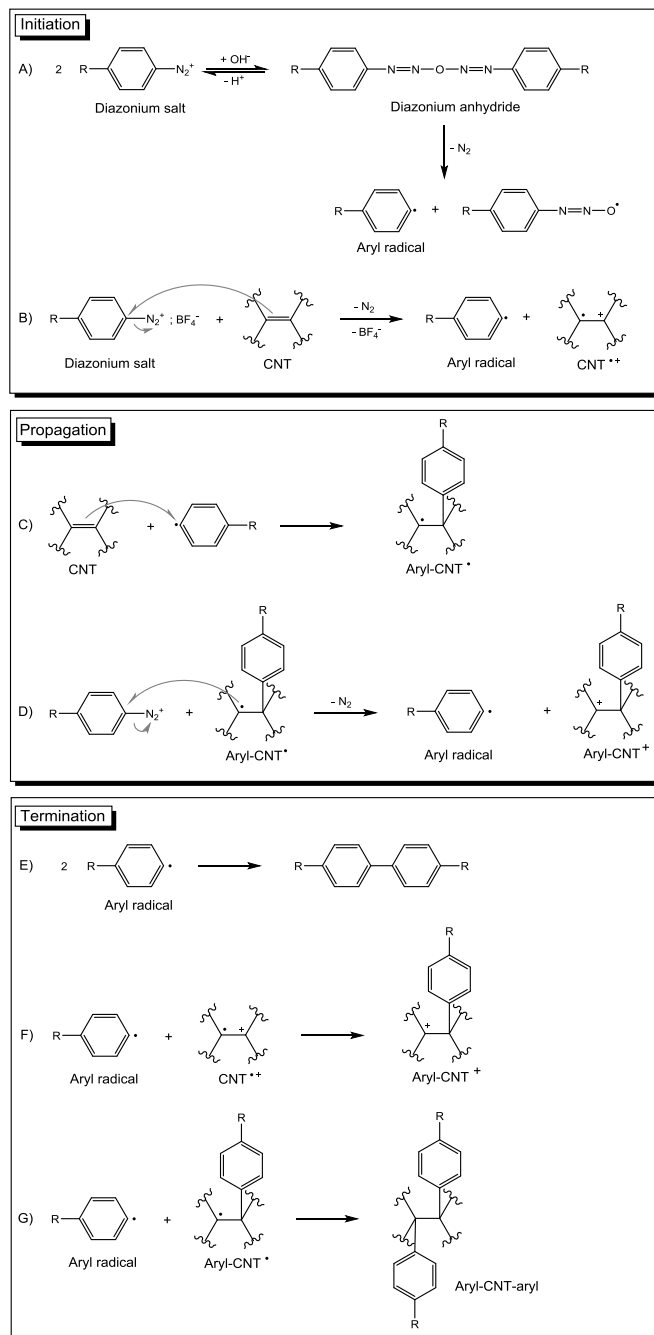
Figure IV.2. Radical chain mechanism for the covalent functionalization of carbon nanotubes with aryl diazonium salts, proposed by G. Schimdt *et al.* Figure inspired from [226].

A theoretical study demonstrates that isolated phenyl groups grafted on carbon nanotubes would easily desorb or diffuse on the surface at room temperature. Only phenyl pairs appear to be stable at room temperature. These pairs come from the grafting of a second phenyl on the delocalized free radical issued from the first covalent grafting.[208] They also concluded from their study that the *para*-configuration (1,4-addition) appears to be more stable than the *ortho*-configuration (1,2-addition), as represented in Figure IV.3.
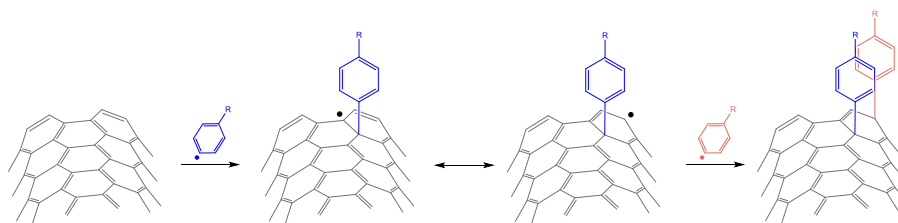
Figure IV.3. Schematic representation of the addition of phenyl pairs on carbon nanotube surface.

Moreover, although diazonium salts are commonly used for the functionalization of various surfaces, they may become victims of their own success. The highly reactive aryl radicals produced during the functionalization process can indeed attack the already grafted aryl moieties, instead of the carbon nanotube surface. This may lead to the formation of cross-linking or branching functionalization, as illustrated in Figure IV.4.[227,228] These polymerization reactions can lead to high functionalization rate estimation, sometimes overestimating the number of functionalized carbon atoms.
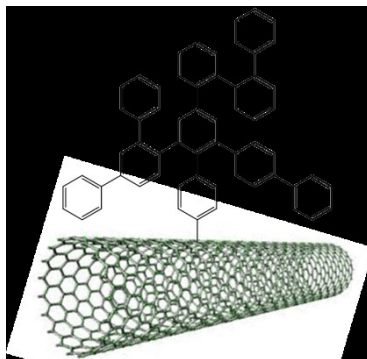
Figure IV.4. Schematic representation of the possible cross-linking reaction of aryl radicals on carbon nanotube surface. Figure inspired from Mattiuzi *et al.*[227]

As discussed in Chapter II, carbon nanotube properties are significantly affected by the covalent addition of a phenyl pair on its surface. The functionalization indeed induces a rehybridization of sp^2 carbon atoms into sp^3, hence altering the delocalized π electron system. This phenomenon is accompanied by a significant decrease of the nanotube conductivity. However, the initial properties of the nanotube can be restored by thermal annealing.[208–211]

IV.1.2 *Preparation of nanoparticle decorated CNTs*

Several precursors can be used for the preparation of nanoparticles on carbon nanotube surface, for the purpose of catalytic applications. Among them, molecular clusters[iii] constitute ideal candidates. These compounds indeed allow to obtain well-defined nanoparticles, with controlled size, shape and composition of the final particles. The formation of nanoparticles is obtained by thermal annealing (under vacuum or under

---

[iii] According to Cotton, a molecular cluster is an inorganic or organometallic compound containing at least 3 metal atoms, linked by minimum 2 metal-metal bonds and surrounded by a ligand sphere.[355]

a flow of inert gas) of the clusters immobilized on carbon nanotubes. This annealing can be performed at a low activation temperature, since metals embedded in clusters are in low oxidation state, thus limiting the agglomeration of the metal atoms.[87] Theoretically, clusters keep their initial composition, leading to the formation of identical nanoparticles, at each active site. This precise control of the structure can be advantageous for the preparation of bimetallic catalytic sites, leading to synergetic effect, which can be useful for catalytic applications.[229,230] Bimetallic clusters, containing M_1-M_2 metal bonds, can indeed be used for the preparation of bimetallic nanoparticles for the purpose of catalyst preparation, with controlled composition and M_1:M_2 ratio at each active site.[229] The presence of two metals enables synergetic effects during the catalytic reaction arising from the presence of the two metals in the same particle, surpassing the catalytic properties of each separated metal.[230] Several examples of the use of bimetallic clusters for the preparation of supported catalysts have been reported. Namely, Nashner *et al.* prepared Ru-Pt bimetallic nanoparticles supported on carbon black, from $[Ru_5PtC(CO)_{16}]$ cluster. *In situ* extended X-ray absorption fine structure spectroscopy (EXAFS) and STEM-EDX (Scanning transmission electron microscopy coupled with energy dispersive X-ray) were used to control the structure and composition of the obtained nanoparticles.[231,232] The anchoring of similar bimetallic Ru-Pt cluster was further investigated in S. Hermans laboratory.[233] STEM-EDX was used to demonstrate the presence of both constitutive metals (i.e. Ru and Pt) inside the nanoparticles.[234] These bimetallic nanoparticles supported on carbon lead to applications in heterogeneous catalysis, for the selective hydrogenation of cinnamaldehyde.[235]

IV.2 Methodology

For the purpose of catalytic applications, we developed a chemical functionalization route for the deposition of metallic nanoparticles on carbon nanotubes (Figure IV.5). In order to ensure a good anchoring of the desired functions on the nanotube surface, we opted for the covalent functionalization. This functionalization process also ensures an homogeneous dispersion of the catalytic sites along the carbon nanotube wall.[236] More specifically, we used diazonium salts for the covalent anchoring of nitrophenyl functions. Those grafted moieties were then modified in order to anchor nanoparticle precursors. For this purpose, phosphines constitute good ligands for the coordination of metallic compounds. In this project, we chose molecular clusters as nanoparticle precursors, allowing to easily control the composition of the nanoparticles, which can be useful for comprehensive catalytic activity study. Finally, a thermal activation process is performed. This step removes ligands and organic moieties, leaving "naked" nanoparticles directly deposited on carbon nanotube surface.
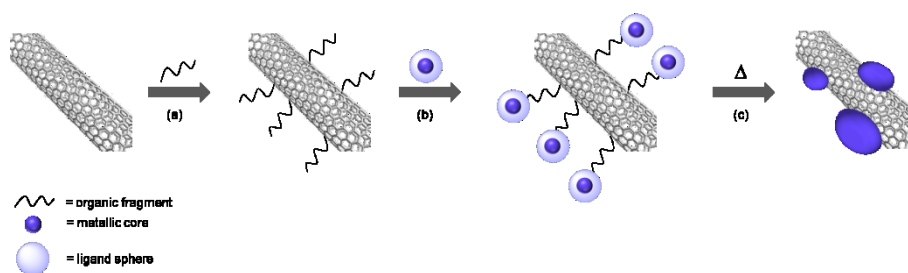
Figure IV.5. Schematic representation of the chemical pathway developed for the deposition of metallic nanoparticles on the carbon nanotube surface: (a) covalent functionalization of SWCNTs; (b) *post*-functionalization and anchoring of the nanoparticle precursors; (c) thermal activation.

The present chapter is devoted to the development of this functionalization process. First, physico-chemical characterization by common analytical techniques (X-ray photoelectron spectroscopy (XPS), Raman spectroscopy, thermogravimetric analysis (TGA) and elemental analysis (EA)) is presented. The second part of this chapter deals with the electrical characterization at each step of the preparation of these catalytic materials.

IV.3 Results and discussion

IV.3.1 Chemical functionalization route

The monovalent chemical route developed for the preparation of heterogeneous supported catalysts is schematically represented in Figure IV.6. Two different approaches have been used in parallel for the development of this chemical functionalization pathway. First, ***"bulk" SWCNTs***, or as-received − powder form − SWCNTs, purchased from Sigma-Aldrich and available in large quantity, were selected for their possible use for catalytic applications. Secondly, SWCNTs were also used after being deposited on a Si/SiO$_2$ substrate. Bulk SWCNTs can easily be characterized by common analytical techniques adapted to solid compounds, while ***"substrate-deposited" SWCNTs*** allow to mimic the chemical reactivity of carbon nanotube transistors, in which SWCNTs are also immobilized on Si/SiO$_2$ substrate.
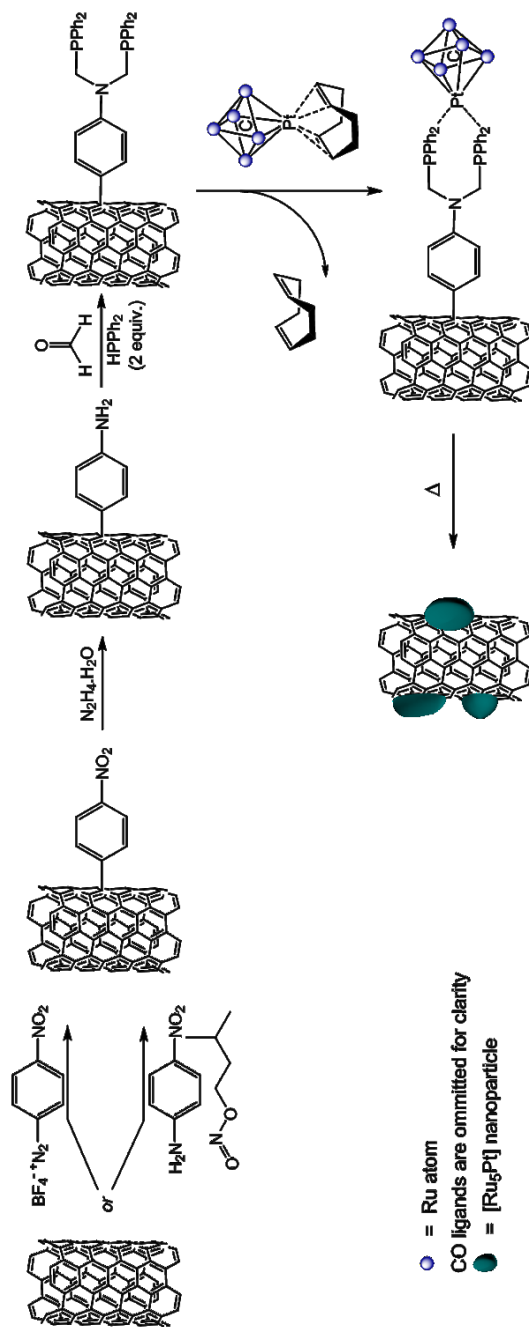
Figure IV.6. Scheme of the chemical functionalization pathway developed for the preparation of heterogeneous supported catalysts.

104

The deposition process of SWCNT films on Si/SiO$_2$ substrate, inspired from Rinzler and coworkers,[237] is schematically represented in Figure IV.7. First, SWCNTs (0.1 mg/ml) were suspended in aqueous solution with a low concentration of surfactant (sodium cholate, 0.1%). 20 ml of this homogeneous suspension was then filtered on nitrocellulose filter membrane, to form a stable film of SWCNTs with a concentration of approximately 2 mg.cm^{-2}. This film was finally transferred on a silicon substrate by dissolving the nitrocellulose membrane with acetone. A thermal annealing under vacuum was carried out to remove all remaining nitrocellulose residuals. This annealing also helps to maintain the SWCNT film on the substrate.
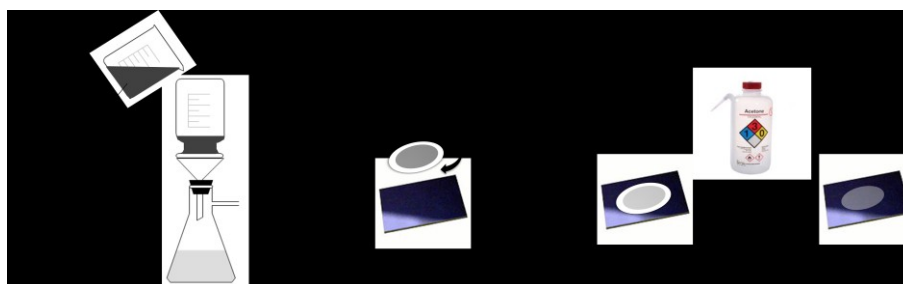
Figure IV.7. Schematic representation of the deposition process of SWCNTs films on Si/SiO$_2$ substrate: (a) a SWCNTs film is prepared by filtration on nitrocellulose membrane of a diluted suspension of SWCNTs in aqueous solution; (b) the film is deposited on a clean Si/SiO$_2$ wafer; (c) the nitrocellulose membrane is dissolved by acetone.

IV.3.1.1   Covalent functionalization of SWCNTs

SWCNTs were first functionalized by 4-nitrophenyldiazonium salts. The procedure depended on the form of nanotube. In the case of bulk SWCNTs, diazonium salts were synthesized *in situ* from 4-nitroaniline and isopentylnitrite, while aqueous solutions of preformed diazonium salts were used for the functionalization of substrate-deposited SWCNTs.

Raman spectroscopy was used to confirm the covalent nature of the chemical bond formed between the nanotube and the nitrophenyl function (Figure IV.8). Raman spectra of bulk SWCNTs show I_D/I_G ratios of 0.21 and 0.39 for pristine and functionalized bulk-SWCNTs, respectively (Figure IV.8a). This 85 % increase of the D-band, comparatively to the G-band, highlights an increase of the defects in the nanotube sample after functionalization. This defect increase can be explained by the rehybridization of sp^2 carbon atoms into sp^3 carbon atoms, during the covalent functionalization of the nanotube.[140,238] For substrate-deposited SWCNTs, I_D/I_G ratios of 0.05 and 0.075 are found for *p*- and *f*-SWCNTs, respectively, which corresponds to a 50 % increase. As can be seen, bulk and substrate-deposited SWCNTs exhibit different functionalization rates. This difference arises from the distinct approaches used for the functionalization, depending on the nanotube form. Moreover, the reactivity is expected to vary from one CNT source to another. Minor differences in diameters indeed results in major differences of reactivity, since it modifies the curvature of the graphene sheet.[171]
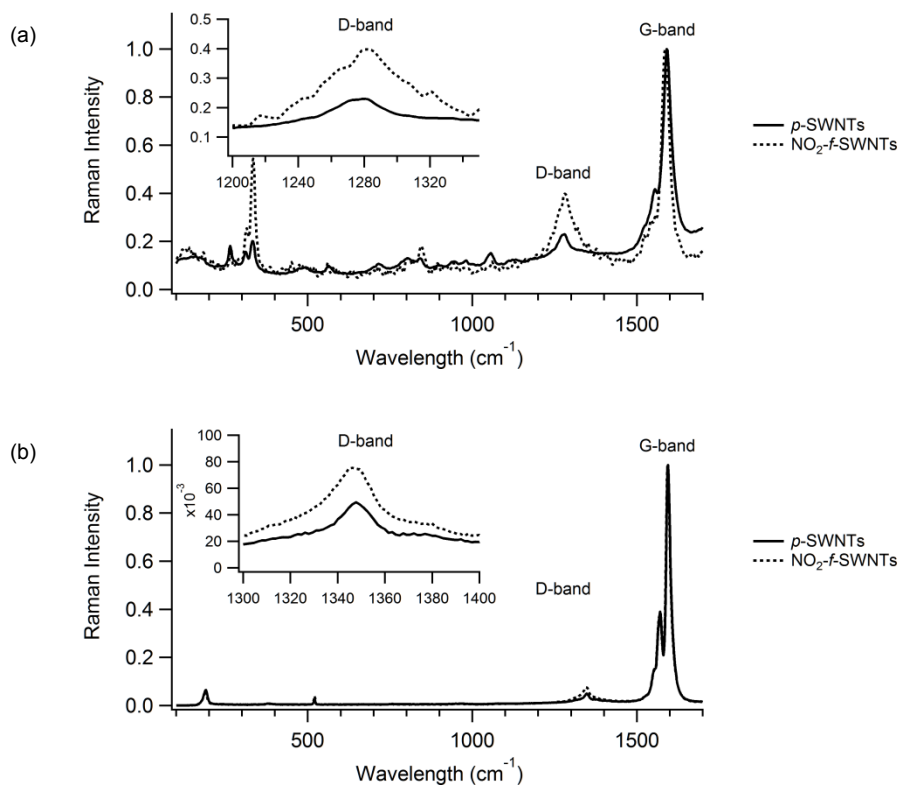
Figure IV.8. Raman spectra of pristine and functionalized (a) bulk SWCNTs and (b) substrate-deposited SWCNTs. Insets show a magnification of the D-band area.

XPS was also performed at each step of the functionalization process, for element analysis of the nanotube surface (see Annex IX.5.1 for complete characterization). XPS is a commonly used technique for the characterization of CNT functionalization. However, given the low ratio of grafted functions, the quantified results should be considered with caution due to the intrinsic error of the analysis, combined with the error caused by data processing. For this reason, the atomic percentages determined by XPS are usually considered to be accurate within ± 0.3 %, for the equipment used in this thesis. However, Annex IX.5.2 shows batch-to-batch reproducibility experiments performed on functionalized MWCNTs.

These experiments highlight a precision of ± 0.12 and 0.13 %. In this thesis, we did not perform sample-to sample reproducibility experiments, but the precision is expected to be higher, as previously reported by our laboratory.[186,239]

XPS analyses, performed on both bulk and substrate-deposited SWCNTs, reveal the presence of nitro functions after functionalization of the nanotubes. Table IV.1 shows the content in NO_2 functions before and after functionalization. As can be seen, *pristine*-SWCNTs did not contain any trace of nitro compounds in the case of bulk nanotubes, while substrate-deposited nanotubes already contain a few NO_2 functions at their surface, even before the functionalization process. This small amount of NO_2 functions is assumed to come from the preparation process of the SWCNT films (i.e. *via* filtration on nitrocellulose membrane and dissolution of the filtering membrane). After the functionalization process, both bulk and substrate-deposited carbon nanotubes exhibit significant concentration of nitrophenyl functions.

Element contents determined by XPS for substrate-deposited SWCNTs need to be interpreted with some caution. Indeed, the content in carbon depends strongly on the area analyzed, due to the heterogeneity of the SWCNT film on the silicon substrate. For this reason, XPS results are expressed as molar ratio, relative to carbon content, allowing easier interpretation and comparison between samples. A closer look at Table IV.1 evidenced significant differences in the NO_2/C ratios depending on the nanotube source. According to the XPS results of bulk *f*-SWCNTs, 4.2 % of the carbon atoms are functionalized, which corresponds to about one carbon atom out of 24. This value is very similar to reported grafting yield (N/C = 4.1 %), for the same reaction.[225] This functionalization yield

decreases for substrate-deposited SWCNTs to 2.7 %, i.e. one carbon atom out of 37. As previously discussed, this was predictable since differences of reactivity are expected from one source of nanotube to another. Moreover, different reagents were used depending on the nanotube form, which inevitably involves variation of the grafting yield. Finally, the two approaches (namely bulk and substrate-deposited SWCNTs) involve obvious variations of the functionalization yield. For substrate-deposited SWCNTs, the functionalization can indeed only occur on one side of the nanotube, the other side being stuck on the silicon substrate. For bulk SWCNTs, the entire nanotube surface can be functionalized, if the nanotubes are well-dispersed during functionalization.

Table IV.1. Element contents and molar ratios determined by XPS before and after covalent anchoring of nitrophenyl functions on SWCNTs.

		XPS (at. %)		Molar ratio
		C 1s	**N 1s (NO_2)**	**NO_2/C**
Bulk	*p*-SWCNTs	91.59	0.00	0.0 %
	NO_2-*f*-SWCNTs	84.67	3.56	4.2 %
Substrate-deposited	*p*-SWCNTs	93.16	0.12	0.1 %
	NO_2-*f*-SWCNTs	78.60	2.11	2.7 %

In summary, XPS results, together with Raman spectroscopy, confirm the success of the covalent anchoring of nitrophenyl functions in both cases. Both techniques also reveal significant differences in the functionalization rate of bulk and substrate-deposited SWCNTs. Raman spectroscopy highlights an increase of the D/G band ratio 1.7 times higher for bulk SWCNTs. XPS gives concordant results, with a functionalization rate 1.6 times higher with bulk-SWCNTs. These significant differences of grafting yield depending on the nanotube form is attributed to a combination of phenomenon: varying reactivity from one CNT source to

another, variations induced by the different approaches considered (i.e. bulk or substrate-deposited) and by the different reagents (i.e. preformed or *in situ* synthesized phenyldiazonium salts).

IV.3.1.2   *Post*-functionalization

IV.3.1.2.1 *Nitro reduction*

The NO_2-*f*-SWCNTs were then modified in order to anchor nanoparticle precursors. In a first step, the nitro function was reduced into an amino function. Different processes are commonly used to perform this kind of reaction in classical organic chemistry. $NaBH_4$,[240,241] hydrazine hydrate,[242–247] and hydrogen[248,249] are common reducing agents for the transformation of nitrobenzene into aniline. However, these reduction processes require the use of metallic catalysts (in the form of nanoparticles, metal oxides, metal sulfides, or complexes). The use of metallic compounds becomes a problem when functionalizing substrate-deposited carbon nanotubes. Silicon substrates indeed easily adsorb various chemicals at their surface. For this reason, we searched to avoid the use of such metallic catalysts. A closer look at the literature reveals the possible use of carbonaceous compounds as catalytic species for the reduction of nitroarenes. Moreover, these carbocatalytic alternatives decrease the toxicity and cost of these processes. Graphite,[250] activated carbon,[251] carbon nanotubes[252,253] and graphene[254,255] were hence reported to advantageously replace metallic catalysts in the reduction of nitrobenzene using hydrazine hydrate as reducing agent. A few studies dealing with carbon-catalyzed hydrogenation[256] or reduction assisted by $NaBH_4$[257] of nitrobenzene have also been published. Knowing this, we expected that functionalized carbon nanotubes could serve both as reactant and catalyst, for the reduction of nitrophenyl-*f*-CNTs into aminophenyl-*f*-CNTs. We

110

used three different reducing agents for this reduction step: $NaBH_4$, hydrazine monohydrate and trifluoroacetic acid (TFA, inspired from references [258,259]). The functionalized bulk SWCNTs were analyzed by XPS spectroscopy. This spectroscopy allows to quantitatively differentiate nitrophenyl and aminophenyl functions. Indeed, binding energy of a core electron in an element is affected by changes of its chemical environment. When amine functions are oxidized to form nitro functions, valence electrons are withdrawn from nitrogen. This decreases the electrostatic shielding of the nuclear charge, resulting in an increase of the binding energy. Binding energies of N 1s for aminophenyl and nitrophenyl species are reported in the literature to be 399.4 and 405.9 eV respectively.[260] Figure IV.9 shows high resolution N1s XPS spectra of bulk-*f*-SWCNTs before and after treatment with the different reducing agents used. N 1s XPS spectrum of NO_2-Ph-*f*-SWCNTs reveals the presence of 0.83 at. % of amine functions. N1s XPS spectra of the pristine SWCNTs is given in Annex IX.5.3. As can be seen, these pristine-CNTs already contain a small amount (0.36 at. %) of amino functions before the functionalization. For this reason, the amine functions present before the reduction step can be attributed to carbon nanotube defect induced by the synthesis or atmospheric contamination.

As can be seen in Figure IV.9, hydrazine turned out to be efficient for this chemical reduction step, as evidenced by the emergence of a peak at ~ 399.7 eV, corresponding to NH_2-Ph functions. $NaBH_4$ and TFA treatment did not cause any significant change in the oxidation state of the N1s peak.
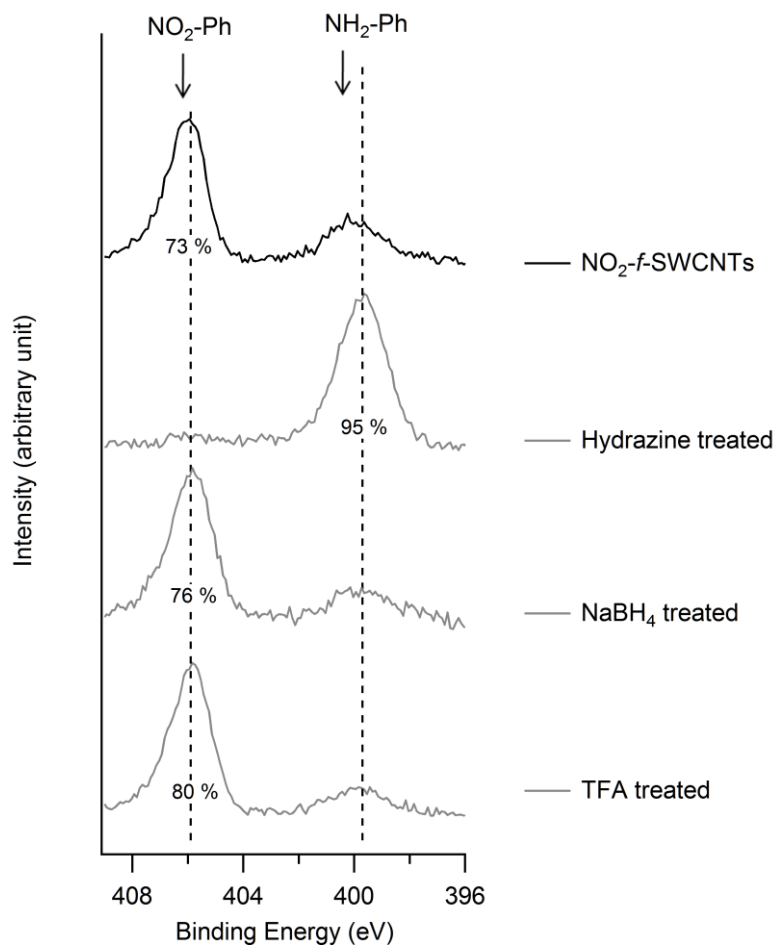
Figure IV.9. High resolution N1s XPS spectra of bulk-NO$_2$- *f*-SWCNTs before and after treatment with hydrazine, NaBH$_4$ and trifluoroacetic acid.

In light of these results, hydrazine monohydrate was chosen as reducing agent for further transformation of NO$_2$-*f*-CNTs into NH$_2$-*f*-CNTs. Both bulk and substrate-deposited NO$_2$-*f*-CNTs were successfully reduced using this process (Figure IV.10).

	NO$_2$/C	NH$_2$/C
——	4.2 %	1.0 %
- - -	0.1 %	5.6 %
——	2.7 %	2.1 %
- - -	0.7 %	3.2 %
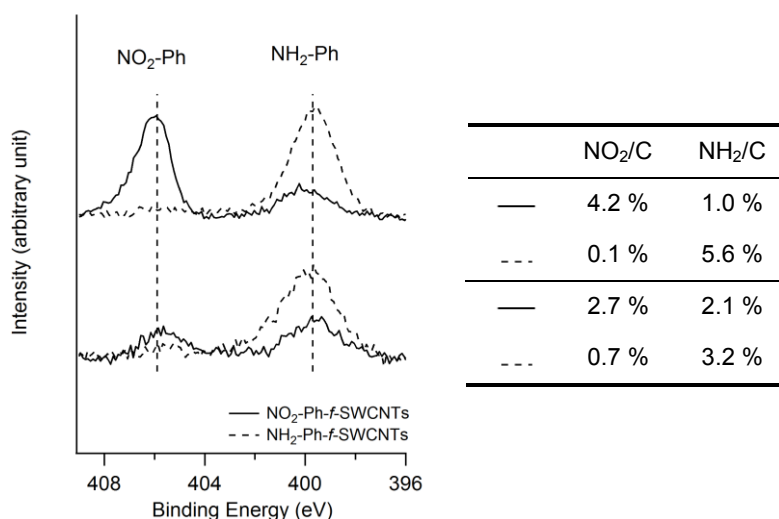
Figure IV.10. High resolution N1s XPS spectra of (top) bulk-NO$_2$-*f*-SWCNTs* and (bottom) substrate-deposited-NO$_2$-*f*-SWCNTs before and after treatment with hydrazine monohydrate. *Same spectra as in Figure IV.9

IV.3.1.2.2 Phosphine anchoring and cluster coordination

For the purpose of the catalyst preparation, ligands need to be anchored on the NH$_2$-*f*-SWCNTs for the subsequent coordination of metallic nanoparticle precursors. Phosphines are well-known for their affinity for a number of late transition metals in low oxidation state.[261] For this reason, phosphines are commonly used for the immobilization of organometallic species on various supports.[262–265] Following a procedure previously developed in S. Hermans laboratory,[233,236] we used NH$_2$-*f*-SWCNTs to anchor phosphine chelating ligands. These ligands will be further used for the coordination of metallic clusters (Figure IV.11).

○ = Ru atom
CO ligands are ommitted for clarity
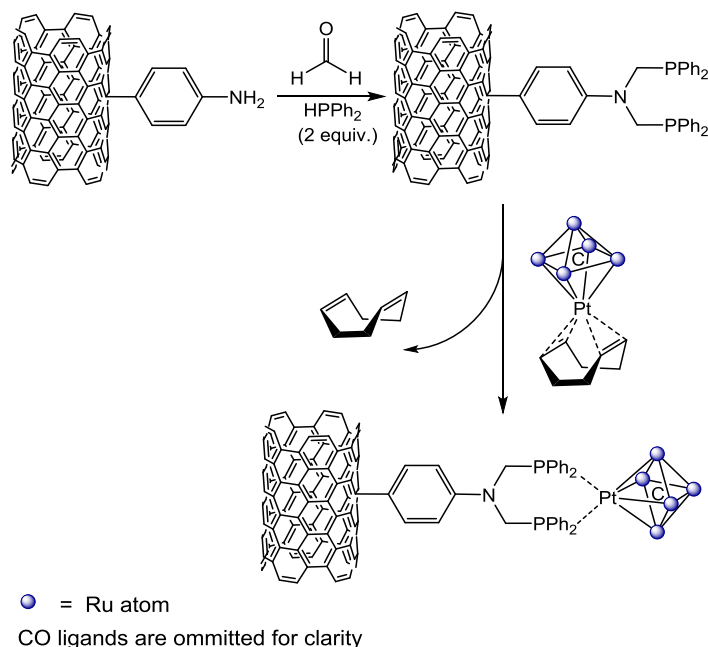
Figure IV.11. Anchoring of phosphine ligands on NH$_2$-Ph-*f*-SWCNTs and coordination of [Ru$_5$PtC(CO)$_{14}$COD].

XPS analysis confirms the appearance of phosphorus atoms on the surface of the *f*-SWCNTs (Table IV.2). According to Figure IV.11, two diphenylphosphines should be grafted on each amine function. The P/N atomic ratio is thus expected to be around 2. As demonstrated by XPS analysis, this ratio is significantly weaker than expected (around 0.5 instead of 2 for bulk-SWCNTs). It means that only about 25 % of the amine functions were modified into chelating phosphines, while about 75 % remained unmodified. This P/N ratio is even weaker for substrate-deposited SWCNTs. Within the context of this project, the fact that each step of the functionalization process does not reach a 100 % yield, meaning that different functions are present on the nanotube surface, does not raise any issue, since a thermal activation step will subsequently remove organic functions. If we had planned to use the cluster supported

on carbon nanotubes without this activation step, more attention should have been paid to this point.

The Ru-Pt bimetallic cluster [Ru$_5$PtC(CO)$_{14}$COD] was then anchored onto the functionalized nanotubes thanks to the chelating phosphine. Previous work[233] demonstrates that the cluster is attached onto (PPh$_2$)$_2$ modified carbon support by an exchange ligand mechanism, by removal of the COD ligand. XPS (Table IV.2) highlighted the presence of ruthenium and platinum on carbon nanotube surface. Despite the fact that the amount of cluster anchored onto the chelating phosphine differs from the calculated values for 100 % yield (Pt/P ratio of ~ 0.11 and 0.64 instead of 0.5, for bulk and substrate-deposited SWCNTs, respectively), the Ru/Pt ratio is close to the expected ratio of 5, meaning that the metallic core of the cluster remains almost unmodified after being anchored on the *f*-SWCNTs.[234] However, as pointed out earlier, the amount of metal detected is so low (especially for Pt) that the precision of XPS is not sufficient to be quantitative.

Table IV.2. Molar ratios determined by XPS for (PPh$_2$)$_2$-*f*-SWCNTs and [Ru$_5$PtC(CO)$_{14}$COD] immobilized on *f*-SWCNTs.

		Molar ratios				
		P/N	**Pt/P**	**Ru/C**	**Pt/C**	**Ru/Pt**
Bulk	(PPh$_2$)$_2$-*f*-SWCNTs	0.42	N/A	N/A	N/A	N/A
	Cluster-*f*-SWCNTs	0.56	0.11	1.1 %	0.3 %	4.3
Substrate-deposited	(PPh$_2$)$_2$-*f*-SWCNTs	0.06	N/A	N/A	N/A	N/A
	Cluster-*f*-SWCNTs	0.12	0.64	1.0 %	0.2 %	6.2

IV.3.1.3 Thermal activation

Finally, these cluster decorated carbon nanotubes were thermally activated under nitrogen. This crucial step removes the ligand shell and the organic functionalization, leaving activated "naked" nanoparticles on carbon nanotube surface. The platinum and ruthenium atoms being already in zero oxidation state in the $[Ru_5PtC(CO)_{14}COD]$ cluster, "low" temperatures can be used for the activation. This limits the aggregation of the nanoparticles during the annealing, which would result in a decrease of catalytic activity.[87] Activation temperature was determined thanks to TGA analysis of the unsupported cluster. The mass loss corresponding to ligand removal finishes around 300 °C.[233] For this reason, we fixed the activation temperature at 350 °C.

The activated nanoparticles supported on CNTs were analyzed by XPS, in order to examine the composition of the nanoparticles formed after the activation process (Table IV.3). As can be seen, modification of the element contents occurred during the thermal activation process. Slight change of Ru/Pt ratio after thermal activation indicates that the cluster core structure underwent some modification during the annealing. These results suggest that a rearrangement occurred during thermal annealing.[234] Moreover, significant amounts of nitrogen and phosphorous are still present on the nanotube surface, notwithstanding the thermal annealing (see Annex IX.5.1). This observation indicates that some organic residues coming from the organic functionalization binding the cluster to the carbon nanotube remain on the surface, even after the activation. However, this organic residue is not a problem for catalytic applications. On the contrary, previous work demonstrated that it can act as a "stabilizer" to avoid leaching of the nanoparticles.[249]

116

Table IV.3. Molar ratios determined by XPS for $[Ru_5PtC(CO)_{14}COD]$ cluster immobilized on *f*-SWCNTs and Ru-Pt bimetallic nanoparticles supported on SWCNTs after thermal activation.

		Molar ratios		
		Ru/C	**Pt/C**	**Ru/Pt**
Bulk	Cluster-*f*-SWCNTs	1.1 %	0.3 %	4.3
	NPs/SWCNTs	0.9 %	0.2 %	4.8
Substrate-deposited	Cluster-*f*-SWCNTs	1.0 %	0.2 %	6.2
	NPs/SWCNTs	0.4 %	0.1 %	5.1

We also performed elemental analysis (ICP-OES) on the bulk NPs/SWCNTs samples. The obtained results are reported in Table IV.4. As can be seen, metal content determined by ICP is lower than the metal content determined by XPS. The large difference between XPS and EA results may be attributed to problems of metal solubilization when preparing the sample for elemental analysis. Moreover, as discussed earlier, the metal contents determined here are really low and XPS is not reliable for quantification of such low concentrations.

Ruthenium content determined by XPS also suffers from possible imprecision. The most intense peak of ruthenium indeed corresponds to Ru 3d, with a binding energy (282 eV) which is very close to the main peak of carbon, C 1s. As a consequence, XPS data treatment of ruthenium containing compounds necessitate carbon peak decomposition, involving unavoidable imprecision. Ru 3p peak was hence chosen throughout this thesis as the Ru quantification peak by XPS, although being less intense and thus less reliable.

Table IV.4. Element ratios determined by XPS and elemental analysis for Ru-Pt bimetallic nanoparticles supported on bulk SWCNTs.

	Ratios				
	Ru/C		**Pt/C**		**Ru/Pt**
XPS	7.9 wt. %	0.9 mol. %	3.2 wt. %	0.2 mol. %	4.8
EA	2.1 wt. %	0.2 mol. %	0.6 wt. %	0.04 mol. %	6.5

Imaging was performed to visualize nanoparticles deposited on the carbon nanotube surface. Different techniques were considered, depending on the sample form; i.e. bulk or substrate-deposited. TEM was used to image NPs supported on bulk SWCNTs (Figure IV.12). This microscopy technique highlighted the presence of a large amount of nanoparticles well dispersed along the nanotubes. These nanoparticles present an average diameter of 1 nm ± 0.3 nm, with a size distribution represented in the histogram shown in Figure IV.12 right. If we take a closer look at the TEM image shown in Figure IV.12, we can see that the nanotubes seem to be coated by an organic layer. This confirms that organic residues remain present on the nanotube surface, even after the thermal activation process, as suggested earlier.
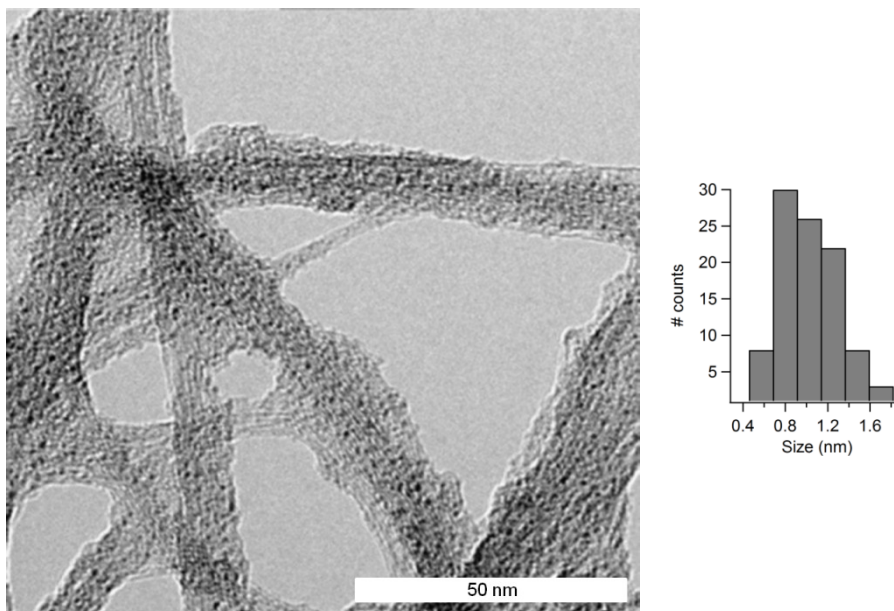
Figure IV.12. (Left) TEM image of NPs supported on bulk-SWCNTs and (right) size distribution of the nanoparticles.

TEM can also be used to determine the average distance between the nanoparticles (Figure IV.13). This distance is comprised between 0.85 and 4.27 nm, with an average value centered at 2.45 nm ± 0.88 nm. Knowing this, we can consider that a 1 μm portion of CNT contains approximately 290 nanoparticles. This information allows evaluating the number of nanoparticles present on individual CNT-FETs, for subsequent real-time electrical detection of catalysis (Chapter VII).
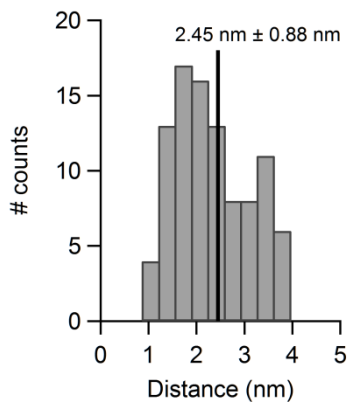
Figure IV.13. Distribution of distances between two neighboring nanoparticles. Distribution calculated on 100 NP-NP distances, determined by TEM.

Substrate-deposited SWCNTs cannot be imaged by transmission electron microscopy. In order to get images of individualized nanotubes, we used SEM to image one single nanotube (Figure IV.14). These images also evidenced the presence of metallic nanoparticles, distributed along the nanotube.
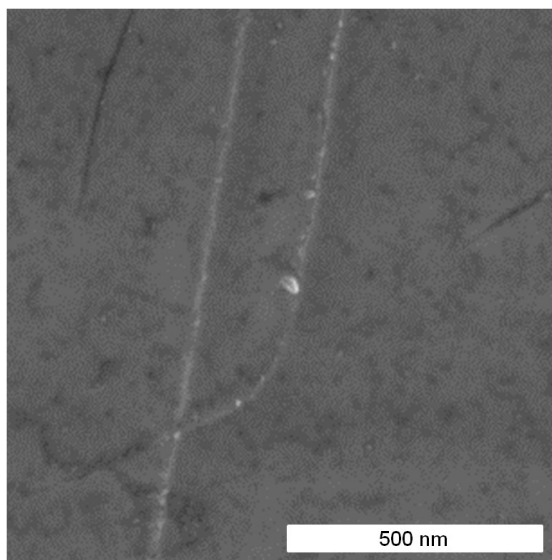
Figure IV.14. SEM image of NPs supported on individualized SWCNTs.

IV.3.1.4   Control experiments

In order to control this functionalization pathway and demonstrate the importance of the nanotube functionalization for the subsequent anchoring of the nanoparticles, additional control experiments were performed. Various "blank samples" were prepared, depending on the sample form, i.e. bulk or substrate-deposited SWCNTs. Two different blanks were prepared in the case of bulk SWCNTs (see Annex IX.5.4 for further details). First, carbon nanotubes were covalently functionalized by phenyl diazonium salts. Second, blank samples were prepared by reacting carbon nanotubes with nitroaniline, without the presence of isamylnitrite, which is essential for the reaction to occur. Both blanks were then allowed to react following the procedure developed for the *post*-functionalization of NO_2-*f*-SWCNTs. The absence of substituent on the phenyl-*f*-SWCNTs in the first blank makes the subsequent *post*-functionalization steps ineffective. In the second blank, carbon nanotubes remain unfunctionalized and the subsequent *post*-functionalization steps do not allow the anchoring of the nanoparticle precursors on the nanotube.

In the case of substrate-deposited SWCNTs, the blank sample consisted in bromophenyl-*f*-SWCNTs (see Annex IX.5.4). These Br-*f*-SWCNTs were unable to react with the *post*-functionalization reagents, resulting in no anchoring of the nanoparticle precursors.

These three blanks were characterized by XPS at each step of the functionalization pathway (See Annex IX.5.4 for complete XPS characterization). Table IV.5 summarizes the metal contents determined by XPS for the various blanks after activation of the samples previously immersed in $[Ru_5PtC(CO)_{14}COD]$ cluster solution. As can be seen, XPS does not reveal significant amount of Ru or Pt atoms at the nanotube

surface, before or after activation process, in the three cases. This result demonstrates the importance of the functionalization for the deposition of the nanoparticles on nanotube surface. This process allows the anchoring of the nanoparticle precursors, which remain on the nanotube surface, even after removal during the activation step of the covalent bond formed between the nanotube and the nanoparticle.

Table IV.5. Metal contents determined by XPS of the thermal activated blanks after immersion in a solution of $[Ru_5PtC(CO)_{14}COD]$.

| | | Element contents (at. %) | | |
		C	Ru	Pt
Bulk	Blank with aniline	91.95	0.04	0.02
	Blank without isoamylnitrite	90.60	0.00	0.01
Substrate-deposited	Blank functionalized with bromophenyl	98.75	0.00	0.00

IV.3.2 *Electrical characterization*

For the purpose of electrical detection of catalytic activity with carbon nanotube supported nanoparticles, SWCNTs were embedded into electronic devices. Individual SWCNT field effect transistors were prepared using various fabrication processes and geometry, as described in Chapter III. These SWCNT-FETs were functionalized following the procedure developed above, in order to obtain bimetallic nanoparticles supported on the carbon nanotube surface. Current-voltage curves were recorded at each step of the preparation of the catalyst.

The three different sources (a), (b) and (c), described in Chapter III, were implemented into electronic devices. The electrical characterization

leads to the same conclusion, regardless of the nanotube source used. For this reason, we will only describe the electrical results obtained from source (c) of SWCNTs in the present section. I-V_G curves from sources (a) and (b) can be found in appendix (Annex IX.5.5).

Chemical functionalization of carbon nanotubes has significant impact on their electronic properties. Covalent functionalization indeed introduces disorder in the nanotube sp^2 structure, dramatically altering its electrical conductivity.[200] Adsorption of selective gas[26] or organic molecules[201] on SWCNT surface is also known to modify transport properties of this material. Knowing this, electrical measurements can be used to probe the functionalization of carbon nanotubes. The evolution of I-V_G curves is summarized in Figure IV.19.

IV.3.2.1   Effect of the covalent functionalization

Figure IV.15 shows transfer curves of semiconducting SWCNT before and after covalent functionalization with nitrophenyldiazonium salt. As can be seen from the transfer curve of pristine SWCNT, the electrical conductivity switches from high current in the ON state (large negative gate voltage, V_G = - 20 V) to low current in the OFF state (large positive gate voltage, V_G = + 20 V). This modification of the current, when varying the gate bias, is due to changes of charge carriers density. After covalent functionalization, ON and OFF state conductances are affected in an opposite way. More details can be found in the next sections.
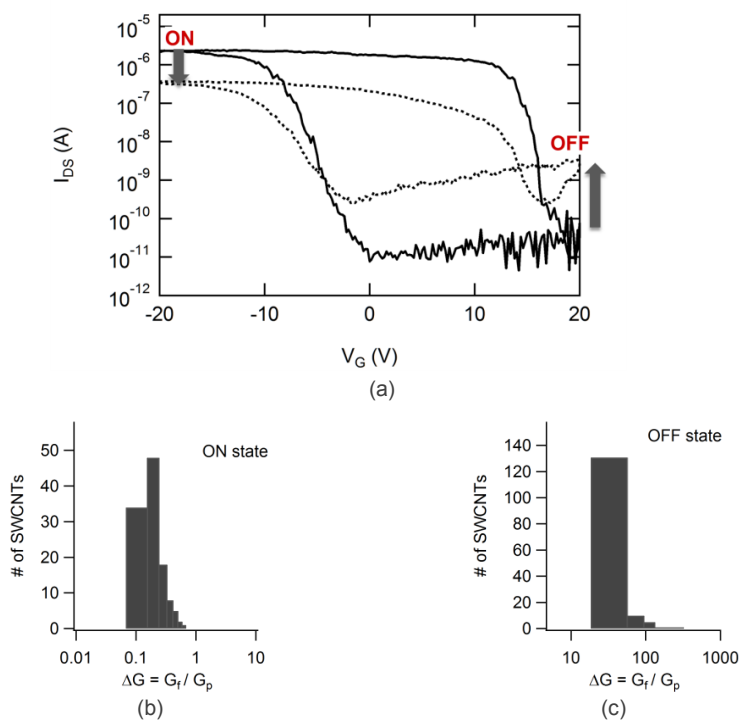
Figure IV.15. Effect of covalent functionalization of sc-SWCNT in the ON and OFF states: (a) Transfer curves for pristine (___) and functionalized (......) SWCNT; distribution of $\Delta G = G_f/G_p$ (b) in the ON state for 116 devices and (c) in the OFF state for 153 devices.

IV.3.2.1.1 ON state

As shown in Figure IV.15a, conductance in the ON state dramatically decreases after the covalent functionalization by aryl diazonium salts. This current loss of about one order of magnitude is in agreement with previous works.[205,210] This phenomenon is due to the rehybridization of sp^2 carbon atoms of the nanotube into sp^3 after the covalent anchoring of aryl radicals. These sp^3 sites constitute structural defects, which alter the sp^2 delocalized electron system, responsible for electrical conductivity of carbon nanotubes. For this reason, the nanotube

conductance is significantly disrupted by the covalent functionalization performed here.[210,266]

In order to quantify this current modification after functionalization, $\Delta G = G_f/G_p$[iv] ratios were calculated for 116 devices (Figure IV.15b). This G_f/G_p ratio, calculated as I_f/I_p at V_G = -20 V, is representative of the conductance modification after the functionalization process. A G_f/G_p ratio superior to 1 would indicate an increase of the conductance, while a ratio inferior to 1 reveals a decrease of the conductance. In the ON state, all ratios are lower than 1, meaning that the conductance decreases for all the devices. The distribution of G_f/G_p ratios is centered at 0.17 ± 0.1, corresponding to a decrease of about 1 order of magnitude. The narrow distributions observed in Figure IV.15b can easily be explained by the device configuration (Geometry 2; Chapter III) used here : all devices are connected along the same SWCNT. Each device is thus expected to exhibit the same reactivity towards diazonium salts, resulting in similar impact on their electrical properties.

IV.3.2.1.2 OFF state

The OFF state is completely differently affected by covalent functionalization process than the ON state. Figure IV.15a indeed reveals a large increase of the OFF state conductance after functionalization of about two orders of magnitude. Although appearing surprising, this phenomenon has already been observed in previous work.[267] It has been attributed to the formation of midgap states induced by the functionalization. These

---

[iv] G_f = conductance in *f*-SWCNTs; G_p = conductance in *p*-SWCNTs

intermediate electronic states make charge carriers injection easier. Distribution of G_f/G_p ratios, centered at ~ 20 (Figure IV.15c), is representative of the constant conductance increase in the OFF state after the functionalization process.

IV.3.2.2   Modification of the grafted functions

IV.3.2.2.1 Hydrazine treatment

Covalent functionalized CNT-FETs were then allowed to react with hydrazine monohydrate, in order to reduce nitrophenyl functions into aminophenyl. Hydrazine is well-known as a n-dopant molecule for the conversion of p-type nanotubes into n-type nanotubes.[268] This n-doping effect of hydrazine is attributed to its high electron donating properties. Carbon nanotube doping is highlighted by current-voltage curves. This doping effect indeed results in a lateral shift of the curve. A shift towards negative gate voltage is attributed to a decrease of the hole carrier density in the nanotube, corresponding to a n-doping. On the contrary, a shift towards positive gate voltage results of a p-doping of the nanotube. As can be seen from the I-V_G curves represented in Figure IV.16, the transfer curve is shifted towards more negative gate voltage after treatment in hydrazine. This is in agreement with the n-doping action of hydrazine. Moreover, hydrazine has been reported to decrease contact resistances, increasing therefore nanotube conductance.[269] This conductance increase is indeed observed in the transfer curve of hydrazine-treated functionalized SWCNT-FETs (Figure IV.16).
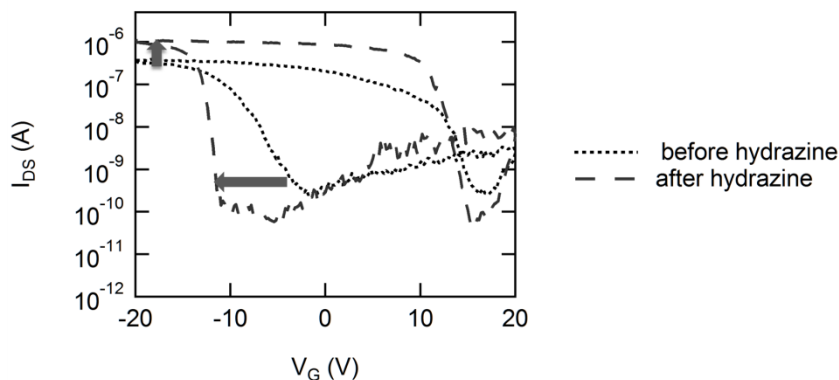
Figure IV.16. Effect of hydrazine treatment on transfer curves of functionalized sc-SWCNT-FET.

IV.3.2.2.2 Cluster anchoring

Once the nitro function has been reduced into an amino function with hydrazine, a phosphine ligand can be grafted on SWCNTs, for further immobilization of the nanoparticle precursors. Phosphines are particularly air-sensitive compounds. For this reason, precautions need to be taken for the anchoring of this ligand on the functionalized SWCNT-FETs. Among other things, these phosphine functionalized devices were maintained in inert atmosphere, until the coordination of the cluster took place. Hence, phosphine functionalized devices were not electronically characterized, in order to avoid air exposition.

Typical transfer curve of cluster supported SWCNT transistor is given in Figure IV.19d. As can be seen, no significant change appears after the immobilization of nanoparticle precursors. This is consistent with the fact that we do not modify the nanotube itself, but just the functionalized moieties. Electrical properties of the nanotubes remain consequently unchanged.

127

This absence of electrical modification, observed in all the 83 devices considered in this study, is consistent with the fact that clusters are molecular compounds rather than metals. They are indeed surrounded by a ligand sphere, with which they form molecular orbitals. For this reason, they cannot be viewed as solid compounds with band diagrams, which could have interacted with the nanotube. Moreover, the organic bond between the cluster and the carbon nanotube is non-conjugated, hence preventing charge-transfer interaction between the cluster and the CNT.

IV.3.2.3   Thermal activation

Finally, thermal activation process was performed to remove all the ligands and organic moieties, forming nanoparticles directly deposited on the carbon nanotube surface. Two effects are clearly observed in the transfer curve presented in Figure IV.17. First, nanotube conductance increases to recover its initial value. This observation demonstrates that the grafts were indeed removed, while nanotube structure was almost totally recovered, restoring its electronic features. This observation is in agreement with previous study on the effect of thermal defunctionalization of nanotubes on their electronic properties.[210,267] As previously discussed, TEM and XPS demonstrate the fact that a residual organic layer is present on the nanotube, even after the thermal activation of the nanoparticles. This organic layer is formed by the decomposition and rearrangement of the organic functionalized moieties and is therefore probably composed of polyaromatic compounds, containing P and N heteroatoms. It is worth noting that this kind of tar could be conducting, hence influencing the electrical measurements.

Second, a large shift of the potential threshold toward positive gate voltage appears after the formation of the nanoparticles. This shift

128

indicates the presence of an electron transfer between the carbon nanotube and its supported nanoparticles. More specifically, carbon nanotubes are p-doped, proving that the nanotube gives electrons to the nanoparticles. This charge transfer is relevant for catalytic applications, as it means that nanoparticles can be viewed as an electron sink that enables a give or take of electrons during the catalytic reaction.
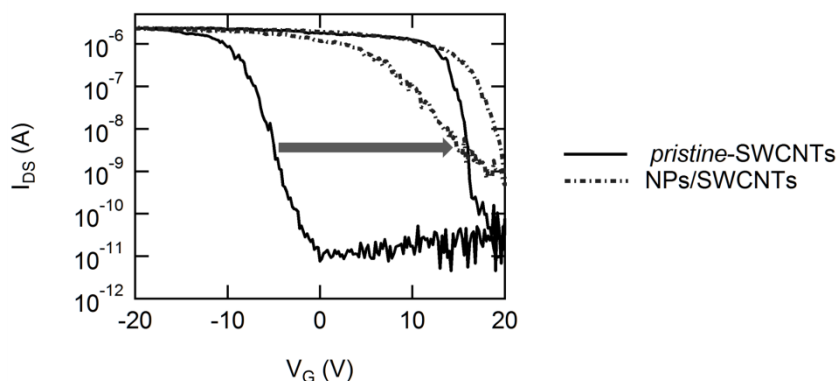
Figure IV.17. Comparison of I-V_G curves of pristine-sc-SWCNT and nanoparticles supported on sc-SWCNT, after thermal activation.

Figure IV.18 depicts the distribution of the gate voltage shifts observed in all the considered devices (i.e. 83 SWCNT-FETs, made of SWCNTs from sources a, b and c, in geometries 1 (sources a and b) and 2 (source c)). A shift towards positive gate voltage was observed in 96 % of the considered devices. The remaining 4 % did not shift after the thermal activation. As illustrated in the histogram (Figure IV.18), the distribution of the V_G shift is very broad. This point demonstrates that the doping intensity varies from one nanotube to another. The explanation lies in the fact that each CNT possesses its own reactivity. The number of nanoparticles deposited on their surface is therefore expected to vary between CNTs. This is consistent with the fact that for the devices in

129

geometry 2 (i.e. made of the same CNT), the distribution is narrower (centered at 14 V ± 2 V).
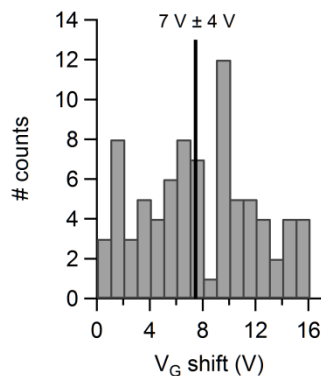
Figure IV.18. Histogram showing the distribution of the V_G shift observed between pristine-SWCNTs and NPs/SWCNTs. Distribution calculated on 83 devices, from sources a, b and c in geometries 1 and 2.

In practice, for considering real-time electrical detection of single-events (see Chapter VII), it is advantageous to apply a gate voltage at which the current is very sensitive towards doping effect, i.e. in the slope of the transfer curve. For this reason, extremely high doping, such as those observed in geometry 2 (Figure IV.17) can be disadvantageous for this application. Yet, it could be advantageous for applications requiring n-doped transistors.

Charge transfer effect has already been observed for NPs/CNTs hybrids by other analytical techniques. Raman spectroscopy was mainly used to probe interactions between carbon nanotubes and metallic nanoparticles[270,271], typical n or p dopants[272] or organic molecules.[273] Position shifts of the G-band and RBM indeed reveal the presence of electron transfer between metallic nanoparticles or electron-donor/acceptor molecules and SWCNTs.[272] This charge transfer results in metal ↔

semiconductor transitions.[270,274] XPS can also be used to detect changes in the electronic state of metallic nanoparticles when supported on carbon nanotubes.[271] However, given the low amount of metal content relatively to carbon, it may be difficult to detect such small chemical shifts. Theoretical calculations also confirmed the presence of charge transfers between supported compounds and carbon nanotubes, which are attributed to Coulombic interactions.[270,274]

This electron transfer between the nanotube and the supported nanoparticles suggests the possibility of inducing changes in the reactivity of the supported NPs.[80,86] As a consequence, by applying various voltage through the carbon nanotube, we should be able to control the effective charge on the nanoparticles, thus varying the catalytic activity of these active sites. On the contrary, a modification of the nanoparticles during catalytic reaction, due to reduction/oxidation reaction of the metal, should result in modification of the electronic properties of the nanotube. This effect was explored during this thesis, as will be described in Chapter VII.
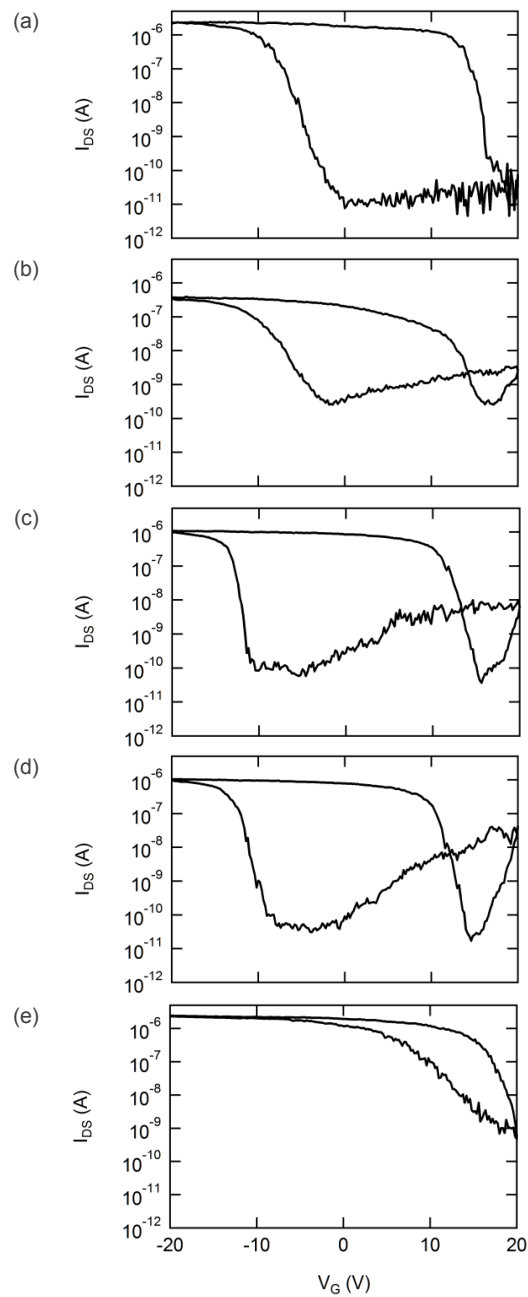
Figure IV.19. Transfer curves (V_{DS} = 1 V) of (a) *pristine*-SWCNT; (b) NO_2-Ph-*f*-SWCNT; (c) NH_2-Ph-*f*-SWCNT; (d) cluster supported on SWCNT and (e) Ru-Pt bimetallic nanoparticles deposited on SWCNT.

IV.4 Conclusion

In this chapter, we described a chemical functionalization pathway developed for the deposition of bimetallic nanoparticles on the surface of a single-walled carbon nanotube. This chemical route is composed of five steps, which can be gathered in three stages. First, SWCNTs were covalently functionalized, using diazonium salts. Second, these *functionalized*-SWCNTs were modified in order to anchor bimetallic clusters. Lastly, a thermal activation process was performed to remove ligands and organic moieties, allowing to obtain bimetallic nanoparticles directly deposited on the carbon nanotube surface.

This functionalization pathway was developed for both bulk and substrate-deposited SWCNTs in parallel, in order to mimic the behavior of SWCNT-FETs that will be further used in this thesis. Raman spectroscopy was used to prove the covalent nature of the bonds formed between the nanotube and the grafted functions, while XPS highlighted the appearance of the desired grafted functions at the nanotube surface. These two techniques demonstrated that the functionalization rates are significantly different depending on the nanotube form (i.e. bulk or substrate-deposited). According to XPS analysis, the following functionalization rates were obtained: 4.2 % for bulk-SWCNTs (i.e. one carbon atom out of 24 functionalized) and 2.7 % for substrate-deposited SWCNTs (i.e. one carbon atom out of 37 functionalized). In other words, the functionalization was 1.6 times higher in bulk CNTs. According to Raman spectroscopy, the functionalization rate was 1.7 times higher in bulk SWCNTs. This significant difference of functionalization rates depending on the nanotube form used were attributed to several phenomenon: varying reactivity from one CNT source to another, variations induced by the

different approaches considered (i.e. bulk or substrate-deposited) and by the different reagents (i.e. preformed or *in situ* synthesized phenyldiazonium salts).

Each step of the functionalization process was subsequently characterized by XPS. This technique confirmed the reduction of nitrophenyl functions into aminophenyl, as well as the appearance of phosphine functions and ruthenium and platinum at the CNT surface. After thermal activation, XPS revealed that significant amounts of phosphorous and nitrogen were still present on the nanotube surface. This observation demonstrated that organic residues coming from the functionalization remained on the nanotube surface. This organic residue acts as stabilizer for the nanoparticles.

These activated nanoparticles supported on CNTs were also characterized by elemental analysis. Significant differences in metal contents were obtained depending on the analysis method considered. In a general way, higher metal contents were obtained by XPS. Various facts can explained these differences: (i) high imprecision of the XPS, which is not reliable to quantitatively determine element content in such low concentration; (ii) additional imprecision due to the overlap of Ru and C main XPS peaks; (iii) problems of metal solubilization for elemental bulk analysis, resulting in metal content underestimation.

Finally, TEM (for bulk SWCNTs) and SEM (for substrate-deposited SWCNTs) imaging were performed to visualize the nanoparticles deposited on carbon nanotube surface. Both microscopy techniques highlighted the presence of a large number of nanoparticles homogeneously dispersed on the nanotube sidewalls. TEM imaging confirmed the presence of the residual organic layer on the nanotube

134

surface. Moreover, TEM allowed to determine the average diameter of the nanoparticles (1 nm ± 0.3 nm) and the average distance separating two neighboring nanoparticles (2.45 nm ± 0.88 nm). This observation allowed to conclude that about 290 nanoparticles are present on a 1 μm section of carbon nanotube. This information allows evaluating the number of nanoparticles present on each CNT-FET.

Transport measurements were also performed to follow the fabrication process of these nanoparticles decorated carbon nanotubes. This electrical characterization highlighted a decrease (of about 1 order of magnitude) of the nanotube conductivity after covalent functionalization. This current loss was attributed to the rehybridization of sp^2 carbon atoms into sp^3 induced by the covalent anchoring of nitrophenyl functions. The reduction of these nitro functions by hydrazine was accompanied by a n-doping of the CNT, due to the strong electron-donating properties of hydrazine. The coordination of the clusters did not lead to modification of the transfer curve. This absence of electrical properties modification is explained by the fact that the cluster does not interact with the nanotube due to the non-conjugated link between these two species. Finally, the thermal activation step allowed restoring the initial conductivity of the nanotube and lead to a p-doping of the SWCNTs. This charge transfer demonstrated that a strong interaction occurs between the nanotube and its supported nanoparticles. This result is of particular interest for the purpose of catalytic applications, that will be studied in Chapters V and VII.

In conclusion, common chemical analytical techniques, together with electrical measurements, confirmed the success of the functionalization strategy developed in this chapter. We also demonstrated

the possibility of using electrical measurements as a probe to monitor multi-step chemical reaction at the surface of carbon nanotubes.

Main results of Chapter IV

❖ Development of a *chemical functionalization strategy* for the deposition of bimetallic nanoparticles on carbon nanotube surface

❖ Similar functionalization reactivity on both *"bulk" SWCNTs* and *"substrate-deposited" SWCNTs*

❖ *Consistency of chemical and physical characterization data* to prove the success of the chemical pathway

❖ Revealing the presence of a *charge transfer between carbon nanotube and its supported nanoparticles*

Experimental section

Instrumentals

A complete instrumental section can be found in Annex IX.1.

Materials

"Bulk" SWCNTs were purchased from Sigma Aldrich (carbon > 90 %, SWNTs ≥ 77 %) and used as received without further purification.

"Substrate-deposited" SWCNTs were prepared following a procedure adapted from Wu and co-workers.[237]

SWCNT-FETs presented in this chapter were prepared with flow-aligned CVD-growth. See Chapter III and Annex IX.4.1 for more experimental details.

SWCNTs films fabrication

Purified laser ablation produced SWCNTs are dispersed in a 1 % sodium cholate aqueous suspension by sonication. 20 ml of this suspension is then filtered over nitrocellulose membrane (0.22 μm pore size) to obtain SWCNTs films. Those films are transferred to SiO_2/Si substrate and the nitrocellulose membrane was dissolved in acetone.[237]

Individual SWCNT-FETs fabrication

Individual SWCNT-FETs were prepared according to the fabrication process described for Geometry 2. See Chapter III for further details.

Synthetic procedures

<u>Cluster synthesis</u>

[Ru$_6$C(CO)$_{17}$] synthesis.[275] 1 g of [Ru$_3$(CO)$_{12}$] (1.56 mmol) and 100 ml of n-heptane were introduced in a 250 ml autoclave. The reaction mixture was heated to 167 °C under ethylene pressure (30 bar) with stirring for 4 hours. The solution was then cooled down to room temperature overnight in the autoclave. The obtained purple crystals of [Ru$_6$C(CO)$_{17}$] were filtrated and washed with n-heptane (567 mg, 63%). IR ν_{CO} (CH$_2$Cl$_2$) (cm^{-1}): 2067 (s), 2047 (s), 2002 (w), 1838 (w).

[Ru$_5$C(CO)$_{15}$] synthesis.[275] 600 mg of [Ru$_6$C(CO)$_{17}$] (0.548 mmol) and 110 ml of n-heptane were introduced in a 250 ml autoclave. The reaction mixture was heated to 90 °C under carbon monoxide pressure (90 bar) with stirring for 6 hours. The solution was then cooled down to room temperature overnight in the autoclave. The obtained red crystals of [Ru$_5$C(CO)$_{15}$] were filtrated and washed with n-heptane (392 mg, 83%). IR ν_{CO} (CH$_2$Cl$_2$) (cm^{-1}): 2068 (s), 2034 (s), 2017 (w).

(PPN)$_2$[Ru$_5$C(CO)$_{14}$] synthesis.[276] 500 mg of [Ru$_5$C(CO)$_{14}$] (0.533 mmol) and 40 ml of anhydrous methanol were introduced in a 100 ml schlenk. Twelve pellets of KOH were added and the mixture was stirred at room temperature for 1h15. Three equivalents of bis(triphenylphosphoranylidene)ammonium chloride (PPNCl, 918 mg; 1.6 mmol) were added to the solution, leading to the precipitation of (PPN)$_2$[Ru$_5$C(CO)$_{14}$]. This red solid was collected by filtration, washed with hexane and dried under vacuum (1.026 g, 96%). IR ν_{CO} (CH$_2$Cl$_2$) (cm^{-1}): 2030 (w), 1973 (vs), 1962 (s), 1916 (m), 1749 (w).

[Ru$_5$PtC(CO)$_{14}$(COD)] synthesis.[276] 200 mg of (PPN)$_2$[Ru$_5$C(CO)$_{14}$] (0.1 mmol) and 20 ml of anhydrous dichloromethane were introduced in a 100 ml schlenk flask. 37.4 mg

of Pt(COD)Cl$_2$ (0.1 mmol, 1 equiv.) and silica in excess were added to the solution with 10 ml of anhydrous dichloromethane. After stirring at room temperature for 4 hours, the reaction mixture was filtrated under argon. The filtrate was evaporated to dryness under vacuum, to obtain [Ru$_5$PtC(CO)$_{14}$(COD)] as a red powder (52 mg, 43 %). IR ν_{CO} (CH$_2$Cl$_2$) (cm^{-1}): 2077 (m), 2050 (s), 2033 (s), 2011 (s), 1989 (w), 1965 (w), 1818 (w).

Carbon nanotube functionalization

Nitrophenyl-*f*-SWCNTs (NO$_2$-Ph-*f*-SWCNTs). *Substrate-deposited SWCNTs* were functionalized by immersing them in 20 ml of a solution of deoxygenated ultrapure water adjusted to pH=9 (using NaOH) containing 0.8 mM of 4-nitrophenyl diazoniumtetrafluoroborate. Substrates were allowed to react for 10 minutes at room temperature. They were extensively rinsed with ultrapure water, followed by 2-propanol.

Bulk SWCNTs were functionalized by in situ generated diazonium compounds adapting a procedure described by J. M. Tour.[183] Pristine-SWCNTs (24 mg) were suspended in 35 ml of 1,2-dichlorobenzene (o-DCB) by sonication. A solution of 4-nitroaniline (287 mg, 2.1 mmol) in 20 ml of acetonitrile was added to the suspension. Ar was bubbled through the reaction mixture for 15 minutes. The reaction mixture was heated to 70 °C, and isoamylnitrite (0.42 ml, 3.1 mmol) was added. The reaction mixture was allowed to stir at 70 °C for 15 hours. After cooling down to RT, the suspension was diluted with 70 ml of dimethylformamide (DMF). The diluted suspension was then filtered over a PTFE membrane (0.45 μm pore size) and successively washed with 150 ml of DMF, ethanol (EtOH), tetrahydrofurane (THF) and diethyl ether, followed by sonication in 200 ml of DMF for 15 minutes. The suspension was filtered and washed again as previously described.

Aminophenyl-*f*-SWCNTs (NH$_2$-Ph-*f*-SWCNTs). Nitro-substituent was reduced by hydrazine monohydrate following a procedure inspired from the literature.[277] *Substrate-deposited NO$_2$-Ph-f-SWCNTs* were immersed in 50 ml ethanol. Hydrazine monohydrate (0.13 ml) was added dropwise under stirring at 90°C. Substrates were allowed to react at 90°C for 3 hours. After cooling down to room temperature (RT), substrates were extensively rinsed with EtOH, followed by 2-propanol.

Bulk NO$_2$-Ph-f-SWCNTs (25 mg) were suspended in 50 ml of EtOH by sonication. Hydrazine monohydrate (10 equiv. related to the SWNTs amount) was added dropwise to the suspension at 90°C. The suspension was then stirred at 90°C for 3 hours. After cooling down to RT, the suspension was filtered over a PVDF membrane (0.22 μm pore size) and successively washed with 150 ml of EtOH, THF and diethyl ether, followed by sonication in 200 ml of EtOH for 15 minutes. The suspension was filtered and washed again as previously described.

Similar procedures were followed for the attempted reduction of nitrophenyl-*f*-SWCNTs by trifluoroacetic acid (TFA) or NaBH$_4$. For the reduction by TFA, *bulk NO$_2$-Ph-f-SWCNTs* were suspended in 10 ml of TFA and ultrasonicated at room temperature for 3 hours. For the NaBH$_4$ reduction, *bulk NO$_2$-Ph-f-SWCNTs* were suspended in 10 ml of a solution of THF/H$_2$O - 0.5:1 and stirred at 55 °C. 1 ml of a solution containing 6.5 mg of NaBH$_4$ in 10 ml of THF/H$_2$O - 0.5:1 was portionwise added over 2 hours. Similar work-up procedures were applied.

Phosphine-*f*-SWCNTs (PPh$_2$-*f*-SWCNTs). Addition of diphenylphosphine (HPPh$_2$) on NH$_2$-Ph-*f*-SWCNTs was performed following a procedure previously described.[278] Under argon flow, HPPh$_2$ (0.3 ml, 1.7 mmol) was added to a solution of paraformaldehyde (50 mg, 1.7 mmol) in 30 ml MeOH. This reaction mixture was stirred at 70°C for 15 minutes, to yield HOCH$_2$PPh$_2$.

Substrate-deposited NH$_2$-Ph-f-SWCNTs were immersed in 10 ml of distilled MeOH. HOCH$_2$PPh$_2$ solution (0.01 ml) was added to the immerged NH$_2$-Ph-*f*-SWCNTs and the reaction mixture was stirred at room temperature for 15 minutes. Afterwards, 30 ml of toluene were added and the mixture was stirred at 70°C for 30 minutes. The reaction mixture was then cooled down to RT and allowed to stir for 24 hours. Substrates were then extensively rinsed with MeOH, followed by 2-propanol.

To a *bulk suspension of NH$_2$-Ph-f-SWCNTs* in 25 ml of MeOH, 2 equivalents (with respect to the number of NH$_2$ functions on NH$_2$-Ph-*f*-SWCNTs as determined by XPS) of the HOCH$_2$PPh$_2$ solution were added. This suspension was stirred at RT for 15 minutes. Afterwards, 20 ml of toluene were added and the mixture was stirred at 70°C for 30 minutes. The reaction mixture was then cooled down to RT and allowed to stir for 24 hours. The suspension was finally filtrated under argon flow using schlenk techniques and rinsed with anhydrous MeOH.

[Ru$_5$PtC(CO)$_{14}$(COD)] anchoring. This reaction was performed under inert Ar atmosphere, using schlenk glassware and distilled solvents. The amount of cluster engaged corresponded to 0.5 equiv. related to the phosphorous content on PPh$_2$-*f*-SWCNTs (as determined by XPS). *Substrate-deposited PPh$_2$-f-SWCNTs* were immerged in a solution of 1,2-dichloromethane (DCM) containing a given amount of [Ru$_5$PtC(CO)$_{14}$(COD)]. Substrates were allowed to react under stirring at RT for 24 hours. They were then extensively washed with DCM and 2-propanol.

Bulk PPh$_2$-f-SWCNTs (15 mg) were suspended in 20 ml of DCM by sonication. [Ru$_5$PtC(CO)$_{14}$(COD)] was added to this suspension, which was stirred at RT for 24 hours. The suspension was then filtered over a PVDF membrane (0.22 μm pore size) and successively washed with 100 ml of DCM, EtOH, THF and diethyl ether followed by sonication in 150 ml of DCM for 15 minutes. The suspension was filtered and washed again as previously described.

Activation. Thermal activation was performed at 350°C under inert gas (N_2 or Ar) flow (100 sccm) for 1 hour, with a heating ramp of 100 °C/hour, in a Carbolite tubular oven.

CHAPTER V - HETEROGENEOUS SUPPORTED CATALYSIS

Abstract

This chapter deals with the use of Ru, Pt and bimetallic Ru-Pt nanoparticles supported on multi-walled carbon nanotubes for the catalytic transformation of dimethylphenylsilane in dimethylphenylsilanol. Despite the fact that these three heterogeneous supported catalysts appeared to be active for this specific reaction, we demonstrate in this chapter that the catalytic activity can be strongly modulated by changing the nanoparticle composition. In particular, the presence of Pt, even in low amount, turns out to be advantageous for this reaction. Moreover, the catalysts can be easily recovered at the end of the reaction by filtration and reused.

V.1 Introduction

Keeping in mind the primary objective of this thesis − i.e. to use carbon nanotubes as sensors for the detection of catalytic activity − we were looking for a catalytic reaction which can be carried out in ambient conditions. We hence tried to find a catalytic reaction which can be handled in air at room temperature and does not require the presence of gas under pressure. In this context, catalytic transformation of silanes into silanols was brought to our attention.

Great emphasis is placed on the synthesis of silanols in organic chemistry. These compounds indeed constitute useful building blocks for silicon-based polymeric materials as well as in organic synthesis since silanols are used as nucleophilic partners in organometallic cross-coupling reactions.[279,280] The importance of silanol synthesis is attested by the > 400 000 tons annual production of silicones.[281] Silanols are usually synthesized from siloxanes, halosilanes, or hydrosilanes. Various methods can be used for the preparation of silanols from hydrosilanes. Among them, oxidation of silanes can be performed by using stoichiometric oxidant,[282] or by water with metal catalysts.[280,283–297] The latter is largely preferred since the side-product is limited to molecular hydrogen, hence reducing toxic wastes. Figure V.1 depicts the mechanism of the catalytic transformation of silane into silanol with water. First, the hydrosilane undergoes a dissociative adsorption on the surface of the metal nanoparticle, yielding to the formation of M−Si and M−H bonds. According to kinetic studies,[291] the reaction rate is independent on the R_3−Si−H concentration, indicating that this first step is very fast. Second, water adsorbs on the nanoparticle surface. As reported by experimental[280,291,292] and theoretical[292] studies, this step is rate-determining

and is significantly enhanced by the presence of oxygenated functions on the surface of the metal. These functions allow to stabilize the adsorption of water, thanks to the formation of hydrogen bonds.[280,291,292] Third, OH functions coming from water reacts with R_3−Si functions, leading to the formation of the desired silanol product. Finally, hydrogen is desorbed from the metal surface, which regenerates the catalyst. This step is facilitated by the presence of oxygenated functions on the metal surface.[292]
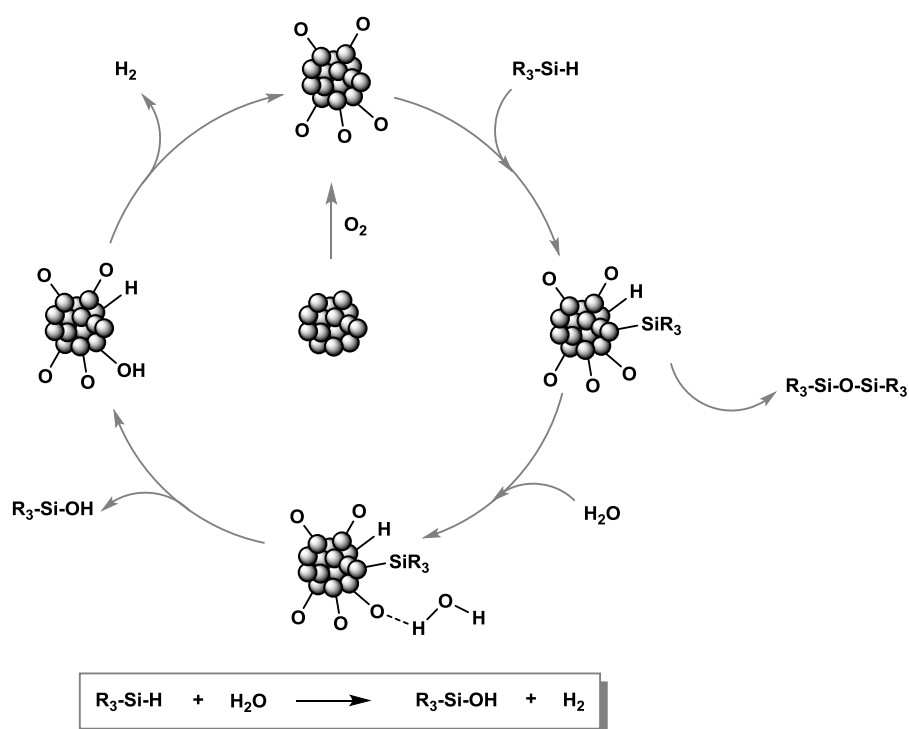
Figure V.1. Proposed mechanism for the hydrolytic transformation of hydrosilanes to silanols on the surface of metal nanoparticles. Figure inspired from J. Park *et al.*[279]

Several studies have demonstrated the role of water for this reaction. By using D_2O, $^{18}OH_2$ and Et_3SiD, isotope labeling experiments proved that the OH function on the silanol comes from water, as shown in reactions V.1 to V.3.[298]

145

$$Et_3Si-H + {}^{18}OH_2 \xrightarrow{\text{1 mol \% Re cat.}} Et_3Si-({}^{18}OH) + H_2 \qquad (V.1)$$

$$Et_3Si-D + H_2O \xrightarrow{\text{1 mol \% Re cat.}} Et_3Si-OH + HD \qquad (V.2)$$

$$(HD : H_2 : D_2 = 94.2 : 5.6 : 0.2)$$

$$Et_3Si-H + D_2O \xrightarrow{\text{1 mol \% Re cat.}} Et_3Si-OD + HD \qquad (V.3)$$

$$(HD : H_2 : D_2 = 97.6 : 2.0 : 0.4)$$
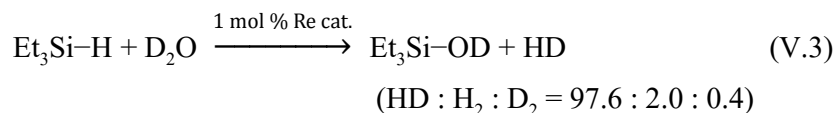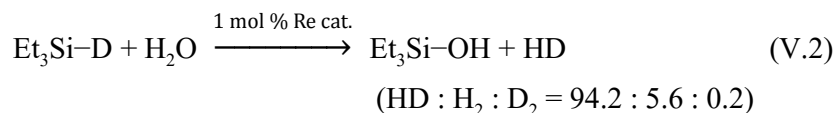
In addition, water increases the reaction selectivity for the silanol. Disiloxane side-product can indeed be produced during this reaction, arising either from the condensation of two hydrosilanes, two silanols or one hydrosilane and one silanol.[279] An experimental study highlights that this side reaction is inhibited by the presence of water, which should be used in excess rather than in stoichiometric amount.[287] Finally, the selectivity of this reaction was shown to increase by using a buffered reaction mixture.[289] For this reason, our experiments were performed in a buffered solution containing sodium dihydrogen phosphate, NaH_2PO_4.

The catalytic transformation of dimethylphenylsilane in dimethylphenylsilanol with water has been strongly studied, both in homogeneous[283–288] and heterogeneous conditions (Figure V.2).[280,289–297]
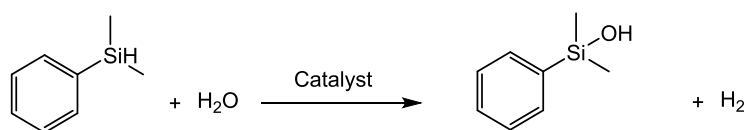
Figure V.2. Catalytic transformation of dimethylphenylsilane in dimethylphenylsilanol with water.

Homogeneous catalysts based on Rh, Ru, Ir, Re and Ag surrounded by various kinds of organic ligands have been reported to be active in this reaction. However, these catalysts lack selectivity for the

146

dimethylphenylsilanol, leading to the formation of a side-product, the disiloxane derivative.[286,288]

Numerous examples of heterogeneous supported catalysts are also reported in the literature for the transformation of dimethylphenylsilane in dimethylphenylsilanol with water. The main advantage of using such heterogeneous catalysts lies in the easy recovery of the catalyst. Moreover, heterogeneous catalysts were reported to yield better activity and selectivity than their homogeneous homologues for this reaction.[279] Several metals (Pd, Au, Rh, Cu, Ag, Ru, Pt, Ni) have been studied on various supports (charcoal, alumina, hydroxyapatite...). Some of these catalysts have been tested at ambient conditions, with good activity and selectivity. Among others, Ru/C has been known for a long time as an efficient catalyst for this reaction under ambient conditions.[289] Besides, Pt nanoclusters were successfully used for this reaction, with high yield at room temperature.[290] Although Ru and Pt were both used for this catalytic reaction with good yields, Ru-Pt bimetallic nanoparticles have never been studied. In this chapter, we will compare the activity of Ru, Pt and Ru-Pt bimetallic nanoparticles supported on CNTs for the hydrolytic transformation of dimethylphenylsilane into dimethylphenylsilanol. A synergetic effect is expected from the combination of ruthenium and platinum in the same active site.

V.2 Methodology

Three different heterogeneous supported catalysts were prepared (Ru, Pt and Ru-Pt/MWCNTs), following the chemical strategy developed in Chapter IV. These catalysts were supported on multi-walled carbon nanotubes. The choice of this support was motivated by its availability in

large amounts in our laboratory, while being more affordable than SWCNTs.

As a first step, a commercial Ru/C catalyst was used to optimize the reaction conditions for the hydrolytic transformation of dimethylphenylsilane into dimethylphenylsilanol. Once these conditions were adjusted, the three catalysts were tested for this reaction. These comparative experiments highlighted the possibility of catalytic activity modulation, by changing metallic nanoparticle composition.

Finally, recyclability tests were performed for all three catalysts, in order to demonstrate the possibility of catalyst recovering and reuse.

V.3 Results and discussion

V.3.1 Preparation of the catalysts

Figure V.3 illustrates the preparation processes of the three different heterogeneous supported catalysts. The difference between these catalysts lies in the nature of the nanoparticles supported on carbon nanotubes. One of them was composed of bimetallic nanoparticles of ruthenium and platinum obtained from the mixed-metal cluster $[Ru_5PtC(CO)_{14}COD]$. The two others were monometallic, containing only ruthenium atoms (obtained from the monometallic cluster $[Ru_6C(CO)_{17}]$) or only platinum (obtained from the complex $Pt(COD)Cl_2$). The quantity of nanoparticle precursor added was calculated so that each catalyst approximately contains the same metal/carbon (M/C) ratio, i.e. 5 wt. %. These catalysts are denoted respectively: **Ru₅Pt/MWCNTs**; **Ru/MWCNTs** and **Pt/MWCNTs**.
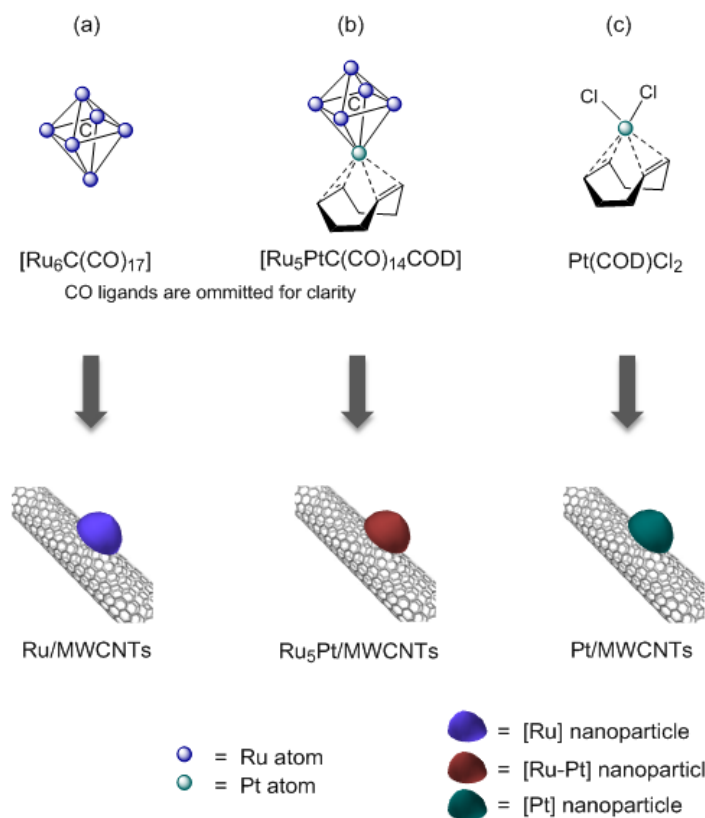
Figure V.3. Schematic representation of the different nanoparticle precursors and the heterogeneous supported catalysts obtained from them.

These catalysts were prepared on a relatively large scale (200 mg), in order to obtain enough material for both characterization and catalytic tests. XPS and elemental analysis were used for the characterization (Table V.1). The first conclusion that can be drawn from this table is the fact that the metal loading estimated by XPS is higher than the M/C ratio calculated by elemental analysis. This can easily be explained by the nature of the catalytic support and the difference between the two techniques used for analysis. Indeed, MWCNTs contain several concentric enrolled graphene sheets (approximately 10) and XPS constitutes a surface analysis, while

EA provides bulk analysis. As a result, XPS only probes a narrow surface layer of the samples, underestimating the carbon content in the sample.[186] Consequently, metal loading on MWCNTs determined by XPS are overestimated. If we only rely on elemental analysis, we can see that M/C wt. ratios are really close to 5, as expected. A second important point to note is that Ru quantification by XPS is rendered difficult by the fact that the main XPS peak of Ru is superimposed to the C 1s peak of carbon. The quantification of Ru by XPS is hence complicated and affected by errors.

However, given its availability in our laboratory, we used XPS to follow the preparation of the catalysts. XPS results (see Table V.2 to Table V.4) are consistent with the results obtained for the functionalization of SWCNTs in the previous chapter. The presence of nitrophenyl functions is revealed by the appearance of a peak at 406.2 eV, after the covalent addition of nitrophenyldiazonium salt. The reduction step by hydrazine is revealed by an increase of the NH_2 peak intensity at 399.9 eV. The evolution of NO_2/C and NH_2/C ratios for nitrophenyl-*f*-MWCNTs and aminophenyl-*f*-MWCNTs respectively is in adequation with a complete reduction of the nitro function by hydrazine (**Ru/MWCNTs**: NO_2/C ~ 2.9 % → NH_2/C ~ 2.9 %; **Ru$_5$Pt/MWCNTs**: NO_2/C ~ 2.7 % → NH_2/C ~ 3.0 % ; **Pt/MWCNTs**: NO_2/C ~ 2.5 % → NH_2/C ~ 2.5 %). Grafting of phosphine functions gives rise to a peak in the XPS spectra attributed to P atoms, with a P/N ratio comprised between 0.22 and 0.30 (**Ru/MWCNTs**: P/N ~ 0.30; **Ru$_5$Pt/MWCNTs**: P/N ~ 0.25 ; **Pt/MWCNTs**: P/N ~ 0.22). These small differences indicate slight variations in the reaction yield from batch to batch. Finally, the nanoparticle precursors were grafted, in proportions calculated in order to obtain a M/C ratio close to 5 wt. %. This 5 wt. % metal loading was chosen to be comparable with the commercial Ru/C catalyst, which was used for the optimization of the reaction.

Table V.1. Element contents and ratios determined by XPS and EA for Ru/MWCNTs, Ru$_5$Pt/MWCNTs and Pt/MWCNTs catalysts.

		Element contents			Ratios		
		C	Ru	Pt	M/C		Ru/Pt (mol %)
Ru/MWCNTs	XPS	85.24 at. %	0.63 at. %	N/A	9.46 wt. %	1.12 mol %	N/A
	EA	81.25 wt. %	3.83 wt.%	N/A	**4.71 wt. %**	0.56 mol %	N/A
Ru$_5$Pt/MWCNTs	XPS	86.78 at. %	0.56 at. %	0.11 at. %	6.79 wt. %	0.70 mol %	5.0
	EA	79.91 wt. %	3.33 wt. %	1.13 wt. %	**5.58 wt. %**	0.58 mol %	5.7
Pt/MWCNTs	XPS	90.50 at. %	N/A	0.42 at. %	6.15 wt. %	0.38 mol %	N/A
	EA	83.67 wt. %	N/A	3.84 wt. %	**4.59 wt. %**	0.28 mol %	N/A

TableV.2. Element contents determined by XPS at each step of the preparation of the Ru/MWCNTs catalyst.

	C 1s	O 1s	N 1s NO₂-Ph	NH₂-Ph	P 2p	Ru 3p
			Element contents (at. %)			
***p*-MWCNTs**	95.66	3.78	0.00	0.11	N/A	N/A
NO₂-Ph-*f*-MWCNTs	89.54	7.33	2.56	0.57	N/A	N/A
NH₂-Ph-*f*-MWCNTs	94.53	2.55	0.14	2.78	N/A	N/A
(PPh₃)₂-Ph-*f*-MWCNTs	94.03	2.41	0.00	2.75	0.81	N/A
Ru-*f*-MWCNTs	87.34	6.20	0.00	2.09	1.18	0.98
NPs/MWCNTs	85.24	9.84	0.00	2.20	0.84	0.63

Table V.3. Element contents determined by XPS at each step of the preparation of the Ru$_5$Pt/MWCNTs catalyst.

| | | | Element contents (at. %) | | | | |
| | | | N 1s | | | | |
	C 1s	O 1s	NO$_2$-Ph	NH$_2$-Ph	P 2p	Ru 3p	Pt 4f
p-MWCNTs	95.66	3.78	0.00	0.11	N/A	N/A	N/A
NO$_2$-Ph-*f*-MWCNTs	90.71	6.25	2.49	0.55	N/A	N/A	N/A
NH$_2$-Ph-*f*-MWCNTs	94.22	2.72	0.25	2.81	N/A	N/A	N/A
(PPh$_2$)$_2$-Ph-*f*-MWCNTs	97.78	3.62	0.09	2.81	0.70	N/A	N/A
Cluster-*f*-MWCNTs	87.54	8.03	0.00	2.12	0.74	0.51	0.10
NPs/MWCNTs	86.78	8.80	0.00	2.05	0.97	0.56	0.11

Table V.4. Element contents determined by XPS at each step of the preparation of the Pt/MWCNTs catalyst.

			Element contents (at. %)			
			N 1s			
	C 1s	O 1s	NO$_2$-Ph	NH$_2$-Ph	P 2p	Pt 4f
p-MWCNTs	95.66	3.78	0.00	0.11	N/A	N/A
NO$_2$-Ph-*f*-MWCNTs	90.89	6.31	2.25	0.55	N/A	N/A
NH$_2$-Ph-*f*-MWCNTs	93.82	3.72	0.11	2.35	N/A	N/A
(PPh$_2$)$_2$-Ph-*f*-MWCNTs	90.60	6.66	0.00	2.24	0.50	N/A
Pt-*f*-MWCNTs	89.86	6.37	0.10	1.93	0.83	0.34
NPs/MWCNTs	90.50	5.98	0.00	2.00	1.05	0.42

V.3.2 Catalytic transformation of dimethyl-phenylsilane

All three catalysts (Ru/MWCNTs, Ru$_5$Pt/MWCNTs and Pt/MWCNTs) were tested in the same conditions, i.e. with 70 mg of catalyst, 4.4 mmol of dimethylphenylsilane and with a constant stirring of 1000 rpm (see experimental section for more details). Conversion rates were determined by GC. In order to demonstrate that the conversion of dimethylphenylsilane in dimethylphenylsilanol is attributable to a catalytic activity of our metallic nanoparticles supported on carbon nanotubes, blank reaction without catalyst was carried out. This test did not lead to the formation of the desired silanol product. A second blank was also carried out to prove that the catalytic activity does not originate from the carbon nanotube themselves.

Figure V.4 shows the evolution of the conversion rate over time, depending on the nature of the catalyst. As can be seen from this graph, Ru/MWCNTs catalyst leads to a slow conversion of the silane function into silanol. After 24 hours of reaction, the conversion reaches about ~ 90 %. In comparison, Pt/MWCNTs shows higher reaction rate, reaching 90 % of conversion after only ~ 7 hours of reaction, and a total conversion after 24 hours. We can conclude from this first observation that Pt seems to be more active than Ru for this reaction. Moreover, we can see that bimetallic Ru-Pt/MWCNTs and monometallic Pt/MWCNTs catalysts lead to similar conversion rates.
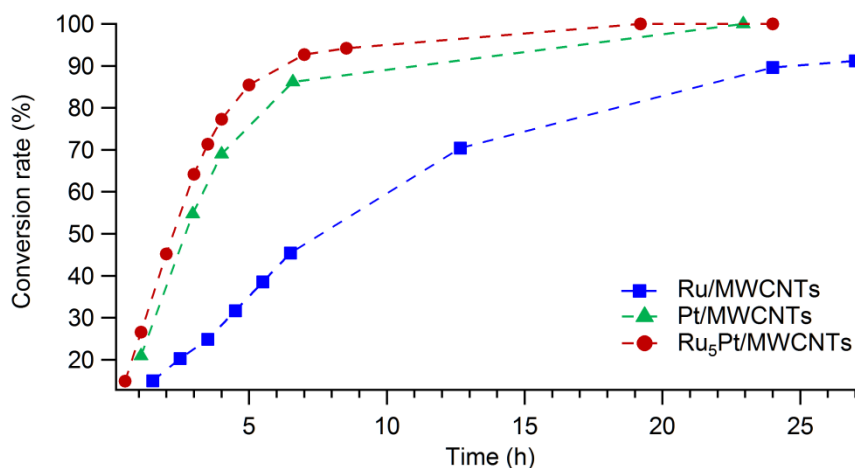
Figure V.4. Conversion curves of dimethylphenylsilane oxidation with water for Ru, Pt and Ru_5Pt/MWCNTs catalysts.

The curves shown in Figure V.4 also give information about the reaction kinetics. The initial slopes of the curves indeed determine the apparent rate constants, for each catalyst. The general expression of the reaction rate v is given in equation V.4, wherein k_{cat} is the rate constant of the catalyzed reaction, [silane] and [H_2O] are the concentration of dimethylphenylsilane and water, respectively, and a and b are the partial order of silane and water, respectively. As previously mentioned, the reaction rate of the considered reaction is independent on the silane concentration. In other words, the partial order a is zero. Moreover, since the water is introduced in large excess, [H_2O] can be considered as a constant. The expression of the reaction rate is therefore simplified (eq. V.5) to equal the apparent rate constant $k_{cat,app}$.

$$v = k_{cat} . [silane]^a . [H_2O]^b \qquad (V.4)$$

$$v = k_{cat,app} \qquad (V.5)$$

According to the initial slope of the curves depicted in Figure V.4, $k_{cat,app}$ is equal to 0.07 for Ru/MWCNTs (with a R^2 = 0.96), 0.22 for Ru$_5$Pt/MWCNTs (with a R^2 = 0.98) and 0.18 for Pt/MWCNTs (with a R^2 = 0.99). However, the slope of the curve in Figure V.4 slightly decreases after a few hours, demonstrating deactivation phenomena.

Furthermore, considering the active site composition, it is worth noting that even in a ratio as low as one Pt atom for five Ru atoms, the presence of platinum considerably increases the catalytic activity, compared to the ruthenium monometallic catalyst. This demonstrates the benefit of using bimetallic nanoparticles, which enable to obtain a synergic effect between the two constitutive metals. This totally justifies the approach of cluster immobilization on the support for the preparation of our catalysts. Cluster chemistry indeed allows to control the nanoparticle composition, ensuring that each nanoparticle is bimetallic.[234] This would not be the case if we had simply impregnated ruthenium and platinum complexes on carbon nanotube surface, followed by a reduction step.

Moreover, it should be noted that Ru$_5$Pt/MWCNTs and Pt/MWCNTs give similar conversion rate, but given the price of these two metals[260] (Ru average price in February 2016: 42.0 US$/Oz compared to Pt average price over the same period: 943.5 US$/Oz), it seems clearly advantageous to use Ru$_5$Pt/MWCNTs instead of Pt/MWCNTs at same metal loading.

In order to be able to compare the activity of our three catalysts, reaction rate should be expressed as turnover frequency (TOF). These TOFs values are calculated by estimating the number of metal atoms at the surface of the nanoparticles. The surface metal content is estimated on the basis of the nanoparticle average diameter, metal atom radius and

considering the nanoparticles as being hemispheres. Table V.5 reports the estimated surface metal atom content for each catalyst.

Table V.5. Estimation of the proportion of surface metal atoms for Ru/MWCNTs, Ru$_5$Pt/MWCNTs and Pt/MWCNTs catalysts.

	Average nanoparticle diameter	Atomic radius [299]	Proportion of surface metal atoms
Ru/MWCNTs	1.24	Ru: 1.34 Å	81.7 %
Ru$_5$Pt/MWCNTs	1.29	Ru: 1.34 Å Pt: 1.39 Å	80.8 %
Pt/MWCNTs	0.86	Pt: 1.39 Å	95.6 %

Knowing this surface metal atom %, TOFs are calculated from the metal content determined by elemental analysis (Table V.6). It is important to note that by using this model, we assume that each metal atom constitutes one active site. In practice, the number of active site is lower, since an active site is composed of several atoms. For this reason, the calculated TOFs are underestimated. Table V.6 gives an overview of the conversion and TOF values for Ru, Ru$_5$Pt and Pt/MWCNTs after 4 hours of reaction.

Table V.6. Conversion and TOF of Ru/MWCNTs, Ru$_5$Pt/MWCNTs and Pt/MWCNTs.

	Metal loading (wt. %)	Conversion (%)	Reaction time (h)	TOF[a] (h^{-1})
Ru/MWCNTs	4.71	32	4.5	14
Ru$_5$Pt/MWCNTs	5.58	77	4	39
Pt/MWCNTs	4.59	69	4	58

[a] TOF values calculated using the expression:

$$\text{TOF}(h^{-1}) = \frac{\text{\# mol of converted product}}{\text{Time (h)} \times \text{\# mol of surface M atom}}$$

As can be seen from this Table, although Ru$_5$Pt/MWCNTs shows a better conversion than Pt/MWCNTs after the same reaction time, Pt/MWCNTs presents a higher turnover frequency. This can be attributed to the fact that for the same metal mass loading, Pt/MWCNTs contains less metallic atoms than Ru$_5$Pt/MWCNTs, Pt being a heavy element. As a consequence, the number of active site decreases, increasing the TOF value.

As a comparison, TOF for the same reaction, carried out in the same conditions (i.e. same solvent, silane reagent and temperature) with Ru/charcoal was reported to be 3.9 h^{-1}.[279] This value is lower than the results obtained with the synthesized Ru/MWCNTs (TOF = 12 h^{-1}), which indicates that our catalyst exhibits better activity for this reaction. To the best of our knowledge, there is no comparable result reported so far for Pt/C catalyst.

V.3.3 Recyclability

V.3.3.1 Recyclability tests

All the three catalysts were recovered at the end of the reaction by filtration. They were then reused in 5 subsequent runs of catalysis. The recyclability tests are shown in Figure V.5. As can be seen, Ru/MWCNTs maintains a constant activity, even after 6 catalytic runs. Ru$_5$Pt/MWCNTs activity gradually decreases as catalytic cycles progress, while Pt/MWCNTs catalyst shows a steep decrease of its activity after 3 runs, to become totally inactive after 5 runs. In order to determine the reasons for this activity loss, the catalysts were recovered after 6 catalytic runs and carefully characterized.
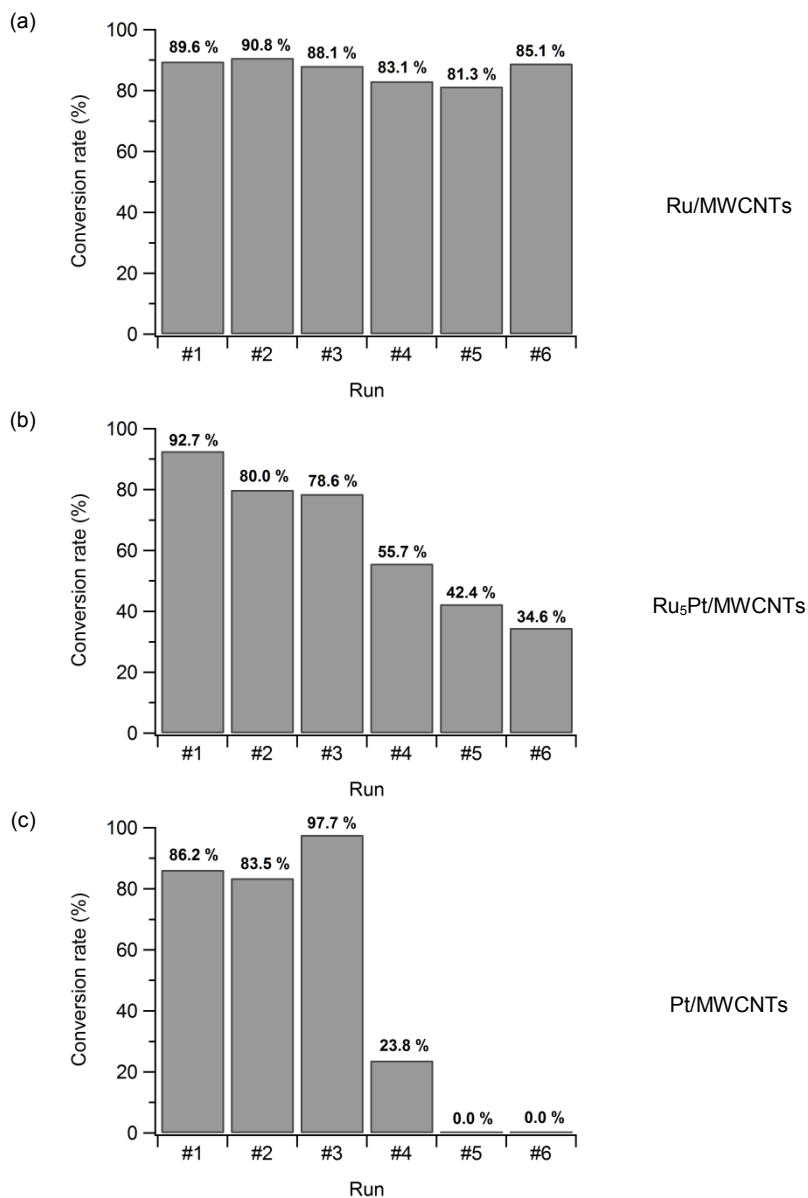
Figure V.5. Recyclability tests for the conversion of dimethylphenylsilane in dimethylphenylsilanol with water catalyzed by (a) Ru/MWCNTs; (b) Ru$_5$Pt/MWCNTs and (c) Pt/MWCNTs. Catalytic runs were carried out for 24 hours when using Ru/MWCNTs, and 7 hours when using Ru$_5$Pt/MWCNTs and Pt/MWCNTs.

V.3.3.2   Catalyst deactivation

Transmission electron microscopy was used to image the catalysts before and after the 6 runs of catalysis (Figures V.6 to V.8). These images allowed to measure the nanoparticle sizes, as depicted in Figure V.9. As can be seen, Ru nanoparticles supported on MWCNTs did not significantly increase in size (1.24 nm ± 0.30 nm of diameter, increased to 1.29 nm ± 0.30 nm after catalysis). This limited increase of nanoparticle diameter proves that the NPs did not sinter during the catalytic reaction. Ru_5Pt/MWCNTs catalyst also shows only a limited increase of nanoparticle size after catalysis (1.29 nm ± 0.28 nm of diameter, to 1.39 nm ± 0.33 nm after catalysis). Pt/MWCNTs catalyst exhibits a larger increase of nanoparticle size after catalysis (0.86 nm ± 0.17 nm of diameter to 1.31 nm ± 0.27 nm). This large increase highlights the sintering of the Pt NPs during catalysis. This sintering process results in a decrease of the active phase surface area, causing a loss of activity.[300–302] This coalescence of Pt atoms could thus explain, partially at least, the decrease of activity observed when reusing Pt/MWCNTs catalyst. However, this phenomenon cannot be solely responsible for a total loss of catalytic activity (Fig. V.5c), since Pt nanoparticles are still present on the CNT surface, as revealed by TEM imaging. Other processes can potentially affect the catalytic activity, namely metal leaching, active phase surface restructuration, or poisoning.[302–304] Quantitative analysis of the catalysts, before and after catalysis is required to detect such deactivation phenomena.
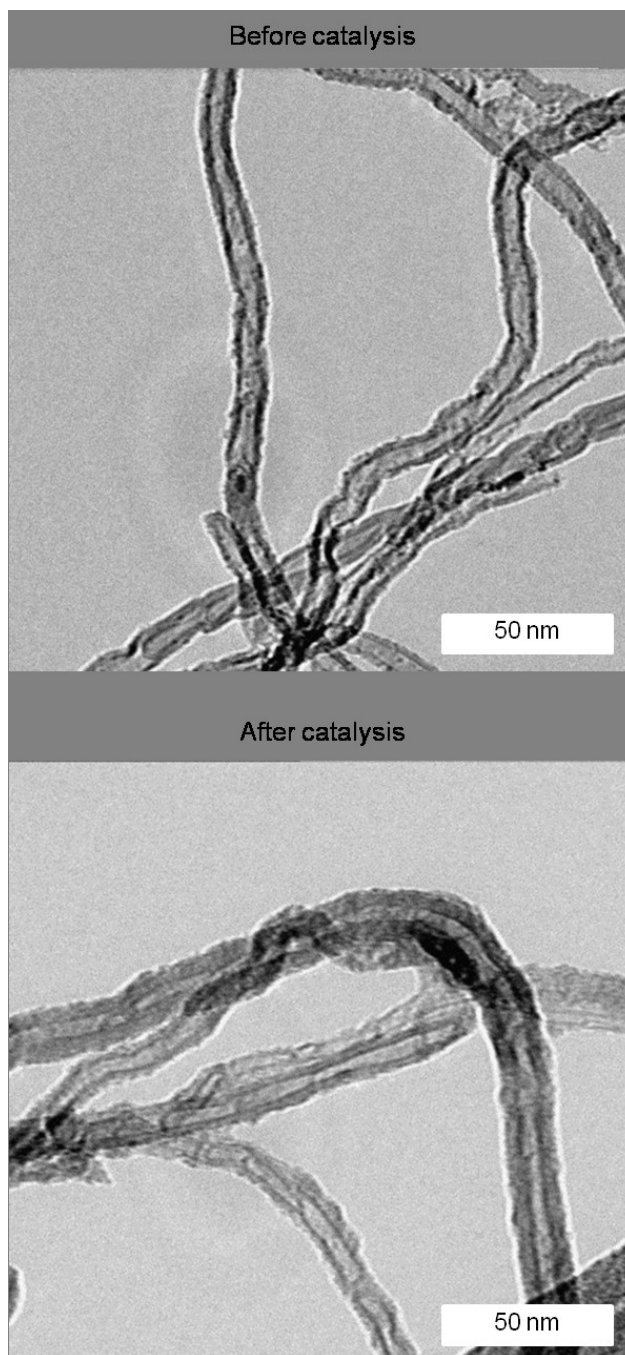
Figure V.6. TEM images of Ru/MWCNTs before catalysis and after 6 runs of catalysis.

162
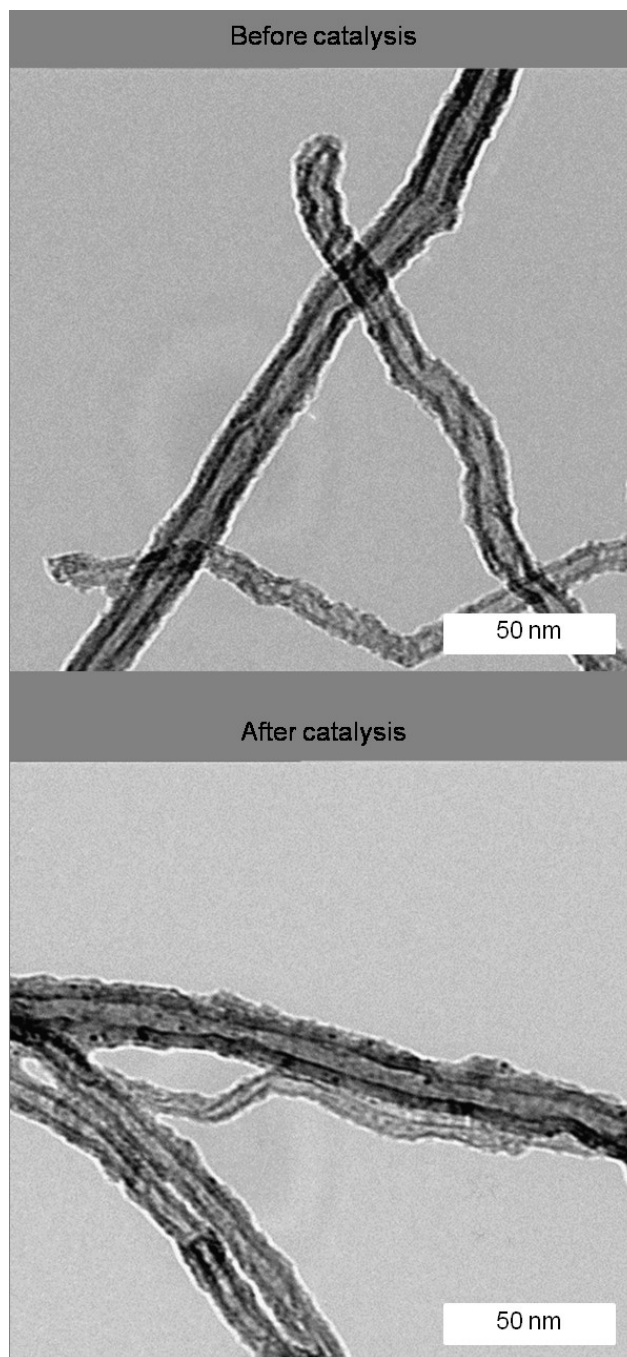
Figure V.7. TEM images of Ru$_5$Pt/MWCNTs before catalysis and after 6 runs of catalysis.
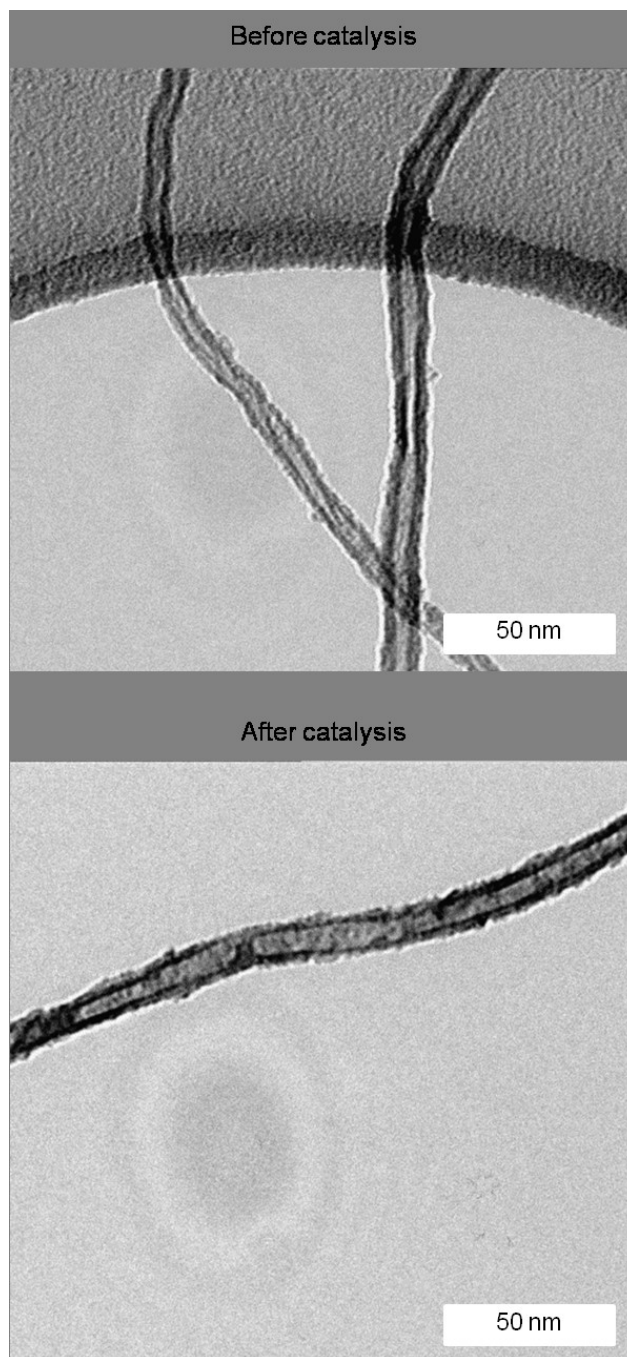
Figure V.8. TEM images of Pt/MWCNTs before catalysis and after 6 runs of catalysis.
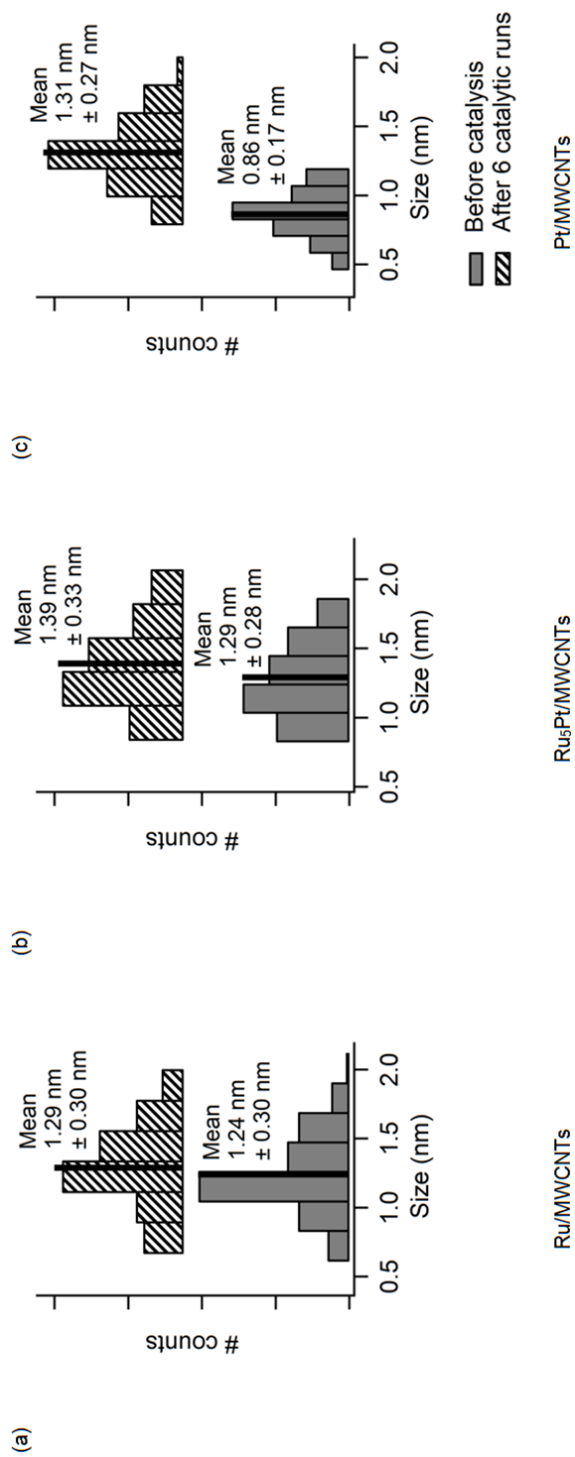
Figure V.9. Histograms showing the size distribution of nanoparticles in (a) Ru/MWCNTs; (b) Ru$_5$Pt/MWCNTs and (c) Pt/MWCNTs before catalysis and after 6 runs of catalysis, as determined by TEM. Size distribution was deduced from measurement of 100 nanoparticle diameter, for each sample.

XPS was performed on each catalyst after 6 runs of catalysis (Table V.7). These quantitative analyses could allow to detect variations of metal content after catalysis, as well as poisoning of the catalyst surface by reagents and/or product involved during the catalytic reaction. As can be seen from Table V.7, metal surface concentration decreased for Ru/MWCNTs and Pt/MWCNTs catalysts, while Ru$_5$Pt/MWCNTs keeps its initial metal surface concentration. This metal surface content decrease revealed that leaching of metallic nanoparticles could occur during catalysis, as will be discussed below. XPS also revealed the appearance of a considerable concentration of sodium after catalysis, while oxygen and phosphorus contents increased. The presence of Na, P and O is attributed to the NaH$_2$PO$_4$.H$_2$O buffer. However, this buffer is soluble in the reaction solvent, and should therefore not be detected in the XPS analysis of the catalyst. Moreover, the ratios between the increase of Na, P and O contents after catalysis vary for each catalyst. This point seems to indicate the presence of a mixture of various sodium and phosphate-based compounds on the catalyst surface, such as sodium phosphate, or sodium polyphosphate, which could be adsorbed on the catalyst surface via remaining phosphorus functions on the nanotube, as already evidenced by XPS of the activated catalysts (Chapters IV and V).

In addition, it is worth noting that the Na content significantly increases with the concentration of platinum. This observation means that platinum NPs are more largely covered by sodium atoms. This surface poisoning results in a decrease of the catalytic activity. To a lesser extent, silicon content also increases after catalysis. This silicon poisoning can come from the silane and/or the silanol, which would remain adsorbed on the surface.

Table V.7. Element contents determined by XPS for Ru/MWCNTs, Ru$_5$Pt/MWCNTs and Pt/MWCNTs catalysts, before catalysis and after 6 runs of catalysis.

		Element contents (at. %)							
		C 1s	**O 1s**	**N 1s**	**P 2p**	**Ru 3p**	**Pt 4f**	**Si 2p**	**Na 2s**
Ru/MWCNTs	Before catalysis	85.24	9.84	2.20	0.84	0.63	N/A	N/A	0.00
	After 6 catalytic runs	84.57	10.89	1.10	1.08	0.36	N/A	0.17	1.34
Ru$_5$Pt/MWCNTs	Before catalysis	86.78	8.80	2.05	0.97	0.56	0.11	N/A	0.00
	After 6 catalytic runs	79.50	12.38	1.91	2.03	0.54	0.13	0.75	2.12
Pt/MWCNTs	Before catalysis	90.50	5.98	2.00	1.05	N/A	0.42	N/A	0.00
	After 6 catalytic runs	71.96	15.51	1.26	3.60	N/A	0.25	0.66	6.85

In order to understand the decrease of surface metal concentration observed in Ru/MWCNTs and Pt/MWCNTs catalysts, bulk elemental analysis was also performed on the catalysts. Comparison of the XPS and EA results is depicted in Table V.8. However, it should be remembered that XPS overestimates M/C ratios since it is a surface analysis.

As can be seen in Table V.8, both XPS and EA highlight a decrease of ca. 25 % of Pt content in Pt/MWCNTs catalyst after 6 runs of catalysis. This result demonstrates that Pt is partially leached out during the catalytic reaction. This phenomenon is partially responsible for the activity decrease observed (Figure V.5c).

Concerning Ru/MWCNTs catalyst, XPS shows a significant decrease of Ru surface concentration after catalysis. Elemental analysis shows only a limited decrease of Ru content after catalysis. This important difference between Ru surface concentration determined by XPS and EA could be attributed to the difficulty of Ru quantification by XPS, as explained above. As a consequence, XPS results must be interpreted with caution, and the high decrease of Ru content observed in this study may be overestimated.

Finally, Ru_5Pt/MWCNTs catalyst shows comparable Ru/C and Pt/C ratios before and after catalysis according to the XPS and EA results. This seems to indicate that there is no leaching of metal atoms during the catalytic reaction. However, variations of the Ru/Pt ratio are observed. As mentioned above, Ru quantification by XPS is subject to large imprecision. For this reason, we only focused on EA results. According to these results, Ru/Pt ratio increases after catalysis, which is consistent with Pt leaching during catalysis.

Table V.8. Ratios determined by XPS and EA for Ru/MWCNTs, Ru_5Pt/MWCNTs and Pt/MWCNTs catalysts before and after 6 catalytic runs.

		Ru/C		Pt/C		Ru/Pt (mol %)	
		XPS	EA	XPS	EA	XPS	EA
Ru/MWCNTs	**Before catalysis**	0.74 mol % / 6.24 wt. %	0.56 mol % / 4.71 wt. %	N/A / N/A	N/A / N/A	N/A / N/A	N/A / N/A
	After 6 catalytic runs	0.42 mol % / 3.54 wt. %	0.48 mol % / 4.03 wt. %	N/A / N/A	N/A / N/A	N/A / N/A	N/A / N/A
Ru_5Pt/MWCNTs	**Before catalysis**	0.65 mol % / 5.44 wt. %	0.50 mol % / 4.17 wt. %	0.12 mol % / 2.02 wt. %	0.09 mol % / 1.41 wt.%	5.2	5.7
	After 6 catalytic runs	0.68 mol % / 5.71 wt. %	0.51 mol % / 4.33 wt. %	0.16 mol % / 2.57 wt. %	0.08 mol % / 1.26 wt. %	4.3	6.6
Pt/MWCNTs	**Before catalysis**	N/A / N/A	N/A / N/A	0.46 mol % / 7.50 wt. %	0.28 mol % / 4.59 wt. %	N/A / N/A	N/A / N/A
	After 6 catalytic runs	N/A / N/A	N/A / N/A	0.34 mol % / 5.55 wt. %	0.20 mol % / 3.23 wt. %	N/A / N/A	N/A / N/A

In order to prove this leaching effect, we performed inductively coupled plasma-atomic emission spectroscopy (ICP-AES) on the reaction mixture, after filtration of the catalyst. This analysis allowed to quantitatively detect traces of metal in solution. As can be seen in Table V.9, while Ru/MWCNTs catalyst shows only limited leaching, Pt/MWCNTs is more subject to leaching, with a concentration in solution as high as 0.2 mg/L. $Ru_5Pt/MWCNTs$ catalyst also undergoes small leaching in solution. Proportionally, this leaching is more pronounced for Pt than Ru. Unfortunately, while previous analyses were performed after 6 runs of catalysis, ICP-AES was performed on the filtrated reaction mixture after only one run of catalysis, therefore we cannot quantitatively compare this latter result with the previous ones.

Table V.9. Amount of metal determined by ICP-AES in filtrated reaction mixture after one run of catalysis.

	Amount of metal in solution (mg/L)	
	Ru	Pt
Ru/MWCNTs	< 0.005	N/A
Ru₅Pt/MWCNTs	0.013	0.013
Pt/MWCNTs	N/A	0.201

V.3.3.3   Summary of the deactivation processes involved

In a nutshell, various deactivation processes are present at the same time. The combination of these diverse deactivation processes explain the evolution of the catalytic activity of the three catalysts used in this chapter.

- **Sintering of the Pt nanoparticles** was revealed by TEM and explains the decrease of catalytic activity for Pt/MWCNTs catalyst as catalytic cycles progress.

- XPS revealed the accumulation of Na, P and O on the catalyst surface after catalysis, highlighting a possible **poisoning** mechanism of the catalyst. The Na content was observed to increase with the Pt proportion. This result explains why Pt/MWCNTs catalyst showed a high decrease of the catalytic activity, to finally become totally inactive: the accumulation of Na on the Pt nanoparticles was so high that these active sites are not anymore accessible for the reagents.

  In comparison, $Ru_5Pt/MWCNTs$ catalyst only showed a limited decrease of its catalytic activity, since the NPs are less covered by Na, as the Pt proportion is lower.

  This O, P and Na poisoning was attributed to the buffer used for the reaction, i.e. NaH_2PO_4. While the presence of a buffer is important to avoid the formation of undesired disiloxane side-products by controlling the pH,[289] the present study evidenced that NaH_2PO_4 is not appropriate for this reaction using nanotube-supported catalysts.

- **Leaching of the Pt nanoparticles** occurred, as revealed by XPS and EA performed on the catalysts after reaction, as well as by elemental analysis performed on the reaction mixture.

V.4 Conclusion

In this chapter, we reported the preparation of mono- (Ru or Pt) and bimetallic (RuPt) nanoparticles supported on multi-walled carbon nanotubes. These nanoparticles decorated CNTs were prepared following the covalent functionalization process developed in Chapter IV, using molecular clusters and complexes as nanoparticle precursors.

We studied the catalytic activity of these materials for the hydrolytic transformation of dimethylphenylsilane into dimethylphenylsilanol. The

catalytic results highlighted a significant difference of conversion rate depending on the nature of the constitutive metals of the active site. Platinum-based catalysts indeed show faster conversion of the silane in silanol than when using monometallic ruthenium nanoparticles. Among the three tested catalysts, RuPt bimetallic nanoparticles supported on CNTs turned out to be the most efficient catalyst for this reaction. This led to the conclusion that a synergetic effect is obtained between the two constitutive metals of the nanoparticle. Indirectly, this conclusion also demonstrated the interest of using clusters as nanoparticle precursors, since it offers the possibility of formation of bimetallic nanoparticles, while allowing to precisely control the nanoparticle composition.

Finally, the recyclability of these three catalysts was tested over six runs. These recyclability tests revealed that Ru/MWCNTs catalyst did not exhibit a loss of activity, even after 6 catalytic runs. Catalytic activity of Ru_5Pt/MWCNTs progressively decreased, while Pt/MWCNTs catalyst became totally inactive after five catalytic runs. This catalyst deactivation was attributed to a combination of sintering, poisoning and leaching processes. Moreover, we also evidenced in this study that the selected buffer was not appropriate for this reaction, as it leads to undesired catalyst deactivation.

Main results of Chapter V

❖ *Preparation of Ru-, Pt- and RuPt-based heterogeneous catalysts supported on MWCNTs*

❖ Use of these catalysts for the *hydrolytic transformation of dimethylphenylsilane into dimethylphenylsilanol* at room temperature and atmospheric pressure

172

❖ *Importance of platinum in the active site* to increase the conversion rate

❖ Highlighting of the *synergic effect of bimetallic nanoparticles* in catalysis

❖ Demonstration of the *recyclability* of Ru/MWCNTs

❖ Demonstration of the *gradual deactivation* of Ru_5Pt/MWCNTs and Pt/MWCNTs catalysts, attributed to a combination of leaching, poisoning and sintering processes.

Experimental section

Instrumentals

A complete instrumental section can be found in Annex IX.1.

Materials

Catalysts were prepared following the functionalization process reported in Chapter IV. The SWCNTs were replaced by MWCNTs, and the reaction was scaled-up to be performed on 200 mg of MWCNTs.

Commercially available 5wt. % Ru/C catalyst from Alfa Aesar was used for the optimization of the catalysis conditions.

Catalytic tests

In a typical procedure, catalyst was suspended in 90 ml of 1,4-dioxane, by ultrasonication during 30 min. The suspension was then transferred to a glass catalytic reactor with 18 ml of $NaH_2PO_4.H_2O$ buffer solution[v] and 5 ml of 1,4-dioxane. This suspension was vigorously stirred (1000 rpm). Dimethylphenylsilane (0.6 g, 4.4 mmol) was added to the reaction mixture with 6 ml of 1,4-dioxane. The reaction was allowed to stir at room temperature for a given time.

Samplings (2 ml) were taken at various time intervals. Those sampling solutions were filtered by means of HPLC PTFE filters (0.22 μm pore size). 1.5 ml of the filtered samplings were introduced in a 5 ml graduated flask, with 1 ml of an internal standard (dodecane) 1 % solution. The volume was brought up to 5 ml with

---

[v] $NaH_2PO_4.H_2O$ buffer solution contains 65 mg of $NaH_2PO_4.H_2O$ and 39.8 ml of 0.1 M NaOH solution per liter.

1,4-dioxane. This solution was injected in GC for conversion rate quantification.

Quantification process

Conversion rates were quantified by GC. The temperature separation program used for theses analyses was based on the following: (i) 1 min isothermal plateau at 50°C; (ii) linear increase of the temperature until 180°C, with a ramp temperature of 5 °C/min; (iii) 2 min isothermal plateau at 180°C.

Calibration lines of both reagent (dimethylphenylsilane) and product (dimethylphenylsilanol) have been established using known concentrations of commercial compounds and dodecane as internal standard. All GC results are expressed in terms of compound on internal standard ratio and reagent or product concentrations are extracted from these calibration lines.

Recyclability tests

The catalysts were recovered at the end of the reaction by filtration of the reaction mixture on PTFE membrane (0.45 µm pore size). The solids were extensively rinsed with dioxane and diethyl ether and were further dried overnight under vacuum. They were then reused in further catalytic runs following the general procedure described above.

CHAPTER VI - DIVALENT FUNCTIONALIZATION AND HOMOGENEOUS SUPPORTED CATALYSIS

Abstract

In this chapter, we develop a second approach for the functionalization of carbon nanotubes in order to prepare supported catalysts. This approach involves divalent chemistry, allowing to preserve electrical properties of the nanotube while functionalizing its surface. These functionalized carbon nanotubes are then coordinated to homogeneous Pd(0) complexes, thus forming homogeneous supported catalysts.

The development of this chemical strategy, along with its chemical and electronic characterization are described in this chapter. Transport measurements demonstrate the preservation of nanotube conductivity even after the covalent functionalization, while XPS and TGA confirm the presence of the desired functions on carbon nanotube surface. The catalytic activity of these homogeneous supported catalysts for the well-known Suzuki-Miyaura reaction is studied.

VI.1 Introduction

VI.1.1 Divalent functionalization

VI.1.1.1 Impact of the divalent functionalization on carbon nanotube conductance

During these two last decades, numerous processes have been developed for carbon nanotube functionalization.[147,159,160] Among these, covalent approaches remain the preferred pathways for many applications, since it provides a strong binding between the nanotube surface and the grafted moieties, ensuring high stability of the functions. Most of these covalent processes implies monovalent binding of the grafted functionalities onto the nanotube surface. This kind of functionalization implies a rehybridization of a sp^2 carbon atom of the nanotube backbone into a sp^3 carbon atom and loss of aromaticity in that point. As a consequence, carbon nanotube electrical properties are greatly affected by this monovalent functionalization process, as demonstrated by both theory[203,212] and experiment.[210,266]

As discussed in Chapter II, divalent functionalization appears to be an interesting alternative to monovalent functionalization to overcome these limitations.[179,180,203,212–214] As far as we know, experimental evidence of the impact of divalent functionalization on carbon nanotube conductance only concerned carbene chemistry.[179,180] However, there are other ways for divalent functionalization of carbon nanotubes. A brief description of these functionalization processes is given in the next section.

VI.1.1.2   Methods for the divalent functionalization of carbon nanotubes

Among the processes developed so far for the divalent functionalization of carbon nanotubes, the addition of carbenes on CNT sidewalls is certainly the most documented. Initially developed by Haddon and coworkers,[187,305–307] this functionalization strategy usually leads to the formation of dichlorocarbene or methylene *f*-SWCNTs, denoted by SWCNT>CCl$_2$ and SWCNT>CH$_2$ respectively, as illustrated in Figure VI.1a and b. Azidocarbonates have also been used for the anchoring of divalent nitrene adducts on carbon nanotube sidewalls (Figure VI.1c).[188,308–311] Although widely studied, concrete applications of these carbene and nitrene functionalized carbon nanotubes remain limited because of the difficulty of *post*-functionalization, due to the absence of derivable functions.

SWCNT>CCl$_2$	SWCNT>CH$_2$	SWCNT>NCOOR
dichlorocarbene-*f*-SWCNT	methylene-*f*-SWCNT	nitrene-*f*-SWCNT
(a)	(b)	(c)
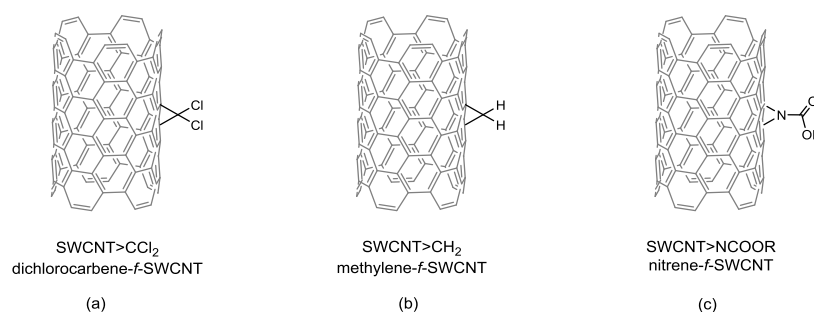
Figure VI.1. Schematic representation of (a) dichlorocarbene-*f*-SWCNTs; (b) methylene-*f*-SWCNTs and (c) nitrene-*f*-SWCNTs.

Other approaches are commonly used for the divalent functionalization of carbon nanotubes, namely 1,3-dipolar cycloaddition of azomethine ylides[312] and Diels-Alder reaction.[313] However, these functionalization processes lead to the formation of 5- or 6-membered rings merged together with the nanotube sidewalls (Figure VI.2), instead of

3-membered rings, as is the case for the addition of carbenes or nitrenes. As a consequence, these divalent adducts are stable, and the *open* configuration is not preferred anymore. These functionalization processes, although being divalent in nature, hence induce a rehybridization of sp^2 into sp^3 carbon atoms, significantly altering the electrical properties of the nanotube.
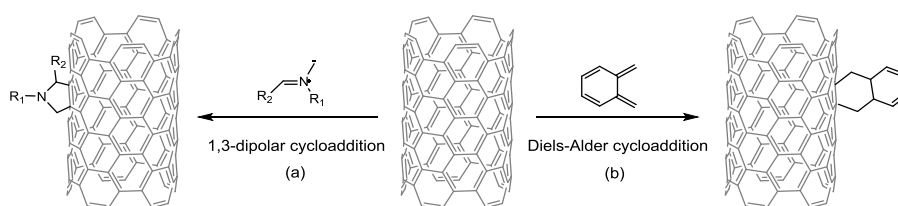
Figure VI.2. Schematic representation of (a) 1,3-dipolar cycloaddition of azomethine yilide and (b) Diels-Alder cycloaddition of o-quinodimethane on a carbon nanotube sidewall.

Among the cyclopropanation reactions of carbon nanotubes,[314] Bingel reaction allows the divalent anchoring of malonate compounds on sp^2 carbonaceous surfaces. Such malonate compounds can be easily tailored, thus offering a large choice of functionalities, which can be anchored to the nanotube surface. In the context of this thesis, we wish to test such divalent functionalization for applications in catalysis. For this reason, we need to be able to *post*-functionalize our divalent *f*-CNTs for the anchoring of an active site on the surface of the nanotube. For this reason, Bingel reaction appears as an ideal candidate for the preparation of such divalent adducts.

Bingel reaction was initially developed for the functionalization of fullerene compounds by α-bromomalonates (Figure VI.3 top).[315] A base such as NaH or DBU ensures the deprotonation of the malonate, which is then allowed to react with the fullerene surface. This step yields to the

180

formation of an anionic intermediate. A substitution then rapidly occurs to eliminate the bromide, forming a divalent bond.[316]

A few years later, Hirsch proposed to divalently functionalize fullerenes by *in situ* formation of the α-bromomalonate from carbon tetrabromide (CBr_4) and the starting malonate, in presence of DBU (Figure VI.3 bottom).[317] This reaction, subsequently named Bingel-Hirsch reaction, together with the initial Bingel reaction, were reported to be efficient for the functionalization of various nanocarbons, i.e. nanodiamond,[318] carbon nanohorns,[319] carbon nanotubes[190,320,321] and graphene.[322]
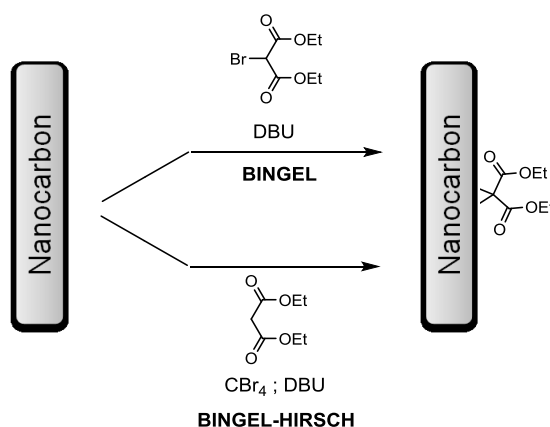
Figure VI.3. Schematic representation of Bingel and Bingel-Hirsch addition reactions.

Although being only barely used so far for the functionalization of carbon nanotubes, this reaction can be advantageously used for applications that require the anchoring of specific functions on nanotube surface, while conserving their electrical properties, such as for the preparation of carbon nanotube-based sensors. To the best of our knowledge, no electrical study has been carried out so far to demonstrate the retention of electronic properties, even though it has been suggested once, according to optical characterization.[323] This chapter will thus

emphasize on the electrical characterization of these functionalized nanomaterials.

VI.1.2   *Towards catalytic application*

The large panel of available or synthesizable malonate compounds makes Bingel-Hirsch reaction a very versatile approach for the functionalization of carbon nanotubes. The grafted functions can be tailored for *post*-functionalization for the purpose of specific applications. In particular, metallic complexes can be coordinated for catalytic applications. Among the numerous application of transition metals in catalysis, palladium is a first choice metal for C−C bond formation reactions.

Carbon-carbon bonds are building blocks for any organic molecule. For this reason, carbon-carbon bond formation reactions are highly desirable in organic chemistry. Among them, Suzuki-Miyaura cross-coupling reaction is one of the most useful reaction in organic synthesis chemistry. This reaction, first reported in 1979, consists in a cross-coupling reaction between an organoboron compound and a halide, using a palladium (0) catalyst and a base.[324] This reaction was reported in 1981 as the first method to prepare biaryl compounds (Figure VI.4).[325] To emphasize the importance of this work, Suzuki, together with Heck and Negishi, were awarded the 2010 Nobel Prize in Chemistry for their progress in palladium-catalyzed cross-coupling reactions.[326,327] The Suzuki-Miyaura reaction is widely used, both in research and at industrial scale, as illustrated by the more than 15000 publications and patents related to Suzuki-Miyaura reaction so far.[328]
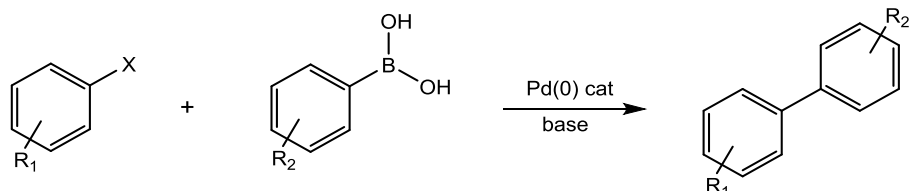
Figure VI.4. Schematic representation of the Suzuki Miyaura cross-coupling reaction between an aryl halide and an aryl boronic acid, to form biaryl compounds.

The success of Suzuki-Miyaura over others C−C bond formation reactions can be explained by the use of organoboron compounds. The use of such organoborons offers (i) versatility, due to the availability of a large panel of boronic acids; (ii) mild and convenient reaction conditions, thanks to the activation of the boronic acid by a suitable base, as well as air- and moisture-stable nature of the organoboron compounds and (iii) easy recovery of less toxic inorganic by-products.[325,327,329–332]

The proposed mechanism for this reaction is illustrated in Figure VI.5. This catalytic cycle is composed of three main steps, i.e. oxidative addition, transmetalation and reductive elimination. The first step consists in an **oxidative addition** of the halide to the palladium (0) complex, to form the stable *trans*-palladium (II) complex. This oxidative addition is often referred as the rate determining step. The rate of this addition depends however on the reactivity of the halide towards the Pd(0) complex, known as: R^1−I > R^1−Br >> R^1−Cl.[330] This oxidative addition is then followed by a **transmetalation** step, leading to a Pd(II) complex coordinated to the two organic moieties R^1 and R^2, coming from the halide and the organoboron respectively. Finally, a reductive elimination step takes place, leading to the formation of the desired cross-coupling product, and restoring the Pd(0) catalyst.

183
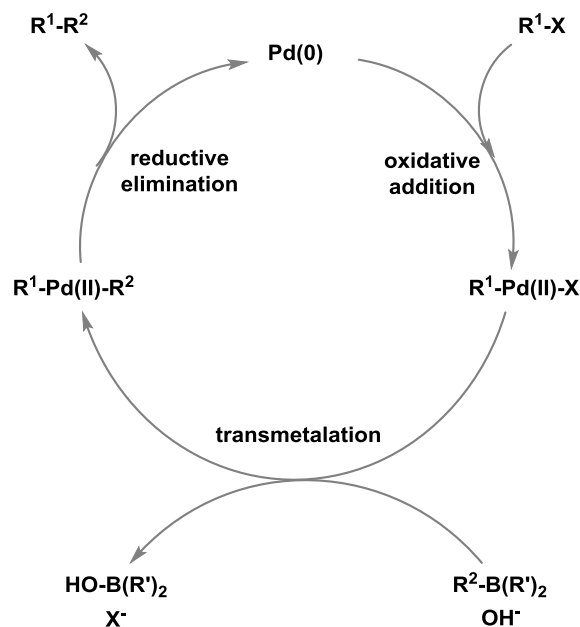
Figure VI.5. Schematic representation of the general catalytic cycle for the Suzuki-Miyaura reaction. In this catalytic cycle, the base is considered to be OH⁻ for clarity, but other bases can be used.

Although the mechanism of the catalytic cycle of the Suzuki-Miyaura reaction is well established, the transmetalation step is not yet fully understood. More specifically, the role of the base for this transmetalation step is still debated. The reason for this misunderstanding is likely due to the fact that the mechanism is highly dependent on the reaction conditions.[330,333] Two possible pathways have been proposed to describe this transmetalation step (Figure VI.6).[333–335] In path A, the base reacts with the palladium complex, by an exchange of the halogen atom with the anion coming from the base. This intermediate then reacts with the organoboron compound, through a transmetalation process. In path B, the base first reacts with the organoboron, forming the corresponding borate. This activated borate is then able to react with the palladium complex, to form the R^1-Pd(II)-R^2 complex, by transmetalation. While path

B has long be considered as the more energetically favored pathway, recent experimental studies cast doubt on this general assumption.[334,335] Given the number of conflicting theoretical and experimental studies, it seems that the precise role of the base for the transmetalation step strongly depends on the nature of both organoboron and base compounds. A better understanding of this step mechanism should lead to a better optimization of the reaction conditions.
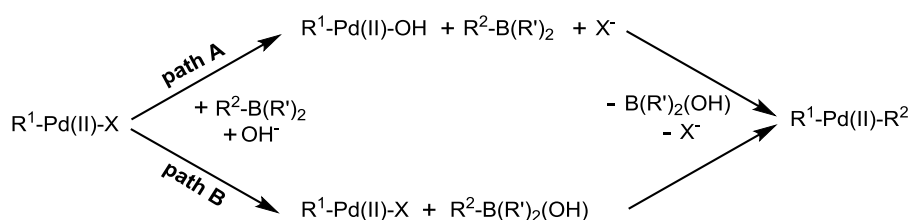
Figure VI.6. Schematic representation of the two pathways proposed to describe the transmetalation step of the Suzuki-Miyaura reaction. In this scheme, the base is considered to be OH⁻ for clarity, but other bases can be used. Figure inspired from Lima *et al.*[333]

VI.2 Methodology

Aiming at preparing homogeneous catalysts supported on carbon nanotubes, we developed the pathway in Figure VI.7 for the anchoring of active sites. For considering future sensing applications, it is important to preserve nanotube conductivity through the functionalization. By using a divalent functionalization approach, we hypothesize that the high nanotube conductance can be preserved while having functionalities covalently attached to the nanotube, for the purpose of catalytic applications. More specifically, we used Bingel-Hirsh reaction to covalently anchor malonate derivatives, containing alkyne functions. These alkyne functions were then used for the coordination of metallic complexes, known to be active in homogeneous catalysis (Figure VI.7).

185
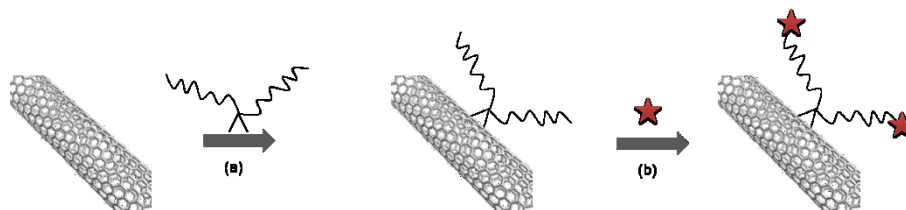
Figure VI.7. Schematic representation of the chemical pathway developed for the heterogenization of homogeneous catalysts on carbon nanotube surface: (a) divalent functionalization of SWCNTs; (b) anchoring of homogeneous catalysts, represented by the stars.

As a first step, we verified the feasibility of the divalent functionalization of single-walled carbon nanotubes by the Bingel-Hirsch reaction. Second, we anchored metal complexes on these *f*-SWCNTs. These steps were characterized by XPS and TGA. Electrical measurements were also performed on these materials to control if the nanotube conductance is well preserved as expected. Finally, the catalytic activity of these materials was tested for the Suzuki cross-coupling reaction of 4-iodotoluene with phenylboronic acid.

In practice, we anchored on the CNT surface a malonate derivative **(1)**, bearing two alkyne functions. Alkynes can easily coordinate transition metals.[336–338] As a consequence, divalent functionalized SWCNTs bearing alkyne functions can be used to coordinate metal complexes, for subsequent applications in catalysis. In this work, we chose to anchor palladium complexes, which are known to be catalytically active for the Suzuki-Miyaura cross-coupling reaction.[329] Particularly, the active species for this reaction consists in Pd(0). Although being very stable, the 18 electrons Pd^0L_4 (L being a 2 electrons donor ligand) complex undergoes two successive deligations, to form the 14 electrons Pd^0L_2, which is the active species in catalysis.[339] In practice, $Pd^0(PPh_3)_2$ complex and mixtures

of $Pd^0(dba)_2$ and PPh_3 ligands are commonly used as species able to generate 14 electrons Pd(0) species. $Pd^0(dba)_2$ is a very air stable complex, unlike phosphine coordinated complexes, such as $Pd^0(PPh_3)_2$. By using a mixture of $Pd^0(dba)_2$ and PPh_3 ligands instead of $Pd^0(PPh_3)_n$, we can avoid the synthesis of air-sensitive complexes. As demonstrated by NMR, $Pd^0(dba)_2$ contains one ligated and one free dba (equation (VI.1)). When in presence of PPh_3 ligands, the complex $Pd^0(dba)(PPh_3)_2$ is formed (equation (VI.2)).[339]

$$Pd^0(dba)_2 \rightleftarrows Pd^0(dba) + dba \qquad\qquad\qquad (VI.1)$$

$$Pd^0(dba) + PPh_3 \rightleftarrows Pd^0(dba)(PPh_3)_2 \qquad\qquad (VI.2)$$
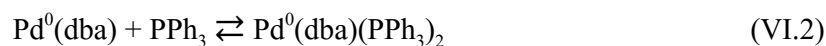
For this reason, we anchored $Pd^0(dba)_2$ in presence of PPh_3 ligands on alkyne functionalized SWCNTs (Figure VI.8).
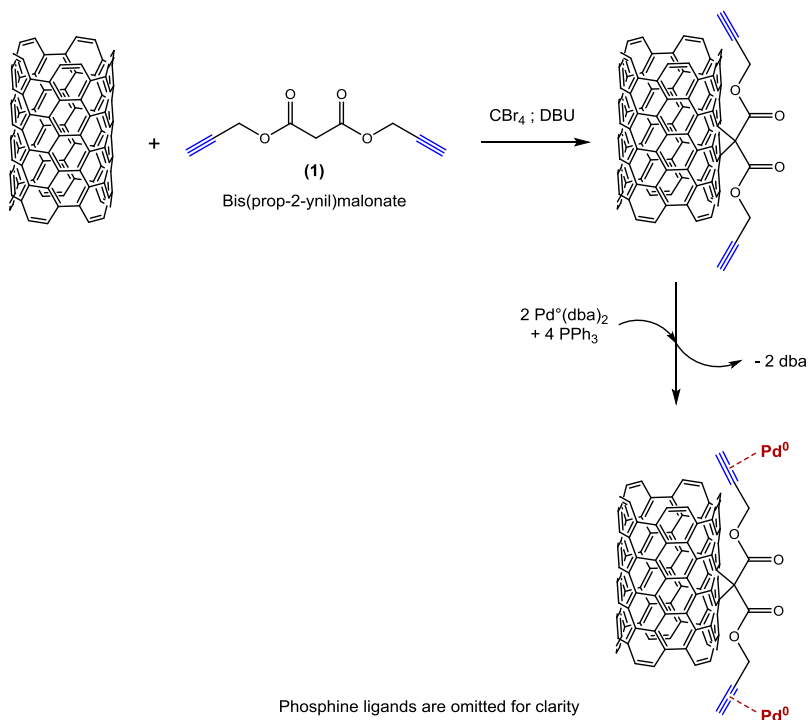
Figure VI.8. Chemical pathway developed for the preparation of homogeneous supported catalysts: (a) divalent functionalization of SWCNTs through Bingel-Hirsch reaction; (b) anchoring of Pd(0) complexes.

Finally, the catalytic activity of these Pd(0) complexes divalently coordinated to carbon nanotubes is studied for the Suzuki-Miyaura cross-coupling reaction. More specifically, we investigated the cross-coupling reaction between 4-iodotoluene and phenylboronic acid (Figure VI.9).
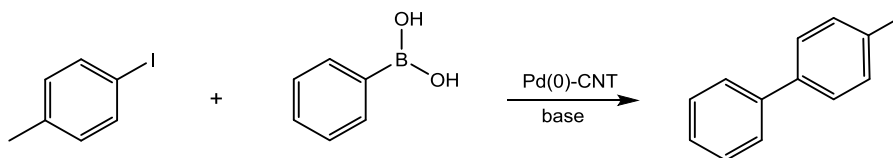
Figure VI.9. Schematic representation of the Suzuki Miyaura cross-coupling reaction between 4-iodotoluene and phenylboronic acid.

188

VI.3 Results and discussion

VI.3.1 Chemical functionalization route

VI.3.1.1 Addition of malonate derivatives on SWCNTs

Alkyne functions were grafted on bulk single-walled carbon nanotubes *via* the Bingel-Hirsch reaction. The grafting was followed by thermogravimetric analysis (Figure VI.10). As can be seen, a mass loss (about 2.4 %) appears at around 320 °C, which corresponds to the detachment of the grafted functions. This high temperature proves the covalent nature of the bond formed between the nanotube and the grafted moieties. Physically adsorbed functions would indeed desorb at lower temperature. In order to verify this statement, we prepared a mechanical mixture of SWCNTs and alkyne malonate. TGA reveals a mass loss before 200 °C (see Annex IX.6.1) This result confirms the covalent nature of the bond formed between the malonate and the SWCNT.
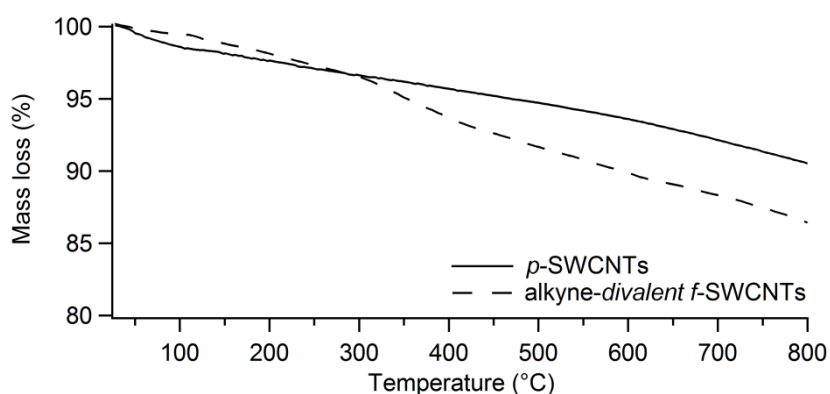
Figure VI.10. Thermograms (under nitrogen) of pristine SWCNTs (solid line) and alkyne- *divalent f*-SWCNTs (dashed line).

TGA was used as a semi-quantitative technique to estimate the functionalization rate. The thermogram depicted in Figure VI.10 shows a mass loss of 2.4 % between 300 and 450 °C. Taking into account the mass of the grafted moiety (i.e. $C_9H_6O_4$; MM = 178.14 g.mol^{-1}), the functionalization rate is estimated to be 0.17 %. This rate corresponds to the anchoring of a malonate function on 1 carbon atom out of 588.

Raman spectroscopy is commonly used to probe the covalent functionalization of carbon nanotubes. However, due to the divalent nature of the functionalization considered here, Raman spectroscopy cannot be used to clearly identify bonding (e.g. using the D/G band ratio) because carbon atoms conserve their sp^2 hybridization (see Annex IX.6.2 for the Raman spectrum of the alkyne-*divalent f*-SWCNTs).

We also used XPS for the characterization of these alkyne-*divalent f*-SWCNTs. As shown in Figure VI.8, the functionalized-SWCNTs only bear carbon, oxygen and hydrogen atoms. The absence of heteroatoms makes their characterization difficult. However, the grafted malonate compounds contain CO_2 ester functions (binding energy = 289 eV), that could be distinguished from the main graphitic peak of carbon (284.8 eV).[340] Superimposed C 1s XPS spectra of pristine-SWCNTs and alkyne-*divalent f*-SWCNTs is depicted in Annex IX.6.3. As can be seen in inset, a very small contribution of ester appears after the functionalization, but this contribution is lost in the shake-up structure. For this reason, XPS did not allow to firmly conclude that the malonate is indeed anchored on the nanotube surface.

Given the limited characterization possibilities of the alkyne-*f*-SWCNTs, other malonates containing heteroatoms (see Figure VI.11) were used to control the functionalization progress by XPS, and determine the reaction conditions. The evolution of Br content was followed by XPS, for various reaction conditions, namely time and solvent nature (see Annex IX.6.4).
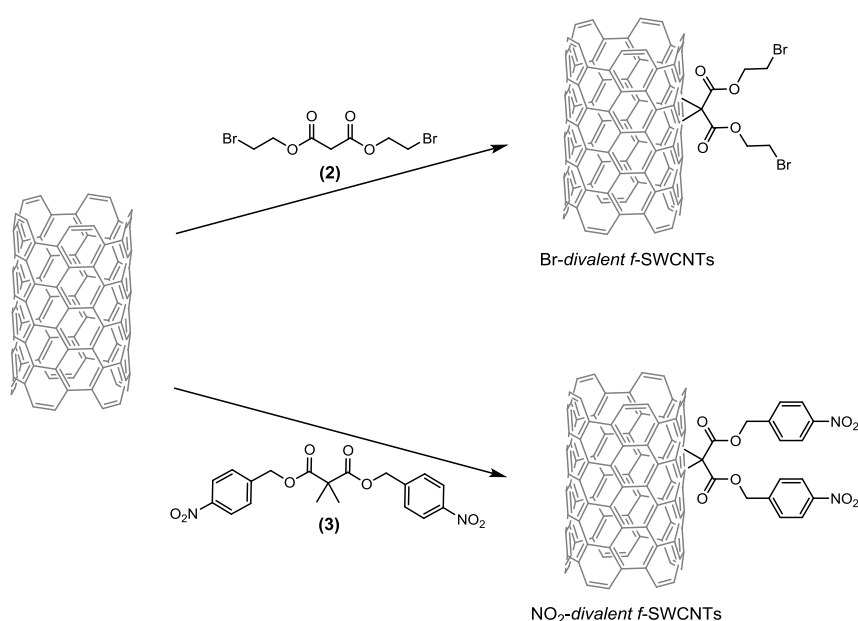
Figure VI.11. Schematic representation of the divalent functionalization of SWCNTs by Br-malonate (**2**) and NO$_2$-malonate (**3**).

Table VI.1 shows the element contents determined by XPS for Br- and NO$_2$-*divalent* *f*-SWCNTs functionalized in the optimized reaction conditions. As can be seen, Br and N contents increase by ~ 0.45 % after the functionalization by malonate **(2)** and **(3)**, respectively. This heteroatom content increase demonstrates the successful grafting of the malonate compounds on carbon nanotube surface.

Table VI.1. Element contents and molar ratios determined by XPS for pristine SWCNTs, Br-*divalent f*-SWCNTs and NO_2-*divalent f*-SWCNTs.

	Element contents (at. %)				Molar ratios
	C 1s	O 1s	N 1s	Br 3d	
p-SWCNTs	95.66	3.78	0.11	0.00	N/C = **0.11 %**
Br-*divalent f*-SWCNTs	93.36	6.24	N/A	0.40	Br/C = **0.43 %**
NO_2-*divalent f*-SWCNTs	94.89	4.56	0.55	N/A	N/C = **0.58 %**

The increase of the heteroatom on carbon ratio after functionalization is close to 0.45 %, whichever the malonate used in the reaction. Given the fact that each malonate contains 2 heteroatoms, the number of anchored moieties should be divided by a factor 2, i.e. ~ 0.22 %. This means that about 1 malonate is anchored on every 450 carbon atoms on the nanotube surface. This functionalization yield is really close to the grafting yield obtained by TGA (i.e. 0.17 %). The agreement of these two techniques allows to conclude that similar functionalization rates are obtained with the three considered malonates. However, this functionalization yield is far lower than the results obtained with the monovalent functionalization described in Chapter IV. NO_2/C ratio was indeed reported as 4.2 % for bulk-SWCNTs, which corresponds to about 1 carbon atom out of 24 being functionalized. The higher functionalization yield of the monovalent functionalization is attributed to the radical nature of the reaction, associated with higher reactivity. By comparison, Bingel reaction performed on SWCNTs were reported to exhibit functionalization rate of about 2 %,[190] i.e. 9 times higher than our functionalization rate. However, these results are not really comparable, since they arise from Bingel and Bingel-Hirsch reactions, respectively. Bingel-Hirsch reaction implies the *in situ* formation of the bromomalonate in addition to the CNT functionalization and is thus expected to exhibit lower functionalization

rate. To the best of our knowledge, there is no experimental study reporting functionalization rates of Bingel-Hirsch addition of malonate compounds on pristine-SWCNTs.

However, the functionalization rate obtained for the divalent functionalization is sufficient to consider catalytic applications. If each grafted moiety bears one Pd atom, we would indeed obtain 2 wt. % of Pd, which is comparable to common catalysts.[341,342]

VI.3.1.2   Anchoring of Pd°(dba)$_2$

Alkyne-*divalent* *f*-SWCNTs were used to anchor Pd^0(dba)$_2$ complexes in presence of PPh$_3$. We performed XPS on the samples after reaction with Pd(0) to determine the metal loading (Table VI.2). As can be seen, a significant amount of Pd is present on the carbon nanotube surface, as high as ~ 2 mol %. This large amount exceeds the expected loading, as approximated by the content in Br or NO$_2$ functions in the functionalization control experiments described above. We indeed expected to obtain maximum two Pd complexes per divalent graft. More precisely, depending on the flexibility of the anchored divalent grafts on the nanotube surface, Pd complexes could be coordinated by one or two alkyne functions, as illustrated in Figure VI.12. However, it should be remembered that the functionalization rate of our alkyne-*divalent* *f*-SWCNTs has not been directly determined due to the absence of heteroatoms. Some variations are thus likely to happen, but probably not important. The high Pd loading reported in Table VI.2 suggests that part of the Pd amount is simply adsorbed on the nanotube surface. However, the work-up performed to recover the Pd(0)-*divalent* *f*-SWCNTs solid consisted in extensive washing and sonication treatments. This procedure

should have removed weakly physisorbed species, and we can thus assume that the Pd content is sufficiently anchored for catalytic applications.

Table VI.2. Element contents and Pd/C ratio determined by XPS for Pd(0) complexes coordinated on alkyne-*divalent f*-SWCNTs.

	Element contents (at. %)				Pd/C
	C 1s	O 1s	Pd 3d	P 2p	
Pd(0)-*divalent f*-SWCNTs	80.06	17.74	1.87	0.34	2.3 mol % 20.7 wt. %
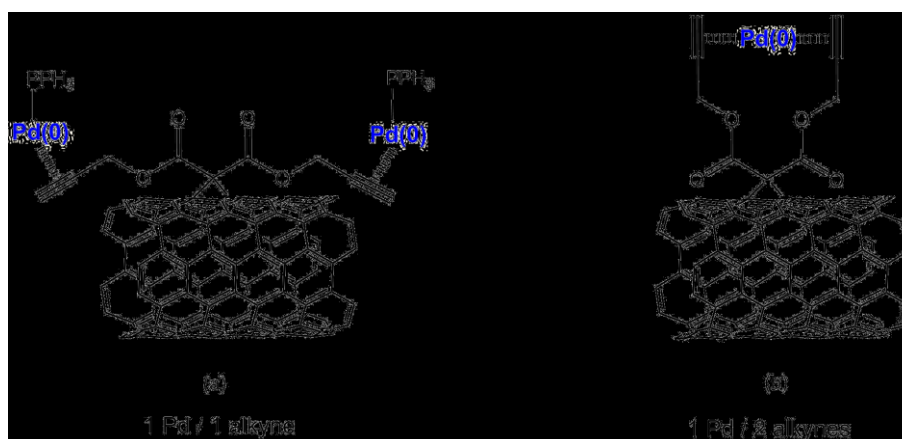
Figure VI.12. Schematic representation of the two possible ways of Pd complexes coordination on alkyne-*divalent f*-SWCNTs.

As depicted in Table VI.2, phosphorus content is lower than Pd, with a P/Pd ratio of 0.18. This result seems to indicate that the two proposed ways of Pd coordination on the *f*-SWCNTs (Fig. VI.14) are both present. Indeed, in the 1 Pd / 1 alkyne configuration (Fig. VI.14a), each Pd atom is expected to bear one PPh$_3$ ligand, which would lead to a P/Pd ratio of 1, while in the 1 Pd / 2 alkynes configuration (Fig. VI.14b), Pd atoms are not expected to bear phosphine ligands, which would lead to a P/Pd ratio of 0.

XPS also gives information concerning the oxidation state of the Pd present on the nanotube surface. This spectroscopy indeed allows to distinguish Pd(0) and Pd(II). Binding energy of Pd 3d 5/2 peak is reported to be 336.2 eV and 338.2 eV for Pd(0) and Pd(II) complexes, respectively.[343] As can be seen from the XPS spectrum, the Pd 3d 5/2 peak possesses a binding energy of 336.3 eV, thus corresponding to Pd(0) (Figure VI.13). The zero oxidation state of the Pd supported on carbon nanotube surface is particularly important, since the active species in Suzuki cross-coupling reaction is reported to be Pd(0).
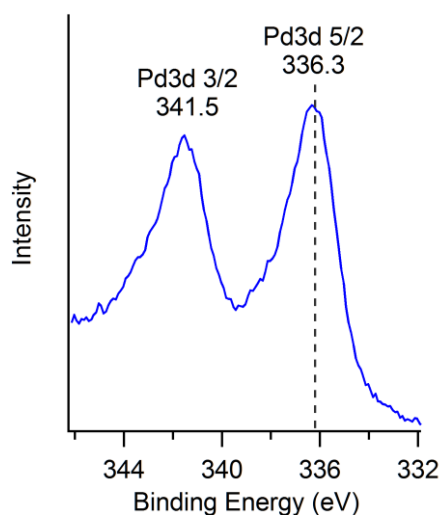
Figure VI.13. High resolution Pd XPS spectrum of Pd(0)-*divalent f*-SWCNTs, demonstrating the zero oxidation state of the Pd atoms. The dashed line corresponds to Pd(0) 3d 5/2 as reported in the literature (336.2 eV).[343]

Moreover, as can be observed on the spectrum depicted in Figure VI.13, Pd 3d peak is asymmetric, due to charge effects. For this reason, the decomposition of the spectrum is difficult. Especially, a Pd-P contribution is difficult to highlight, if not impossible. No chemical shift is indeed expected to arise from a Pd-P interaction, since Pd and P exhibit the same

electronegativity. Furthermore, given the low proportion of P content relative to Pd content (i.e. 1 P atom for 5-6 Pd atoms, or a P/Pd ratio of 18 %), the peak deformation induced by P would be less than 20 %. Given the spectrum resolution and the natural peak asymmetry, such a low deformation would be impossible to detect.

VI.3.2   SWCNT-FETs functionalization

VI.3.2.1   Electrical characterization

As mentioned above, we used divalent functionalization for its ability to preserve the conductivity of carbon nanotubes, while covalently anchoring functions on their surface. These electrical properties are crucial for future sensing applications. As a result, it is of critical importance to probe the evolution of the conductivity at each step of the catalyst preparation. Figure VI.14 shows transfer curves for pristine SWCNT and divalently functionalized SWCNT before and after Pd(0) coordination. As can be seen, the electrical conductance of the SWCNT remain constant, even after the covalent functionalization. This absence of current decrease after covalent functionalization demonstrates the divalent nature of the functionalization, in open configuration, preserving the sp^2 hybridization of the carbon atoms of the nanotube sidewall. At this stage, it is important to note that even the introduction of a single defect by covalent functionalization is known to significantly impact the nanotube conductivity, as demonstrated by both theoretical[203] and experimental[63] studies. As a consequence, even at low functionalization rates, such as in the present case, electrical measurements should allow to detect the impact of this functionalization on the nanotube conductivity. An absence of conductivity decrease can hence be interpreted as an evidence of the divalent nature of the functionalization.

196

As can be observed in Figure VI.14, the SWCNT is slightly n-doped after the divalent anchoring of malonate functions. In order to determine the origin of this doping, we measured transfer curves of blank samples, prepared by immersing pristine SWCNT-FETs in DBU and CBr_4, in absence of the alkyne malonate (See Annex IX.6.5). As can be seen, the nanotube is also n-doped after immersion in a solution containing DBU and CBr_4. This experiment demonstrates that the doping is not due to the functionalization of the nanotube sidewall, but rather to charge effects that occurs due to chemical reagents which are required for the reaction to take place.
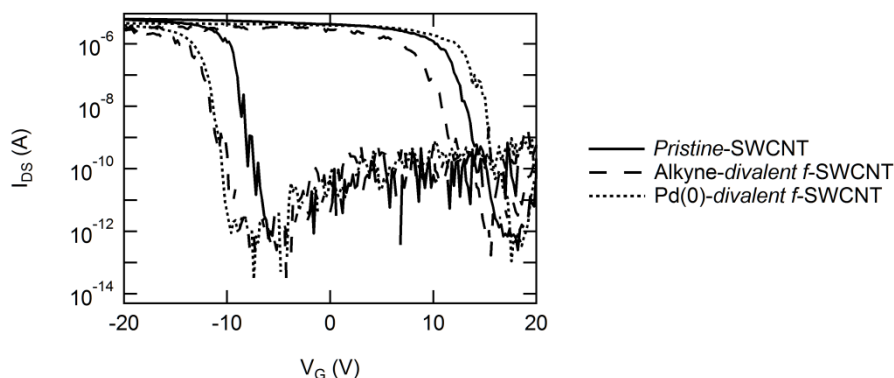
Figure VI.14. Transfer curves (V_{DS} = 1 V) of *pristine*-SWCNT, alkyne-*divalent f*-SWCNT and Pd(0) complexes coordinated on *divalent f*-SWCNT.

VI.3.2.2   Control experiments

The transfer curves shown in Figure VI.14 demonstrate the preservation of the nanotube conductivity, even after the functionalization, as expected given the divalent nature of the functionalization. However, this lack of current modification arises issues when trying to prove that the functionalization indeed occurred. In order to prove this, we prepared blank SWCNT-FET samples, that were characterized by other techniques.

These control samples were not used for catalytic applications. They allowed to indirectly demonstrate that the functionalization indeed occurred on SWCNT-FETs, despite the fact that no significant changes were measured in the transfer curves.

Due to the configuration of the SWCNT-FETs, i.e. only one nanotube present on the chip, common surface characterization techniques such as XPS or TGA cannot be used. Microscopy appears as a good technique to visualize the presence of metallic species on the nanotube surface. However, following this functionalization pathway (see Figure VI.8), carbon nanotubes are decorated by single atoms of palladium. These individualized Pd atoms cannot be detected by microscopic techniques, unless by using HRTEM, which would allow to reach atomic resolution. However, due to the configuration of the SWCNT-FETs, transmission microscopy is not an option in the present case. We tried using SEM-EDX to determine the nature of the elements present on the nanotube surface. Unfortunately, this analysis requires a very energetic electron beam, which resulted in degradation of the sample. For this reason, we were unable to identify Pd using this technique.

To be able to visualize the presence of metal on the Pd(0)-*divalent f*-SWCNTs surface, we prepared blank samples. This control experiment consisted in thermally annealing the Pd(0)-*divalent f*-SWCNTs, to transform single Pd atoms into larger nanoparticles. At the end of this annealing, the obtained nanoparticles were expected to be detectable by imaging. Moreover, in order to demonstrate the necessity of functionalization for the anchoring of Pd complexes, another blank was prepared, following the same process, without divalent addition of malonate. Without this malonate, the carbon nanotubes remain

unfunctionalized, and the coordination of Pd is not likely to occur. On the contrary, the grafted moieties on functionalized blank act as nucleation sites, which favor the accumulation of Pd complexes on the nanotube. More details concerning the preparation of these blanks are given in Annex IX.6.6.1.

Pictures were taken after immersing overnight unfunctionalized SWCNT-FETs and alkyne-*divalent f*-SWCNT-FETs in the same concentration Pd(0) solution (see Annex IX.6.6.2). After one night, the two solutions are visually very different. In the case of *f*-SWCNTs, the solution is bleached, while in the other case, the solution remained bright red. This observation is in agreement with a favored anchoring of the Pd complexes on carbon nanotubes thanks to the functionalization.

The thermally annealed blanks were imaged by AFM in order to visualize the presence of nanoparticles on the sample (see Annex IX.6.6.3). AFM reveals the presence of a large amount of large metallic flakes located around the nanotube, in the case of functionalized blank. On the contrary, non-functionalized blank does not show an accumulation of metal on the nanotube, but rather a homogeneous dispersion of nanoparticles everywhere on the substrate. This observation highlights the importance of the chemical functionalization for the coordination of the Pd(0) complexes on carbon nanotubes. Indirectly, this proves that the functionalization indeed occurs, even if no change is detected in the electrical properties.

VI.3.3 Catalytic application

VI.3.3.1 Catalytic activity
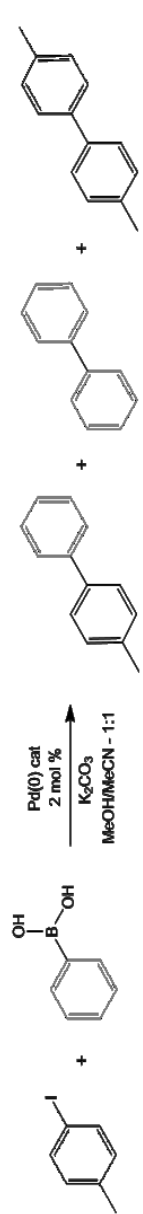
The Pd(0)-SWCNTs prepared in this chapter were used as catalyst for the Suzuki-Miyaura cross-coupling reaction between 4-iodotoluene and phenylboronic acid, in presence of potassium carbonate as a base. Different products can be obtained from this reaction: first, the desired 4-methylbiphenyl can be obtained from the heterocoupling of the two reagents. Moreover, biphenyl and 4,4'-dimethylbiphenyl can be obtained from the homocoupling of phenylboronic acid and 4-iodotoluene, respectively.

Although numerous examples of Suzuki-Miyaura cross-coupling reaction are reported to require high temperature and prolonged reaction time, a recent publication revealed the possibility of operating this reaction in ambient conditions.[111] In addition to the positive environmental aspects of this approach, it is also advantageous for considering future ambient sensing applications. As a consequence, the reaction conditions were carefully adapted to match this operating process.

The Suzuki-Miyaura cross-coupling reaction was performed by using two different catalysts, in order to compare the activity and selectivity of our Pd(0)-SWCNTs homogeneous supported catalyst with the Pd(0)(dba)$_2$ complex as homogeneous catalyst. The reaction products were analyzed by gas chromatography. The results are summarized in Table VI.3. Blank experiments were also performed without catalysts or only in presence of carbon nanotubes without Pd complexes. These blank experiments highlighted the importance of catalytic species for this reaction, which does not work in absence of an appropriate catalyst. As can be seen from Table VI.3, the Pd(0)-SWCNTs homogeneous supported catalyst prepared

200

here is active for this reaction. The main product obtained comes from the heterocoupling between the two reagents. By comparison, the homogeneous catalysts exhibits higher activity and selectivity, in the same reaction conditions. However, this homogeneous catalyst is difficult to recover for its reuse in subsequent catalytic reaction cycles.

Table VI.3. Conversion rates determined by GC obtained after 6 hours of reaction between 4-iodotoluene and phenylboronic acid, for various catalysts.
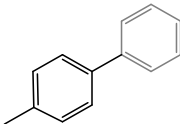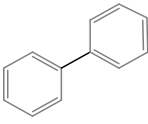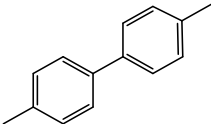
	Conversion rates		
Homogeneous supported catalyst Pd(0)-SWCNTs	**35.5 %**	**6.7 %**	N/A*
Homogeneous catalyst Pd(0)(dba)₂	54.3 %	2.0 %	N/A*

* This product is not detected by GC.

VI.3.3.2   Recyclability

In order to demonstrate the recyclability of the supported catalyst, we recover it at the end of the reaction and reuse it in a second catalytic run. As can be seen in Table VI.4, our catalyst shows a partial activity loss from one catalytic run to another. Despite this partial deactivation, we demonstrate here that the catalyst can easily be recovered at the end of the reaction, while remaining active for subsequent reaction runs, contrarily to the homogeneous catalyst.

Table VI.4. Recyclability test performed with the homogeneous supported catalyst Pd(0)-SWCNTs.

	Conversion rate		
Run #1	35.5 %	6.7 %	N/A*
Run #2	24.5 %	3.5 %	N/A*

* This product is not detected by GC.

VI.4 Conclusion

In this chapter, we used divalent functionalization for the preparation of homogeneous supported catalysts. More specifically, we used Bingel-Hirsch reaction to divalently anchor alkyne substituted malonate compounds on single-walled carbon nanotube sidewalls. These alkyne functions were then used to coordinate Pd(0) complexes. Thermogravimetric analysis and X-ray photoelectron spectroscopy were used to characterize the materials.

Transport measurements were also performed to follow the fabrication process of these Pd(0) complexes decorated carbon nanotubes. This electrical characterization highlighted the preservation of the nanotube conductivity, even after the covalent anchoring of alkyne functions at its surface. This phenomenon proves the divalent nature of the functionalization, with an open configuration, allowing to preserve the initial sp^2 hybridization of the carbon atoms of the nanotube. This conservation of electrical properties is of significant importance for future sensing applications. However, the absence of modifications of the transfer curves after the coordination of Pd(0) complexes raises some doubts related to the possibility of probing the catalytic activity in real-time through electrical measurements. The electrical characterization reported in this chapter indeed did not demonstrate that the Pd complexes are electrostatically coupled with the nanotube, a condition required to be able to observe conductance fluctuations induced by the reactions taking place on the Pd atoms.

Finally, the catalytic activity of these Pd(0)-SWCNTs was also demonstrated for the cross-coupling Suzuki-Miyaura reaction between 4-iodotoluene and phenylboronic acid.

Main results of Chapter VI

❖ Development of a *divalent functionalization strategy* for the coordination of Pd(0) complexes on carbon nanotube surface, *via* Bingel-Hirsch reaction

❖ *Preservation of carbon nanotube electrical properties*, even after the functionalization steps

❖ *Catalytic activity* of the prepared material *for the Suzuki-Miyaura reaction*

Experimental section

Instrumentals

A complete instrumental section can be found in Annex IX.1.

Materials

"Bulk" SWCNTs were purchased from Sigma Aldrich (carbon > 90 %, SWNTs ≥ 77 %) and used as received without further purification.

SWCNT-FETs presented in this chapter were prepared with flow-aligned CVD-growth, in the configuration described as "geometry 2". See Chapter III and Annex IX.4.1 for more experimental details.

Malonate syntheses

Bis(2-bromoethyl)malonate synthesis

Bis(2-bromoethyl)malonate was synthesized following a procedure adapted from the literature.[318,344] Malonic acid (10 mmol), 2-bromoethanol (20 mmol) and paratoluenesulfonic acid (0.037 mmol) were added to 30 ml of toluene. The reaction mixture was heated under reflux at 120 °C in a round bottom flask equipped with a Dean-Stark trap for 24 hours. After cooling to room temperature, 50 ml of DI water and 20 ml of toluene were added to the reaction mixture and the layers were separated. Organic phases were washed with $NaHCO_3$ (3x25 ml), water (2x50 ml) and brine (2x30 ml). The extract was dried over $MgSO_4$, filtered and the solvent was evaporated. ^{1}H-NMR (300 MHz, $CDCl_3$): δ = 4.47 (t, J = 6.12 Hz, 4H, O-CH_2); δ = 3.53 (t, J = 6.12 Hz, 4H, CH_2-Br); δ = 3.47 (s, 2H, CH_2-CO). ^{13}C-NMR (300 MHz, $CDCl_3$): δ = 165.9 (C=O); δ = 64.9 (CH_2-O); δ = 41.2 (CH_2); δ = 28.2 (CH_2-Br); HRMS (ESI): m/z calculated for $C_7H_{11}O_4{}^{79}Br_2$: 316.90186, measured: 316.90216.

Bis(prop-2-ynil)malonate

Bis(prop-2-ynil)malonate was synthesized following a procedure from the literature.[318] Malonic acid (1 g, 9.6 mmol), propargyl alcohol (1.16 g, 20.76 mmol) and paratoluenesulfonic acid (0.38 g, 2.0 mmol) were added to 30 ml toluene. The reaction mixture was heated under reflux at 120°C in a round bottom flask equipped with a Dean-Stark trap for 17 h. After cooling to room temperature, 50 ml of DI water and 20 ml of toluene were added to the reaction mixture and the layers were separated. Organic phases were washed with $NaHCO_3$ (3x25 ml), water (2x50 ml) and brine (2x30 ml). The extract was dried over $MgSO_4$, filtered and the solvent was evaporated. The crude product was purified by column chromatography on silica gel (ethyl acetate/cyclohexane 1:2). ^{1}H-NMR (300 MHz, $CDCl_3$): δ = 4.76 (d, J = 2.46 Hz, 4H, 2 CH_2); δ = 3.49 (s, 2H, CH_2); δ = 2.51 (t, J = 2.43 Hz, 2H, C≡C-H). ^{13}C-NMR (300 MHz, $CDCl_3$): δ = 165.4 (C=O); δ = 77.0 (HC≡CCH₂); δ = 75.7 (HC≡C); δ = 53.2 (HC≡CCH_2); δ = 41.0 (C(=O)CH_2C(=O)); HRMS (ESI): m/z calculated for $C_9H_9O_4$: 181.04954, measured: 181.04958.

Carbon nanotubes functionalization

Bingel-Hirsch divalent functionalization

Three different malonate compounds (bis(4-nitrobenzyl)malonate (*TCI*); bis(2-bromoethyl)malonate) and bis(prop-2-ynil)malonate were used for divalent functionalization of carbon nanotubes through Bingel-Hirsch cyclopropanation reaction. The same procedure was followed whichever the malonate compound involved.

Bulk carbon nanotubes (20.0 mg, 1.66 mmol) are suspended in 20 ml of 1,2-dichlorobenzene (o-DCB) by ultrasonication. To this suspension, desired malonate compound (1.66 mmol) and carbon

tetrabromide (CBr$_4$ - 550.5 mg; 1.66 mmol) are added. 1,8-diazabicyclo[5.4.0]-7-undecene (DBU - 0.22 ml; 2.49 mmol) is added dropwise to the reaction mixture, which is allowed to stir at RT overnight. The suspension is then filtered over a PTFE membrane (0.45 µm pore size) and successively washed with 100 ml of o-DCB, EtOH, THF and diethyl ether, followed by sonication in 50 ml of DCM for 30 minutes. The suspension is filtered and washed again as previously described.

SWCNT-FETs are immersed in a solution of o-DCB (20 ml) containing malonate (2.10^{-4}mol), carbon tetrabromide (66 mg, 2.10^{-4}mol) and 1,8-diazabicyclo[5.4.0]-7-undecene (45 µl, 3.10^{-4}mol). The samples were allowed to react overnight at room temperature, with stirring. At the end of the reaction, samples are removed from the solution and extensively rinsed with o-DCB, toluene and 2-propanol.

Anchoring of Pd(0) on *divalent f*-CNTs

Bulk alkyne divalent-f-CNTs (20.0 mg, 1.66 mmol) are suspended in 20 ml of anhydrous toluene, under argon. To this suspension, bis(dibenzylideneacetone)palladium(0) (Pd(dba)$_2$ - 13 mg ; 0.023 mmol) and triphenylphosphine (PPh$_3$ - 11,8 mg ; 0.045 mmol) are added with 10 ml of an anhydrous solution of toluene/THF (20:1). The suspension is allowed to stir at room temperature overnight. The suspension is then filtered over a PVDF membrane (0.22 µm pore size) and successively washed with 100 ml of toluene, EtOH, THF, ethyl acetate (AcOEt) and diethyl ether, followed by sonication in 50 ml of toluene for 30 minutes. The suspension is then filtered and washed again as previously described.

Alkyne-divalent f-SWCNT-FETs are immersed in a solution of toluene (20 ml) containing Pd(dba)$_2$ (1.4 mg ; 0.0024 mmol) and PPh$_3$ (1.5 mg ; 0.0057 mmol). The samples were allowed to react overnight at room temperature, with stirring. At the end of the

reaction, samples are removed from the solution and extensively rinsed with toluene, followed by 2-propanol.

High Pd(0) loading control experiments

Alkyne-divalent f-SWCNT-FETs are immersed in a solution of toluene (20 ml) containing Pd(dba)$_2$ (15 mg ; 0.026 mmol) and PPh$_3$ (15 mg ; 0.057 mmol). The samples were allowed to react overnight at room temperature, with stirring. At the end of the reaction, samples are removed from the solution and extensively rinsed with toluene, followed by 2-propanol.

Catalytic tests

In a typical procedure, catalyst (in proportion adapted to obtain 2 mol % of Pd) was suspended in 10 ml of MeOH/MeCN - 1:1 solvent mixture during 30 min. Potassium carbonate (K$_2$CO$_3$; 2 mmol, 276.4 mg), 4-iodotoluene (1 mmol, 218 mg) and phenylboronic acid (1.5 mmol, 182.9 mg) were added to this suspension, which was allowed to stir at room temperature for a given time.

Quantification process

Conversion rates were quantified by GC. The temperature separation program used for theses analyses was based on the following: (i) 12 min isothermal plateau at 120°C; (ii) linear increase of the temperature until 160 °C, with a ramp temperature of 5°C/min; (iii) 2 min isothermal plateau at 180°C.

Calibration lines of 4-iodotoluene, 4-methylbiphenyl and biphenyl have been established using known concentrations of commercial compounds and dodecane as internal standard. All GC results were expressed in terms of compound on internal standard ratio.

Recyclability tests

The catalyst was recovered at the end of the reaction by filtration of the reaction mixture on PTFE membrane (0.45 µm pore size). The solid was extensively rinsed with MeOH and MeCN and diethyl ether and was further dried overnight under vacuum. It was then reused in another catalytic run, following the procedure described above.

CHAPTER VII - *IN SITU* DETECTION OF CATALYTIC ACTIVITY BY REAL-TIME ELECTRICAL MEASUREMENTS

Abstract

In this chapter, we demonstrate for the first time the possibility of using carbon nanotubes as sensors for in situ detection of catalytic activity. In order to do this, heterogeneous catalysts supported on carbon nanotubes are prepared following the process described in Chapter IV. These carbon nanotube supported catalysts are integrated into electronic devices and their activity for the hydrolytic transformation of dimethylphenylsilane in dimethylphenylsilanol is probed through real-time electrical measurements. Upon exposure to dimethylphenylsilane, carbon nanotube devices exhibit two-level current fluctuations. The evolution of these current fluctuations when varying the reaction conditions is investigated in this chapter.

VII.1 Introduction

In Chapter IV, we developed a chemical pathway for the deposition of metallic nanoparticles on the surface of carbon nanotubes. Electrical measurements of carbon nanotube devices were performed at each step of the chemistry and highlighted that nanoparticle formation results in a strong p-doping of the CNT (see Figure IV.17). This doping effect demonstrated the presence of an electrostatic coupling between the nanoparticles and the CNT. For this reason, we postulate that the conductance of nanoparticle-decorated carbon nanotube devices should be sensitive to charge transfer reactions occurring on the nanoparticles. Such charge transfer reactions would indeed result in a give or take of electrons from the nanotube to the nanoparticles, which directly impacts the nanotube conductance.

In this chapter, we will investigate the use of carbon nanotubes as a tool to detect *in situ* catalytic activity. In order to do this, electrical measurements will be used to qualitatively probe catalytic activity in real-time.

Compared to other methods developed so far for the *in situ* characterization of catalysis,[91,92,104] our approach can be performed in ambient conditions. As mentioned in the general introduction, one major drawback of operando catalysis is indeed the fact that the catalysis is often performed in suboptimal reaction conditions, as required by the characterization methods considered. Another advantage of the present approach for the detection of catalytic activity is its ability to cover a large breadth of timescales, allowing the detection of single events.

VII.2 Measurement setup

In Chapter IV, we showed that carbon nanotube field-effect transistors can be used to monitor changes in the nanotube chemical environment. These measurements were performed in air and asynchronously. In order to detect catalytic reactions, we need to perform electrical measurements in solution. This can be done by using conducting solution, or electrolyte solution.[345,346] We also need to record real-time measurements, thanks to an adapted experimental setup.

VII.2.1 Real-time measurements

Figure VII.1 schematically represents the experimental setup used for the real-time electrical measurements and developed at Columbia University by Scott Trocchia (Prof K. Shepard). A PDMS (polydimethylsiloxane) microfluidic flow cell (800 μm large x 7 mm long) was placed on top of the CNT-FETs, along the nanotube. Polyethylene capillary tubes (internal diameter: 0.58 mm) were inserted into both ends of the flow cell, for flowing the desired solutions. The injection of the reaction mixture was done by using a syringe connected to the outlet capillary. An Al wire, serving as electrolyte gate, was inserted inside the inlet capillary and connected to an adjustable voltage source (Yokogawa GS200).
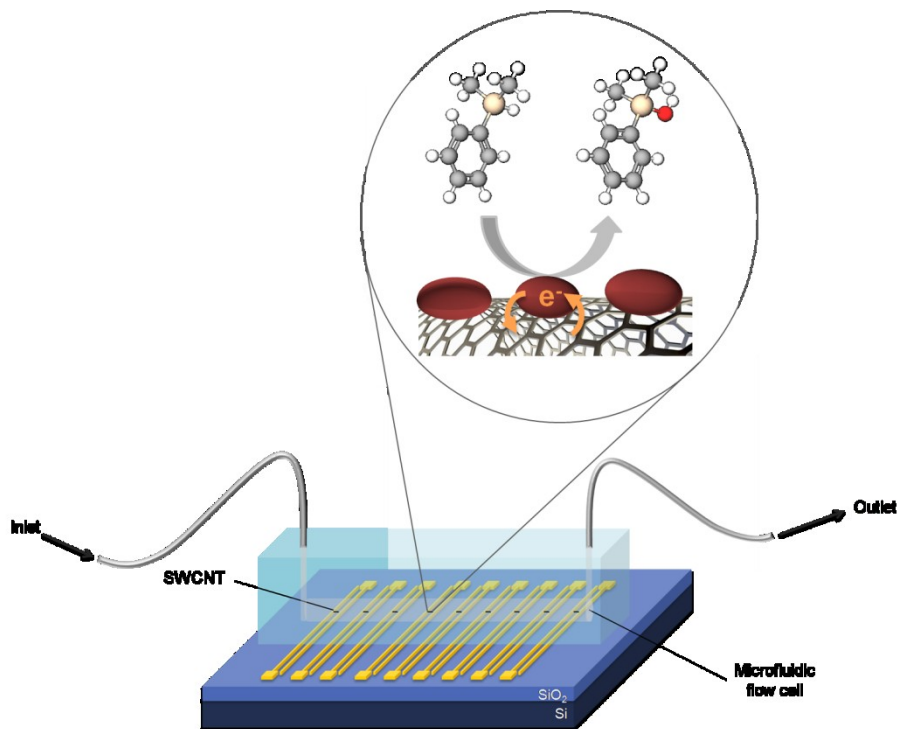
Figure VII.1. Schematic representation of the experimental setup used for the real-time electrical detection of catalytic activity with carbon nanotube sensors.

Each pair of source and drain electrodes was connected to a chip carrier, using Au wire bonds, made by Jason Hon (Figure VII.2a). Devices were independently powered and measured in real-time using a custom printed circuit board (Figure VII.2b), specifically designed to operate multiple devices simultaneously and kindly provided by Scott Trocchia, Columbia University.

214
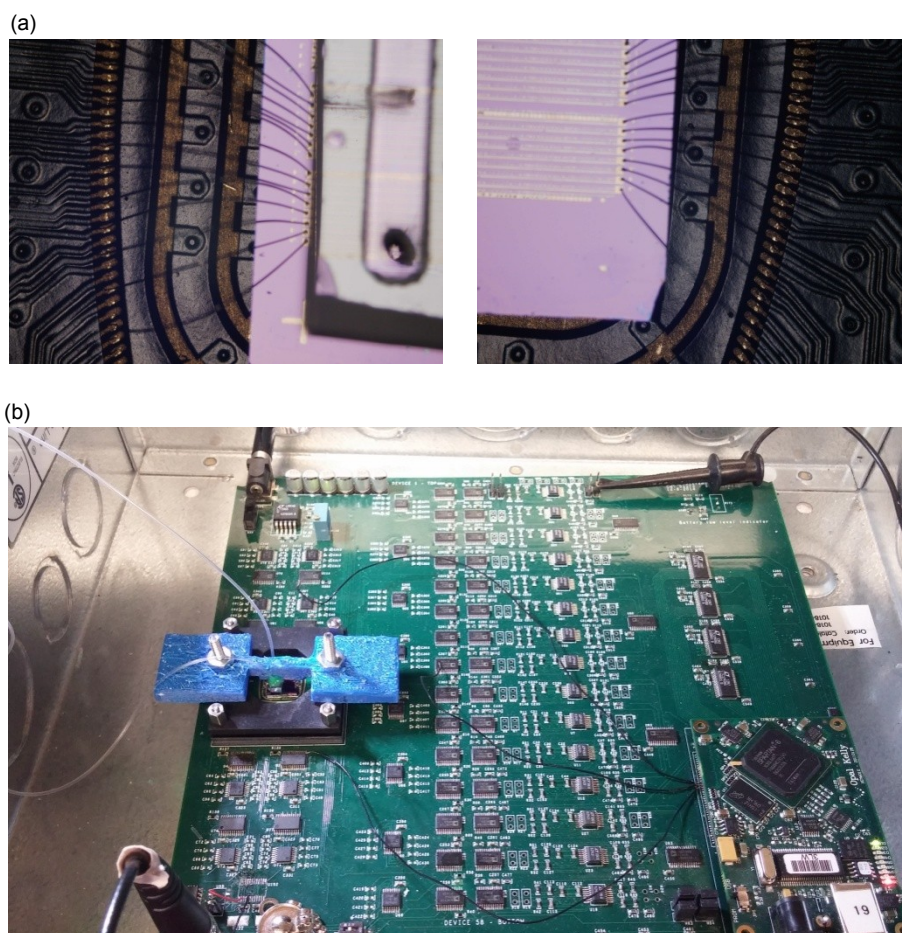
Figure VII.2. (a) Optical microscopy images showing the Au wire-bonds and the microfluidic flow cell; (b) circuit board used for the real-time electrical measurements.

VII.2.2 Measurements in solution

One difference between air and liquid measurements lies in the gating method. While nanotubes are generally gated by applying a voltage to a back-gate electrode when performing electrical measurements in air (Figure II.14), the gate voltage is applied through a reference electrode when operating in an electrolyte solution (Figure VII.3). This alternative gate is required since the back gate electrode is screened by the charges contained in the electrolyte solution.
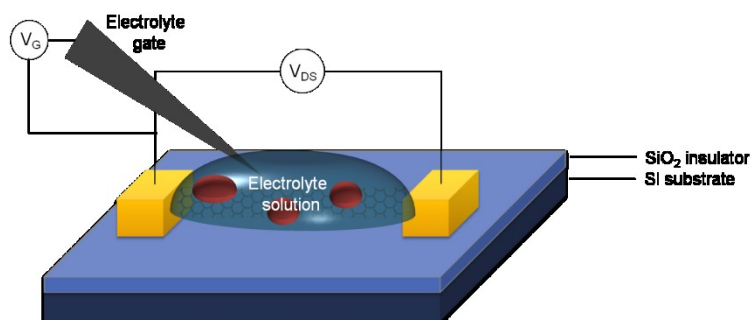
Figure VII.3. Schematic representation of an electrolyte gated SWCNT-FET. Both V_G and V_{DS} are constant values.

In the majority of studies reported for carbon nanotube sensing experiments, the electrolyte gate usually consists in a Pt electrode. The use of such electrode in the present project raises some issues due to the well-known activity of platinum in many catalytic reactions. Alternatively, Ag/AgCl electrodes are also commonly used for carbon nanotube sensing. However, Ag has been reported for the catalytic transformation of silane into silanol in presence of water[347,348] and can obviously not be used for the present experiment. In order to avoid undesired catalytic reactions on the electrolyte gate, we selected Al as a gate electrode material. This metal is indeed known to be rapidly passivated by an oxide layer, which prevents catalytic reactions to occur at its surface.

In practice, this Al gate electrode was made of an Al wire inserted in the inlet capillary and the gate voltage was set to zero. This setup is not ideal since the wire is far from the CNT-FETs and moves during the measurements and between experiment runs. The potential of the solution is quite unstable as a result and the nanotube current baseline evolves over time. For this reason, we will not discuss in the following sections the absolute values of the current. Although the relatively instable gate voltage with this setup, this Al electrode prevents parasitic catalytic activity induced by changes of the nanotube doping state. It is worth noting that despite the slight evolution of the current baseline over time, the measurements allow to distinguish current fluctuations induced by the catalytic activity, as will be shown in the next sections. Ideally, this movable Al wire should be replaced by an Al gate electrode directly patterned on the chip by lithography. This setup improvement is envisioned for further experiments.

VII.3 Prerequisites

VII.3.1 Monovalent vs divalent functionalization pathways

In this thesis, we developed two distinct approaches for the preparation of carbon nanotube supported catalysts. On one hand, a heterogeneous supported catalyst was prepared by a monovalent functionalization pathway (Chapter IV). The catalytic activity of this material was demonstrated for the transformation of dimethylphenylsilane into dimethylphenylsilanol (Chapter V). On the other hand, a homogeneous supported catalyst was prepared thanks to a divalent functionalization pathway (Chapter VI). This catalyst was used for the

Suzuki-Miyaura cross-coupling reaction between 4-iodotoluene and phenylboronic acid (Chapter VI).

In Chapter VI, we encountered difficulties in characterizing the prepared homogeneous supported catalytic materials. These difficulties came from the different features of the functionalization pathway considered. First, the divalent nature of the bond formed between the CNT and the grafted moiety allow preserving the electrical properties of the nanotube. While this is advantageous for many applications, namely for sensor design, it can be disadvantageous for the monitoring of the chemical functionalization by Raman spectroscopy or electrical characterization, as evidenced in Chapter VI. Second, the absence of heteroatoms on the malonate compound grafted on the CNTs prevents the use of XPS to determine the grafting yield.

On the contrary, heterogeneous supported catalysts prepared according to the chemical process described in Chapter IV were carefully characterized by an appropriate combination of chemical and physical characterization techniques, such as XPS, Raman spectroscopy, elemental analysis, SEM and TEM as well as electrical characterization. Especially, the electrical characterization highlighted the presence of a strong interaction between the nanotube and its supported nanoparticles. For this reason, we expect to be able to detect the catalytic activity of these nanoparticles through real-time measurement of the nanotube conductance.

These considerations provide the rational that led us to select the monovalent pathway for the real-time detection of catalytic activity experiments.

VII.3.2 Summary of the main results obtained with the monovalent *f*-CNTs

In Chapter IV, we developed a chemical functionalization pathway for the preparation of heterogeneous catalysts supported on carbon nanotubes. This functionalization process comprised three main steps: (i) covalent functionalization of CNTs by phenyldiazonium salts; (ii) *post*-functionalization of these *f*-CNTs in order to coordinate nanoparticle precursors (molecular clusters) and (iii) thermal activation of these materials to obtain "naked" metallic nanoparticles supported on carbon nanotube surface, NP/CNTs.

The first step was characterized by Raman spectroscopy and XPS. The covalent nature of the bond formed between the nanotube and the grafted diazonium was proven by the increase of the D/G band ratio in the Raman spectra after functionalization. XPS was used to demonstrate the presence of the desired functions on the nanotube surface and determine the functionalization rate. For bulk-SWCNTs, the functionalization rate was 4.2 %, meaning that one carbon atom out of 24 was functionalized. For substrate-deposited SWCNTs, this functionalization rate decreased to 2.7 %, i.e. one carbon atom out of 37 functionalized. The combination of Raman and XPS hence demonstrated significant variation in the functionalization rate depending on the form and/or source of nanotube considered.

The *post*-functionalization process was also monitored by XPS to estimate the content of the various functions present on the nanotube surface.

Finally, the activated NP/CNTs were characterized by XPS, EA as well as SEM and TEM. XPS revealed that significant amounts of phosphorous and nitrogen were still present on the nanotube surface. This observation demonstrated that organic residues coming from the functionalization remained on the nanotube surface. This organic residue is already known to act as stabilizer for the nanoparticles, hence avoiding the leaching of the nanoparticles during the catalysis. M/C ratios of 1.1 mol % and 0.24 % were obtained by XPS and EA, respectively. The significant difference depending on the technique considered was attributed to the high imprecision of the XPS analysis, especially for such low concentrations. Moreover, elemental analysis is also subjected to errors due to the difficulty in solubilizing noble metals for analysis.

According to TEM imaging, the obtained nanoparticles possess a diameter of 1 nm ± 0.3 nm, separated by an average distance of 2.45 nm ± 0.88 nm. This observation allowed estimating that about 290 nanoparticles are present on a 1 μm section of carbon nanotube.

Electrical transport measurements were also performed to study the influence of the NPs on the nanotube electrical properties. This characterization highlighted the presence of a strong p-doping of the nanotube after formation of the nanoparticles. This charge transfer demonstrated the strong interactions between the nanotube and its supported nanoparticles.

In Chapter V, we have demonstrated the catalytic activity of Ru, Pt and Ru-Pt/MWCNTs catalysts for the hydrolytic transformation of dimethylphenylsilane into dimethylphenylsilanol. The reactions were monitored by gas chromatography, which allowed to quantitatively determine the conversion rates, in function of reacting time. This study

highlighted the influence of the nanoparticle composition on the catalytic activity. Bimetallic RuPt nanoparticles supported on carbon nanotubes turned out to be the most efficient catalyst. For this reason, we selected this catalyst composition for the sensing experiments.

Recyclability tests also highlighted catalyst deactivation. A combination of techniques (XPS, TEM, EA, ICP) provided results suggesting that multiple sources lead to this deactivation, i.e. metal leaching, sintering and poisoning.

VII.3.3 Predictions

In the present chapter, CNT-FET of geometry 3 (see Chapter III for a detailed description of these devices) were functionalized to deposit bimetallic RuPt nanoparticles on carbon nanotube surface, according to the process developed in Chapter IV. According to the results obtained in the previous chapters, the following approximate predictions can be made:

❖ Deposition of bimetallic RuPt nanoparticles on SWCNT-FETs with an **average diameter of 1 nm**;

❖ The obtained nanoparticles should be separated by an average distance of 2.45 nm ± 0.88 nm, i.e. about **a thousand of nanoparticles** on a 4 μm section of CNT comprised between two source and drain electrodes.
In addition, it is worth noting that an active site for the catalysis is not a nanoparticle, but a few metallic atoms. The number of active sites is thus expected to be higher than the estimated number of nanoparticles;

❖ These nanoparticles can possibly be partially covered by an **amorphous organic layer** resulting from the thermal

rearrangement of organic ligands, hence decreasing their catalytic activity;

❖ A strong **electrostatic coupling** is expected between the nanoparticles and the CNT;

❖ This material is expected to exhibit a strong **catalytic activity** for the transformation of dimethylphenylsilane in dimethylphenylsilanol;

❖ The catalyst can possibly suffer from **deactivation;**

❖ Given the fact that the experiment carried out in the present chapter will be performed under static conditions, i.e. without stirring the reaction mixture, possible diffusion problem may occur. It is indeed expected that the catalytic reaction is controlled by reagent and/or product diffusion;

❖ The catalytic activity is expected to vary depending on the NPs sizes. For these reasons, we do not expect all the nanoparticles (~ 1000) to be active at the same time.

VII.4 Methodology

To examine the effect of catalytic activity on the nanotube conductance, the CNT-FETs were connected to the real-time, microfluidic measurement setup, as described in the previous section. Devices were immersed in a buffered solution (saline solution of NaH_2PO_4 in water/ethanol), while recording real-time electrical measurements. The gate voltage was set to zero, using an Al wire. All the measurements were recorded in static mode, i.e. in absence of a continuous flow. After 2 minutes, without interrupting the electrical measurements, the buffered solution was replaced by a solution of dimethylphenylsilane of a given

concentration and typically measured for an additional 15 minutes. This operating process allows to easily compare the electrical signal of the nanotube in absence or presence of the dimethylphenylsilane, hence highlighting the effect due to the presence of silane.

In order to study the effect of the silane concentration on the nanotube conductance, the devices were exposed to dimethylphenylsilane solutions of various concentration. In order to limit effects from residual reagents from one experiment to another, the devices were extensively rinsed in the buffered solution before introducing a new solution. All experiments were performed following the process described above, i.e. 2 minutes in buffered solution, followed by 15 minutes in the desired solution. Moreover, the measurements were recorded from the smallest to the highest concentration for the same reason.

VII.5 Results and discussion

VII.5.1 Prior control experiments and selection of the devices for the catalysis experiments

Before carrying out the measurement series, we performed control experiments. These blank experiments demonstrated that in absence of specific nanoparticle-dimethylphenylsilane interactions, there is no current fluctuations over time.

In order to do this, two approaches were considered. First, we studied the effect of the dimethylphenylsilane on non-functionalized CNT-FETs. Pristine CNT-FETs were therefore exposed to dimethylphenylsilane and real-time measurements were recorded. No silane-specific current

fluctuations were recorded at any concentration between 0M and 400 mM and in any pristine device tested.

Second, before exposing the nanoparticle decorated CNT-FETs to the dimethylphenylsilane, we controlled their behavior in absence of the silane reagent. While recording real-time electrical measurements in the buffered solvent without silane, we noticed that a few devices were continuously exhibiting current fluctuations. We speculate that these intrinsic current fluctuations are due to defects in the nanotube being able to interact with the solution, causing current fluctuations. Another hypothesis for these unexpected fluctuations lies in weak CNT-metal contacts, which would result in current variations. These intrinsically fluctuating devices were excluded from the present study. The other non-fluctuating devices were measured in the buffered solvent for more than 1 hour before experiments. For the present study, we only selected the devices stable over the duration of the measurements, i.e. more than 3600 s.

The flowchart depicted in Figure VII.4 illustrates the decision process used for the selection of the devices for catalysis detection experiments.
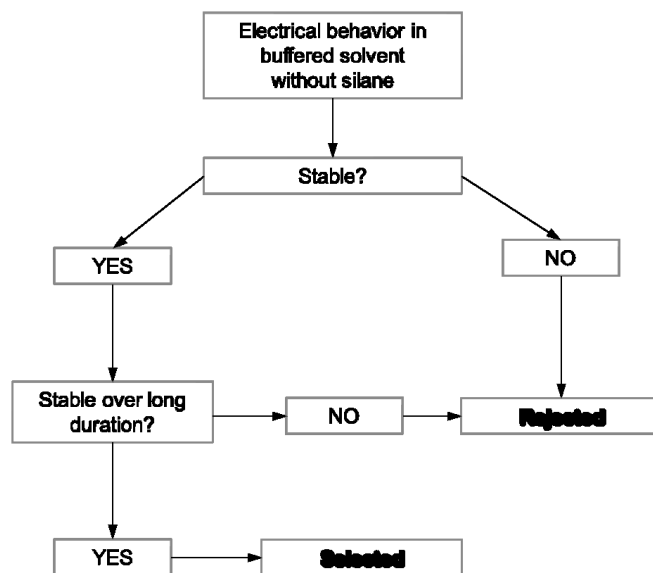
Figure VII.4. Flowchart illustrating the device selection process.

VII.5.2 Effect of the presence of dimethylphenylsilane on the CNT conductance

When measuring CNT conductance in real-time in buffer solution without silane, we observe constant I(t) curves (Figure VII.5 left). After introduction of specific concentrations of dimethylphenylsilane in the flow cell, some devices exhibited fluctuations between two levels of conductance (Figure VII.5). The variation of current, or ΔI(t), of these fluctuations represents about 1.9 - 2.4 % of the baseline current, which is distinguishable from the noise (about 0.3 % of the initial current).

Thanks to the above-described control experiment, we can confidently state that these current fluctuations are due to interactions between dimethylphenylsilane molecules and active sites on the nanoparticles.
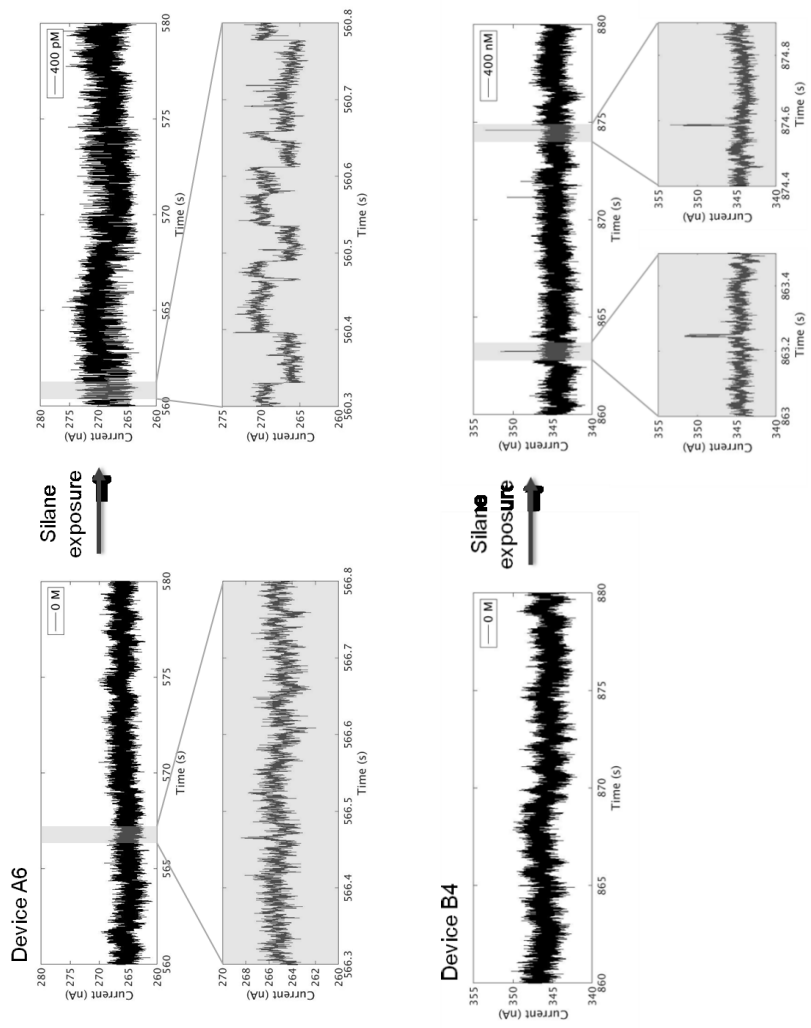
Figure VII.5. *To be continued*
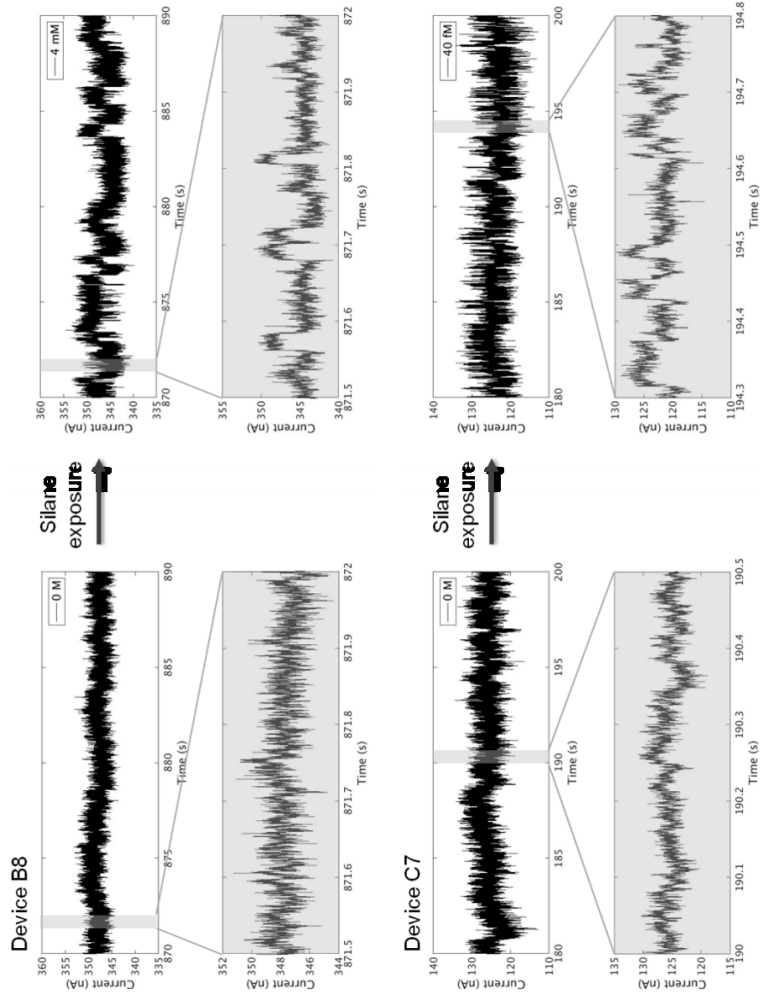
Figure VII.5. Real-time electrical response of four different CNT-FETs when exposed to (left) buffer and (right) dimethylphenylsilane. I(t) curves are shown over 20 s and 0.5 s time intervals (zoom, grey shaded areas). $V_G = 0$ V; $V_{DS} = 100$ mV for devices A6, B8 and C7; $V_{DS} = 50$ mV for device B4.

Among nanoparticle decorated devices, it should be noted that not all devices showed 2-state fluctuations. Two-level current fluctuations were indeed only observed in semiconducting CNT-FETs. This can be explained by the constant non-zero density of states at the Fermi level in metallic CNTs (see Figure II.5b). This makes them insensitive to charge transfer processes. For this reason, we only selected semiconducting devices for these sensing experiments. Furthermore, these two-level fluctuations appeared only in specific concentration ranges, as will be discussed in the next section.

It is worth noting that we only observed two levels of current, whichever the concentration or device considered. Moreover, for each device, the ΔI(t) between the two levels is always of the same value. These observations are suggestive of local modulation due to midgap states created by the functionalization having interactions with the dimethylphenylsilane / nanoparticle. As depicted in Figure VII.6, specific interactions between active sites of the nanoparticles and dimethylphenylsilane molecules and discrete, localized states in the bandgap is considered to explain the behavior. That is, charge transfer at the active site by the dimethylphenylsilane interacts with the midgap states to open and close an alternative pathway for the current to flow across the structure. In this scheme, the current level fluctuation is simply due to a charging-uncharging of the gap states.

According to this hypothesis, the reason why we only observed two levels of current is the fact that the current is allowed either blocked by the nanotube bandgap or flows through the uncharged midgap states. Hence, we do not expect to observe steps in the current, but rather fluctuations

between two discrete current levels. This binary aspect highlights fluctuations between resting phases and interaction phases.
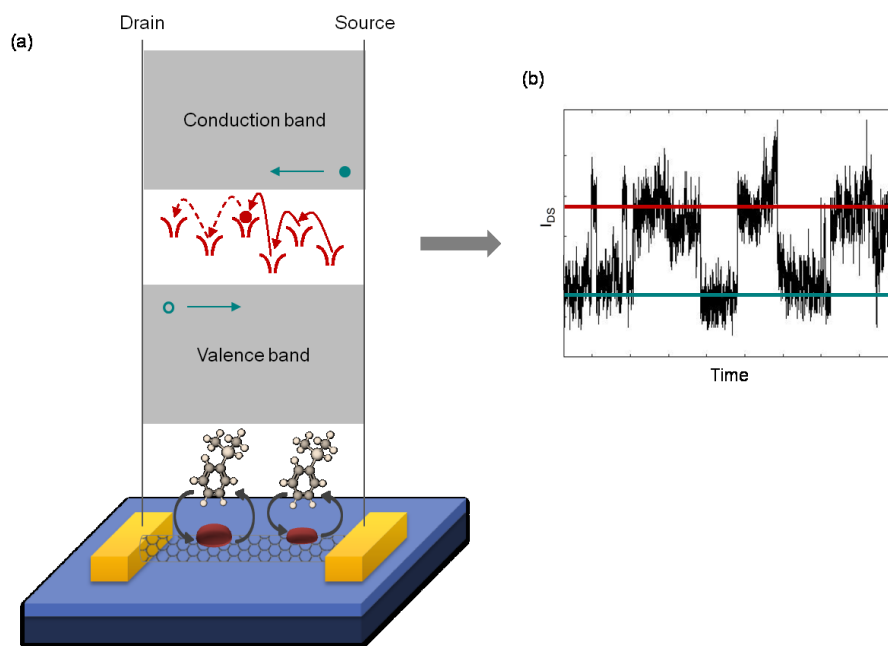
Figure VII.6. Schematic representation of the midgap states-induced two level current fluctuations: (a) formation of midgap states induced by specific interactions between nanoparticles and dimethylphenylsilane molecules and (b) impact of these midgap states on the nanotube conductance. Red line in (b) corresponds to the current flowing through valence or conduction band and blue line corresponds to the current flowing through the midgap states induced by the NP/silane interactions.

VII.5.3 *Two-level fluctuation rate and concentration-dependence*

As shown in Figure VII.5, introduction of dimethylphenylsilane in the flow cell induces the appearance of fluctuations between two levels, at certain concentrations. In order to study the effect of the concentration of dimethylphenylsilane on the current fluctuation, we exposed the devices to various concentrations of dimethylphenylsilane, ranging from 4 aM to 400 mM, by 10-fold steps.

Figures VII.7 and VII.8 show the current evolution of two devices while increasing the silane concentration. As can be seen, slow fluctuations between two current levels appear when introducing a given concentration of silane. When increasing the concentration, these fluctuations become faster and more frequent. They finally disappear when exceeding a certain concentration. The amount of two-level fluctuations in function of the concentration was counted and is plotted in Figure VII.9 for the two devices. As can be seen, we observe a constant increase of the fluctuation frequency, until a threshold concentration, at which the fluctuations entirely disappear.
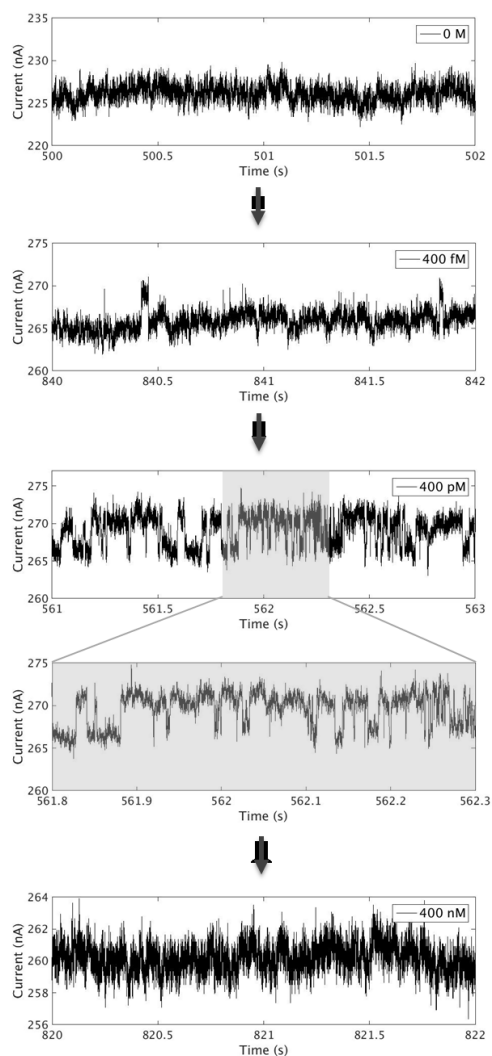
Figure VII.7. Real-time electrical response of device A6 (V_G = 0 V; V_{DS} = 100 mV) upon exposure to dimethylphenylsilane solutions in concentrations of 0 M, 400 fM, 400 pM and 400 nM. I(t) curves are shown over 2 s and 0.5 s time intervals (zoom, grey shaded areas).
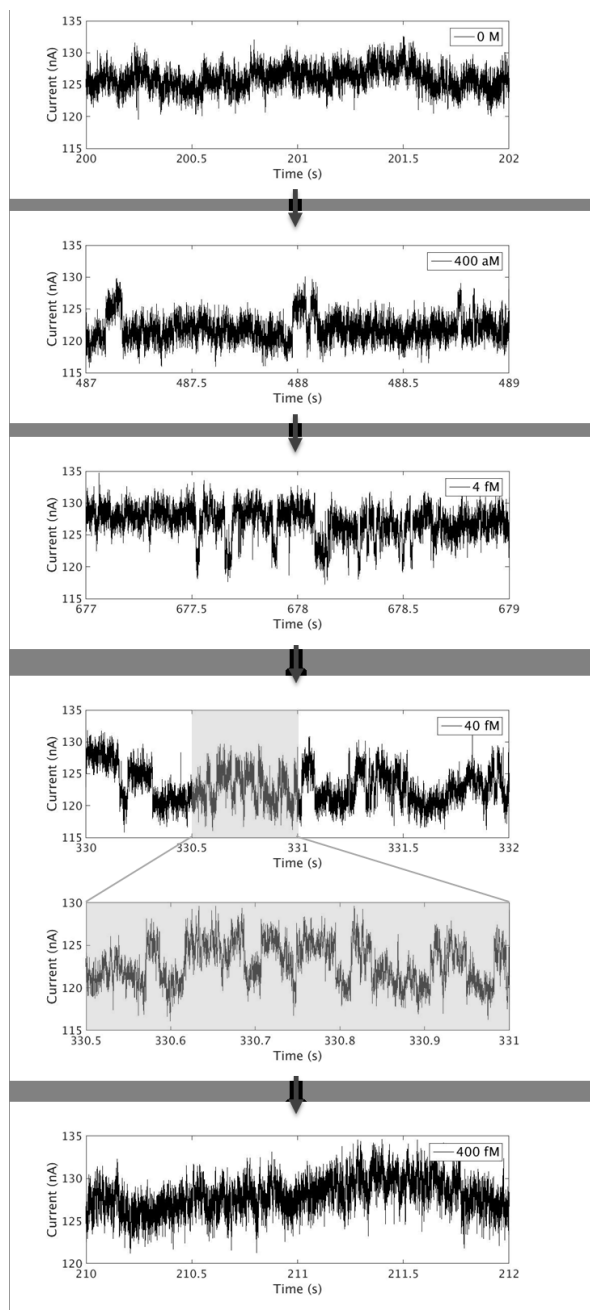
Figure VII.8. Real-time electrical response of device C7 (V_G = 0 V; V_{DS} = 100 mV) upon exposure to dimethylphenylsilane solutions in concentrations of 0 M, 400 aM, 4 fM, 40 fM and 400 fM. I(t) curves are shown over 2 s and 0.5 s time intervals (zoom, grey shaded areas).
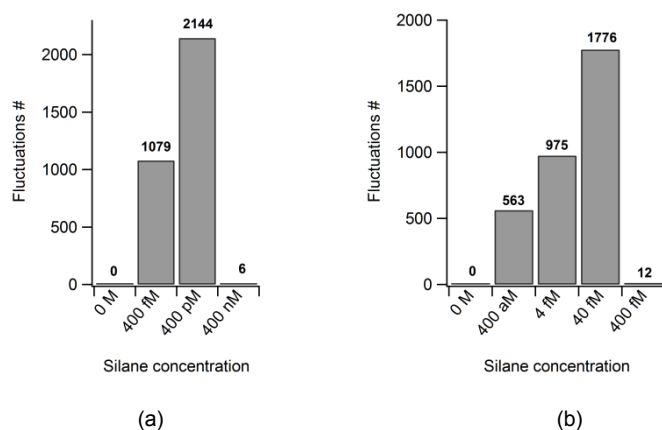
Figure VII.9. Evolution of the fluctuation frequency in function of the dimethylphenylsilane concentration for (a) device A6 and (b) device C7. The number of fluctuations was counted over 15 minutes of recorded data.

The evolution of the fluctuations frequency with the concentration (Figure VII.9) is in agreement with an increase of the likelihood of these interactions with the increasing number of dimethylphenylsilane molecules in the flow cell. As mentioned earlier, there are lower and upper concentration thresholds between which two-state fluctuations are observed. The lower concentration limit is attributed to the minimal amount of silane molecules required in the flow cell to obtain a sufficient likelihood of interactions between silane molecules and active sites. The upper concentration threshold corresponds to the concentration at which there is always at least one silane/active site interaction occurring somewhere on the nanotube. For this reason, the nanotube is constantly in "interaction mode", and two-level fluctuations are not observed anymore.

Figure VII.10 illustrates this concept: when the concentration of silane molecules is too small, the likelihood of interaction is low, and no current fluctuations are detected (Fig. VII.10a). When the silane

concentration reaches the lower concentration threshold, a single interaction is detected (Fig. VII.10b). Such isolated events can be detected thanks to the quasi-1D nature of the nanotube: although the CNT is very long, a single event impacts the whole nanotube. When the silane concentration gradually increases, the number of silane-active site interactions increases (Fig. VII.10c-d). Finally, above an upper concentration threshold, there is always at least one silane-active site interaction, and the nanotube is therefore constantly in "interacting phase" (Fig. VII.10e).
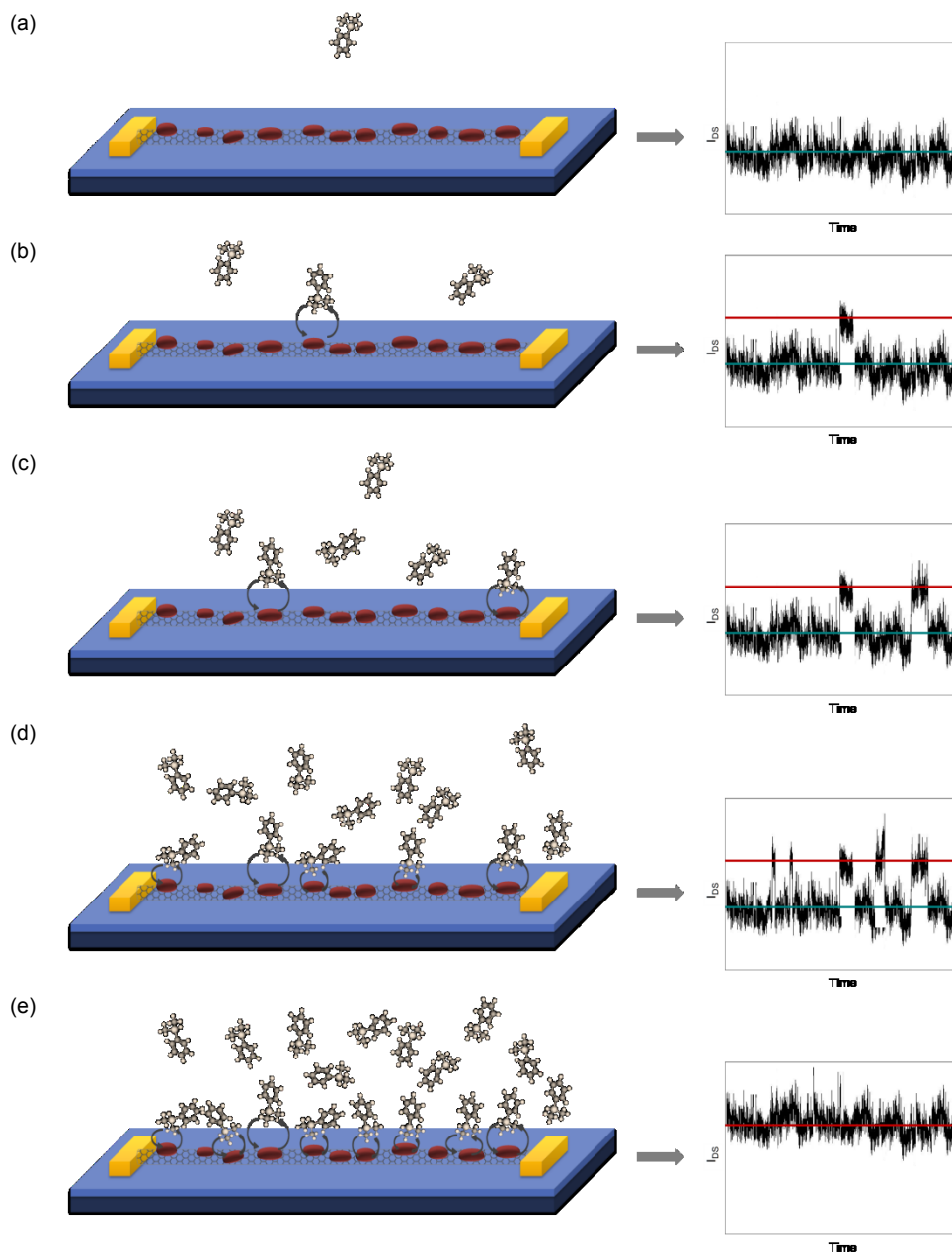
Figure VII.10. Evolution of the CNT conductance when the dimethylphenylsilane concentration is gradually increased to be (a) below the lower concentration threshold; (b) at the lower concentration threshold; (c, d); above the lower concentration threshold and (e) above the upper concentration threshold.

Figure VII.9b reveals the occurrence of more than 500 two-level fluctuations over 15 minutes when device C7 was exposed to a 400 aM silane solution. At this concentration, approximately 1000 dimethylphenylsilane molecules are present in the flow cell. Given the fact that the measurements are operated in static conditions, the likelihood of having interactions between dimethylphenylsilane molecules and catalytic active sites is expected to be significantly limited by diffusion. As a consequence, it seems very unlikely that one out of every two molecules are catalytically transformed. For this reason, all of the fluctuations observed in the real-time electrical experiments cannot be the result of a catalytic transformation. It is thus likely that parts of the fluctuations are due to adsorption and desorption of the silane molecules on the nanoparticles.

As a reminder, the first step of the catalytic transformation of silane into silanols consists in a dissociative adsorption of the silane at the surface of the metal nanoparticle (see Figure V.1). For the reaction to take place, both silane and water molecules need to be adsorbed on the nanoparticle, in close proximity to each other. According to previous studies, the adsorption of water is slow and rate determining.[280,291,292] It can therefore be assumed that the silane could adsorb and desorb from the nanoparticle surface several times without being transformed until water adsorption occurs.

In a similar experiment involving enzymatic reactions, Collins and coworkers were able to distinguish active phases (i.e. catalytic transformation in the present case) and non-active phases (i.e. adsorption/desorption of silane molecules at nanoparticle surface) by the

fluctuation rate.[65,70,71] In a similar way, Figure VII.11 highlights three different phases which can be distinguished based on the fluctuation rate.

A deeper data processing, for each device and each concentration is in progress and should allow assigning these distinct phases to catalytic transformation or chemisorption at the surface of the nanoparticles. In particular, we aim to determine the duration of the current fluctuations in the different phases. This feature (i.e. the duration of the fluctuations) should distinguish adsorption and desorption phenomena from real chemical transformation.

In order to accurately assign these distinct phases (i.e. rapid and slow fluctuations) to chemisorption or chemical transformation, we could vary the temperature. Increasing the temperature would indeed promote the chemical reaction, hence increasing the ratio between chemical transformation and chemisorption phases. By varying the temperature, we should thus be able to clearly determine which fluctuation rate corresponds to the chemical reaction and which fluctuation rate corresponds to chemisorption phenomena.
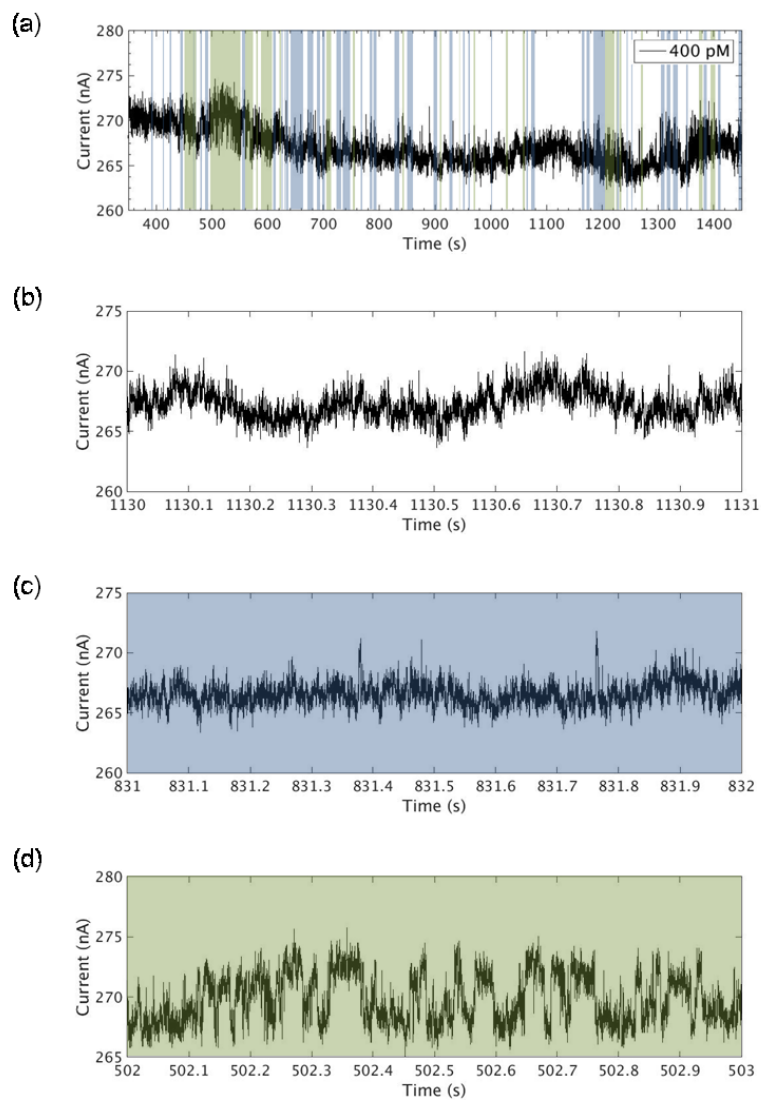
Figure VII.11. Real-time electrical response of device A6 ($V_G = 0$ V; $V_{DS} = 100$ mV) upon exposure to a 400 pM dimethylphenylsilane solution: (a) long duration (15 min) electrical measurements highlighting the variation of the fluctuation rate over time; (b) short-time (1 s) electrical measurements in inactive phase; (c, blue) short-time (1 s) electrical measurements in slow two-level fluctuation phase and (d, green) electrical measurements in fast two-level fluctuation phase.

Another interesting experiment consists in replacing the dimethylphenylsilane by another silane, which could not be transformed in silanol, such as the trimethylphenylsilane. This silane indeed comprises four organic substituents, and the absence of Si−H bond prevents this compound from being transformed into silanol in the presence of water (Figure VII.12). By replacing the dimethylphenylsilane by trimethylphenylsilane, we expect to only observe adsorption and desorption phenomena but no reaction.

Figure VII.12. Envisioned control experiment with trimethylphenylsilane, which cannot be catalytically transformed into silanol, due to the absence of Si-H bond.

However, in practice, the catalyst rapidly deactivates, and we are therefore limited in the number of experiments that can be carried out using the same devices. A more detailed discussion about this deactivation process will be given in a dedicated section (VII.5.5).

VII.5.4 Origin of the two-level fluctuations

As we pointed out earlier, the appearance of two-level fluctuations is dependent on the silane concentration. As can be seen when comparing Figures VII.7 and VII.8 and Figures VII.9a and VII.9b, the lower and upper concentration thresholds vary from device to device. This could probably be related to the number of catalytic active sites on each nanotube.

In our system, it is difficult to determine this number of catalytic sites, since it depends mainly on the amount and size of the nanoparticles. According to the TEM images of RuPt nanoparticles supported on bulk SWCNTs (see Chapter IV, Fig IV.12), a 4 μm section of a SWCNT between source and drain is expected to exhibit about one thousand nanoparticles. We used AFM to image the CNT-FET supported nanoparticles. According to this technique, about 10-15 particles are present on the CNT surface. However, AFM has a limited resolution of about 10 nm and is thus not really appropriate to probe smaller nanoparticles of diameter size around 1 nm, as revealed by TEM (Figure IV.12) on bulk catalysts. We hence postulate that there is a higher number of nanoparticles, with a range of size dispersion. Since the catalytic activity is known to be dependent on the nanoparticle size,[235,349–351] the dispersion of nanoparticle sizes is also expected to induce device to device variation of the catalytic activity. Finally, as evidenced in Chapters IV and V, the nanoparticles can be partially covered by a residual organic layer, resulting from the thermal annealing. Their catalytic activities can therefore be hampered by this layer, which may be different for each nanoparticle.

The number of silane molecules, on the other side, can be easily estimated knowing the volume of the flow cell. The lowest concentration (4 aM) hence corresponds to the presence of about 10 molecules in the flow cell, while the highest concentrated solution (400 mM, nearly saturated solution) corresponds to about 10^{18} molecules in the flow cell.

Given the fact that the measurements are operated in static conditions, we can expect that a high amount of dimethylphenylsilane

molecules ($\geq$ 1000) is required to obtain a sufficient likelihood of interactions between silane molecules and nanoparticle active sites.

In device A6, current fluctuations appear at 400 fM. This concentration corresponds to the presence of approximately 10^6 dimethylphenylsilane molecules in the flow cell. In device C7, this lower concentration threshold is at 400 aM, or 10^3 dimethylphenylsilane molecules in the flow cell. This variation can partially be attributed to the varying number of active sites in each device, and the size-dependant difference of reactivity of the nanoparticles as discussed earlier. Another explanation lies in the fact that the data shown in Figure VII.8 for device C7 were the first experiments performed with this device, while the data reported for device A6 (Figure VII.7) corresponds to the fourth run of experiments. In a general way, we observed a shift of the threshold concentrations towards bigger values when reproducing the results over time with the same device. This shift is attributed to nanoparticle deactivation as will be discussed in the next section.

VII.5.5 Deactivation of the catalytic sites

During the experiments, we observed that the dimethylphenylsilane concentration range at which the devices exhibit current fluctuations increased over time. After multiple experiment runs, the fluctuations even entirely disappeared. This observation can be explained by catalyst deactivation. If the catalyst partially deactivates, the number of active sites available for the catalytic reaction indeed decreases over time. As a consequence, the likelihood of having interactions between the silane molecules and the nanoparticles decreases. In order to obtain a sufficient

interaction likelihood, it is thus necessary to increase the concentration of dimethylphenylsilane in the flow cell to counteract the deactivation.

Figure VII.13 illustrates this concept: at the very first experiment, the amount of active sites is quite high and really low concentrations are required to be able to detect interactions between silane molecules and available active sites (Figure VII.13 top). As the experiments progress, the catalyst undergoes partial deactivation. Since the amount of active sites decreases, the concentration required to observe current fluctuations progressively increases (Figure VII.13 bottom).
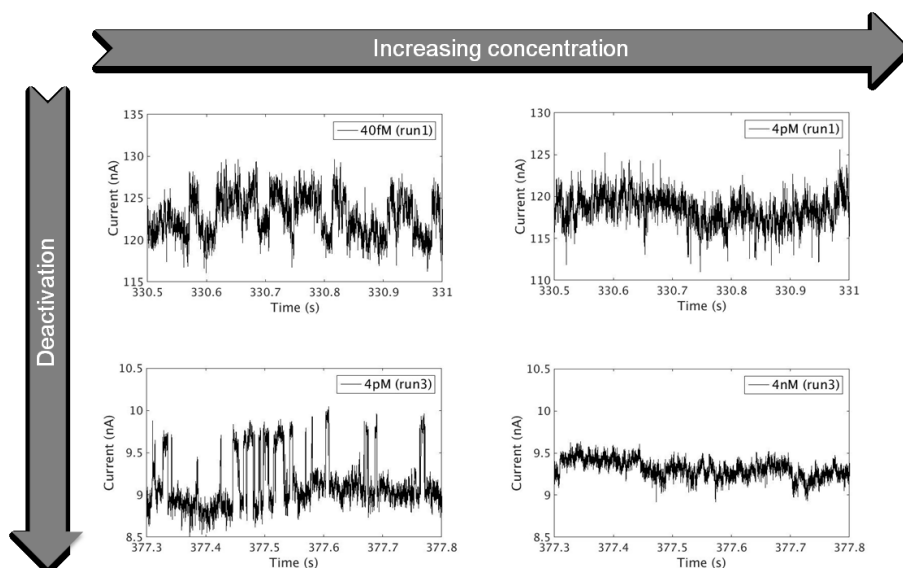
Figure VII.13. Evolution of the electrical response of device C7 (V_G = 0 V; V_{DS} = 100 mV) with the dimethylphenylsilane concentration and catalyst deactivation: (top) first run of experiments, (bottom) third run of experiments. I(t) curves are shown over 0.5 s time intervals.
Note: The sharp decrease of current between runs 1 and 3 occurred after the devices were thoroughly rinsed in hot solvent, in order to desorb residual reagents and/or products.

As a reminder, we already observed deactivation processes in the bulk catalysis experiments described in Chapter V. Different sources of deactivation were evidenced: sintering of the nanoparticles, Pt leaching and poisoning of the nanoparticle surface by sodium. During the real-time electrical measurement experiments, the devices were exposed for several days to sodium-containing electrolyte solution. This point, together with the fact that the experiments are performed in ambient and static conditions, allows assuming that sodium poisoning constitutes the major source of deactivation in the present case.

In order to confirm this hypothesis, the chip was removed from the experimental setup, extensively rinsed and thermally annealed under inert atmosphere. The annealing was expected to remove poisoning species adsorbed on the nanoparticle surface. After this procedure, the chip was reconnected and we were again able to observe two-level fluctuations at low silane concentration. This result confirms that the nanoparticles underwent surface poisoning, which results in a decrease of activity.

Knowing this, it would be preferable to use monometallic Ru nanoparticles decorated CNT-FETs instead of bimetallic RuPt/CNT-FETs in these real-time experiments, since we demonstrated in Chapter V that monometallic Ru/CNTs is less likely to deactivate.

VII.6 Conclusion

In this chapter, we demonstrate for the first time the possible use of carbon nanotube-based sensors for the *in situ* detection of catalytic activity. In order to do this, Ru-Pt bimetallic nanoparticles were deposited on individual SWCNT-FETs following the monovalent functionalization

pathway developed in Chapter IV. The catalytic activity of these materials for the transformation of dimethylphenylsilane in dimethylphenylsilanol was investigated through real-time electrical measurements.

These measurements highlighted the apparition of two-level fluctuations when the devices were exposed to dimethylphenylsilane. These current fluctuations were attributed to the formation of midgap states induced by interactions between dimethylphenylsilane molecules and active sites of the nanoparticles.

We also evidenced a strong dependence of these fluctuations on the silane concentration. Each device indeed exhibits lower and upper concentration thresholds between which two-state fluctuations are observed. These concentration limits were related to the number of available active sites in the concerned devices and therefore differed from device to device.

Long-duration real-time electrical measurements allowed to evidence the presence of various two-level fluctuation rates, allowing to distinguish two different phases attributed to catalytic transformation or adsorption of dimethylphenylsilane molecules on nanoparticle surface.

Finally, these electrical measurements confirmed the presence of catalyst deactivation process, as already evidenced in Chapter V. This deactivation resulted in an increase of the minimal concentration required to observe two-level fluctuations.

Main results of Chapter VII

- ❖ *First detection of catalytic transformation with carbon nanotube-based sensors through real-time electrical measurements*

❖ Detection of *two-level current fluctuations* attributed to interactions between reagent and catalytic active sites

❖ Study of the *current fluctuations dependence on the reagent concentration*

❖ Evidence of *various current fluctuation rates related to true chemical transformation or reagent chemisorption*

❖ *Observation of catalyst deactivation* through electrical measurements

VII.7 Perspectives

This chapter gives the proof of concept that it is possible to use carbon nanotubes to probe catalytic transformations in real-time. The observations reported in this chapter are extremely encouraging and pave the way for further investigations in this field.

Among the numerous perspectives arising from the present work, the following points should be considered in order to get a better understanding of the mechanism involved in the electrical detection of catalytic activity.

First, the present study highlighted the presence of a reagent concentration range in which we were able to detect two-level current fluctuations. Ideally, to get a better understanding of the electrical response induced by catalysis, it would be interesting to have only one silane molecule interacting with a single active site. In order to do this, the functionalization process should be performed in pre-patterned nanowells to obtain a single active site at the surface of the nanotube. This approach,

developed by D. Bouilly,[204] consists in protecting the nanotube by a thin polymer layer (PMMA) and exposing only lithographically-patterned nanowells to the functionalization. By modulating the nanowell width, we can obtain point-functionalization, and thus get devices exhibiting single molecular clusters for subsequent real-time experiments.

Second, the results presented above confirmed the presence of catalyst deactivation processes. This deactivation is a source of concern since it shifts the concentration range at which current fluctuations are observed, and thus decreases the reproducibility of the results. In Chapter V, we already observed the presence of such deactivation processes, and highlighted that Ru catalyst underwent only a negligible deactivation, compared to Ru-Pt and Pt catalysts. For this reason, we should consider using monometallic Ru nanoparticles decorated SWCNT-FETs for these measurements. Moreover, as already evidenced in Chapter V and confirmed in this last Chapter, one major source of deactivation comes from the sodium buffer used in the reaction. It seems therefore useful for the future to modify the nature of the buffer compound, to avoid catalyst poisoning by sodium.

Finally, it would be interesting to study the influence of the gate voltage on the catalysis. Applying a voltage to the electrolyte gate would indeed involves a doping of the nanotube. This doping would increase or decrease its ability to give electrons to the metal nanoparticle for the catalytic reaction. However, in the experimental setup used for this study, the electrolyte gate is made of an Al wire inserted in the inlet capillary. This electrode is hence at a considerable distance from the nanotube, which limits the efficiency of the gating. As a consequence, it would be advantageous to pattern Al wire directly on the chip by lithography.

Experimental section

Instrumentals

A complete instrumental section can be found in Annex IX.1.

Materials

SWCNTs used in this chapter were prepared with flow-aligned CVD-growth. See Chapter III and Annex IX.4.1 for more experimental details.

Individual SWCNT-FETs fabrication

Individual SWCNT-FETs were prepared according to the fabrication process described for Geometry 3. See Chapter III and Annex IX.4.1 for further details.

Synthetic procedures

SWCNT-FETs functionalization

SWCNT-FETs were functionalized according to the procedure described in Chapter IV .

Preparation of the dimethylphenylsilane solution

Buffer solution. 32 ml of a $NaH_2PO_4.H_2O$ buffer solution[vi] were diluted in 168 ml of ethanol.

Dimethylphenylsilane solutions. A stock solution of 400 mM dimethylphenylsilane was prepared by dissolving 4 mmol of

---

[vi] $NaH_2PO_4.H_2O$ buffer solution contains 65 mg of $NaH_2PO_4.H_2O$ and 39.8 ml of 0.1 M NaOH solution per liter.

dimethylphenylsilane in 10 ml of the buffer solution. Other solutions of various dimethylphenylsilane concentrations were prepared by successively diluting this stock solution by a factor 10.

CHAPTER VIII - CONCLUSION AND PERSPECTIVES

VIII.1 Summary of the scientific contributions of the thesis

In this thesis, we aimed to use carbon nanotubes as sensors to detect catalytic activity in real-time. In order to do this, we prepared catalysts supported on carbon nanotubes thanks to an appropriate functionalization pathway. These catalytic materials were integrated into electronic devices and real-time electrical measurements were recorded while exposing them to a specific reagent. These time-resolved measurements allowed to probe catalytic activity through modification of the nanotube electrical conductivity.

In practice, the achievements of this thesis can be split into three distinct parts:

a) Functionalization

We developed two functionalization methods for the preparation of heterogeneous and homogeneous supported catalysts. First, we developed a **monovalent functionalization** pathway for the preparation of heterogeneous supported catalysts. In order to do this, CNTs were functionalized by diazonium salts. These grafted moieties were then used

as anchoring point for the coordination of metallic clusters. A thermal activation was then performed to allow the formation of metallic nanoparticles deposited on the nanotube surface. Two different approaches were considered, i.e. bulk or substrate-deposited SWCNTs in order to prove the success of the functionalization for both bulk CNTs and supported CNTs for subsequent device experiments. These two approaches exhibited similar reactivity towards the functionalization.

Second, homogeneous supported catalysts were prepared by a **divalent functionalization** process. In practice, we used Bingel-Hirsch reaction to covalently anchor malonate compounds on the nanotube sidewalls. Pd(0) complexes were then coordinated to these functionalized CNTs.

These two functionalization methods were monitored by a combination of characterization techniques such as XPS, Raman spectroscopy, TGA, elemental analysis and electron microscopy. The materials were also electrically characterized at each step of the catalyst preparation in order to study the influence of the functionalization process on the nanotube conductivity. In particular, these electrical measurements revealed important differences between the two considered functionalization pathways.

On one hand, monovalent functionalization of the nanotube induced a significant decrease of its electrical conductivity. This observation resulted from the rehybridization of sp^2 carbon atoms of the nanotube into sp^3 after the monovalent functionalization. The nanotube initial conductivity was however almost totally recovered after the thermal annealing process, which is known to partially remove the nanotube defects. Finally, the electrical measurements revealed the presence of a

250

strong electron transfer between the carbon nanotube and its supported nanoparticles. This result evidenced the strong interaction between the CNT and the nanoparticles, which is of particular interest for the purpose of catalytic applications involving electron transfer mechanisms.

On the other hand, electrical transport measurements highlighted the preservation of the nanotube conductivity when using the divalent functionalization. This phenomenon was attributed to the adoption of an open configuration, preserving the sp^2 hybridization, responsible for the nanotube electrical conductivity.

Finally, by using a combination of analytical characterization techniques and electrical measurements, we demonstrated in this thesis the possibility of using carbon nanotubes as a probe to monitor multi-steps chemical reactions.

b) Catalysis

A second part of this thesis dealt with the catalytic applications of the prepared catalysts. Monometallic (Ru, Pt) and bimetallic (Ru-Pt) **heterogeneous supported catalysts**, prepared following the monovalent functionalization method developed above, were tested for the catalytic transformation of dimethylphenylsilane into dimethylphenylsilanol with water. The catalytic tests highlighted a strong influence of the nature of the constitutive metals within the nanoparticle on the catalytic activity. Interestingly, bimetallic Ru-Pt catalyst turned out to be the most efficient catalyst, highlighting the presence of a synergetic effect between the two constitutive metals. However, recyclability tests revealed a partial loss of activity over time for Pt-based catalysts. This activity decrease was

attributed to a combination of several deactivation processes, i.e. sintering, poisoning and leaching.

Second, we demonstrated that Pd(0)-based **homogeneous supported catalysts**, prepared following the divalent functionalization method described above, are active for the well-known Suzuki-Miyaura cross-coupling reaction between 4-iodotoluene and phenylboronic acid.

c) *Real-time detection of catalytic activity*

Finally, the third part of this thesis was devoted to the *in situ* detection of catalytic activity by means of real-time electrical measurements. In order to do this, the electrical conductivity of nanoparticle-decorated SWCNT-FETs was measured in real-time when exposing the devices to a specific reagent. Thanks to these measurements, we highlighted the apparition of two-level fluctuations. Thanks to appropriate blank experiments, we were able to firmly attribute these current fluctuations to interactions between reagent molecules and active sites of the nanoparticles. The recorded real-time electrical measurements are consistent with a catalytic mechanism involving midgap states offering an alternative pathway for the current to flow. This explains why the current only fluctuates between two levels: (i) the current can be ensured by holes flowing in the valence band (current level 1); or (ii) by charge carriers flowing through the midgap states (current level 2).

These two state-fluctuations appeared to be strongly dependent on the reagent concentration. This concentration effect was attributed to the concentration-related likelihood of having interactions between a reagent molecule and a nanoparticle active site.

Moreover, we evidenced the presence of various fluctuation rates, which are related to alternating catalytic transformation and reagent adsorption phases.

Finally, these sensing experiments confirmed that the catalysts underwent some deactivation, as already evidenced in bulk catalysis.

These results demonstrated the consistency and complementarity of gas chromatography and real-time electrical measurements for the monitoring of catalytic activity. While GC allowed to determine quantitative conversion yields at given reaction time, electrical measurements allowed to qualitatively probe the catalysis dynamics in real-time, towards a better comprehension of the catalytic mechanism.

VIII.2 Concluding remarks and perspectives

In this thesis, we investigated two very distinct approaches for catalytic applications of carbon nanotubes.

On one hand, "bulk catalysis" was studied by using carbon nanotube supported catalysts for given reactions. The reactions were monitored by gas chromatography, a characterization technique commonly used for the determination of conversion yields in catalysis. In this approach, carbon nanotubes are used as support materials for the catalytic active sites. This allows an easy recovering of the catalyst at the end of the reaction. Carbon nanotubes possess high specific surface area, mesoporosity, high mechanical stability and chemical inertia, which makes them ideal supports in catalysis, as shown by the number of publications in this field.[79,80,82,352,353] However, as mentioned at the beginning of this

manuscript, carbon nanotubes exhibit unique properties, and their use as catalyst support does not fully exploit all the potential of these materials.

On the other hand, we developed in this thesis a new application of carbon nanotubes in catalysis, through sensing experiments for the detection of catalytic activity. In this approach, carbon nanotubes were used as sensors, in addition to their role of catalyst support. The sensing component of this second approach relies on the electrical properties of carbon nanotubes. We indeed show that the interactions between reagent molecules and catalytic active sites supported on CNTs induce current fluctuations in the nanotube itself, thanks to an electrostatic coupling of the active sites and the nanotube.

Although this innovative approach is still in its early stages, it seems very promising. As a consequence, it opens the doors to many perspectives. Among the numerous perspectives arising from the present work, the following points should be considered, in order to improve our understanding of catalytic activity:

- **Avoid catalyst deactivation**
  - In order to do this, we could use monometallic Ru/CNTs catalysts, which were highlighted in this thesis as being more recyclable than the bimetallic Ru-Pt catalysts;

  - Another solution consists in replacing the sodium-containing buffer by another buffer solution, since sodium was highlighted as an important source of catalyst poisoning.

254

- **Single-molecule measurements**

  In order to get a better understanding of the electrical response induced by specific silane-active site interactions, it would be interesting to have only one silane molecule interacting with a single active site. In order to do this, an appropriate lithographic approach can be used to perform the functionalization on a very small area of the nanotube, in order to obtain a single-point functionalization.

- **Distinction between adsorption/desorption phenomena and real chemical transformations**

  In order to be able to firmly distinguish adsorption/desorption phenomena from real catalytic transformation, it would be interesting to perform control experiments. Especially, in the context of this thesis, the use of trimethylphenylsilane was suggested.

- **Application to other reactions**

  We investigated so far the real-time electrical detection of catalytic activity for one selected catalytic reaction, namely the hydrolytic transformation of dimethylphenylsilane in dimethylphenylsilanol. Nevertheless, our approach is versatile and should be able to detect other catalytic reactions. Among them, we could apply this sensing experiment to the detection of catalytic activity for the Suzuki-Miyaura cross-coupling reaction, thanks to the catalyst preparation process developed in Chapter VI.

- **Modulation of the catalytic yield by doping the nanotube**

  By modifying the gate voltage, we are able to positively or negatively dope the nanotube. Such a modulation of the ability of the nanotube to give or take electrons should allow facilitating or disfavoring the catalytic reaction on the nanoparticles surface.

  This perspective should also be considered on a more general level. We could indeed fabricate electronic devices based on networks of carbon nanotube supported catalysts. By modifying the charge carriers density in the nanotube, we should be able to modulate the catalytic activity of the supported catalysts. This could yield to a substantial improvement of the catalytic yield.

CHAPTER IX - ANNEXES

IX.1 Instrumentals

IX.1.1 X-ray photoelectron spectroscopy (XPS)

XPS analyses were carried out at room temperature with a SSI-X-probe (SSX 100/206) photoelectron spectrometer from Surface Science Instruments (USA) equipped with a monochromatized microfocus Al X-ray source. The samples were held in place on small sample holders with double-sided adhesive tape and then placed on an insulating home-made ceramic carousel (Macor®, Switzerland). Charge effects were avoided by placing a nickel grid above the samples and using a flood gun set at 8 eV. The energy scale was calibrated with reference to the Au 4f7/2 peak at 84 eV and the binding energies were calculated with respect to the C-(C,H) component of the C 1s peak fixed at 284.8 eV. Data treatment was performed with the CasaXPS program (Casa Software Ltd., UK). The peaks were decomposed into a sum of Gaussian/Lorentzian (85/15) after subtraction of a Shirley type baseline.

This instrument has the following limitations:

Detection limit: 0.1 %

Quantification error: ± 0.3 %

Peak position error: ± 0.3 eV

IX.1.2 Thermogravimetric analysis (TGA)

Thermograms were recorded on a TGA/SDTA 851^e simultaneous DSC-TGA instrument from Mettler Toledo. These analyses were carried out with a heating ramp of 10 °C/min under N_2 flow (100 ml/min) with the samples (3 – 5 mg) placed into alumina containers.

IX.1.3 Raman spectroscopy

Two different Raman spectrometer were used, depending on the sample form.
Raman spectra of bulk SWCNTs were recorded on a Bruker RFS 100/S FT-Raman spectrometer equipped with a 1064 nm laser.
Raman spectra of substrate-deposited SWCNTs were collected using a Renishaw RM3000 spectrometer using a 514 nm laser.

IX.1.4 Gas chromatography (GC)

GC chromatograms were recorded on a GC trace, Finnigan Mat equipped with an AS-3000 Autosampler (FID detector). The GC column is a Chirasil-Dex CB (Agilent - 30 m x 25 mm x 0.25 µm). Helium was used as gas vector (1.2 ml/min), 0.1 µl of solution was injected in the column.

IX.1.5 Nuclear magnetic resonance (NMR)

NMR spectra were recorded on Brucker spectrometers (300 MHz). Chemical shifts are reported in δ ppm from tetramethylsilane with the solvent resonance as the internal standard.

IX.1.6 Elemental analysis (EA)

Bulk elemental analyses were performed by the independent company Medac Ltd. in UK.

IX.1.7 Mass spectrometry (MS)

HRMS were recorded on a Q-Ectractive orbitrap from ThermoFisher. Samples were ionized by ESI.

IX.1.8 Scanning electron microscopy (SEM)

SEM was carried out using a Hitachi S-4700 high-resolution cold-field emission scanning electron microscope.

IX.1.9 Transmission electron microscopy (TEM)

TEM images were acquired with a LEO 922 transmission electron microscope equipped with an OMEGA energy filter. The samples were suspended in hexane and then drop casted on a holey carbon film supported on a copper grid.

Particle size distribution was determined by measuring the length of 100 particles with *Image J*® software.

IX.1.10 Optical lithography

Electrode patterns of electronic devices were defined by optical lithography using a Karl Suss MA-4 and MA-6 mask aligners.

IX.1.11 Electron beam lithography

Electrode patterns of electronic devices of Geometry 1 were defined by e-beam lithography using a Nanobeam nB4 electron beam lithography system.

IX.1.12 Electron beam evaporation

Metal electrodes of electronic devices of Geometry 1 were deposited by e-beam evaporation using a Boc Edwards Auto 306 electron beam evaporator system.

Metal electrodes of electronic devices of Geometry 2 and 3 were deposited by e-beam evaporation using an Angstrom EvoVac Deposition system.

IX.1.13 Reactive ion etching (RIE)

Reactive ion etching was performed using an oxygen plasma (10 sccm O_2, 125 mTorr, 100 W) during 1 minute, using a Technics Serie 800 RIE (Oxygen Plasma Asher).

IX.1.14 Current-voltage measurements

The transfer measurements of SWCNT-FETs in geometry 1 were performed with an ambient probe station using tungsten probes at room temperature. Current and voltage data were acquired using and Agilent B1500A semiconductor parameter analyzer.

The transfer measurements of SWCNT-FETs in geometry 2 and 3 were performed with an autoprobe station (Cascade Microtech RF-1) using tungsten probes at room temperature. Current and voltage data were acquired using and Agilent 4155C semiconductor parameter analyzer.

IX.1.15 Atomic force microscopy (AFM)

Different atomic force microscopes were used, depending on the location. Each AFM images were obtained using tapping mode.

AFM images of functionalized divalent SWCNT-FETs were recorded using a Digital Instruments Nanoscope V (Université catholique de Louvain, Belgium).

AFM images of sensing experiment devices were recorded using VEECO AFM, equipped with Nanoscope IIIa software (Columbia University, NY, USA).

Other AFM images were recorded by using a Di Dimension 3100 AFM (Université de Montréal, QC, Canada).

IX.2 Spectral data

IX.2.1 Cluster synthesis

	IR – ν_{CO} (cm^{-1})		Ref.
	Experimental	**Literature**	
[Ru$_6$C(CO)$_{17}$]	2067 (s)	2067 (s)	354
	2047 (s)	2047 (s)	
	2002 (w)	2002 (w)	
	1838 (w)	1838 (w)	
[Ru$_5$C(CO)$_{15}$]	2068 (s)	2067 (s)	275
	2034 (s)	2034 (m)	
	2017 (w)	2015 (w)	
(PPN)$_2$[Ru$_5$C(CO)$_{14}$]	2030 (w)	2031 (w)	276
	1973 (vs)	1974 (vs)	
	1962 (s)	1972 (s)	
	1916 (m)	1915 (m)	
	1749 (w)	1747 (w)	
[Ru$_5$PtC(CO)$_{14}$(COD)]	2077 (m)	2077 (m)	276
	2050 (s)	2049 (s)	
	2033 (s)	2033 (s)	
	2011 (s)	2011 (s)	
	1989 (w)	1989 (w)	
	1965 (w)	1965 (w)	
	1818 (w)	1818 (w)	

IX.2.2 Bis(2-bromoethyl)malonate
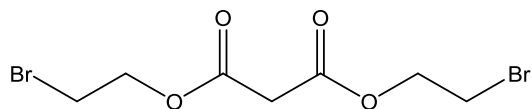
¹H-NMR

¹H-NMR (300 MHz, CDCl$_3$): δ = 4.47 (t, J = 6.12 Hz, 4H, O-CH$_2$); δ = 3.53 (t, J = 6.12 Hz, 4H, CH$_2$-Br); δ = 3.47 (s, 2H, CH$_2$-CO).
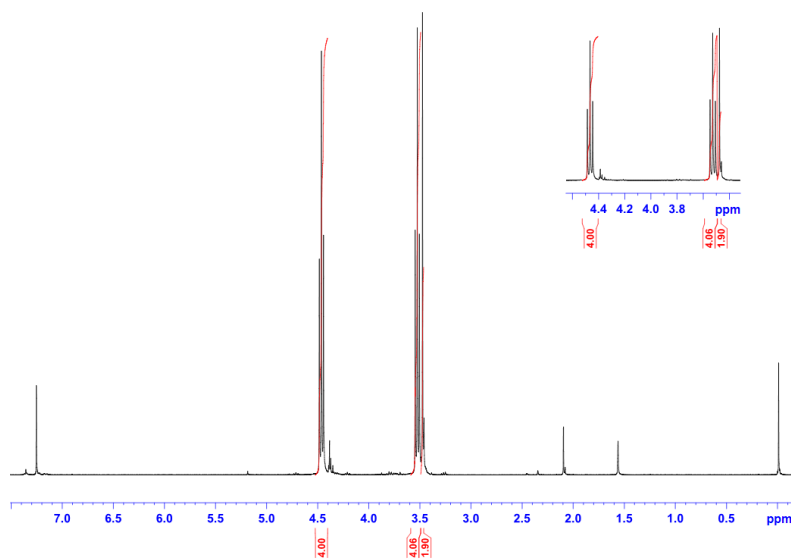
^{13}C-NMR

^{13}C-NMR (300 MHz, CDCl$_3$): δ = 165.9 (C=O); δ = 64.9 (CH$_2$-O); δ = 41.2 (CH$_2$); δ = 28.2 (CH$_2$-Br).
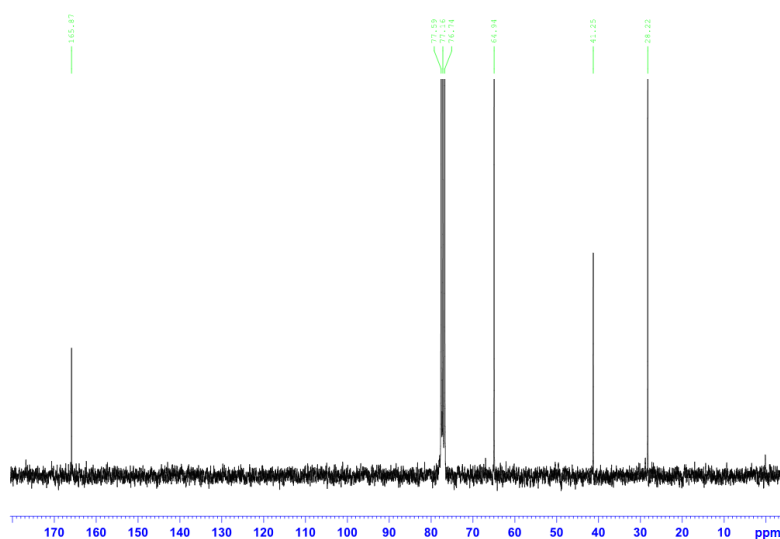
HR-MS

HRMS (ESI): m/z calculated for C$_7$H$_{11}$O$_4$^{79}Br$_2$: 316.90186, measured: 316.90216

```
Spectral Fit: 100.00
Max dM: 5.00[Ppm]  max dI 20.00%  Threshold 0.04
   Mass      Intensity[%]   dM[Ppm]    dI[%]     Fit[%]   Contrib[%]
 316.90186     51.4          0.95      -1.03     100.00    100.00
 317.90525      4.0          0.79      -0.28     100.00    100.00
 318.89981    100.0          0.48       0.00     100.00    100.00
 319.90321      7.8          0.81      -0.38     100.00    100.00
 320.89777     48.6          0.52      -0.62     100.00    100.00
 321.90116      3.8          0.52      -0.21     100.00    100.00
 322.90246      0.5          0.26      -0.24     100.00    100.00
```

Mass	Intensity	Intensity[%]	Resolution
316.90216	133439128	25	59988

Mass	Composition	Fit
316.90186	C$_7$ H$_{11}$ O$_4$ ^{79}Br$_2$	100.00

IX.2.3 Bis(prop-2-ynil)malonate

^{1}H-NMR

^{1}H-NMR (300 MHz, CDCl$_3$): δ = 4.76 (d, J = 2.46 Hz, 4H, 2 CH$_2$); δ = 3.49 (s, 2H, CH$_2$); δ = 2.51 (t, J = 2.43 Hz, 2H, C≡C-H).

^{13}C-NMR

^{13}C-NMR (300 MHz, CDCl$_3$): δ = 165.4 (*C*=O); δ = 77.0 (HC≡*C*CH$_2$); δ = 75.7 (H*C*≡C); δ = 53.2 (HC≡C*C*H$_2$); δ = 41.0 (C(=O)*C*H$_2$C(=O));

HR-MS

HRMS (ESI): m/z calculated for C$_9$H$_9$O$_4$: 181.04954, measured: 181.04958.

```
Spectral Fit: 100.00
Max dM: 3.00[Ppm]  max dI 10.00%  Threshold 0.02
  Mass       Intensity[%]    dM[Ppm]    dI[%]     Fit[%]   Contrib[%]
181.04954    100.0            0.25       0.00     100.00    100.00
182.05290      9.8            0.88       0.05     100.00    100.00
183.05387      0.8           -0.15      -0.27     100.00    100.00
184.05716      0.1            0.76      -0.07     100.00    100.00
```

Mass	Intensity	Intensity[%]	Resolution
181.04958	149482880	11	76636

Mass	Composition	Fit
181.04954	C$_9$ H$_9$ O$_4$	100.00

IX.3 Annexes related to Chapter II

IX.3.1 Kataura Plot and Raman spectroscopy
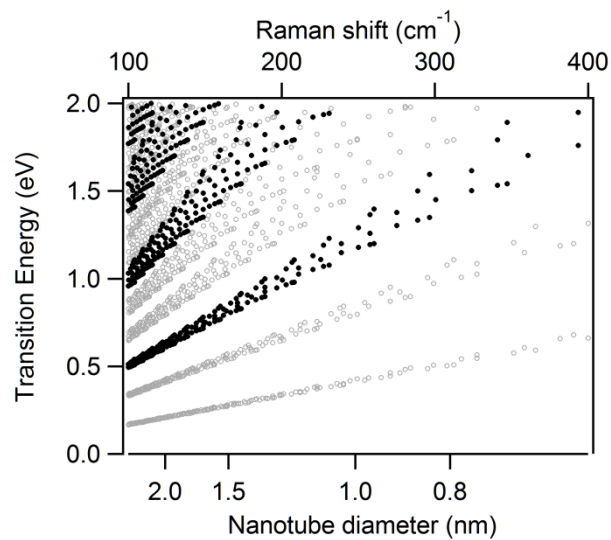
Kataura plot showing the relation between Raman RBM wavenumbers and carbon nanotube diameter. Black and grey points are for m- and sc-SWCNTs, respectively. Data collected from [137].

IX.3.2 *Temperature induced shifts of the G- and D-bands of CNT Raman spectra*
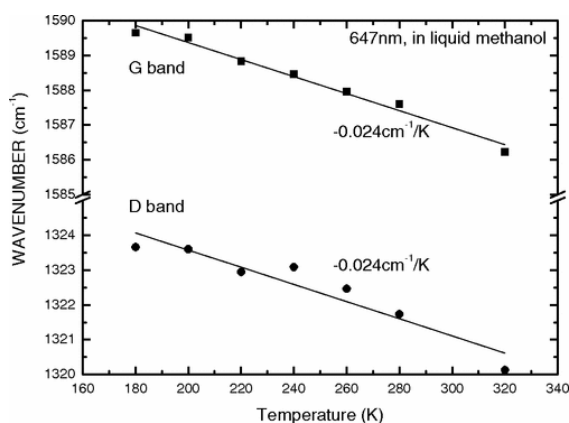
Shift of the Raman G- and D-bands positions of DWCNTs in methanol as a function of the temperature. Reprinted with permission from [143]. Copyright © 2009 by The American Chemical Society, http://dx.doi.org/10.1103/PhysRevB.79.085418.

IX.3.3 *Laser power induced shifts of the G- and D-bands of CNT Raman spectra*
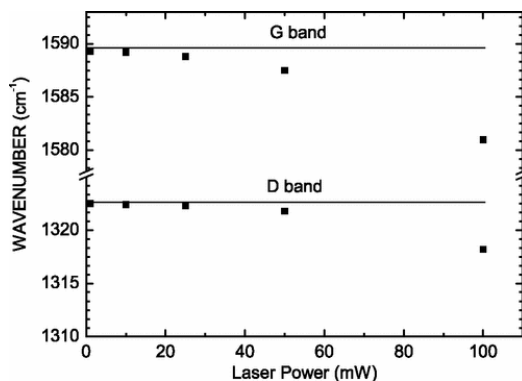
Shift of the Raman G- and D- band positions of DWCNTs as a function of the laser power (633 nm). Reprinted with permission from [143]. Copyright © 2009 by The American Chemical Society, http://dx.doi.org/10.1103/PhysRevB.79.085418.

IX.4 Annexes related to Chapter III

IX.4.1 *Experimental details for the fabrication of CNT-FETs*

Fabrication of SWCNT-FETs (geometry 1)

SWCNTs purification

SWCNTs of sources (a) and (b) were integrated into field-effect transistors (Geometry 1). Both sources of pristine SWCNTs were refluxed in a 70 % HNO_3 solution for 4 h followed by filtration on a PTFE membrane (1.2 μm pore size). A subsequent reflux in ultrapure water was done overnight. Purified SWCNTs were then suspended in N-methyl-2-pyrrolidone (NMP), and the suspension was sonicated and centrifugated (1 h, 5400 rpm) to decrease the concentration of SWCNTs bundles.

SiO_2/Si substrate silanization

Single-crystal 100 nm oxidized silicon wafers of ~ 1 cm² are used as substrates. Those substrates are cleaned by successive sonication (10 minutes) in acetone and isopropanol, followed by annealing (20 minutes) in a piranha solution (3:1 H_2SO_4 / H_2O_2). They were then exposed to the vapor of 1 ml of 3-(aminopropyl)triethoxysilane for 1 minute. Finally, the substrate samples were annealed in air at 120 °C for 20 minutes.

SWCNTs deposition

Diluted suspensions of purified SWCNTs were deposited on the functionalized substrates by spin-coating (7000 rpm, 30 s).

SWCNT-FETs fabrication

SWCNT-FETs were fabricated by photolithography process. Lift-off resist undercoat (LOR1A) was spin-coated, followed by S1805 positive photoresist. The samples were then exposed to UV light through a predefined mask. They were then developed in AZ-726 developer with agitation for 1 minute. Titanium electrodes (50 nm) were deposited by e-beam evaporation. The residual resists were lifted-off by immersing the samples in hot ($\sim$ 70 °C) PG-Remover for 20 minutes. The devices were further annealed in a vacuum oven at 500 °C for 1h.

Fabrication of SWCNT-FETs (geometry 2)

SWCNTs CVD-growth

SWCNTs were prepared by CVD growth directly on 285 nm SiO_2/Si substrates. The catalyst (ferritin protein from horse spleen with iron core) was swabbed onto one edge of the substrate. SWCNTs were allowed to growth at 890 °C for 1 h in a H_2/Ar gas mixture (8.7 sccm H_2/40 sccm Ar), using ethanol as carbon source.

SWCNT-FETs fabrication

SWCNT-FETs were fabricated by two successive e-beam lithography processes. First, a double layer of PMMA (A4 495k + A6 950k) was spin-coated on SWCNTs/SiO_2/Si chip. E-beam lithography was performed to define electrodes pattern. Metal electrodes (Ti 3 nm + Au 50 nm) were deposited by e-beam evaporation. The residual PMMA was lifted-off by immersing the samples in hot PG-Remover. A second e-beam lithography step was performed to select one desirable nanotube while removing other CNTs by exposition to an oxygen plasma (250 mTorr, 50 W, 5 x 5

s). The devices were further annealed under Ar flow (100 sccm) for 3.5 hours.

Fabrication of SWCNT-FETs (geometry 3)

SWCNTs CVD-growth

SWCNTs were prepared following the procedure described for Geometry 2.

SWCNT-FETs fabrication

SWCNT-FETs were fabricated by two successive lithography processes. First, lift-off resist undercoat (LOR1A) was spin-coated, followed by spin-coating of S1813 positive photoresist. The samples were then exposed to UV light through a predefined mask. Titanium electrodes (75 nm) were deposited by e-beam evaporation. The residual resists were lifted-off by immersing the samples in hot (~ 70 °C) PG-Remover. A second lithography step was performed to cover one selected nanotube. These protected samples were then exposed to an oxygen plasma (250 mTorr, 50 W, 10 s) to remove all other nanotubes. The devices were further annealed in forming gas (H_2/Ar mixture) at 400 °C for 2 hours.

IX.4.2 Statistical study of the electrical behavior of devices in geometry 2
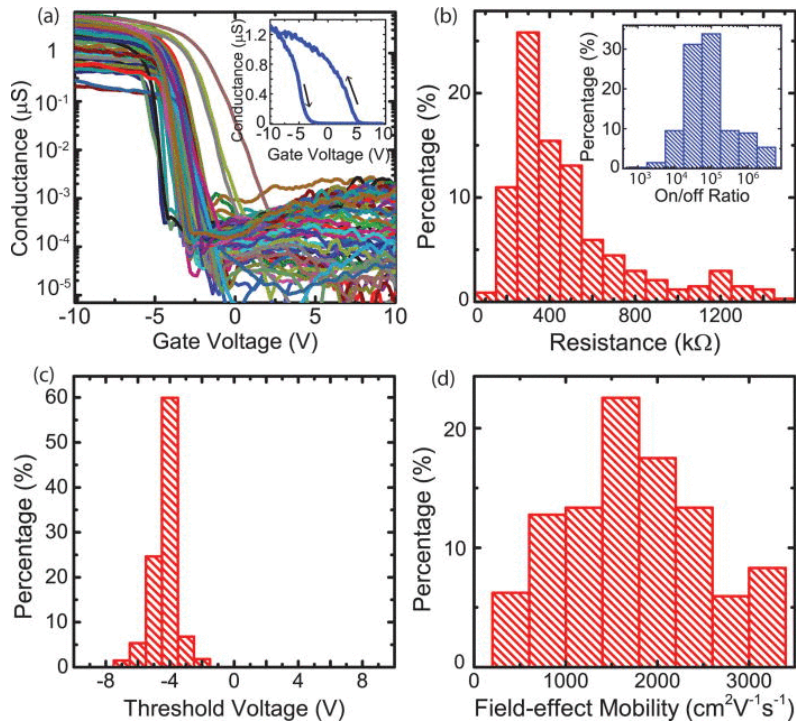
Electrical behavior of sc-CNT-FETs in geometry 2: (a) Transfer characteristics of 82 selected sc-CNT-FETs and (inset) example of the hysteresis behavior; (b) distribution of sc-CNTs ON-state resistance and (inset) distribution of the devices ON/OFF ratio; (c) distribution of the threshold voltage and (d) distribution of the field-effect mobility.
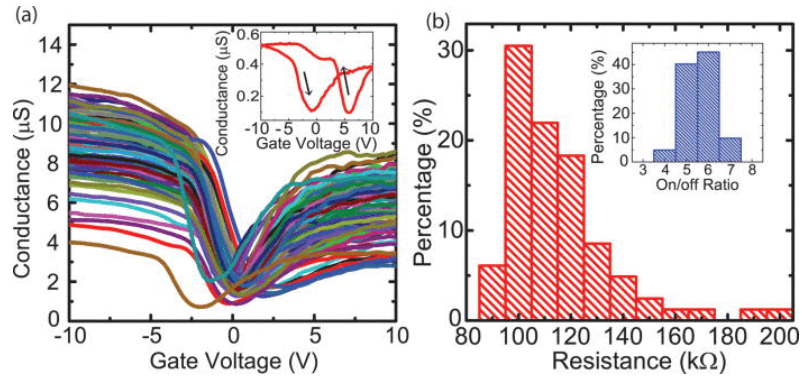
Electrical behavior of m-CNT-FETs in geometry 2: (a) Transfer characteristics of 82 selected m-CNT-FETs exhibiting a small bandgap and (inset) example of the hysteresis behavior; (b) distribution of m-CNTs resistance and (inset) distribution of the devices ON/OFF ratios.

IX.4.3 *Statistical data for the various geometries of devices*

Statistical data for determination of the proportion of connected devices in geometry 1.

Chip	# Devices per chip	# Tested devices	# Connected devices	Proportion of devices connected
1	693	88	462	19 %
2	693	79	462	17 %
3	693	94	693	14 %
4	693	47	693	7 %
5	693	29	693	4 %
6	693	18	231	8 %
7	693	3	231	1 %
8	693	3	231	1 %
9	693	4	231	2 %
10	693	14	231	6 %
11	693	13	231	6 %
12	693	11	231	5 %
13	693	12	231	5 %
14	693	73	693	11 %
15	693	99	693	14 %
16	693	145	693	21 %
17	693	167	693	24 %
Total	**11781**	**7623**	**899**	
		Weighted average		**78 %**
		Weighted standard deviation		**± 9 %**

Statistical data for determination of the proportion of connected devices in geometry 2.

Chip	# Devices per chip	# Tested devices	# Connected devices	Proportion of devices connected
1	175	175	146	83
2	175	175	139	79
3	175	175	117	67
4	175	17	16	94
5	175	17	16	94
6	175	175	158	90
7	175	175	120	69
Total	**1225**	**909**	**712**	
			Weighted average	**12 %**
			Weighted standard deviation	**± 7 %**

Statistical data for determination of the proportion of connected devices in geometry 3.

Chip	# Devices per chip	# Tested devices	# Connected devices	Proportion of devices connected
1	32	32	15	47
2	32	16	16	50
3	32	25	25	78
4	32	31	31	97
5	32	25	25	78
Total	**160**	**160**	**112**	
			Weighted average	**70 %**
			Weighted standard deviation	**± 19 %**

IX.5 Annexes related to Chapter IV

IX.5.1 Element contents determined by XPS

Element contents determined by XPS at each step of the preparation of the catalyst materials, for bulk and substrate-deposited SWCNTs.

		C 1s	Si 2p	O 1s	N 1s NH$_2$-Ph	N 1s NO$_2$-Ph	P 2p	Ru 3p	Pt 4f
Bulk	*p*-SWCNTs	91.59	N/A	7.76	0.36	0.00	N/A	N/A	N/A
	NO$_2$-Ph-*f*-SWCNTs	84.67	N/A	10.94	0.83	3.56	N/A	N/A	N/A
	NH$_2$-Ph-*f*-SWCNTs	90.42	N/A	4.40	5.08	0.101	N/A	N/A	N/A
	(PPh$_2$)$_2$-Ph-*f*-SWCNTs	90.47	N/A	4.40	3.61	0.00	1.52	N/A	N/A
	Cluster-*f*-SWCNTs	83.43	N/A	8.45	3.35	0.00	1.86	0.90	0.21
	NPs/SWCNTs	81.63	N/A	10.78	3.13	0.00	1.86	0.77	0.16
Substrate-deposited	*p*-SWCNTs	93.16	0.72	5.04	0.97	0.12	N/A	N/A	N/A
	NO$_2$-Ph-*f*-SWCNTs	78.60	1.85	15.77	1.68	2.11	N/A	N/A	N/A
	NH$_2$-Ph-*f*-SWCNTs	85.84	1.02	9.83	2.73	0.58	N/A	N/A	N/A
	(PPh$_2$)$_2$-Ph-*f*-SWCNTs	75.65	1.63	20.55	2.06	0.00	0.12	N/A	N/A
	Cluster-*f*-SWCNTs	72.94	0.77	21.39	1.89	0.00	0.23	0.74	0.12
	NPs/SWCNTs	62.14	9.26	26.22	1.21	0.00	0.00	0.24	0.05

Element content (at. %)

IX.5.2   XPS reproducibility

Batch-to-batch reproducibility

XPS measurements of batch-to-batch reproducibility experiments for bulk NO_2-Ph-f-MWCNTs.

Sample [a]	Element contents (at. %)		N 1s	
	C 1s	O 1s	NH$_2$-Ph	NO$_2$-Ph
1	90.41	6.61	0.55	2.43
2	89.54	7.33	0.57	2.56
3	90.89	6.31	0.55	2.25
4	90.71	6.25	0.55	2.49
5	88.88	7.91	0.85	2.36
6	90.27	6.59	0.77	2.37
7	89.76	7.31	0.76	2.17
8	90.26	6.54	0.72	2.47
		Average [b]	0.67	2.39
		Standard deviation [c]	0.12	0.13

[a] Each sample was prepared independently, according to the procedure described in the experimental section of Chapter IV, by replacing the SWCNTs by MWCNTs and scaling the reaction up to 200 mg.

[b] Average value for atomic concentrations determined by XPS on 8 batches.

[c] Standard deviation for atomic concentrations determined by XPS on 8 batches.

IX.5.3   N 1s XPS spectrum of pristine-bulk SWCNTs
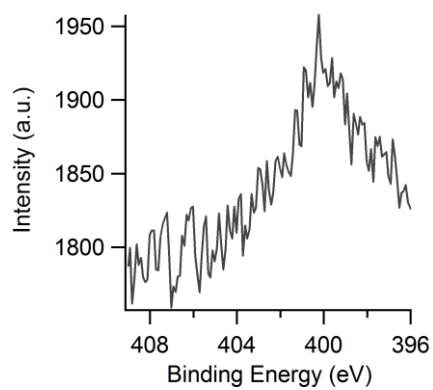
N 1s XPS spectrum of pristine-SWCNTs. (*p*-SWCNTs were washed with the solvents used for the work-up before analysis)

IX.5.4   Control experiments

<u>Bulk SWCNTs</u>
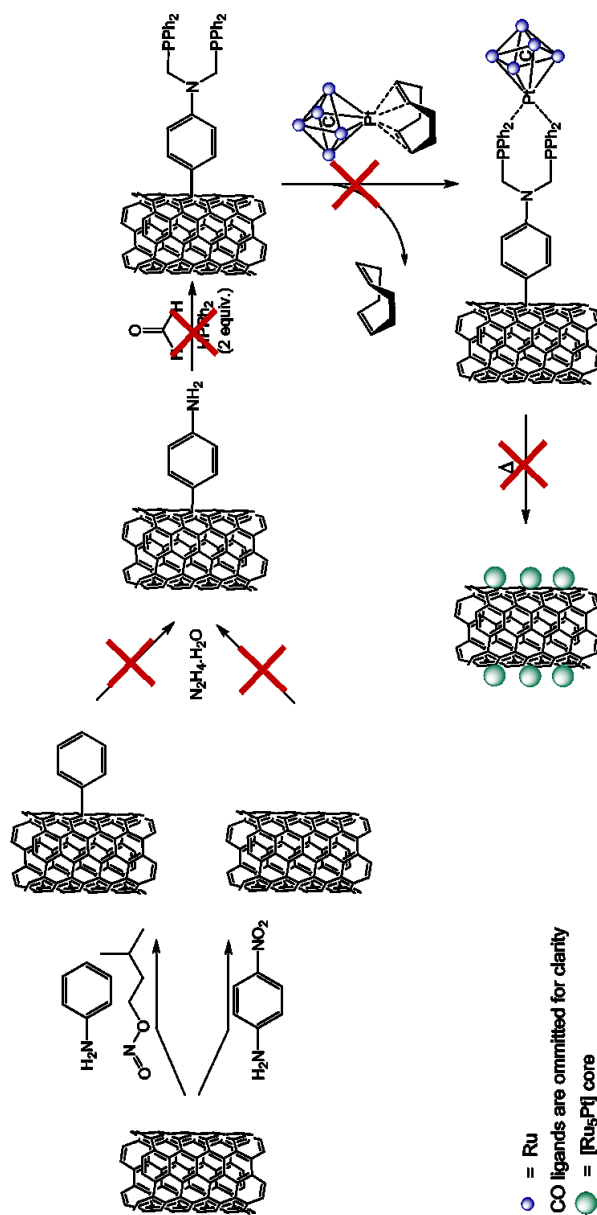
Schematic representation of the control experiments performed for the monovalent functionalization of bulk SWCNTs.

Element contents determined by XPS for the control experiments for bulk SWCNTs

| | | | | Element contents (at. %) | | | | |
| | | | | N 1s | | | | |
	C 1s	O 1s	NH$_2$-Ph	NO$_2$-Ph	P 2p	Ru 3p	Pt 4f
Blank with aniline							
p-SWCNTs	91.59	7.76	0.36	0.00	N/A	N/A	N/A
Ph-*f*-SWCNTs	94.89	3.56	1.55	0.00	N/A	N/A	N/A
"NH$_2$-Ph-*f*-SWCNTs"	91.85	7.00	1.15	0.00	N/A	N/A	N/A
"NPs/SWCNTs"	91.95	7.30	0.64	0.00	0.06	0.04	0.02
Blank without isoamylnitrite							
p-SWCNTs	91.59	7.76	0.36	0.00	N/A	N/A	N/A
"NO$_2$-Ph-*f*-SWCNTs"	95.26	3.98	0.77	0.00	N/A	N/A	N/A
"NH$_2$-Ph-*f*-SWCNTs"	94.41	4.87	0.72	0.00	N/A	N/A	N/A
"(PPh$_2$)$_2$-Ph-*f*-SWCNTs"	90.83	8.68	0.35	0.00	0.15	N/A	N/A
"Cluster-*f*-SWCNTs"	90.32	9.03	0.65	0.00	0.00	0.00	0.00
"NPs/SWCNTs"	90.60	8.94	0.45	0.00	0.00	0.00	0.01

Substrate-deposited SWCNTs
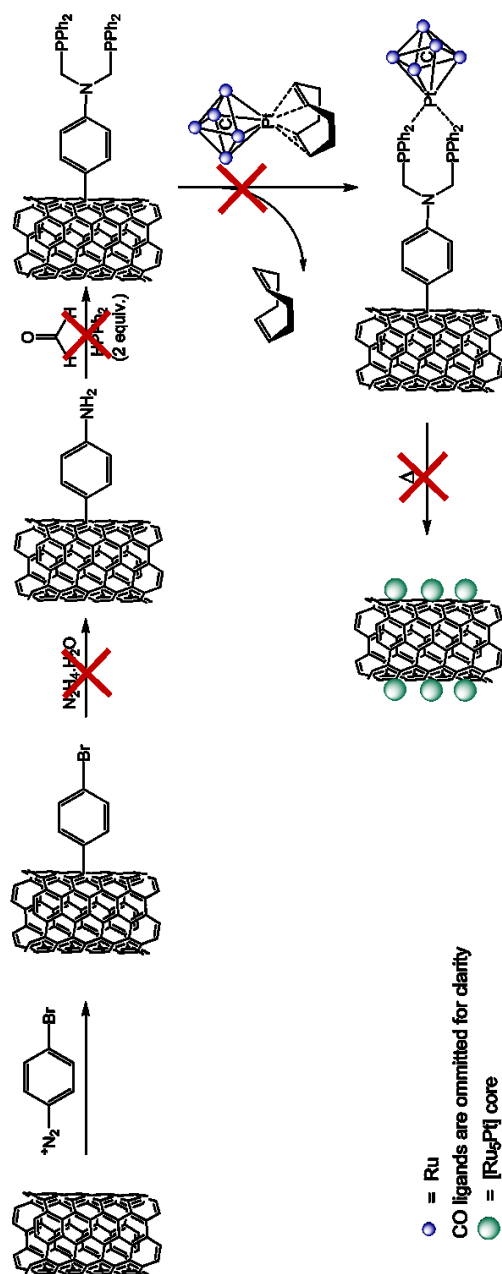
Schematic representation of the control experiments performed for the monovalent functionalization of substrate-deposited SWCNTs.

Element contents determined by XPS for the control experiments for substrate-deposited SWCNTs

	C 1s	**Si 2p**	**O 1s**	**N 1s**	**Br 3d**	**P 2p**	**Ru 3p**	**Pt 4f**
				Element contents (at. %)				
p-SWCNTs	93.16	0.72	5.04	0.97	0.00	N/A	N/A	N/A
Br-Ph-*f*-SWCNTs	90.68	0.58	7.91	0.40	0.44	N/A	N/A	N/A
"NH₂-Ph-*f*-SWCNTs"	91.03	0.13	7.08	1.44	0.33	N/A	N/A	N/A
"(PPh₃)₂-Ph-*f*-SWCNTs"	79.57	1.31	17.39	1.59	0.08	0.00	N/A	N/A
"Cluster-*f*-SWCNTs"	74.79	0.06	21.97	1.50	0.52	0.00	0.07	0.00
"NPs/SWCNTs"	98.75	0.14	1.01	0.04	0.01	0.00	0.00	0.00

Blank with Br

IX.5.5 Electrical characterization

<u>SWCNTs source (a)</u>
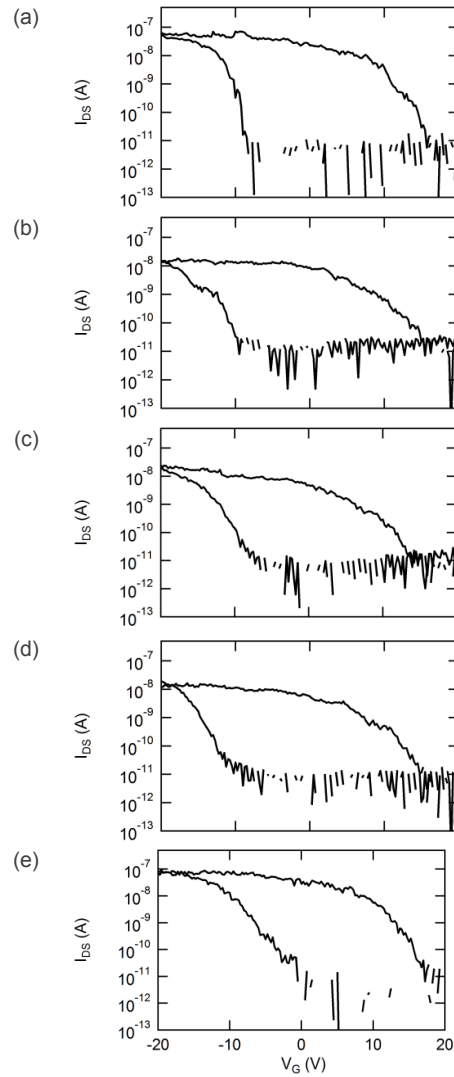
Transfer curves ($V_{DS} = 1$ V) of (a) *pristine*-SWCNT; (b) NO_2-Ph-*f*-SWCNTs; (c) NH_2-Ph-*f*-SWCNTs; (d) cluster supported on SWCNT and (e) Ru-Pt bimetallic nanoparticles deposited on SWCNT, for SWCNTs of source (a) integrated in devices of geometry 1.

SWCNTs source (b)
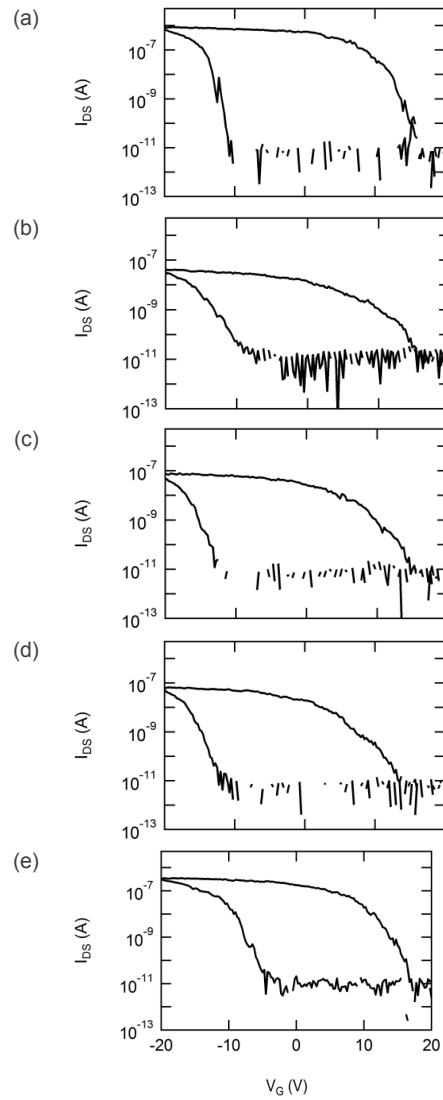
Transfer curves (V_{DS} = 1 V) of (a) *pristine*-SWCNT; (b) NO_2-Ph-*f*-SWCNTs; (c) NH_2-Ph-*f*-SWCNTs; (d) cluster supported on SWCNT and (e) Ru-Pt bimetallic nanoparticles deposited on SWCNT, for SWCNTs of source (b) integrated in devices of geometry 1.

IX.6 Annexes related to Chapter VI

IX.6.1 Alkyne /SWCNT mechanical mixture
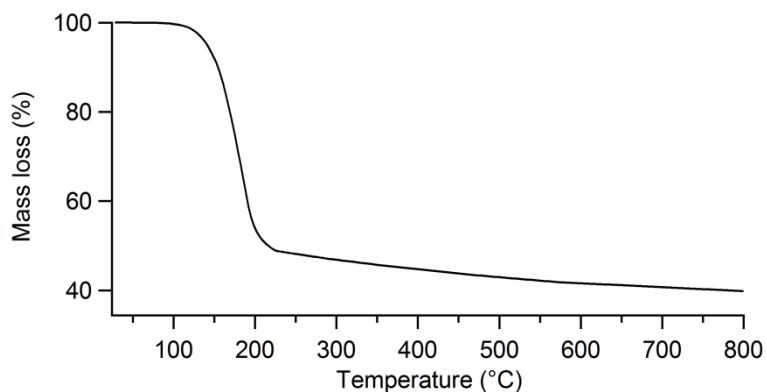
Thermogram (under nitrogen) of alkyne/SWCNTs mechanical mixture.

IX.6.2 Raman spectroscopy
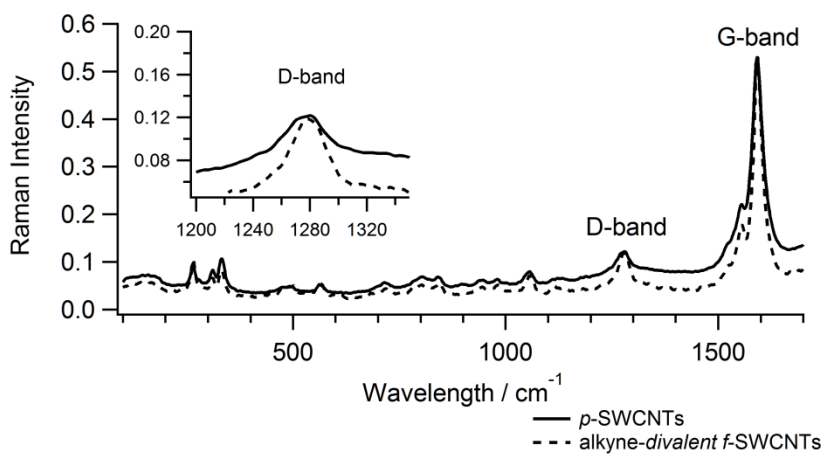
Raman spectra of pristine (solid line) and alkyne divalent functionalized (dashed line) SWCNTs. Insets show a magnification of the D-band area.

283

IX.6.3 C 1s XPS spectrum of alkyne-divalent f-SWCNTs
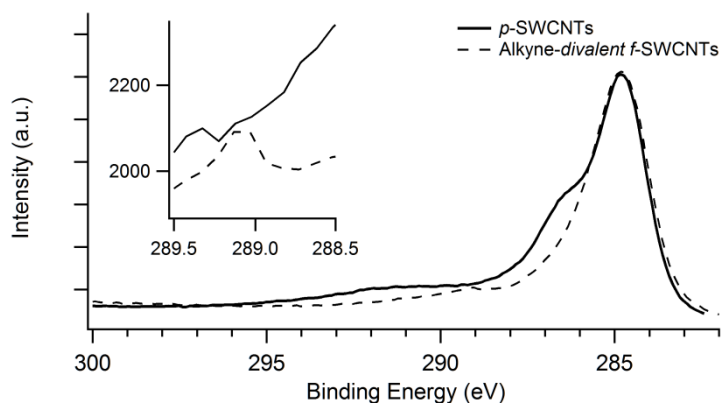
High resolution C 1s XPS spectra of *p*-SWCNTs (full line) and alkyne-*divalent f*-SWCNTs (dashed line). Inset shows a magnification around the binding energy of ester functions (289 eV).

IX.6.4   Optimization of the Bingel-Hirsch reaction

Element contents determined by XPS for Br-divalent f-SWCNTs for various reaction conditions.

| | Reaction conditions | | | Element contents (at. %) | | |
	Solvent	Temp.	Time	C 1s	O 1s	Br 3d
	1,2-dichlorobenzene	RT	3 h	93.80	6.06	0.13
	1,2-dichlorobenzene	**RT**	**16 h**	**93.36**	**6.24**	**0.40**
	1,2-dichlorobenzene	RT	120 h	90.15	9.76	0.09
Br-*divalent f*-SWCNTs	Benzylamine	RT	3 h	95.94	4.03	0.03
	Benzylamine	RT	16 h	95.07	4.78	0.15
	Benzylamine	RT	120 h	88.20	11.40	0.09

Bold entry corresponds to the reaction conditions selected for this thesis.

IX.6.5 Investigation of the origin of n-doping observed after the functionalization
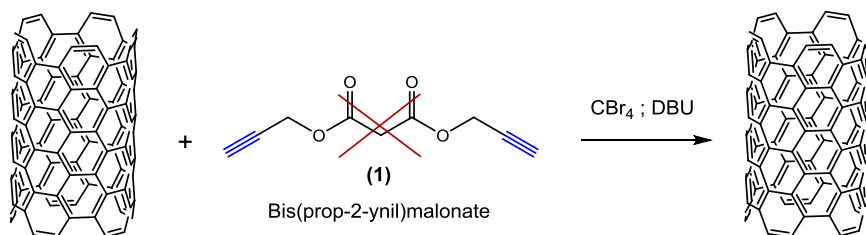
Schematic representation of the preparation of blank SWCNT-FETs sample by immersion of *pristine*-SWCNT-FETs in a solution containing CBr_4 and DBU, in absence of malonate.
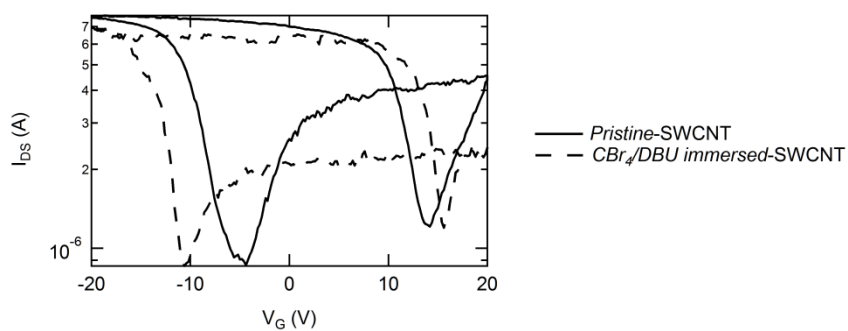
Transfer curves (V_{DS} = 1 V) of *pristine*-SWCNT and SWCNT immersed in a solution containing CBr_4 and DBU.

286

IX.6.6 Control experiments

IX.6.6.1 Preparation of blank samples

Preparation of blank A:

Step 1: Divalent addition of alkyne malonates by Bingel-Hirsch reaction, prepared according to the optimized conditions.

Step 2: Coordination of Pd(0) complexes. The concentration of Pd(0) complexes is increased by up to ten times (compared to previous experiments), in order to induce larger agglomeration of the metal atoms during the third step.

Step 3: Thermal annealing. This step allows forming large nanoparticles from the metallic complexes.

Preparation of blank B:

Same process, but step 1 skipped.
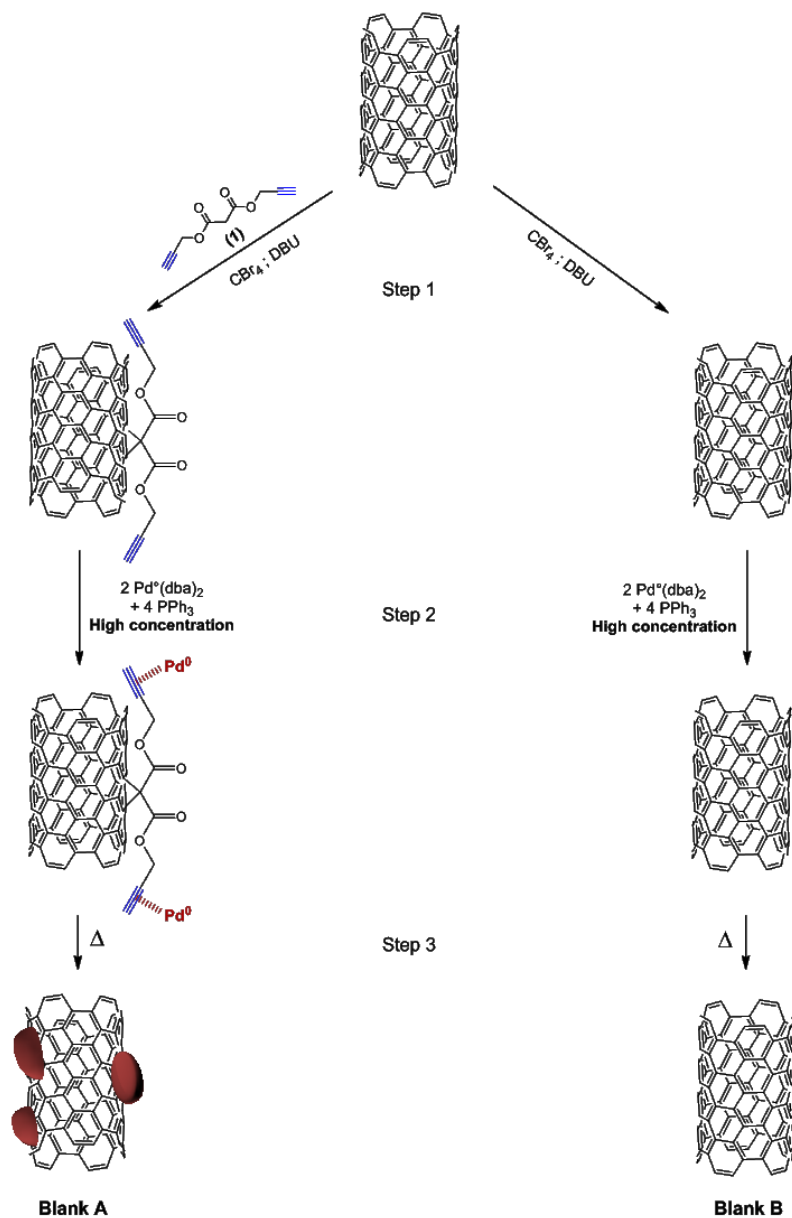
Schematic representation of the preparation of blanks SWCNT-FETs for the detection of metallic species at nanotube surface.

IX.6.6.2   <u>Unfunctionalized *vs* functionalized SWCNT-FETs</u>
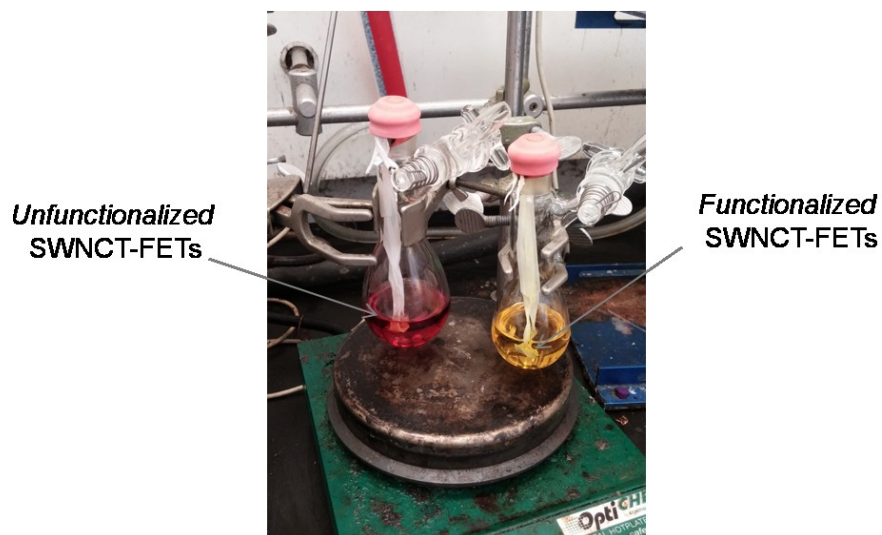
Pictures of (left) unfunctionalized SWCNT-FETs and (right) alkyne-*divalent f-*SWCNT-FETs after immersion in solutions at the same concentration of Pd(0) during one night.

IX.6.6.3   <u>AFM</u>
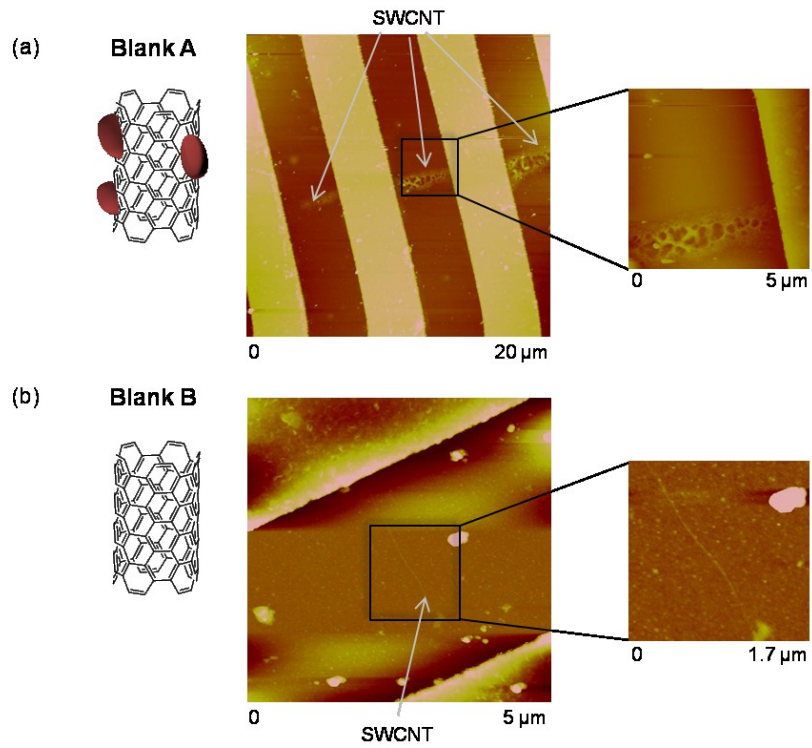
Figure VI.19. AFM images of (a) blank A, showing large amount of large particles along the nanotube; (b) blank B, showing particles homogeneously dispersed on the silicon substrate, without preference for the nanotube.

BIBLIOGRAPHY

(1)   Brooker, G. *Introduction to Sensors for Ranging and Imaging*; SciTech Publishing Inc.: Raleigh, NC, 2009.

(2)   Teyssier, J.; Saenko, S. V.; Marel, D. van der; Milinkovitch, M. C. *Nat. Commun.* **2015**, *6*, 6368.

(3)   Meeker-O'Connell, A. How Venus Flytraps work? http://science.howstuffworks.com/life/botany/venus-flytrap.htm (accessed Jan 1, 2016).

(4)   Bellis, M. History of the Thermometer http://inventors.about.com/od/fstartinventions/a/Fahrenheit.htm (accessed Feb 26, 2016).

(5)   Kalantar-zadeh, K. *Sensors: An Introductory Course*; Springer: New York, 2013.

(6)   van Zee, R. D.; Pomrenke, G. S. *Nanotechnology-Enabled Sensing*; 2009.

(7)   McGrath, M.; Ni Scanaill, C. In *Sensor Technologies: Healthcare, Wellness and Environmental Applications*; 2013; pp 15–50.

(8)   Banica, F.-G. *Chemical Sensors and Biosensors - Fundamentals and Applications*, John Wiley.; Chichester, UK, 2012.

(9)   Sanchez, F.; Sobolev, K. *Constr. Build. Mater.* **2010**, *24* (11), 2060–2071.

(10)   Miyazaki, K.; Islam, N. *Technovation* **2007**, *27* (11), 661–675.

(11)   Kauffman, D. R.; Star, A. *Angew. Chem. Int. Ed.* **2008**, *47* (35), 6550–6570.

(12)   Zhang, T.; Mubeen, S.; Myung, N. V. *Nanotechnology* **2008**, *19*, 332001.

(13)   Kim, S. N.; Rusling, J. F.; Papadimitrakopoulos, F. *Adv. Mat.* **2007**, *19* (20), 3214–3228.

(14)   Allen, B. L.; Kichambare, P. D.; Star, A. *Adv. Mat.* **2007**, *19* (11), 1439–1451.

(15)   Gruner, G. *Anal. Bioanal. Chem.* **2006**, *384* (2), 322–335.

(16)   Fam, D. W. H.; Palaniappan, A.; Tok, A. I. Y.; Liedberg, B.; Moochhala, S. M. *Sensors Actuators, B Chem.* **2011**, *157* (1), 1–7.

(17)   Chikkadi, K.; Muoth, M.; Roman, C.; Haluska, M.; Hierold, C. *Beilstein J. Nanotechnol.* **2014**, *5*, 2179–2191.

(18)   Goldoni, A.; Petaccia, L.; Lizzit, S.; Larciprete, R. *J. Phys. Condens. Matter* **2010**, *22*, 13001.

(19)   Jiménez-Cadena, G.; Riu, J.; Rius, F. X. *Analyst* **2007**, *132*, 1083–1099.

(20)   Kim, J. *J. Nanomater.* **2012**, *2012*, 741647.

(21)   Llobet, E. *Sensor. Actuat. B Chem.* **2013**, *179*, 32–45.

(22)   Luh, N.; Septiani, W.; Yuliarto, B. *J. Electrochem. Soc.* **2016**, *163* (3), 97–106.

(23)   Mittal, M.; Kumar, A. *Sensor. Actuat. B Chem.* **2014**, *203*, 349–362.

(24)   Yeow, J. T. W.; Wang, Y. *J. Sensors* **2009**, *2009*, 493904.

(25)   Kong, J.; Franklin, N. R.; Zhou, C.; Chapline, M. G.; Peng, S.; Cho, K.; Dai, H. *Science* **2000**, *287* (5453), 622–625.

(26)   Collins, P. G.; Bradley, K.; Ishigami, M.; Zettl, A. *Science* **2000**, *287* (5459), 1801–1804.

(27)   Aguirre, C. M.; Levesque, P. L.; Paillet, M.; Lapointe, F.; St-Antoine, B. C.; Desjardins, P.; Martel, R. *Adv. Mater.* **2009**, *21* (30), 3087–3091.

(28)   Someya, T.; Small, J.; Kim, P.; Nuckolls, C.; Yardley, J. T. *Nano Lett.* **2003**, *3* (7), 877–881.

(29)   Penza, M.; Cassano, G.; Rossi, R.; Alvisi, M.; Rizzo, A.; Signore, M. A.; Dikonimos, T.; Serra, E.; Giorgi, R. *Appl. Phys. Lett.* **2007**, *90* (17), 173123.

(30)   Mubeen, S.; Zhang, T.; Yoo, B.; Deshusses, M. a M. a. M. A.; Myung, N. V. N. V. *J. Phys. Chem. C* **2007**, *111* (17), 6321–6327.

(31)   Kumar, M. K.; Ramaprabhu, S. *J. Phys. Chem. B* **2006**, *110* (23), 11291–11298.

(32)   Kong, J.; Chapline, M. G.; Dai, H. *Adv. Mater.* **2001**, *13* (18), 1384–1386.

(33)   Sippel-Oakley, J.; Wang, H.-T.; Kang, B. S.; Wu, Z.; Ren, F.; Rinzler, A. G.; Pearton, S. J. *Nanotechnology* **2005**, *16* (10), 2218–2221.

(34)   Dag, S.; Ozturk, Y.; Ciraci, S.; Yildirim, T. *Phys. Rev. B* **2005**, *72* (15), 155404.

(35)   Sayago, I.; Terrado, E.; Lafuente, E.; Horrillo, M. C.; Maser, W. K.; Benito, A. M.; Navarro, R.; Urriolabeitia, E. P.; Martinez, M. T.; Gutierrez, J. *Synth. Met.* **2005**, *148* (1), 15–19.

292

(36)   Wong, Y. M.; Kang, W. P.; Davidson, J. L.; Wisitsora-At, A.; Soh, K. L. *Sens. Actuators B* **2003**, *93*, 327–332.

(37)   Star, A.; Joshi, V.; Skarupo, S.; Thomas, D.; Gabriel, J.-C. P. *J. Phys. Chem. B* **2006**, *110* (42), 21014–21020.

(38)   Lu, Y.; Li, J.; Han, J.; Ng, H. T.; Binder, C.; Partridge, C.; Meyyappan, M. *Chem. Phys. Lett.* **2004**, *391*, 344–348.

(39)   Kauffman, D. R.; Sorescu, D. C.; Schofield, D. P.; Allen, B. L.; Jordan, K. D.; Star, A. *Nano Lett.* **2010**, *10* (3), 958–963.

(40)   Dilonardo, E.; Penza, M.; Alvisi, M.; Di Franco, C.; Rossi, R.; Palmisano, F.; Torsi, L.; Cioffi, N. *Sensors Actuators, B Chem.* **2016**, *223* (2), 417–428.

(41)   Allen, B. L.; Kichambare, P. D.; Star, A. *Adv. Mater.* **2007**, *19* (11), 1439–1451.

(42)   Balasubramanian, K.; Burghard, M. *Anal. Bioanal. Chem.* **2006**, *385* (3), 452–468.

(43)   Jacobs, C. B.; Peairs, M. J.; Venton, B. J. *Anal. Chim. Acta* **2010**, *662* (2), 105–127.

(44)   Kauffman, D. R.; Star, A. *Chem. Soc. Rev.* **2008**, *37* (6), 1197–1206.

(45)   Kichambare, P. D.; Star, A. In *Nanotechnologies for the Life*; Wiley-VCH, 2007.

(46)   Liu, S.; Guo, X. *NPG Asia Mater.* **2012**, *4* (8), e23.

(47)   Wohlstadter, J. N.; Wilbur, J. L.; Sigal, G. B.; Biebuyck, H. A.; Billadeau, M. A.; Dong, L.; Fischer, A. B.; Gudibande, S. R.; Jameison, S. H.; Kenten, J. H.; Leginus, J.; Leland, J. K.; Massey, R. J.; Wohlstadter, S. J. *Adv. Mater.* **2003**, *15* (14), 1184–1187.

(48)   Bradley, K.; Briman, M.; Star, A.; Grner, G.; Gru, G. *Nano Lett.* **2004**, *4* (2), 253–256.

(49)   Star, A.; Gabriel, J. C. P.; Bradley, K.; Grüner, G. *Nano Lett.* **2003**, *3* (4), 459–463.

(50)   Chen, R. J.; Bangsaruntip, S.; Drouvalakis, K. a; Kam, N. W. S.; Shim, M.; Li, Y.; Kim, W.; Utz, P. J.; Dai, H. *Proc. Natl. Acad. Sci. U. S. A.* **2003**, *100* (9), 4984–4989.

(51)   Katz, E.; Willner, I. *ChemPhysChem* **2004**, *5* (8), 1084–1104.

(52)   Davis, J. J.; Coleman, K. S.; Azamian, B. R.; Bagshaw, C. B.; Green, M. L. H.

293

Chem. - A Eur. J. **2003**, *9* (16), 3732–3739.

(53)   Li, C.; Curreli, M.; Lin, H.; Lei, B.; Ishikawa, F. N.; Datar, R.; Cote, R. J.; Thompson, M. E.; Zhou, C. *J. Am. Chem. Soc.* **2005**, *127* (36), 12484–12485.

(54)   Mu, A. M.; Seo, W.; Morgan, G. J.; Michael, Z. P.; Zhao, Y.; Melzer, K.; Scarpa, G.; Star, A. *J. Phys. Chem. C* **2014**, *118*, 17193–17199.

(55)   Lee, D.; Chander, Y.; Goyal, S. M.; Cui, T. *Biosens. Bioelectron.* **2011**, *26* (8), 3482–3487.

(56)   Mandal, H. S.; Su, Z.; Ward, A.; Tang, X. S. *Theranostics* **2012**, *2* (3), 251–257.

(57)   Singh, R.; Sharma, A.; Jang, J. *Analyst* **2014**, *139* (21), 5415–5421.

(58)   Besteman, K.; Lee, J. O.; Wiertz, F. G. M.; Heering, H. A.; Dekker, C. *Nano Lett.* **2003**, *3* (6), 727–730.

(59)   Cai, D.; Yu, Y.; Lan, Y.; Dufort, F. J.; Xiong, G.; Paudel, T.; Ren, Z.; Wagner, D. J.; Chiles, T. C. *BioFactors* **2007**, *30* (4), 271–277.

(60)   Zhu, Z.; Garcia-Gancedo, L.; Flewitt, A. J.; Xie, H.; Moussy, F.; Milne, W. I. *Sensors* **2012**, *12* (5), 5996–6022.

(61)   Lerner, M. B.; Kybert, N.; Mendoza, R.; Villechenon, R.; Bonilla Lopez, M. A.; Charlie Johnson, A. T. *Appl. Phys. Lett.* **2013**, *102* (18), 3–7.

(62)   Sorgenfrei, S.; Chiu, C. Y.; Gonzalez Jr., R. L.; Yu, Y. J.; Kim, P.; Nuckolls, C.; Shepard, K. L. *Nat Nanotechnol* **2011**, *6* (2), 126–132.

(63)   Goldsmith, B. R.; Coroneus, J. G.; Khalap, V. R.; Kane, A. A.; Weiss, G. A.; Collins, P. G. *Science* **2007**, *315*, 77–81.

(64)   Choi, Y.; Moody, I.; Sims, P.; Hunt, S.; Corso, B. *Science* **2012**, *335* (January), 319–324.

(65)   Choi, Y.; Moody, I. S.; Sims, P. C.; Hunt, S. R.; Corso, B. L.; Seitz, D. E.; Blaszczak, L. C.; Collins, P. G.; Weiss, G. A. *J. Am. Chem. Soc.* **2012**, *134* (4), 2032–2035.

(66)   Lu, H. P. *Science* **2012**, *335*, 300–301.

(67)   Choi, Y.; Olsen, T. J.; Sims, P. C.; Moody, I. S.; Corso, B. L.; Dang, M. N.; Weiss, G. a; Collins, P. G. *Nano Lett.* **2013**, *13* (2), 625–631.

(68)   Olsen, T.; Choi, Y.; Sims, P. *J. Am. Chem. Soc.* **2013**, No. 135, 7855–7860.

(69)   Sims, P. C.; Moody, I. S.; Choi, Y.; Dong, C.; Iftikhar, M.; Corso, B. L.; Gul,

O. T.; Collins, P. G.; Weiss, G. a. *J. Am. Chem. Soc.* **2013**, *135* (21), 7861–7868.

(70)   Choi, Y.; Weiss, G. a; Collins, P. G. *Phys. Chem. Chem. Phys.* **2013**, *15* (36), 14879–14895.

(71)   Choi, Y.; Weiss, G. A.; Collins, P. G. In *Comprehensive Bioelectronics*; Carrera, S., Iniewski, K., Eds.; Cambridge, 2013.

(72)   Färber, E. *Great chemists*; Great Chemists; Interscience Publishers, 1961.

(73)   Busacca, C. A.; Fandrick, D. R.; Song, J. J.; Senanayake, C. H. *Adv. Synth. Catal.* **2011**, *353* (11–12), 1825–1864.

(74)   De Jong, K. P. *Synthesis of Solid Catalysts*, Wiley-VCH.; Weinheim, 2009.

(75)   Collis, A. E. C.; Horváth, I. T. *Catal. Sci. Technol.* **2011**, *1*, 912–919.

(76)   Farnetti, E.; Monte, R. Di; Kašpar, J. *Life Support Syst.* **1999**, *II*, 10–22.

(77)   Astruc, D.; Lu, F.; Aranzaes, J. R. *Angew. Chem. Int. Ed. Engl.* **2005**, *44* (48), 7852–7872.

(78)   Moteki, T.; Murakami, Y.; Noda, S.; Maruyama, S.; Okubo, T. *J. Phys. Chem. C* **2011**, *115* (49), 24231–24237.

(79)   Schaetz, A.; Zeltner, M.; Stark, W. J. *ACS Catal.* **2012**, *2* (6), 1267–1284.

(80)   Su, D. S.; Perathoner, S.; Centi, G. *Chem. Rev.* **2013**, *113* (8), 5782–5816.

(81)   Taboada, C. D.; Batista, J.; Pintar, A.; Levec, J. *Appl. Catal. B Environ.* **2009**, *89* (3–4), 375–382.

(82)   Serp, P.; Corrias, M.; Kalck, P. *Appl. Catal. A Gen.* **2003**, *253*, 337–358.

(83)   Bahome, M. C.; Jewell, L. L.; Padayachy, K.; Hildebrandt, D.; Glasser, D.; Datye, A. K.; Coville, N. J. *Appl. Catal. A Gen.* **2007**, *328*, 243–251.

(84)   Vu, H.; Goncalves, F.; Philippe, R.; Lamouroux, E.; Corrias, M.; Kihn, Y.; Plee, D.; Kalck, P.; Serp, P. *J. Catal.* **2006**, *240*, 18–22.

(85)   Machado, B. F.; Serp, P. *Catal. Sci. Technol.* **2012**, *2* (1), 54–75.

(86)   Zhu, J.; Holmen, A.; Chen, D. *ChemCatChem* **2013**, *5* (2), 378–401.

(87)   Hermans, S. In *Synthesis of Solid Catalysts*; de Jong, K. P., Ed.; Weinheim, 2009; pp 153–171.

(88)   Jones, C. W.; Tao, F.; Garland, M. V. *ACS Catal.* **2012**, *2*, 2444–2445.

(89)   Che, M.; Védrine, J. C. *Characterization of Solid Materials and*

Heterogeneous Catalysts, Wiley-VCH.; Wiley-VCH, 2012.

(90)   Leofanti, G.; Tozzola, G.; Padovan, M.; Petrini, G.; Bordiga, S.; Zecchina, A. *Catal. Today* **1997**, *34*, 307–327.

(91)   Topsøe, H. *Stud. Surf. Sci. Catal.* **2000**, *130*, 1–21.

(92)   Bañares, M. A. *Catal. Today* **2005**, *100*, 71–77.

(93)   Weckhuysen, B. M. *Phys. Chem. Chem. Phys.* **2003**, *5* (20), 4351.

(94)   Weckhuysen, B. M. *Chem. Commun.* **2002**, No. 2, 97–110.

(95)   Tromp, M. *Phil. Trans. R. Soc. A* **2015**, *373*, 20130152.

(96)   Beale, A. M.; van der Eerden, A. M. J.; Kervinen, K.; Newton, M. A.; Weckhuysen, B. M. *Chem. Commun.* **2005**, 3015–3017.

(97)   Ellis, P. J.; Fairlamb, I. J. S.; Hackett, S. F. J.; Wilson, K.; Lee, A. F. *Angew. Chemie - Int. Ed.* **2010**, *49* (10), 1820–1824.

(98)   Topsøe, H. *J. Catal.* **2003**, *216*, 155–164.

(99)   Sattler, J. J. H. B.; Beale, A. M.; Weckhuysen, B. M. *Phys. Chem. Chem. Phys.* **2013**, *15* (29), 12095–12103.

(100)   Li, Q.; Sui, Z.; Zhou, X.; Zhu, Y.; Zhou, J.; Chen, D. *Top. Catal.* **2011**, *54*, 888–896.

(101)   Lee, A. F.; Carr, P.; Wilson, K. *J. Phys. Chem. B* **2004**, *108* (39), 14811–14814.

(102)   Lei, A.; Liu, W.; Liu, C.; Chen, M. *Dalton Trans.* **2010**, *39* (43), 10352–10361.

(103)   Phan, N. T. S.; Van Der Sluys, M.; Jones, C. W. *Adv. Synth. Catal.* **2006**, *348*, 609–679.

(104)   Tinnemans, S. J.; Mesu, J. G.; Kervinen, K.; Visser, T.; Nijhuis, T. A.; Beale, A. M.; Keller, D. E.; van der Eerden, A. M. J.; Weckhuysen, B. M. *Catal. Today* **2006**, *113*, 3–15.

(105)   Patlolla, A.; Baumann, P.; Xu, W.; Senanayake, S. D.; Rodriguez, J. A.; Frenkel, A. I. *Top. Catal.* **2013**, *56*, 896–904.

(106)   Wojcieszak, R.; Ghazzal, M. N.; Gaigneaux, E. M.; Ruiz, P. *Catal. Sci. Technol.* **2014**, *4* (3), 3298–3305.

(107)   Zhao, C.; Wachs, I. E. *J. Phys. Chem. C* **2008**, *112*, 11363–11372.

(108)   Klasovsky, F.; Hohmeyer, J.; Brückner, A.; Bonifer, M.; Arras, J.; Steffan, M.;

Lucas, M.; Radnik, J.; Roth, C.; Claus, P. *J. Phys. Chem. C* **2008**, *112*, 19555–19559.

(109) Rabeah, J.; Bentrup, U.; Stößer, R.; Brückner, A. *Angew. Chemie - Int. Ed.* **2015**, *54* (40), 11791–11794.

(110) Arendt, E.; Ghislain, S.; Gaigneaux, E. M. *Catal. Today* **2010**, *155*, 227–240.

(111) Mandali, P. K.; Chand, D. K. *Catal. Commun.* **2013**, *31*, 16–20.

(112) Hirsch, A. *Nat. Mater.* **2010**, *9* (11), 868–871.

(113) Kroto, H. W.; Heath, J. R.; O'Brien, S. C.; Curl, R. F.; Smalley, R. E. *Nature* **1985**, *318*, 162–163.

(114) Iijima, S. *Nature* **1991**, *354*, 56–58.

(115) Bethune, D. S.; Klang, C. H.; de Vries, M. S.; Gorman, G.; Savoy, R.; Vazquez, J.; Beyers, R. *Nature* **1993**, *363*, 605–607.

(116) Iijima, S.; Ichihashi, T. *Nature* **1993**, *363*, 603–605.

(117) Novoselov, K. S.; Geim, A. K.; Morozov, S. V.; Jiang, D.; Zhang, Y.; Dubonos, S. V.; Grigorieva, I. V.; Firsov, A. A. *Science* **2004**, *306* (5696), 666–669.

(118) Geim, A. K.; Novoselov, K. S. *Nat. Mater.* **2007**, *6* (3), 183–191.

(119) Avouris, P. *Acc. Chem. Res.* **2002**, *35* (12), 1026–1034.

(120) Burghard, M.; Klauk, H.; Kern, K. *Adv. Mater.* **2009**, *21*, 2586–2600.

(121) McEuen, P. L. *Nature* **1998**, *393*, 15–16.

(122) Spitalsky, Z.; Tasis, D.; Papagelis, K.; Galiotis, C. *Prog. Polym. Sci.* **2010**, *35* (3), 357–401.

(123) Monthioux, M. In *Carbon Meta-Nanotubes: Synthesis, Properties and Applications*; John Wiley, 2012; pp 7–39.

(124) Thostenson, E. T.; Ren, Z.; Chou, T.-W. *Compos. Sci. Technol.* **2001**, *61* (13), 1899–1912.

(125) Dai, H. *Surf. Sci.* **2002**, *500* (1–3), 218–241.

(126) Shanov, V.; Yun, Y.; Schulz, M. J. *J. Univ. Chem. Technol. Metall.* **2006**, *41* (4), 377–390.

(127) Van Hooijdonk, E.; Bittencourt, C.; Snyders, R.; Colomer, J.-F. *Beilstein J. Nanotechnol.* **2013**, *4*, 129–152.

(128) Chai, Y.; Xiao, Z.; Chan, P. C. H. *Nanotechnology* **2010**, *21* (23), 235705.

(129) Wind, S.; Neumayer, D.; Appenzeller, J.; Martel, R.; Derycke, V.; Radosavljevic, M.; Avouris, P. *Microelectron. Eng.* **2002**, *64*, 391–397.

(130) Mittal, G.; Dhand, V.; Rhee, K. Y.; Park, S.-J.; Lee, W. R. *J. Ind. Eng. Chem.* **2015**, *21*, 11–25.

(131) Hamada, N.; Sawada, S.; Oshiyama, A. *Phys. Rev. Lett.* **1992**, *68* (10), 1579–1581.

(132) Terrones, M. *Annu. Mater. Res.* **2003**, *33* (1), 419–501.

(133) Wunderlich, D.; Hauke, F.; Hirsch, A. *J. Mater. Chem.* **2008**, *18* (13), 1493–1497.

(134) Strano, M. S. *J. Am. Chem. Soc.* **2003**, *125* (51), 16148–16153.

(135) *Carbon Nanotubes - Properties and Applications*, Taylor & F.; O'Connell, M. J., Ed.; Taylor & F, 2006.

(136) Kataura, H.; Kumazawa, Y.; Maniwa, Y.; Umezu, I.; Suzuki, S.; Ohtsuka, Y.; Achiba, Y. *Synth. Met.* **1999**, No. 103, 2555–2558.

(137) Maruyama. Kataura-Plot for Resonant Raman http://www.photon.t.u-tokyo.ac.jp/~maruyama/kataura/kataura.html#DOS (accessed Oct 16, 2015).

(138) Singh, P.; Campidelli, S.; Giordani, S.; Bonifazi, D.; Bianco, A.; Prato, M. *Chem. Soc. Rev.* **2009**, *38* (8), 2214–2230.

(139) Loiseau, A.; Launois, P.; Petit, P.; Roche, S.; Salvetat, J.-P. *Understanding carbon nanotubes*; Loiseau, A., Launois, P., Petit, P., Roche, S., Salvetat, J.-P., Eds.; Springer, 2006.

(140) Jorio, A.; Pimenta, M. A.; Souza Filho, A. G.; Saito, R.; Dresselhaus, G.; Dresselhaus, M. S. *New J. Phys.* **2003**, *5*, 139.1-139.17.

(141) Graupner, R. *J. Raman Spectrosc.* **2007**, *38*, 673–683.

(142) Jorio, A.; Saito, R.; Hafner, J. H.; Lieber, C. M.; Hunter, M.; McClure, T.; Dresselhaus, G.; Dresselhaus, M. S. *Phys. Rev. Lett.* **2001**, *86* (6), 1118–1121.

(143) Puech, P.; Anwar, A. W.; Flahaut, E.; Dunstan, D. J.; Bassil, A.; Bacsa, W. *Phys. Rev. B* **2009**, *79* (8), 85418.

(144) Dyke, C. A.; Tour, J. M. *Chem. - A Eur. J.* **2004**, *10* (4), 812–817.

(145) Tersoff, J.; Ruoff, R. S. *Phys. Rev. Lett.* **1994**, *73* (5), 676–679.

(146) Tasis, D.; Tagmatarchis, N.; Bianco, A.; Prato, M. *Chem. Rev.* **2006**, *106* (3),

1105–1136.

(147)   Hirsch, A. *Angew. Chem. Int. Ed.* **2002**, *41* (11), 1853–1859.

(148)   Britz, D. A.; Khlobystov, A. N. *Chem. Soc. Rev.* **2006**, *35* (7), 637–659.

(149)   Tasis, D.; Tagmatarchis, N.; Georgakilas, V.; Prato, M. *Chem. Eur. J.* **2003**, *9* (17), 4000–4008.

(150)   Balasubramanian, K.; Burghard, M. *Small* **2005**, *1* (2), 180–192.

(151)   Hirsch, A.; Vostrowsky, O. *Top Curr. Chem.* **2005**, *245*, 193–237.

(152)   Karousis, N.; Tagmatarchis, N.; Tasis, D. *Chem. Rev.* **2010**, *110* (9), 5366–5397.

(153)   Vaisman, L.; Wagner, H. D.; Marom, G. *Adv. Colloid Interfac.* **2006**, *128–130* (2006), 37–46.

(154)   Wang, H. *Curr. Opin. Colloid In.* **2009**, *14* (5), 364–371.

(155)   Zhao, Y.-L.; Stoddart, J. F. *Accounts Chem. Res.* **2009**, *42* (8), 1161–1171.

(156)   Tessonnier, J. P.; Villa, A.; Majoulet, O.; Su, D. S.; Schlögl, R. *Angew. Chem. Int. Ed.* **2009**, *48* (35), 6543–6546.

(157)   Del Canto, E.; Flavin, K.; Movia, D.; Navio, C.; Bittencourt, C.; Giordani, S. *Chem. Mater.* **2011**, *23* (1), 67–74.

(158)   Bahr, J. L.; Tour, J. M. *J. Mater. Chem.* **2002**, *12* (7), 1952–1958.

(159)   Banerjee, S.; Hemraj-Benny, T.; Wong, S. S. *Adv. Mater.* **2005**, *17* (1), 17–29.

(160)   Peng, X.; Wong, S. S. *Adv. Mater.* **2009**, *21* (6), 625–642.

(161)   Chen, R. J.; Zhang, Y.; Wang, D.; Dai, H. *J. Am. Chem. Soc.* **2001**, *123* (16), 3838–3839.

(162)   Haddad, R.; Holzinger, M.; Maaref, a.; Cosnier, S. *Electrochim. Acta* **2010**, *55* (27), 7800–7803.

(163)   Vriamont, C.; Devillers, M.; Riant, O.; Hermans, S. *Chem. Eur. J.* **2013**, *19* (36), 12009–12017.

(164)   Dyke, C. A.; Tour, J. M. *Nano Lett.* **2003**, *3* (9), 1215–1218.

(165)   Yi, W.; Malkovskiy, A.; Xu, Y.; Wang, X.-Q.; Sokolov, A. P.; Lebron-Colon, M.; Meador, M. a.; Pang, Y. *Polymer (Guildf).* **2010**, *51* (2), 475–481.

(166)   Dillon, A. C.; Jones, K. M.; Bekkedahl, T. A.; Kiang, C. H.; Bethune, D. S.; Heben, M. J. *Nature.* 1997, pp 377–379.

(167)   Smith, B. W.; Monthioux, M.; Luzzi, D. E. *Chem. Phys. Lett.* **1999**, *315*, 31–36.

(168)   Fei, B.; Lu, H.; Chen, W.; Xin, J. H. *Carbon* **2006**, *44* (11), 2261–2264.

(169)   Sloan, J.; Cook, J.; Green, M. L. H.; Hutchison, J. L.; Tenne, R. *J. Mater. Chem.* **1997**, *7* (7), 1089–1095.

(170)   Goyanes, S.; Rubiolo, G. R.; Salazar, A.; Jimeno, A.; Corcuera, M. A.; Mondragon, I. *Diam. Relat. Mater.* **2007**, *16* (2), 412–417.

(171)   Hamon, M. A.; Niyogi, S.; Hu, H.; Zhao, B.; Bhowmik, P.; Sen, R.; Itkis, M. E.; Haddon, R. C. *Acc. Chem. Res.* **2002**, *35* (12), 1105–1113.

(172)   Chen, Z.; Thiel, W.; Hirsch, A. *Chem. Phys. Chem.* **2003**, *4* (1), 93–97.

(173)   Strano, M. S. *Science* **2003**, *301* (5639), 1519–1522.

(174)   Ménard-Moyon, C.; Izard, N.; Doris, E.; Mioskowski, C. *J. Am. Chem. Soc.* **2006**, *128* (20), 6552–6553.

(175)   Zhang, H.; Wu, B.; Hu, W.; Liu, Y. *Chem. Soc. Rev.* **2011**, *40* (3), 1324–1336.

(176)   Chen, Z.; Nagase, S.; Hirsch, A.; Haddon, R. C.; Thiel, W.; Schleyer, P. V. R. *Angew. Chem. Int. Ed.* **2004**, *43* (12), 1552–1554.

(177)   Zhao, J.; Chen, Z.; Zhou, Z.; Park, H.; Von Schleyer, P. R.; Lu, J. P. *Chem. Phys. Chem.* **2005**, *6* (4), 598–601.

(178)   Lu, J.; Nagase, S.; Zhang, X.; Maeda, Y.; Wakahara, T.; Nakahodo, T.; Tsuchiya, T.; Akasaka, T.; Yu, D.; Gao, Z.; Han, R.; Ye, H. *J. Mol. Struct. THEOCHEM* **2005**, *725* (1–3), 255–257.

(179)   Liu, C.; Zhang, Q.; Stellacci, F.; Marzari, N.; Zheng, L.; Zhan, Z. *Small* **2011**, *7* (9), 1257–1263.

(180)   Bouilly, D.; Cabana, J.; Martel, R. *Appl. Phys. Lett.* **2012**, *101* (5), 53116.

(181)   Kawasaki, S.; Komatsu, K.; Okino, F.; Touhara, H.; Kataura, H. *Phys. Chem. Chem. Phys.* **2004**, *6*, 1769–1772.

(182)   Bahr, J. L.; Yang, J.; Kosynkin, D. V; Bronikowski, M. J.; Smalley, R. E.; Tour, J. M. *J. Am. Chem. Soc.* **2001**, *123* (27), 6536–6542.

(183)   Bahr, J. J. L.; Tour, J. M. J. *Chem. Mater.* **2001**, *13* (11), 3823–3824.

(184)   Dyke, C. A.; Tour, J. M. *J. Am. Chem. Soc.* **2003**, *125* (5), 1156–1157.

(185)   Peng, H.; Alemany, L. B.; Margrave, J. L.; Khabashesku, V. N. *J. Am. Chem. Soc.* **2003**, *125* (49), 15174–15182.

(186) Vanhorenbeke, B.; Vriamont, C.; Pennetreau, F.; Devillers, M.; Riant, O.; Hermans, S. *Chem. Eur. J.* **2013**, *19* (3), 852–856.

(187) Kamaras, K.; Itkis, M. E.; Hu, H.; Zhao, B.; Haddon, R. C. *Science* **2003**, *301*, 1501.

(188) Leinonen, H.; Rintala, J.; Siitonen, A.; Lajunen, M.; Pettersson, M. *Carbon* **2010**, *48* (9), 2425–2434.

(189) Delgado, J. L.; de la Cruz, P.; Langa, F.; Urbina, A.; Casado, J.; López Navarrete, J. T. *Chem. Commun.* **2004**, *4* (15), 1734–1735.

(190) Coleman, K. S.; Bailey, S. R.; Fogden, S.; Green, M. L. H. *J. Am. Chem. Soc.* **2003**, *125* (29), 8722–8723.

(191) Zheng, M.; Jagota, A.; Strano, M. S.; Santos, A. P.; Barone, P.; Chou, S. G.; Diner, B. A.; Dresselhaus, M. S.; McLean, R. S.; Onoa, G. B.; Samsonidze, G. G.; Semke, E. D.; Usrey, M.; Walls, D. J. *Science* **2003**, *302* (5650), 1545–1548.

(192) Arnold, M. S.; Green, A. A.; Hulvat, J. F.; Stupp, S. I.; Hersam, M. C. *Nat. Nanotechnol.* **2006**, *1* (1), 60–65.

(193) Schmidt, G.; Filoramo, A.; Derycke, V.; Bourgoin, J. P.; Chenevier, P. *Chem. - A Eur. J.* **2011**, *17* (5), 1415–1418.

(194) Darchy, L.; Hanifi, N.; Vialla, F.; Voisin, C.; Bayle, P. A.; Genovese, L.; Celle, C.; Simonato, J. P.; Filoramo, A.; Derycke, V.; Chenevier, P. *Carbon* **2014**, *66*, 246–258.

(195) Brinkman, W. F.; Haggan, D. E.; Troutman, W. W. *IEEE J. Solid-St. Circ.* **1997**, *32* (12), 1858–1864.

(196) Tans, S. J.; Verschueren, A. R. M.; Dekker, C. *Nature* **1998**, *393*, 49–52.

(197) Martel, R.; Schmidt, T.; Shea, H. R.; Hertel, T.; Avouris, P. *Appl. Phys. Lett.* **1998**, *73* (17), 2447–2449.

(198) Jin, S. H.; Islam, A. E.; Kim, T.; Kim, J.; Alam, M. A.; Rogers, J. A. *Adv. Funct. Mater.* **2012**, *22* (11), 2276–2284.

(199) What Is a Source Measure Unit (SMU)? http://www.ni.com/white-paper/6850/en/ (accessed Aug 21, 2015).

(200) Zhao, J.; Park, H.; Han, J.; Lu, J. P. *J. Phys. Chem. B* **2004**, *108* (14), 4227–4230.

(201) Zhao, J.; Lu, J. P.; Han, J.; Yang, C. K. *Appl. Phys. Lett.* **2003**, *82* (21), 3746–

301

3748.

(202)   Lee, Y. S.; Nardelli, M. B.; Marzari, N. *Phys. Rev. Lett.* **2005**, *95*, 76804.

(203)   López-Bezanilla, A.; Triozon, F.; Latil, S.; Blase, X.; Roche, S. *Nano Lett.* **2009**, *9* (3), 940–944.

(204)   Bouilly, D.; Hon, J.; Daly, N. S.; Trocchia, S.; Vernick, S.; Yu, J.; Warren, S.; Gonzalez, R. L.; Shepard, K. L.; Nuckolls, C. *Nano Lett.* **2016**, *16* (7), 4679–4685.

(205)   Wang, C.; Cao, Q.; Ozel, T.; Gaur, A.; Rogers, J. A.; Shim, M. *J. Am. Chem. Soc.* **2005**, *127* (32), 11460–11468.

(206)   Chakraborty, A. K.; Coleman, K. S.; Dhanak, V. R. *Nanotechnology* **2009**, *20* (15), 155704.

(207)   Balasubramanian, K.; Friedrich, M.; Jiang, C.; Fan, Y.; Mews, A.; Burghard, M.; Kern, K. *Adv. Mater.* **2003**, *15* (18), 1515–1518.

(208)   Margine, E. R.; Bocquet, M.-L.; Blase, X. *Nano Lett.* **2008**, *8* (10), 3315–3319.

(209)   Strano, M. S.; Dyke, C. a; Usrey, M. L.; Barone, P. W.; Allen, M. J.; Shan, H.; Kittrell, C.; Hauge, R. H.; Tour, J. M.; Smalley, R. E. *Science* **2003**, *301* (5639), 1519–1522.

(210)   Cabana, J.; Martel, R. *J. Am. Chem. Soc.* **2007**, *129* (8), 2244–2245.

(211)   Cabana, J.; Lavoie, S.; Martel, R. *J. Am. Chem. Soc.* **2010**, *132* (4), 1389–1394.

(212)   Park, H.; Zhao, J.; Lu, J. P. *Nano Lett.* **2006**, *6* (5), 916–919.

(213)   Lee, Y.-S. S.; Marzari, N. *Phys. Rev. Lett.* **2006**, *97* (11), 116801.

(214)   Lopez-Bezanilla, A.; Blase, X.; Roche, S. *Nano Res.* **2010**, *3*, 288–295.

(215)   Jiao, H.; Hommes, N. J. R. V. E.; Schleyer, P. V. R. *Org. Lett.* **2002**, *4* (14), 2393–2396.

(216)   Kingston, C. T.; Jakubek, Z. J.; Dénommée, S.; Simard, B. *Carbon* **2004**, *42*, 1657–1664.

(217)   In *Technical bulletin Single-Walled Carbon Nanotubes*; Sigma-Aldrich.

(218)   Huang, L.; Cui, X.; White, B.; O'Brien, S. P. *J. Phys. Chem. B* **2004**, *108* (42), 16451–16456.

(219)   Zhang, X.; Chenet, D.; Kim, B.; Yu, J.; Tang, J.; Nuckolls, C.; Hone, J. *J. Vac. Sci. Technol. B* **2013**, *31* (6), 06FI01.

(220) Lee, J.-O.; Park, C.; Kim, J.-J.; Kim, J.; Park, J. W.; Yoo, K.-H. *J. Phys. D Appl. Phys.* **2000**, *33* (16), 1953–1956.

(221) Acres, R. G.; Ellis, A. V.; Alvino, J.; Lenahan, C. E.; Khodakov, D. a.; Metha, G. F.; Andersson, G. G. *J. Phys. Chem. C* **2012**, *116*, 6289–6297.

(222) Howarter, J. A.; Youngblood, J. P. *Langmuir* **2006**, *22* (26), 11142–11147.

(223) Gadallah, F. F.; Elofson, R. M. *J. Org. Chem.* **1969**, *34* (11), 3335–3338.

(224) Heinrich, M. R. *Chem. Eur. J.* **2009**, *15* (4), 820–833.

(225) Lipińska, M. E.; Rebelo, S. L. H.; Pereira, M. F. R.; Gomes, J. A. N. F.; Freire, C.; Figueiredo, J. L. *Carbon* **2012**, *50* (9), 3280–3294.

(226) Schmidt, G.; Gallon, S.; Esnouf, S.; Bourgoin, J.-P.; Chenevier, P. *Chem. Eur. J.* **2009**, *15* (9), 2101–2110.

(227) Mattiuzzi, A.; Jabin, I.; Mangeney, C.; Roux, C.; Reinaud, O.; Santos, L.; Bergamini, J.-F.; Hapiot, P.; Lagrost, C. *Nat. Comm.* **2012**, *3*, 1130.

(228) Salice, P.; Fabris, E.; Sartorio, C.; Fenaroli, D.; Figà, V.; Casaletto, M. P.; Cataldo, S.; Pignataro, B.; Menna, E. *Carbon* **2014**, *74*, 73–82.

(229) Braunstein, P.; Rosé, J. In *Metal Clusters in Chemistry*; Braunstein, P., Oro, L. A., Raithby, P. R., Eds.; Wiley-VCH: Weinheim, 1999; pp 616–677.

(230) Hermans, S. In *Atomically-Precise Methods for Synthesis of Solid Catalysts*; Hermans, S., Visart de Bocarmé, T., Eds.; RSC Catalysis Series No. 22, 2015; pp 55–86.

(231) Nashner, M. S.; Frenkel, A. I.; Adler, D. L.; Shapley, J. R.; Nuzzo, R. G. *J. Am. Chem. Soc.* **1997**, *119* (33), 7760–7771.

(232) Nashner, M. S.; Frenkel, A. I.; Somerville, D.; Hills, C. W.; Shapley, J. R.; Nuzzo, R. G. *J. Am. Chem. Soc.* **1998**, *120* (10), 8093–8101.

(233) Willocq, C.; Vidick, D.; Tinant, B.; Delcorte, A.; Bertrand, P.; Devillers, M.; Hermans, S. *Eur. J. Inorg. Chem.* **2011**, *2011* (30), 4721–4729.

(234) Vidick, D.; Ke, X.; Devillers, M.; Poleunis, C.; Delcorte, A.; Moggi, P.; Van Tendeloo, G.; Hermans, S. *Beilstein J. Nanotechnol.* **2015**, *6*, 1287–1297.

(235) Vriamont, C.; Haynes, T.; McCague-Murphy, E.; Pennetreau, F.; Riant, O.; Hermans, S. *J. Catal.* **2015**, *329*, 389–400.

(236) Willocq, C.; Delcorte, A.; Hermans, S.; Bertrand, P.; Devillers, M. *J. Phys. Chem. B* **2005**, *109* (19), 9482–9489.

(237) Wu, Z.; Chen, Z.; Du, X.; Logan, J. M.; Sippel, J.; Nikolou, M.; Kamaras, K.; Reynolds, J. R.; Tanner, D. B.; Hebard, A. F.; Rinzler, A. G. *Science* **2004**, *305* (5688), 1273–1276.

(238) Dresselhaus, M. S.; Dresselhaus, G.; Saito, R.; Jorio, a. *Phys. Rep.* **2005**, *409* (2), 47–99.

(239) Pennetreau, F.; Riant, O.; Hermans, S. *Chem. - A Eur. J.* **2014**, *20* (46), 15009–15012.

(240) Jeon, E. K.; Seo, E.; Lee, E.; Lee, W.; Um, M.-K.; Kim, B.-S. *Chem. Commun.* **2013**, *49* (33), 3392–3394.

(241) Piña, S.; Cedillo, D. M.; Tamez, C.; Izquierdo, N.; Parsons, J. G.; Gutierrez, J. J. *Tetrahedron Lett.* **2014**, *55* (40), 5468–5470.

(242) Boothroyd, S. R.; Kerr, M. A. *Tetrahedron Lett.* **1995**, *36* (14), 2411–2414.

(243) Kim, S.; Kim, E.; Kim, B. M. *Chem. Asian J.* **2011**, *6* (8), 1921–1925.

(244) Huang, L.; Luo, P.; Xiong, M.; Chen, R.; Wang, Y.; Xing, W.; Huang, J. *Chin. J. Chem.* **2013**, *31* (8), 987–991.

(245) Li, H.; Zhang, R.; Wang, H.; Pan, Y.; Shi, Y. *Synth. Commun.* **1997**, *27* (17), 3047–3052.

(246) Gkizis, P. L.; Stratakis, M.; Lykakis, I. N. *Catal. Commun.* **2013**, *36*, 48–51.

(247) Kumbhar, P. S.; Sanchez-Valente, J.; Figueras, F. *Tetrahedron Lett.* **1998**, *39*, 2573–2574.

(248) Kerr, M.; Suckling, C. J. *Tetrahedron Lett.* **1988**, *29* (43), 5545–5548.

(249) Willocq, C.; Dubois, V.; Khimyak, Y. Z.; Devillers, M.; Hermans, S. *J. Mol. Catal. A - Chem.* **2012**, *365*, 172–180.

(250) Byung, H. H.; Dae, H. S.; Sung, Y. C. *Tetrahedron Lett.* **1985**, *26* (50), 6233–6234.

(251) Zhou, H.; Shi, L.; Sun, Q. *Chin. J. Catal.* **2012**, *33* (9–10), 1463–1469.

(252) Gu, X.; Qi, W.; Wu, S.; Sun, Z.; Xu, X.; Su, D. *Catal. Sci. Technol.* **2014**, *4* (6), 1730–1733.

(253) Wu, S.; Wen, G.; Wang, J.; Rong, J.; Zong, B.; Schlögl, R.; Su, D. S. *Catal. Sci. Technol.* **2014**, *4* (12), 4183–4187.

(254) Gao, Y.; Ma, D.; Wang, C.; Guan, J.; Bao, X. *Chem. Commun.* **2011**, *47* (8), 2432–2434.

304

(255)   Feng, C.; Zhang, H. Y.; Shang, N. Z.; Gao, S. T.; Wang, C. *Chin. Chem. Lett.* **2013**, *24* (6), 539–541.

(256)   Li, B.; Xu, Z. *J. Am. Chem. Soc.* **2009**, *131* (45), 16380–16382.

(257)   Zeynizadeh, B.; Setamdideh, D. *Synth. Commun.* **2006**, *36* (18), 2699–2704.

(258)   Ramanathan, T.; Fisher, F. T.; Ruoff, R. S.; Brinson, L. C. *Chem. Mater.* **2005**, *17* (6), 1290–1295.

(259)   Buckland, P. R.; Gourley, R. N. Method for reducing aromatic nitro compounds. EP0347136A2, 1989.

(260)   Precious Metals Management http://www.infomine.com/investment/platinum/ (accessed Feb 17, 2016).

(261)   Foster, D. F.; Harrison, J.; Nicholls, B. S.; Smith, A. K. *J. Organomet. Chem.* **1983**, *248*, C29–C32.

(262)   Braunstein, P. *J. Organomet. Chem.* **2004**, *689*, 3953–3967.

(263)   Mutin, P. H.; Guerrero, G.; Vioux, A. *C. R. Chim.* **2003**, *6*, 1153–1164.

(264)   Tsiavaliaris, G.; Haubrich, S.; Merckle, C.; Blümel, J. *Synlett* **2001**, No. 3, 391–393.

(265)   Behringer, K. D.; Blumel, J. *Chem. Commun.* **1996**, 653–654.

(266)   Klinke, C.; Hannon, J. B.; Afzali, A.; Avouris, P. *Nano Lett.* **2006**, *6* (5), 906–910.

(267)   Bouilly, D.; Janssen, J. L.; Cabana, J.; Côté, M.; Martel, R. *ACS Nano* **2015**, *9* (3), 2626–2634.

(268)   Wang, C.; Ryu, K.; Badmaev, A.; Patil, N.; Lin, A.; Mitra, S.; Wong, H. S. P.; Zhou, C. *Appl. Phys. Lett.* **2008**, *93* (3), 33101.

(269)   Klinke, C.; Chen, J.; Afzali, A.; Avouris, P. *Nano Lett.* **2005**, *5* (3), 555–558.

(270)   Voggu, R.; Pal, S.; Pati, S. K.; Rao, C. N. R. *J. Phys. Condens. Matter* **2008**, *20* (21), 215211.

(271)   Zhang, H.; Pan, X.; Liu, J. J.; Qian, W.; Wei, F.; Huang, Y.; Bao, X. *ChemSusChem* **2011**, *4* (7), 975–980.

(272)   Rao, A. M.; Eklund, P. C.; Bandow, S.; Thess, A.; Smalley, R. E. *Nature* **1997**, *388*, 257–259.

(273)   Star, A.; Han, T.-R.; Gabriel, J.-C. P.; Bradley, K.; Grüner, G. *Nano Lett.* **2003**, *3* (10), 1421–1423.

(274) Rao, C. N. R.; Voggu, R. *Mater. Today* **2010**, *13* (9), 34–40.

(275) Nicholls, J. N.; Vargas, M. D. *Inorg. Synth.* **1989**, *26*, 280–285.

(276) Hermans, S.; Khimyak, T.; Johnson, B. F. G. *J. Chem. Soc., Dalt. Trans.* **2001**, No. 22, 3295–3302.

(277) Sieval, A. B.; Linke, R.; Heij, G.; Meijer, G.; Zuilhof, H.; Sudho, E. J. R. *Langmuir* **2001**, *17* (24), 7554–7559.

(278) Willocq, C.; Hermans, S.; Devillers, M. *J.* **2008**, *112* (14), 5533–5541.

(279) Jeon, M.; Han, J.; Park, J. *ACS Catal.* **2012**, *2*, 1539–1549.

(280) John, J.; Gravel, E.; Hagège, A.; Li, H.; Gacoin, T.; Doris, E. *Angew. Chem. Int. Ed. Engl.* **2011**, *50* (33), 7533–7536.

(281) Moretto, H.-H.; Schulze, M.; Wagner, G. In *Ullmann's Encyclopedia of Industrial Chemistry*; Wiley-VCH Verlag GmbH & Co., 2000.

(282) Valliant-Saunders, K.; Gunn, E.; Shelton, G. R.; Hrovat, D. a.; Borden, W. T.; Mayer, J. M. *Inorg. Chem.* **2007**, *46* (13), 5212–5219.

(283) Corbin, R. A.; Ison, E. A.; Abu-Omar, M. M. *Dalt. Trans.* **2009**, No. 15, 2850–2855.

(284) Kikukawa, Y.; Kuroda, Y.; Yamaguchi, K.; Mizuno, N. *Angew. Chem. Int. Ed.* **2012**, *51* (10), 2434–2437.

(285) Lee, Y.; Seomoon, D.; Kim, S.; Han, H.; Chang, S.; Lee, P. H. *J. Org. Chem.* **2004**, *69* (11), 1741–1743.

(286) Lee, M.; Ko, S.; Chang, S. *J. Am. Chem. Soc.* **2000**, *122* (48), 12011–12012.

(287) Ison, E. A.; Corbin, R. A.; Abu-Omar, M. M. *J. Am. Chem. Soc.* **2005**, *127* (34), 11938–11939.

(288) Krüger, A.; Albrecht, M. *Chem. Eur. J.* **2012**, *18* (2), 652–658.

(289) Barnes, Garret H., J.; Daughenbaugh, N. E. *J. Org. Chem.* **1966**, *31*, 885–887.

(290) Chauhana, B. P. S.; Sarkara, A.; Chauhanb, M.; Rokab, A. *Appl. Organometal. Chem.* **2009**, *23* (10), 385–390.

(291) Shimizu, K. I.; Kubo, T.; Satsuma, A. *Chem. Eur. J.* **2012**, *18* (8), 2226–2229.

(292) Kamachi, T.; Shimizu, K. I.; Yoshihiro, D.; Igawa, K.; Tomooka, K.; Yoshizawa, K. *J. Phys. Chem. C* **2013**, *117* (44), 22967–22973.

(293) Jeon, M.; Han, J.; Park, J. *ChemCatChem* **2012**, *4* (4), 521–524.

306

(294) Asao, N.; Ishikawa, Y.; Hatakeyama, N.; Menggenbateer; Yamamoto, Y.; Chen, M.; Zhang, W.; Inoue, A. *Angew. Chem.* **2010**, *49* (52), 10291–10293.

(295) Mitsudome, T.; Noujima, A.; Mizugaki, T.; Jitsukawa, K.; Kaneda, K. *Chem. Commun.* **2009**, No. 35, 5302–5304.

(296) Mitsudome, T.; Arita, S.; Mori, H.; Mizugaki, T.; Jitsukawa, K.; Kaneda, K. *Angew. Chem. Int. Ed.* **2008**, *47* (41), 7938–7940.

(297) Choi, E.; Lee, C.; Na, Y.; Chang, S. *Org. Lett.* **2002**, *4* (14), 2369–2371.

(298) Mori, K.; Tano, M.; Mizugaki, T.; Ebitani, K.; Kaneda, K. *New J. Chem.* **2002**, *26* (11), 1536–1538.

(299) Smith, D. W. In *Inorganic Substances: A Prelude to the Study of Descriptive Inorganic Chemistry*; Press, C. U., Ed.; Cambridge, 1990; p 117.

(300) Contreras, J. L.; Fuentes, G. A. In *Sintering - Methods and Products*; Shatokha, V., Ed.; InTech, 2012; pp 91–126.

(301) Wanke, S. E.; Flynn, P. C. *Catal. Rev.* **1975**, *12* (1), 93–135.

(302) Forzatti, P.; Lietti, L. *Catal. Today* **1999**, *52*, 165–181.

(303) Bartholomew, C. H. *Appl. Catal. A - Gen.* **2001**, *212*, 17–60.

(304) Argyle, M.; Bartholomew, C. *Catalysts* **2015**, *5* (1), 145–269.

(305) Chen, Y.; Haddon, R. C.; Fang, S.; Rao, a. M.; Eklund, P. C.; Lee, W. H.; Dickey, E. C.; Grulke, E. a.; Pendergrass, J. C.; Chavan, A.; Haley, B. E.; Smalley, R. E. *J. Mater. Res.* **2011**, *13* (9), 2423–2431.

(306) Lee, W. H.; Kim, S. J.; Lee, W. J.; Lee, J. G.; Haddon, R. C.; Reucroft, P. J. *Appl. Surf. Sci.* **2001**, *181*, 121–127.

(307) Hu, H.; Zhao, B.; Hamon, M. A.; Kamaras, K.; Itkis, M. E.; Haddon, R. C. *J. Am. Chem. Soc.* **2003**, *125* (48), 14893–14900.

(308) Holzinger, M.; Vostrowsky, O.; Hirsch, A.; Hennrich, F.; Kappes, M.; Weiss, R. *Angew. Chem. Int. Ed.* **2001**, *40* (21), 4002–4005.

(309) Holzinger, M.; Abraham, J.; Whelan, P.; Graupner, R.; Ley, L.; Hennrich, F.; Kappes, M.; Hirsch, A. *J. Am. Chem. Soc.* **2003**, *125* (28), 8566–8580.

(310) Han, J.; Gao, C. *Nano-Micro Lett.* **2010**, *2* (3), 213–226.

(311) Holzinger, M.; Steinmetz, J.; Samaille, D.; Glerup, M.; Paillet, M.; Bernier, P.; Ley, L.; Graupner, R. *Carbon* **2004**, *42*, 941–947.

(312) Tagmatarchis, N.; Prato, M. *J. Mater. Chem.* **2004**, No. 14, 437–439.

(313)   Lu, X.; Tian, F.; Wang, N.; Zhang, Q. *Org. Lett.* **2002**, *4* (24), 4313–4315.

(314)   Syrgiannis, Z.; Hadad, C.; Prato, M. *Eur. J. Org. Chem.* **2014**, *2014* (20), 4225–4229.

(315)   Bingel, C. *Chem. Ber.* **1993**, *126*, 1957–1959.

(316)   Diederich, F.; Thilgen, C. *Science* **1996**, *271* (5247), 317–323.

(317)   Camps, X.; Hirsch, A. *J. Chem. Soc., Perkin Trans. 1* **1997**, *97*, 1595–1596.

(318)   Betz, P.; Krueger, A. *Chem. Phys. Chem.* **2012**, *13* (10), 2578–2584.

(319)   Economopoulos, S. P.; Pagona, G.; Yudasaka, M.; Iijima, S.; Tagmatarchis, N. *J. Mater. Chem.* **2009**, *19* (39), 7326–7331.

(320)   Worsley, K. A.; Moonoosawmy, K. R.; Kruse, P. *Nano Lett.* **2004**, *4* (8), 1541–1546.

(321)   Ashcroft, J. M.; Hartman, K. B.; Mackeyev, Y.; Hofmann, C.; Pheasant, S.; Alemany, L. B.; Wilson, L. J. *Nanotechnology* **2006**, *17* (20), 5033–5037.

(322)   Bosch-Navarro, C.; Busolo, F.; Coronado, E.; Duan, Y.; Martí-Gastaldo, C.; Prima-Garcia, H. *J. Mater. Chem. C* **2013**, *1* (30), 4590–4598.

(323)   Umeyama, T.; Tezuka, N.; Fujita, M.; Matano, Y.; Takeda, N.; Murakoshi, K.; Yoshida, K.; Isoda, S.; Imahori, H. *J. Phys. Chem. C* **2007**, *111* (27), 9734–9741.

(324)   Miyaura, N.; Suzuki, A. *J. Chem. Soc., Chem. Commun.* **1979**, 866–867.

(325)   Miyaura, N.; Yanagi, T.; Suzuki, A. *Synth. Commun.* **1981**, *11* (7), 513–519.

(326)   The 2010 Nobel Prize in Chemistry http://www.nobelprize.org/nobel_prizes/chemistry/laureates/2010/popular-chemistryprize2010.pdf (accessed Jan 30, 2016).

(327)   Suzuki, A. *Angew. Chem. Int. Ed.* **2011**, *50* (30), 6723–6733.

(328)   Johansson Seechurn, C. C. C.; DeAngelis, A.; Colacot, T. J. In *New Trends in Cross-Coupling: Theory and Applications*; RSC Catalysis Series, 2014; pp 1–19.

(329)   Johansson Seechurn, C. C. C.; Kitching, M. O.; Colacot, T. J.; Snieckus, V. *Angew. Chem. Int. Ed.* **2012**, *51* (21), 5062–5085.

(330)   Miyaura, N.; Suzuki, A. *Chem. Rev.* **1995**, *95*, 2457–2483.

(331)   Suzuki, A. *J. Organomet. Chem.* **1999**, *576*, 147–168.

(332)   Kotha, S.; Lahiri, K.; Kashinath, D. *Tetrahedron* **2002**, *58* (625), 9633–9695.

(333)   Lima, C. F.; Rodrigues, A. S.; Silva, V. L. M.; Silva, A. M. S.; Santos, L. M. *Chem. Cat. Chem.* **2014**, *6*, 1291–1302.

(334)   Lennox, A. J. J.; Lloyd-Jones, G. C. *Angew. Chem. Int. Ed.* **2013**, *52*, 7362–7370.

(335)   Lennox, A. J. J.; Lloyd-Jones, G. C. *Chem. Soc. Rev.* **2014**, *43*, 412–443.

(336)   Grotjahn, D. B. *Comprehensive Organometallic Chemistry II*. 1995, pp 741–770.

(337)   Pan, Y.; Mague, J. T.; Fink, M. J. *Organometallics* **1992**, *11* (11), 3495–3497.

(338)   Dervisi, A.; Edwards, P. G.; Newman, P. D.; Tooze, R. P. *J. Chem. Soc., Dalt. Trans.* **2000**, No. 4, 523–528.

(339)   Amatore, C.; Jutand, A. *Coord. Chem. Rev.* **1998**, *178–180*, 511–528.

(340)   Genet, M. J.; Dupont-Gillain, C. C.; Rouxhet, P. G. In *Medical Applications of Colloids*; Matijevic, E., Ed.; 2008; pp 177–307.

(341)   Cano, M.; Benito, A.; Maser, W. K.; Urriolabeitia, E. P. *Carbon* **2011**, *49* (2), 652–658.

(342)   Cornelio, B.; Rance, G. A.; Laronze-Cochard, M.; Fontana, A.; Sapi, J.; Khlobystov, A. N. *J. Mater. Chem. A* **2013**, *1* (31), 8737–8744.

(343)   Division, E.; Processing, A. P. *Inorg. Chim. Acta* **1979**, *35*, L343–L344.

(344)   Nomura, S.; Itoh, T.; Nakasho, H.; Uno, T.; Kubo, M.; Sada, K.; Inoue, K.; Miyata, M. *J. Am. Chem. Soc.* **2004**, *126*, 2035–2041.

(345)   Krüger, M.; Buitelaar, M. R.; Nussbaumer, T.; Schönenberger, C.; Forró, L. *Appl. Phys. Lett.* **2001**, *78* (9), 1291–1293.

(346)   Rosenblatt, S.; Yaish, Y.; Park, J.; Gore, J.; Sazonova, V.; McEuen, P. L. *Nano Lett.* **2002**, *2* (8), 869–872.

(347)   Mitsudome, T.; Arita, S.; Mori, H.; Mizugaki, T.; Jitsukawa, K.; Kaneda, K. *Angew. Chemie - Int. Ed.* **2008**, *47* (41), 7938–7940.

(348)   Kikukawa, Y.; Kuroda, Y.; Yamaguchi, K.; Mizuno, N. *Angew. Chemie - Int. Ed.* **2012**, *51* (10), 2434–2437.

(349)   Zhou, X.; Xu, W.; Liu, G.; Panda, D.; Chen, P. *J. Am. Chem. Soc.* **2010**, *132* (1), 138–146.

(350)   Jin, R.; Sun, S.; Yang, Y.; Xing, Y.; Yu, D.; Yu, X.; Song, S. *Dalton Trans.*

309

2013, *42* (22), 7888–7893.

(351) Peng, Y.; Wang, Z.; Liu, W.; Zhang, H.; Zuo, W.; Tang, H.; Chen, F.; Wang, B. *Dalt. Trans.* **2015**, *44* (28), 12871–12877.

(352) Georgakilas, V.; Gournis, D.; Tzitzios, V.; Pasquato, L.; Guldi, D. M.; Prato, M. *J. Mater. Chem.* **2007**, *17* (26), 2679–2694.

(353) Serp, P.; Castillejos, E. *ChemCatChem* **2010**, *2* (1), 41–47.

(354) Hermans, S.; Khimyak, T.; Feeder, N.; Teat, S. J.; Johnson, B. F. G. *Dalt. Trans.* **2003**, No. 4, 672–684.

(355) Cotton, F. A. *Inorg. Chem.* **1964**, *3* (9), 1217–1220.